Perylene Bisimide Cyclophanes: Recognition of Alkaloids, Aggregation Behavior in Aqueous Environment and Guest-Mediated Chirality Transfer

Dissertation zur Erlangung des

Naturwissenschaftlichen Doktorgrades

der Julius-Maximilians-Universität Würzburg

vorgelegt von

Meike Sapotta

aus Heilbronn

Würzburg 2019

Eingereicht bei der Fakultät für Chemie und Pharmazie am:

15.12.2019

Gutachter der schriftlichen Arbeit:

1. Gutachter: Prof. Dr. Frank Würthner

2. Gutachter: Priv.-Doz. Dr. Florian Beuerle

Prüfer des öffentlichen Promotionskolloquiums:

1. Prüfer: Prof. Dr. Frank Würthner

2. Prüfer: Priv.-Doz. Dr. Florian Beuerle

3. Prüfer: Prof. Dr. Volker Engel

Datum des öffentlichen Promotionskolloquiums:

20.02.2020

Doktorurkunde ausgehändigt am:

_____

für meine Familie

LIST OF ABBREVIATIONS

Ac	acetate
ADP	adenosine diphosphate
AFM	atomic force microscopy
AMP	adenosine monophosphate
Ar	aryl
ATP	adenosine triphosphate
Bn	Benzyl
Bu	butyl
CD	circular dichroism
CMP	cytidine monophosphate
CTP	cytidine triphosphate
CuAAC	copper(I)-catalyzed alkyne-azide coupling
dba	dibenzylideneacetonyl
DMF	dimethylformamide
DMSO	dimethyl sulphoxide
DNA	deoxyribonucleic acid
eq.	equivalents
exc.	excess
Et	ethyl
fl	fluorescence
GlcNAc	*β*-*N*-acetylglucosamin
GMP	guanosine monophosphate

GTP	guanosine triphosphate
i. e.	which means (latin: *id est*)
ITC	isothermal titration calorimetry
K_a	host-guest association constant ($K_a = 1/ K_d$)
K_d	host-guest dissociation constant ($K_d = 1/ K_a$)
K_{dim}	dimerization constant
LCST	lower critical solution temperature
Me	methyl
NAD	nicotinamide adenine dinucleotide
NBI	naphthalene bisimide
NMP	*N*-methylpyrrolidone
NMR	nuclear magnetic resonance
NOESY	nuclear Overhauser effect spectroscopy
obs	observed
OD	optical density
OEG	oligoethylene glycol
PAH	polycyclic aromatic hydrocarbon
PBA	perylene bisanhydride
PBI	perylene bisimide
ROESY	rotating-frame nuclear Overhauser effect correlation spectroscopy
r.t.	room temperature
rel	relative
TA	transient absorption

TBAF	tetra-*n*-butylammonium fluoride
TBTA	tris(benzyltriazolylmethyl)amine
Tf	triflate
TIPS	triisopropylsilyl
Ts	toluenesulfonyl
TTP	thymidine triphosphate
UMP	uridine monophosphate
UTP	uridine triphosphate
UV-vis	ultraviolet visible
vol%	volume percent

TABLE OF CONTENTS

Chapter 1 – Introduction and Aim of This Thesis 1

Chapter 2 – Literature Survey 5

2.1 Xylylene-Bridged Cyclic Perylene Bisimide Dimers 5

2.2 Recognition of Small Biomolecules and Natural Products by Cyclophanes in Water….. 7

2.2.1 Nucleobase derivatives 8

2.2.2 Amino Acids 16

2.2.3 Neurotransmitters 20

2.2.4 Carbohydrates 22

2.2.5 Alkaloids 29

2.3 Conformational Selection and Induced Fit 31

Chapter 3 – Results and Discussion 39

3.1 Synthesis 39

3.2 A Water-Soluble Perylene Bisimide Cyclophane as a Molecular Probe for the Recognition of Aromatic Alkaloids 42

3.2.1 Introduction 42

3.2.2 Optical Properties of **[2PBI]-1p** 44

3.2.3 Host-Guest Binding Studies of **[2PBI]-1p** with Aromatic Alkaloids 45

3.2.4 Structure Binding-Property Relationship 48

3.2.5 Structural Elucidation 49

3.2.6 Conclusion 51

3.2.7 Appendix I 52

3.3 Entropy-Driven Self-Assembly and Guest-Mediated Disassembly of a Perylene Bisimide Cyclophane in Water 64

3.3.1 Introduction 65

3.3.2 Solvent-Dependent UV-vis Studies of **[2PBI]-1m** and **ref-PBI-1m** 66

3.3.3 Temperature-Dependent Spectroscopic Studies of **[2PBI]-1m** and **ref-PBI-1m** in Water 68
3.3.4 Concentration-Dependent UV-vis Studies of **[2PBI]-1m** and **ref-PBI-1m** 71
3.3.5 Atomic Force Microscopy of **[2PBI]-1m** and **ref-PBI-1m** 73
3.3.6 Discussion of the Thermodynamic Bias 75
3.3.7 Host-Guest Binding Properties of **[2PBI]-1m** in Water 79
3.3.8 Conclusion 82
3.3.9 Appendix II 84
3.4 Guest-Mediated Chirality Transfer in Host-Guest Complexes of an Atropisomeric Perylene Bisimide Cyclophane Host 95
3.4.1 Introduction 96
3.4.2 Synthesis of Chiral Guests (*S*)-**G13** and (*S*)-**G14** 97
3.4.3 Temperature-dependent ^{1}H NMR studies of **[2PBI]-2** 98
3.4.4 Host-Guest Binding Studies of **[2PBI]-2** with Chiral Guests 102
3.4.5 Kinetic Studies 104
3.4.6 Conclusion 108
3.4.7 Appendix III 109
Chapter 4 – Summary 122
Chapter 5 – Zusammenfassung 126
Chapter 6 – Experimental Section 130
6.1 Materials and Methods 130
6.2 Synthesis and Characterization 134
References 152
Danksagung 167

Chapter 1

–

Introduction and Aim of This Thesis

Specific molecular recognition is an essential prerequisite for countless processes in living biological systems. To name but a few examples, the activation of enzymatic reactions requires binding of the right substrate to the enzyme,[1] signal transduction cascades are not initiated unless a particular ligand is complexed by a receptor[2] or responses of the immune system are triggered by the interaction of antigens with antibodies.[3] Consequently, in-depth knowledge of the exact interplay between the participants of such recognition events including mechanistic details of the binding process is of paramount importance for the development of efficient drugs and therapies.[4] However, biological systems are of high complexity and diversity and thus, as of yet, our understanding of them remains unsatisfactory. Further challenges are posed by water, the medium in which biological systems operate. Despite great advances in elucidating how the unique properties of this solvent give rise to the hydrophobic effect,[5] further essential insight on how the thermodynamic forces connected to it drive and direct all recognition and self-assembly processes in living organisms is still required.[6]

In this regard, the field of supramolecular chemistry is ideally positioned to provide complementary details on the way molecules interact.[7] Host-guest chemistry, for example, which represents one of the origins and corner stones of supramolecular chemistry,[8] concerns itself with the design of artificial receptors which mimic or model recognition processes observed in living organisms. Indeed, since the 1960s, when Charles Pedersen's discovery of crown ethers and their ability to bind cations[9] opened up the way for supramolecular chemistry, scientists have been intrigued with synthetic receptors.[10] In particular, macrocyclic hosts have attracted enormous interest. This fascination is equally owed to the synthetic challenges associated with the macrocyclic motif,[11] to unique properties that result from the structural arrangement of the subunits in a cyclic array[12] and, of course, to the ability to include

guest molecules within their void leading to molecular recognition.[10a, 10b, 13] Over the decades, scientists have strived to design more and more refined ring systems not only for the recognition of metal cations[10a] but also for the directed and selective encapsulation of a broad variety of organic substrates.[14] Due to promising biological and medical applications, a particular interest is focused on the water-soluble representatives of such artificial receptors.[15] The most prominent examples in this respect are cyclodextrins[16] and cucurbiturils[17] as well as hydrophilic pillararenes[18] and calixarenes,[19] for which a vast number of functional complexes are known so far.[16-19] Hydrophilic cyclophanes, where hydrophobic binding pockets are tailor-made by diverse aromatic π-surfaces held apart by appropriate linkers, are also of high significance for molecular recognition.[20] When compared to the binding modes of the classic players, like cucurbiturils and cyclodextrins, cyclophanes additionally employ π−π-,[21] cation−π[22] and CH−π-interactions[23] for guest encapsulation. Such non-covalent interactions make cyclophanes suitable hosts not only for biologically important aromatic molecules such as certain amino acids,[24] nucleotides,[20a, 25] the neurotransmitters epinephrine or dopamine,[26] but also for carbohydrates[27] in water.

Perylene bisimide (PBI) dyes are an outstanding class of chromophores with unique optical properties exhibiting absorption and emission maxima in the visible spectral range, which have long since secured their position among the key players in functional supramolecular chemistry.[28] They have also been widely applied as molecular probes for the detection and sensing of biological materials.[29] Recently, a PBI cyclophane host was presented by Spenst and Würthner which acts as a host and fluorescence turn-on/turn-off sensor for polycyclic aromatic hydrocarbons (PAHs) in organic solvents.[30] However, the hydrophobic nature of this cyclophane prohibits its use as synthetic receptor for biologically interesting guests in aqueous environment foreclosing possible promising biological applications.

Inspired by the fact that sufficient solubility in aqueous media can be achieved by functional substitution of PBIs with polar groups,[31] one of the essential aims of this thesis was the design and successful synthesis of the new water-soluble PBI cyclophanes **[2PBI]-1m** and **[2PBI]-1p**, which are appended with branched, hydrophilic oligoethylene glycol (OEG) chains (Figure 1a). The letters m and p in the designation of the cyclophanes refer to the positon of the solubilizing OEG-chains at the aryloxy bay substituents with respect to the PBI core. Subsequently, the focus was set on the elucidation of properties of PBI cyclophane hosts which are also of relevance for recognition processes in biological systems (Figure 1b). The performance of the

new amphiphilic PBI cyclophane **[2PBI]-1p** as synthetic receptors for various natural aromatic alkaloids in aqueous media was thoroughly investigated. Alkaloids represent a prominent class of ubiquitous nitrogen containing natural compounds with a great structural variety and diverse biological activity.[32] As of yet, no chromophore host acting as a molecular probe for a range of alkaloids such as harmine or harmaline is known. In addition, the self-association behavior of cyclophane host **[2PBI]-1m** and its reference monomer in water was studied in order to gain insights into the thermodynamic driving forces affecting the self-assembly process of these two PBI systems in aqueous environment. Moreover, the chirality transfer upon guest binding previously observed for a PBI cyclophane was investigated further.[33] The assignment of the underlying mechanism of guest recognition to either the induced fit or conformational selection model was of particular interest.[34]

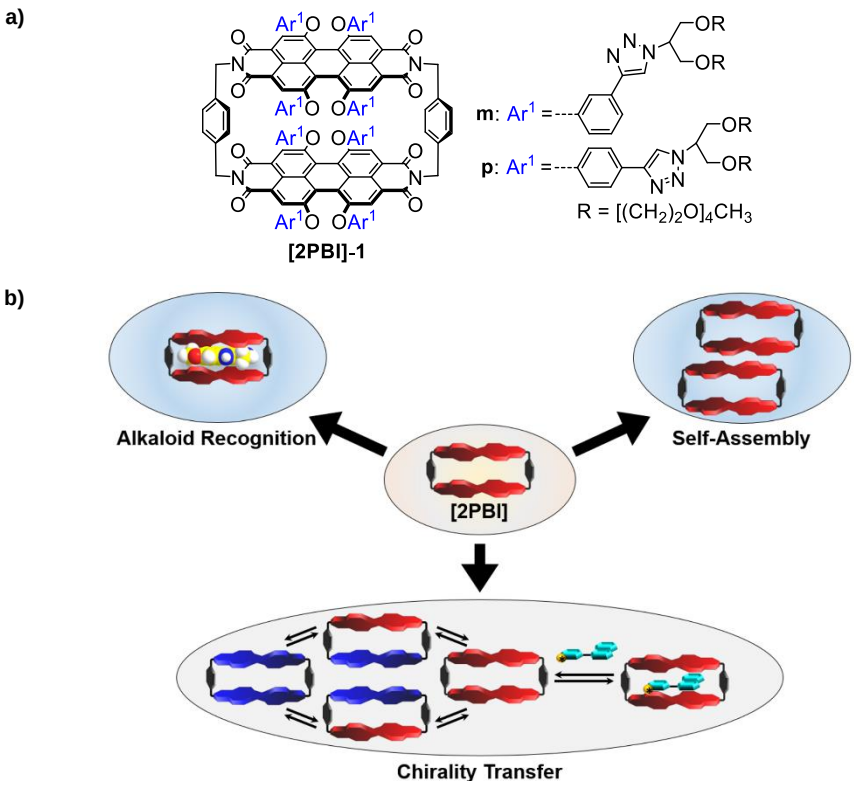

Figure 1. (a) Molecular structures of the novel water-soluble perylene bisimide cyclophanes **[2PBI]-1m** and **[2PBI]-1p**. **(b)** Schematic representation of the properties of the structural motif **[2PBI]** of perylene bisimide cyclophanes which were investigated in this work: alkaloid recognition and self-assembly in water and chirality transfer upon binding of a chiral guest.

In Chapter 2, previous results on *para*-xylylene-bridged PBI cyclophanes are briefly summarized followed by an overview on the versatility of water-soluble cyclophanes as hosts for natural products and biomolecules such as nucleobase derivatives or carbohydrates. Furthermore, the mathematic derivation of the two limiting cases of guest recognition models in biological systems, namely induced fit and conformational selection, is presented.

In Chapter 3, the results of this thesis are discussed in detail. After a brief description of the synthesis of the target compounds the recognition of naturally occurring aromatic alkaloids by a water-soluble perylene bisimide cyclophane host is elucidated along with the structure-binding property relationship observed for the natural product guests. In addition, the thermodynamic bias for the self-assembly behavior of an amphiphilic PBI cyclophane and its reference monomer in water is described and rationalized in terms of the orientation of the solubilizing side chains around the respective PBI derivative. Last but not least, the chirality transfer of chiral guests to a PBI cyclophane host in $CHCl_3$ is outlined together with an attempt to assign the guest recognition mechanism to either the induced fit or conformational selection model.

Chapter 4 and Chapter 5 conclude this work with summaries both in English and in German.

In Chapter 6, a documentation of the materials and methods used in this thesis as well as experimental details is provided.

Chapter 2

–

Literature Survey

2.1 Xylylene-Bridged Cyclic Perylene Bisimide Dimers

Even though a variety of cyclic perylene bisimide (PBI) dimers with different covalent bridging units has been known for some time,[35] only recently the introduction of a rigid *para*-xylylene spacer by Spenst and Würthner resulted in a PBI cyclophane (**[2PBI]-2**) with appropriate features for the binding of guest molecules such as polyaromatic hydrocarbons (PAH) (Figure 2).[30a] The xylylene linker is sufficiently rigid to prevent the intramolecular aggregation of the PBI cores,[36] keeping them at an interchromophoric distance of approximately 6.5 Å instead.[30a]

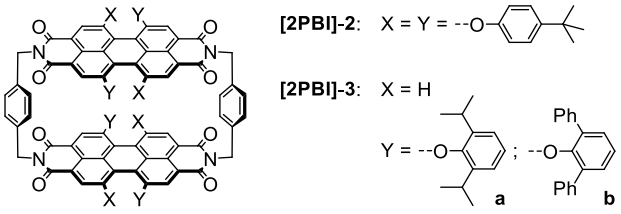

Figure 2. Chemical structures of *para*-xylylene bridged PBI cyclophanes **[2PBI]-2** and **[2PBI]-3a** and **b**.[30a, 37] For **[2PBI]-3a** and **b**, only one of the two possible configurational isomers, the transoid isomer, is exemplarily shown.

By screening numerous PAH guest molecules for **[2PBI]-2** such as perylene, carbazole or 1-phenylnaphthyl, it was deduced that the binding strength at 298 K in $CHCl_3$, which is indicated by the host-guest association constant K_a,[38] depends on the number of guest double bonds interacting with the host (Figure 3a). Consequently, the tightest binding was observed for perylene with 4.6×10^4 L mol^{-1} (Figure 3b). Furthermore, cyclophane host **[2PBI]-2** shows a higher affinity for flexible guest molecules such as 1-phenylnaphthalene, which can adapt to the slightly twisted nature of the tetra bay substituted PBI core,[39] than for rigid guest molecules with a similarly large π-scaffold such as triphenylene. Most interestingly, the electronic nature of the guest has remarkable impact on the fluorescence response of the cyclic PBI dimer upon

guest binding (Figure 3c, d). Encapsulation of carbazole and other PAHs which are more electron rich than host **[2PBI]-2** leads to a fluorescence turn-off due to the formation of charge transfer complexes. In contrast, more electron-poor guests such as perylene result in a fluorescence enhancement as their intercalation into the cavity of the cyclophane host disturbs the weak electronic interaction between the chromophore subunits of **[2PBI]-2** (Figure 3e).[30a]

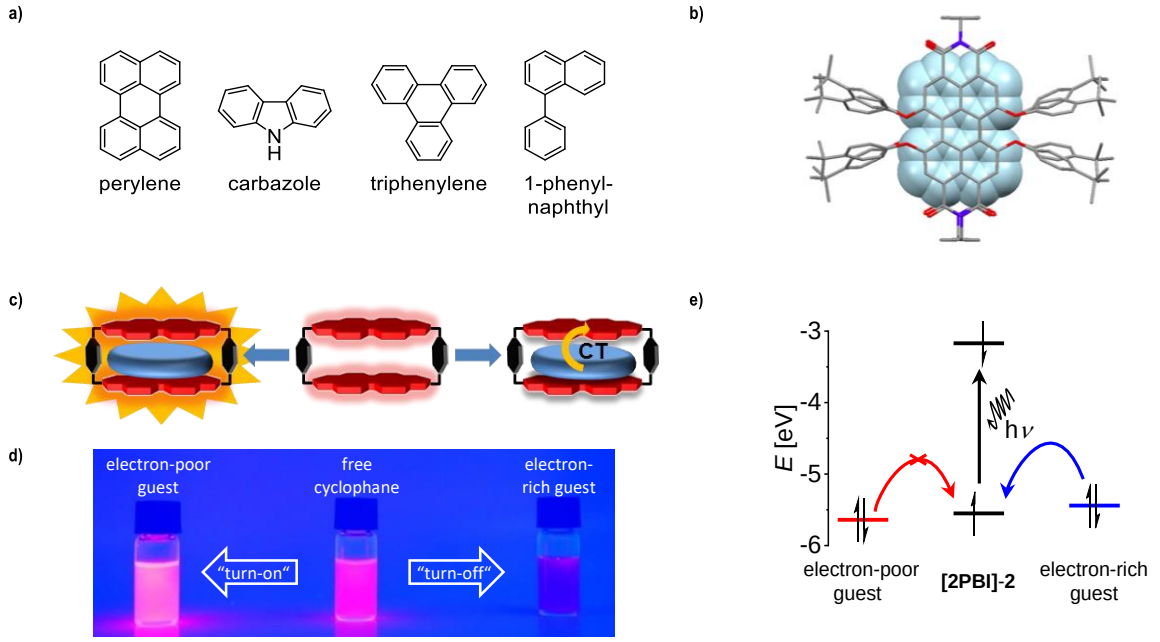

Figure 3. (a) Chemical structures of selected PAHs: tightest binding guest perylene, electron-rich guest carbazole, electron-poor, flexible guest 1-phenylnaphthyl and rather rigid guest triphenylene. **(b)** Calculated structure of the host-guest complex perylene⊂**[2PBI]-2p**. **(c)** Schematic illustration, **(d)** representative photograph and **(e)** schematic energy diagram of the "turn-on" (1-phenylnaphthalene⊂**[2PBI]-2**) and "turn-off" (carbazole⊂**[2PBI]-2**) fluorescence sensing of electron-poor and electron-rich PAHs by cyclophane host **[2PBI]-2**. **(b)** – **(d)** are adapted with permission from Ref. [30a]. Copyright 2015 Wiley VCH.

The unique photophysical properties of cyclophane **[2PBI]-2**, originating from the special arrangement of the PBI chromophores in the cyclic dimer, were investigated further by femtosecond and nanosecond transient absorption (TA) spectroscopy.[30b] After photoexcitation of **[2PBI]-2** in the polar solvent CH_2Cl_2, no excimer formation is observed.[40] Instead, the emergence of characteristic signals for the PBI radical cation and the PBI radical anion in the TA spectrum indicate an intramolecular symmetry-breaking charge transfer between the two chromophore subunits of **[2PBI]-2** (Figure 4, route A).[30b] The charge recombination to the ground state is relatively slow enabling population of the triplet state, which is proven by the generation of singlet oxygen in 27% yield, presumably by radical pair intersystem crossing. In the non-polar solvent toluene where charge-separated states are not well-stabilized[41] the first excited state of **[2PBI]-2** decays by emission (Figure 4, route B).[30b] Furthermore, the deactivation pathway of **[2PBI]-2** in CH_2Cl_2 is altered by intercalation of electron-poor guest

molecules such as anthracene or perylene between the chromophore subunits as this results in an ultrafast electron transfer from the guest to the host (Figure 4, route C). The rates of charge separation between host and guest are located close to the maximum of the Marcus parabola whereas the rates of recombination are located in the Marcus-inverted region.[42]

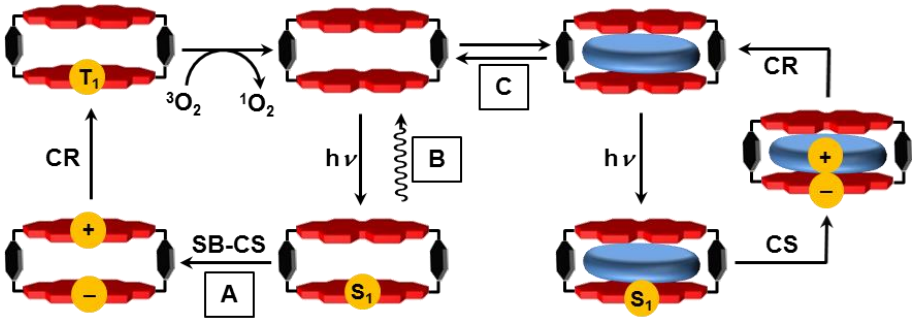

Figure 4. Overview on the different excited state processes of **[2PBI]-2** upon photoexcitation. (A) Symmetry-breaking charge separation (SB-CS) and subsequent charge recombination (CR) to the PBI triplet in CH_2Cl_2 which can be used for singlet oxygen generation; (B) emission in toluene; (C) encapsulation of an electron-rich guest molecule and photo-driven charge separation (CS) between guest and host and recombination (CR) to the ground state. Adapted with permission from Ref. [30b]. Copyright 2016 The Royal Society of Chemistry.

For the PBI cyclophanes **[2PBI]-3a** and **[2PBI]-3b** (Figure 2), the four 4-*tert*-butylphenyl substituents in the bay position of **[2PBI]-2** are formally replaced by two 2,6-difunctionalized phenyl substituents which generates almost planar π-scaffolds for **[2PBI]-3a**, **b**.[37] Consequently, this leads to increased association constants for planar PAH guests of up to 1.6 × 10^6 L mol^{-1} for perylene⊂**[2PBI]-3a** in $CHCl_3$ at 298 K. The binding strength of perylene⊂**[2PBI]-3b**, on the other hand, is approximately tenfold decreased due to steric hindrance of the substituents' aromatic side arms which can self-encapsulate inside the cavity of the cyclophane host. Interestingly, it is mainly due to this self-encapsulation that a drastically enhanced fluorescence quantum yield for **[2PBI]-3b** of 97% is observed when compared to 21% for **[2PBI]-2** in $CHCl_3$.[30a]

2.2 Recognition of Small Biomolecules and Natural Products by Cyclophanes in Water

Due to promising biological and medical applications, host-guest recognition phenomena in water, the solvent of life, are of particular interest for supramolecular chemists.[15b-d] However, the study of such phenomena is challenging which is owed to the unique properties of water as a solvent.[43] Probably the most prominent examples for artificial macrocyclic receptors in

aqueous environment are cyclodextrins[16] and cucurbiturils[17] as well as hydrophilic pillararenes[18] and calixarenes,[19] for which a vast number of functional complexes are known so far (Figure 5).[16-19]

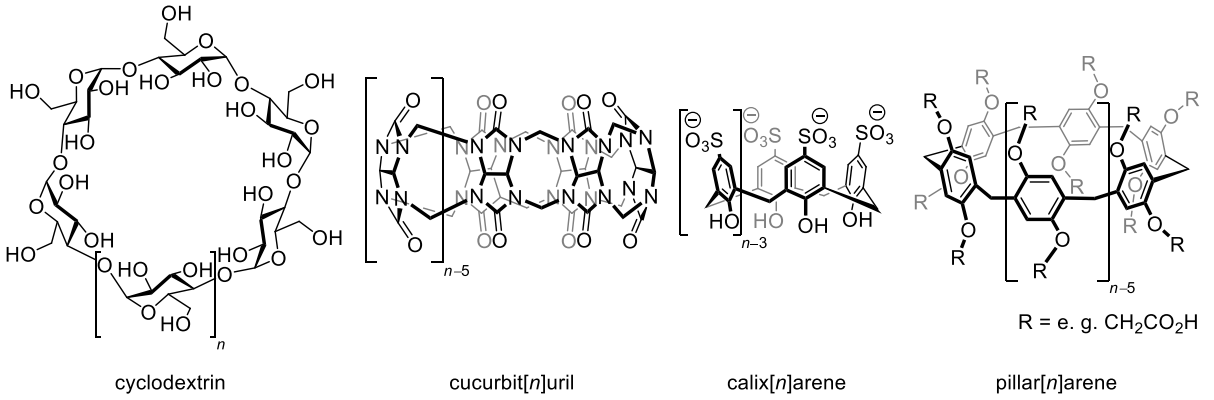

Figure 5. Chemical structures of cyclodextrin (n = 1 – 3)[44] and cucurbit[n]uril (n = 5 – 8, 10)[17] as well as examples of a water-soluble calix[n]arene (n = 4 – 8)[45] and a water-soluble pillar[n]arene (n = 5 – 10).[46]

Hydrophilic cyclophanes, on the other hand, represent yet another class of versatile host molecules which are often endowed with deep hydrophobic cavities for molecular recognition. When compared to the binding modes of the classic players cucurbiturils and cyclodextrins, cyclophanes additionally employ π–π-,[21] cation–π-,[22] and CH–π-interactions[23] for guest binding. Such non-covalent interactions make cyclophanes suitable receptors for a large variety of natural products on which the following chapter will give an overview. Examples for water-soluble cyclophane hosts are presented for which an aromatic cavity is created by at least two aromatic building blocks in the molecular structure. Moreover, in the (proposed) host-guest complex structure the substrate is located between these aromatic building blocks as opposed to flexible systems folding in a way for which no cavity is generated and other binding modes with guests are observed.[47]

2.2.1 Nucleobase derivatives

Nucleotides and nucleosides represent an essential class of biomolecules for example serving as building blocks for nucleic acids, acting as "energy currency" in metabolism or playing an important role in signal transduction pathways (Figure 6).[48] Consequently, specific recognition of nucleobase derivatives by enzymes and receptors is essential for biochemical processes in cells. In the design of artificial hosts for these versatile biomolecules, however, it is exactly this selectivity that poses a major challenge. In an ideal case, a biomimetic receptor specifically

recognizes only one out of the five nucleobases of which nucleic acids are comprised. Moreover, a preference to bind either the mono-, di- or triphosphate of the respective nucleoside should be achieved.[49] Thus, in addition to electrostatic attraction and hydrogen bonding, guest recognition by π–π-interaction as it exerted by the majority of adequately designed cyclophane hosts is advantageous especially when discrimination of the derivatives of pyrimidine bases cytosine, thymine or uracil in contrast to the derivatives of the larger purine bases adenine and guanine is desired.[20a] An even higher degree of selectivity is often achieved by including additional binding sites in the molecular structure of the cyclophane. Cationic functions, for instance, help by targeting the phosphate chain of a nucleotide guest which is deprotonated under physiological conditions.[50]

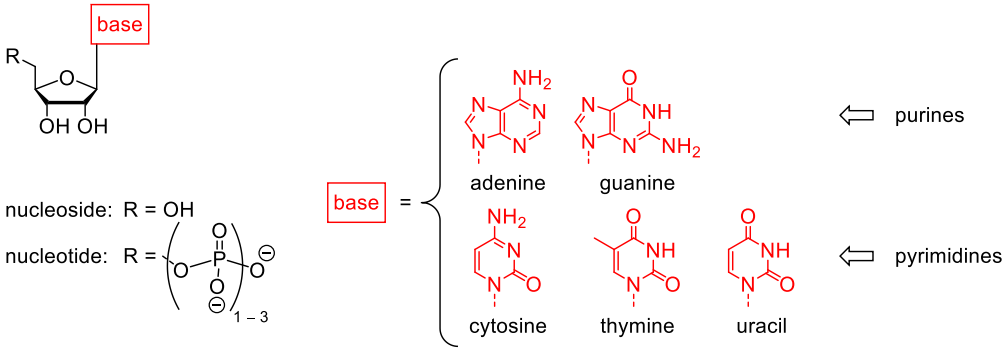

Figure 6. Chemical structures of the nucleobase derivatives functioning as guests for the cyclophane hosts in this chapter.

The potential of water-soluble cyclophanes as artificial receptors for nucleotides was intensely investigated by researchers around Jean-Marie Lehn.[51] Based on the observation that the naturally occurring polyamines spermine or spermidine associate with nucleotides,[52] cationic polyaza cyclophanes with various aromatic building blocks such as acridine (**1**, Figure 7) were investigated.[51c] Fluorescence titration studies confirmed binding of adenosine triphosphate (ATP) by cyclophane **1** in a 1:1 host-guest complex with $K_a = 2.5 \times 10^8$ L mol^{-1} at pH = 6 and 298 K. This value is 16-times higher than the affinity for guanosine triphosphate (GTP) and even 780-times higher than the one for uridine triphosphate (UTP). Moreover, host **1** also recognizes ATP 200-times better than adenosine monophosphate (AMP). The selectivity for the higher charged triphosphate nucleosides when compared to the guests with a di- or monophosphate chain, respectively, is ascribed to electrostatic attraction between a tetraanionic ATP guest molecule and the protonated polyaza cyclophane **1** which constitutes the major part of the driving force for substrate encapsulation. Additional dispersion interaction between the acridine subunits of **1** and the aromatic nucleobase moiety of the substrate presumably play a

role in the discrimination of the pyrimidine bases when compared to the purine bases. Even though the intercalation of the base between the acridine pair is only hinted at in the optical studies, encapsulation of aromatic carboxylate guests is proven by a crystal structure suggesting similar binding modes for other aromatic substrates.[53] Furthermore, **1** also shows a specificity for abasic sites in a deoxyribonucleic acid (DNA) duplex.[54]

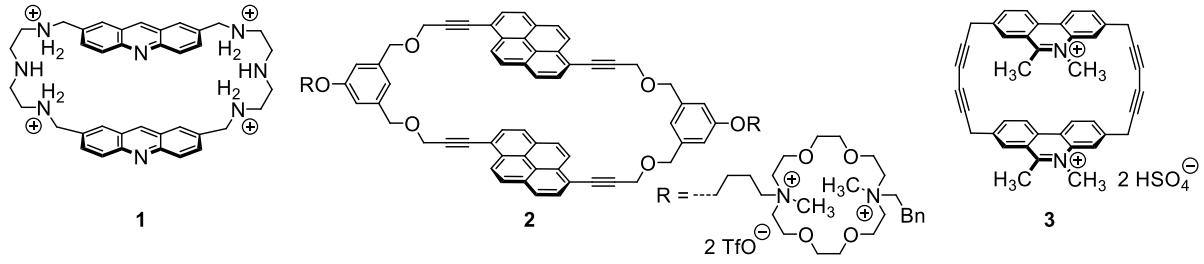

Figure 7. Chemical structures of bisacridine cyclophane host **1** (at pH = 6), bispyrene cyclophane host **2** and bisphenanthridinium cyclophane host **3** for the recognition of nucleotides in water.[51c, 55]

Another example of a cyclophane hosts showing a preference for purine substrates when compared to pyrimidine derivatives due to the larger π-surface of the former is given by the pyrenophane **2** (Figure 7), bearing diazoniacrown residues as water-solubilizing groups.[55b] UV-vis and fluorescence titration experiments in water at 293 K confirm that macrocyclic bispyrene **2** binds nucleoside triphosphates in the order of GTP (1.3×10^6 L mol^{-1}) ≈ ATP (1.0×10^6 L mol^{-1}) > UTP (7.7×10^5 L mol^{-1}) > cytidine triphosphate (CTP) (2.6×10^5 L mol^{-1}). In addition, **2** shows a higher affinity for nucleoside triphosphates when compared to the mono- or diphosphates by up to three orders of magnitude. This selectivity is rationalized by their longer phosphate chain which enables simultaneous intercalation of the nucleobase between the pyrene subunits and coordination of the phosphate to the diazoniacrown macrocycle (Figure 8). The rather rigid phenanthridinium cyclophane **3** (Figure 7) shows a selective fluorescence turn-on upon addition of AMP ($K_a = 6.3 \times 10^5$ L mol^{-1} at pH = 6.2) in contrast to guanosine monophosphate (GMP) or uridine monophosphate (UMP).[55a] Substrates with longer phosphate chains were not investigated.

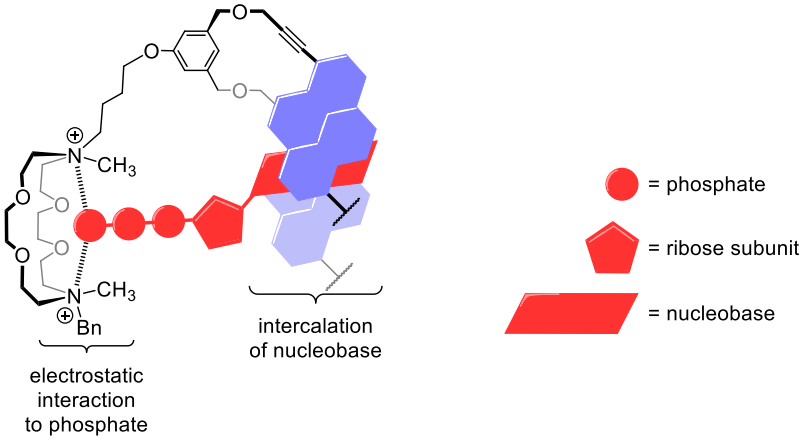

Figure 8. Schematic representation of the suggested binding mode of a nucleotide guest (shown in red) to pyrenophane host **2**.[55b]

In the recent years, several groups undertook various efforts to rationalize the binding propensity and selectivity of different related cyclophane hosts towards nucleobase derivatives in terms of cavity size, linker length or aromatic subunits. Evgeny A. Kataev's group, for example, studied the influence of the linkers on the recognition properties of the rather flexible bisanthracene macrocycles **4** – **6** for nucleoside triphosphates (Figure 9).[47b] All receptors show a slight selectivity for GTP (K_a (**4**, **5**) = 1.1 × 10^4 L mol^{-1}, K_a (**6**) = 3.8 × 10^3 L mol^{-1}) in fluorescence titration experiments at pH = 6.2 when compared to the other four nucleoside triphosphates. Moreover, particular care was taken by the authors to elucidate whether the nucleobases of the substrates truly intercalates between the two aromatic subunits of the rather flexible receptors in the host-guest complex by monitoring the ratio of the excimer and the monomer emission band of the host. Only for the host-guest complexes ATP⊂**4**, thymidine triphosphate (TTP)⊂**4** and UTP⊂**6** this ratio is shifted towards monomer-like emission upon nucleoside addition suggesting disruption of the excited anthracene dimer by intercalation of the substrate between the two aromatic subunits of the host. For the other complexes, different binding modes with a predominance of electrostatic interactions are assumed. Further confirmation for true intercalation in the case of UTP⊂**6** is provided by ^{1}H, ^{1}H ROESY NMR spectroscopy.

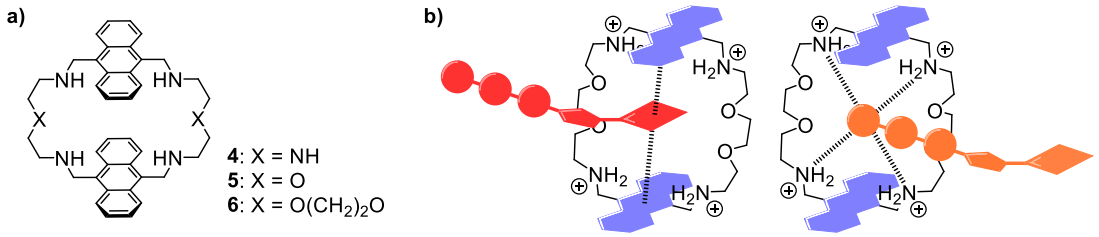

Figure 9. (a) Chemical structures of cyclic bisanthracene hosts **4** – **6**. **(b)** Schematic representation of the two binding modes of the bisanthracene receptors; left: intercalation of the nucleobase between the anthracene dimer in the case of UTP⊂**6** and right: predominance of electrostatic interaction in the case of TTP⊂**6**.[47b]

For the four tetracationic cyclophanes **7** – **10**, containing two 4,4'-bipyridine or two 1,2-bis(4-pyridyl)ethene moieties, respectively, the influence of cavity size on the recognition of nucleoside triphosphates ATP and GTP was studied (Figure 10).[25, 56] In UV-vis absorption titration experiments at pH = 7.4, the binding strength of the triphosphate substrates to the cyclophanes, which are in the range of 2.9×10^3 L mol^{-1} – 4.9×10^3 L mol^{-1}, increases in the order of **9** < **8** < **7**. This trend can be ascribed to the well-defined cavity of the relatively small and rigid **7**. No encapsulation is confirmed for the largest cyclophane host **10**. However, **7** – **9** bind GTP approximately only 1.2-times stronger than ATP yet no interaction of these cyclophanes with the respective mono- or diphosphates is observed. Application of these cyclophanes together with the fluorescence dye 8-hydroxy-1,3,6-pyrene trisulfonate (HPTS) in a fluorescence indicator displacement assay[57] for GTP sensing is demonstrated, as well. The fluorescence of HPTS is quenched upon binding to the cyclophane hosts. Addition of GTP or ATP as competitive binders releases HPTS from the host resulting in a fluorescence turn-on of the dye which is more pronounced for GTP than for ATP.

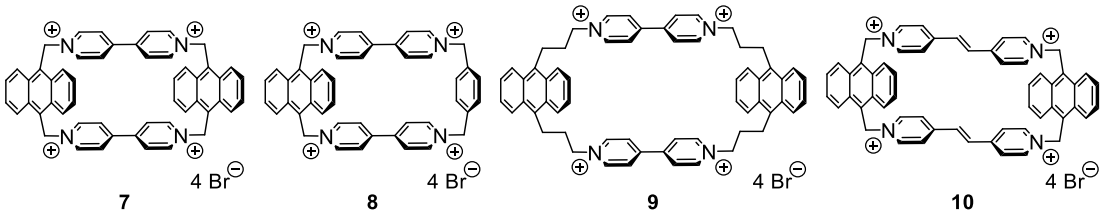

Figure 10. Chemical structures of cyclophane hosts **7** – **10**.[25, 56]

Tetracationic cyclophane hosts **11** and **12** further exemplify the disadvantage of binding pockets which are too large for the substrate (Figure 11a).[58] ^{1}H NMR spectroscopy and isothermal titration calorimetry (ITC) studies verify formation of 1:1 complexes of **11** with ATP ($K_a = 1.17 \times 10^4$ L mol^{-1}), ADP ($K_a = 5.07 \times 10^3$ L mol^{-1}) and AMP ($K_a = 1.09 \times 10^3$ L mol^{-1}) at pH = 7.4 and 298 K showing selectivity for the triphosphate. For **12**, on the other hand, only a very weak

association with nucleotide guests is observed. Nucleotides other than adenosine phosphates are not investigated. Interestingly, shifts in the ^{1}H NMR spectrum and ^{1}H, ^{1}H NOESY data reveal that in the complex ATP⊂**11** the phosphate chain of the ATP guest is located close to the phenyl spacer whereas the adenosine moiety is oriented towards the tetraphenylethenyl spacer (Figure 11b). However, application of this host in a biological environment is most likely limited since binding of aromatic amino acids by **11** is demonstrated (see chapter 2.2.2), as well.

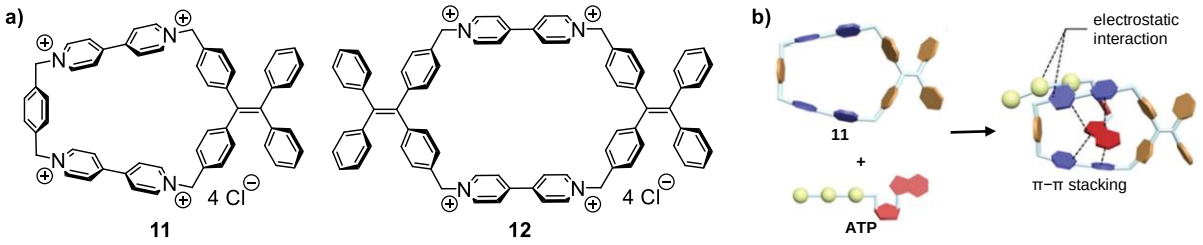

Figure 11. (a) Chemical structures of cyclophane hosts **11** and **12**. **(b)** Schematic representation of the complexation of ATP by **11** based on 1D and 2D NMR data. Adapted with permission from Ref. [58]. Copyright 2019 The Royal Society of Chemistry.

Biphenyl and terphenyl cyclophanes **13** and **14** (Figure 12a) perform as efficient binders of nucleosides,[59] even though they were originally conceived for the recognition of all-equatorial carbohydrates (see Chapter 2.2.4),[60] once again demonstrating the challenge to design selective synthetic hosts for a biological environment. In ^{1}H NMR and ITC complexation studies in water at 298 K, both hosts show slightly higher affinities for guanosine and adenosine than for pyrimidine nucleosides which is explained by the larger π-surface of the purine bases. The selectivity of the two cyclophanes for guanosine is tentatively rationalized by different contributions of hydrogen bonds between nucleobase and the spacers in the respective host-guest complexes. In contrast to previously mentioned examples, host **14** (e. g. K_a (guanosine) = 2.2×10^4 L mol^{-1}) with the extended cavity binds guests more tightly than the smaller host **13** (e. g. K_a (guanosine) = 3.7×10^3 L mol^{-1}) which is ascribed to a partial encapsulation of the ribose subunit into the cavity of cyclophane **14** in addition to nucleobase intercalation (Figure 12b). Furthermore, binding studies of host **13** with nucleotides AMP, ADP and ATP reveal weaker complex stabilities for higher charged substrates demonstrating selectivity for nucleosides over nucleotides which is attributed to electrostatic repulsion between the carboxylates in the side chains of the receptor and the phosphate groups of guest molecules.

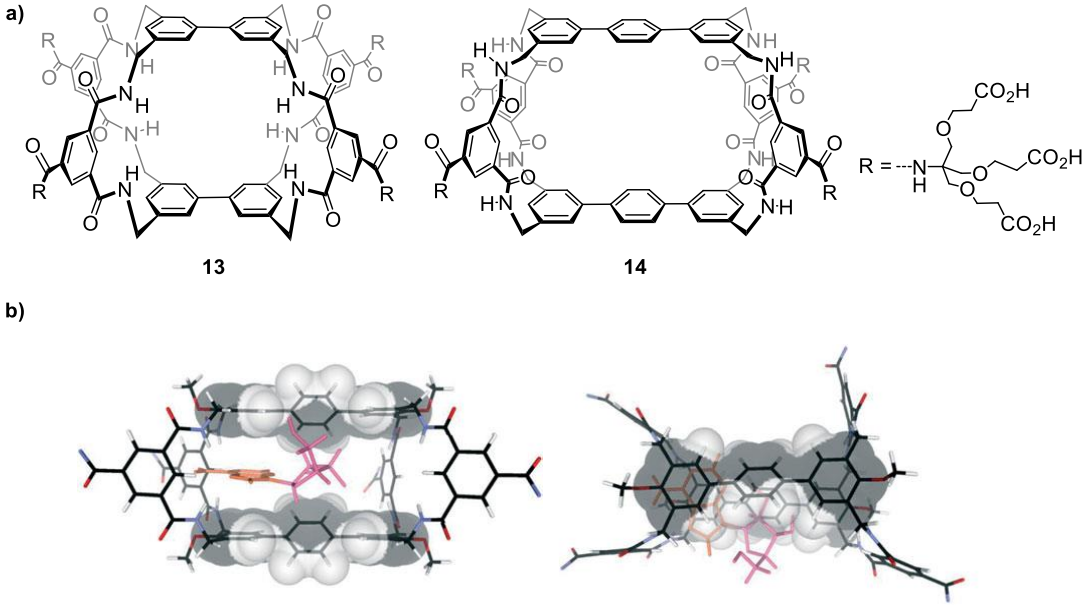

Figure 12. (a) Chemical structures of biphenyl- and terphenyl-based cyclophanes **13** and **14**, respectively. **(b)** Molecular model of the host-guest complex adenine⊂**14**; side view (left) and top view (right) showing the intercalation of the adenine moiety (orange) and partial intercalation of the ribose group (magenta) for host **14**. The terphenyl units of the cyclophane are shown as transparent CPK surfaces. The water-solubilizing side chains are omitted for clarity. Adapted with permission from Ref. [59]. Copyright 2013 Taylor & Francis.

In protein binding pockets, ATP recognition is often associated with coordination of the phosphate anions to metal cations.[61] This structural motif inspired supramolecular chemists to adapt such a concept in the design of artificial nucleotide receptors[62] by including metal-coordinating units into cyclophanes.[63] In bisanthracene macrocycle **15**, for example, two Zn^{2+}-ions are coordinated to the linkers (Figure 13a).[63b] The fluorescence of this host is quenched upon addition of ATP or ADP in a titration experiment at pH = 7.4 and 298 K whereas no response is observed for other nucleobase triphosphates. Interestingly, a 1:2-stoichiometry of the host-guest complexes is confirmed by a Job plot.[64] Moreover, a decrease of the excimer emission band of the bisanthracene host and simultaneous increase of the monomer emission band upon guest addition strongly suggests intercalation of the adenine moiety between the aromatic subunits of the cyclophane.[63b] ^{31}P NMR spectroscopy of ATP in the presence of host **15** reveals stronger downfield shifts for the γ- and β-phosphate groups than for the α-phosphate group of the nucleotide indicating predominant association of the Zn^{2+}-ions to the outer two phosphates. DFT calculations were performed for structural elucidation of the host-guest complex ATP_2⊂**15** demonstrating that the phosphate chain of each ATP guest coordinates to one of the Zn^{2+} cations of host **15** so that a hydrogen-bonded adenosine dimer is sandwiched in the aromatic cavity of the cyclophane.

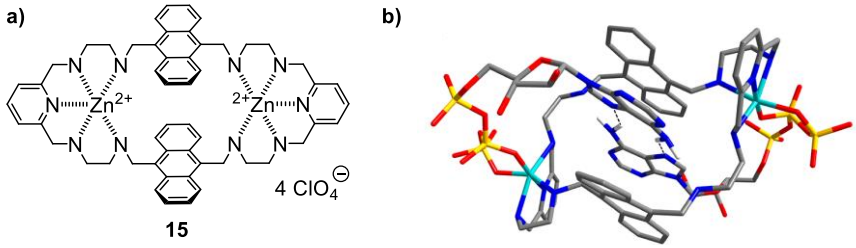

Figure 13. (a) Chemical structure of host **15**. **(b)** Calculated structure (DFT) of the complex ATP_2⊂**15** (grey: C; blue: N; red: O; yellow: P; cyan: zinc; white: H). The assumed hydrogen bonds between the two ATP guests are indicated by black lines. Other hydrogen atoms are omitted for clarity. Adapted with permission from Ref. [63b]. Copyright 2013 Wiley VCH.

This last example shows that, for a suitably designed molecular receptor, the recognition of a base pair instead of a single nucleotide can be achieved, as well. This concept is also supported by cationic bisquinacridine macrocyclic host **16** (Figure 14a).[51d] UV-vis absorption and fluorescence titration experiments at pH = 6 and 293 K show that this cyclophane forms 1:1 complexes with nucleoside di- and triphosphates via electrostatic and dispersion interactions. A preference for purines over pyrimidines is demonstrated with higher affinity for GTP (6.3×10^6 L mol^{-1}) than for ATP (2.5×10^5 L mol^{-1}) which is ascribed to the hydrophobicity of GTP. For the monophosphates, however, 1:2 stoichiometries are observed with the overall formation constant increasing in the order of UMP < CMP < AMP < GMP (Figure 14b). ESI-MS is used for further confirmation of stoichiometries. The different host-guest complex stoichiometries as a function of the number of phosphate groups are explained in terms of charge. Binding of a highly charged di- or triphosphate guest to the cationic host decreases the overall charge of the complex diminishing attraction of a second substrate. Sterics might provide further restrictions. Even though no cooperative effect[65] is observed for the complexation of nucleoside monophosphates, the hydrophobic microenvironment within the cavity of **16** might favour hydrogen bonding interaction between the two encapsulated substrates. Furthermore, recognition of G-quadruplex DNA by cyclophanes such as **1** (Figure 7) and **16** (Figure 14) is discussed in the literature. Yet this is assumed to happen not by intercalation of nucleobases between the aromatic subunit of the hosts but is mainly by electrostatic interaction between the phosphate backbone of the DNA and the cationic linkers of the cyclophane.[66]

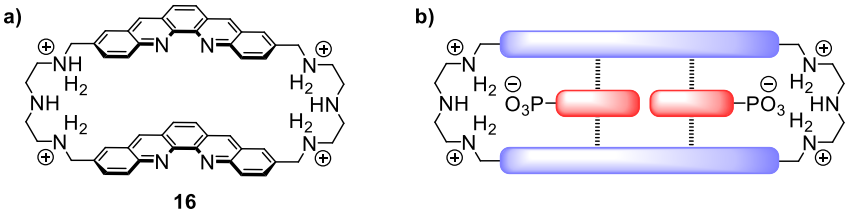

Figure 14. (a) Chemical structure of host **16** (at pH = 6). **(b)** Schematic representation of the 1:2 host-guest complex between **16** and nucleoside monophosphates.[51d]

The redox coenzyme nicotinamide adenine dinucleotide (NAD) is another example of biologically important adenosine derivatives which are of interest for supramolecular chemistry.[67] Cyclophane **17** with crown ether linkers was reported to bind the oxidized NAD^+-form with a moderate association constant of 2.2×10^3 L mol^{-1} as confirmed by ITC and ^1H NMR spectroscopy at neutral pH and 298 K (Figure 15a, b).[68] As the reduced form NADH is not recognized by host **17**, it is assumed that the charged nicotinamide moiety of NAD^+ guest is intercalated between the sulfonylated naphthalene subunits of the cyclophane host accompanied by external stacking of the adenine group (Figure 15c).

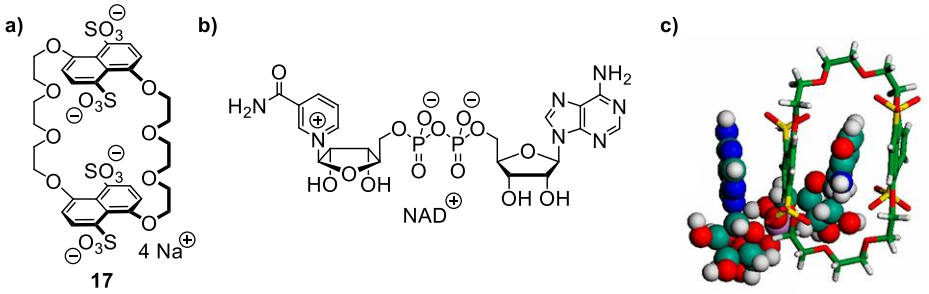

Figure 15. Chemical Structure of **(a)** cyclophane host **17** and of **(b)** redox coenzyme NAD^+. **(c)** Proposed structure of the host-guest complex $NAD^+ \subset$ **17** in which the nicotine moiety of the guest molecule (shown as CPK surface) is intercalated between the two naphthalene subunits of the cyclophane host (green/cyan: C; blue: N; red: O; yellow: S; white: H). Adapted with permission from Ref. [68]. Copyright 2012 The American Chemical Society.

2.2.2 Amino Acids

α-Amino acids are the building blocks of proteins.[48a, 69] They show a great diversity in structure and properties because the specific side chain of an individual amino acid can be basic, acidic or neutral and, moreover, can be comprised of an aliphatic chain or an aromatic group (Figure 16). The following examples will show that, depending on the characteristics of the amino acid guest, water-soluble cyclophane hosts are often well-suited to address these interesting substrates by cation–π- or π–π-interactions.

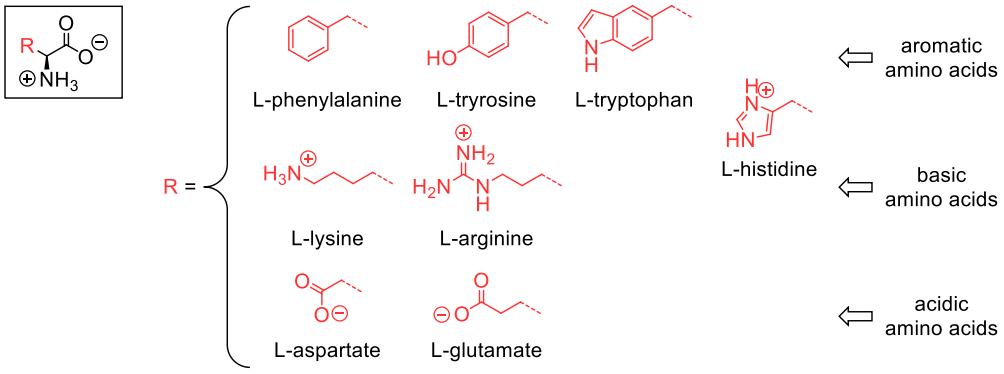

Figure 16. Overview on the proteinogenic amino acid guests for the cyclophane hosts presented in this chapter.

The potential of cyclophanes to bind aromatic *α*-amino acids was recognized by J. Fraser Stoddart and co-workers.[24] Upon addition of the aromatic amino acid tryptophan as a racemate to a solution of cyclobis(paraquat-*p*-phenylene) (**18**) as a tetrachloride salt in aqueous phosphate buffer, a charge transfer band emerges in the UV-vis spectrum indicating the formation of the 1:1 inclusion complex tryptophane⊂**18** with a binding constant of 1.0×10^3 L mol^{-1} at pH = 7 and 298 K (Figure 17a). Tyrosine is encapsulated slightly weaker with $K_a = 6.1 \times 10^2$ L mol^{-1} whereas almost no recognition is detectable for phenylalanine (33 mol L^{-1}) displaying the selectivity of the electron-poor host **18** for electron-rich aromatic amino acids (Figure 16). No recognition was observed for histidine or alanine. Cyclophane **11** with a structure similar to that of **18** also binds tryptophan in the order of 10^3 L mol^{-1} at pH = 7.4 and 298 K (Figure 17b). Complex formation with other amino acids was too weak to be quantified.[24]

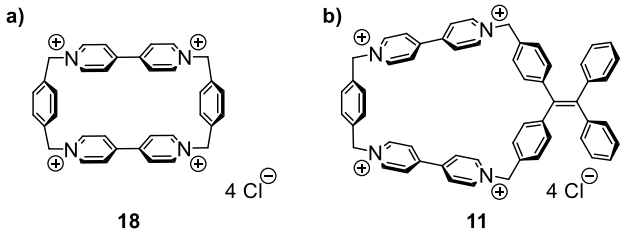

Figure 17. Chemical structures of cyclobis(paraquat-*p*-phenylene) as a chloride salt (**18**) and of cyclophane host **11**.[24, 58]

Host **19** is a phthalhydrazide-based cucurbituril analogue (Figure 18).[70] Compared to cucurbit[*n*]urils, the cavity of cyclophane **19** is elongated and recognizes guest molecules by π–π-interaction in addition to the dipole-dipole interaction inherent to cucurbit[*n*]uril scaffolds.[71] Fluorescence titration experiments of host **19** in acetate buffer at pH = 4.74 and 295 K reveals binding of tryptophan with $K_a = 3.2 \times 10^6$ L mol^{-1} which is two orders of magnitudes higher than the affinity of **19** for the other aromatic amino acids phenylalanine,

tyrosine and the neurotransmitter dopamine. The selectivity is ascribed to the additional aromatic ring of tryptophan. However, **19** also binds a large variety of ammonium derivatives and shows a similarly high affinity in the order of 10^6 L mol^{-1} to the dyes Nile red and Nile blue.

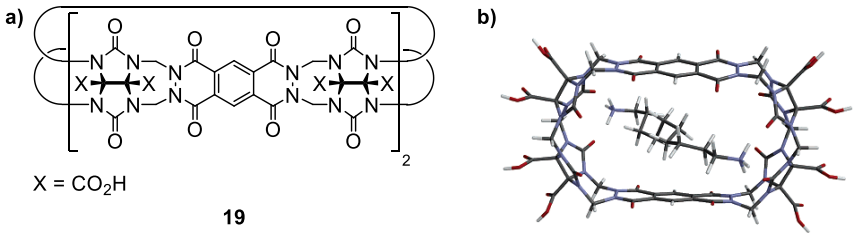

Figure 18. (a) Chemical structure of cucurbituril-based host **19**. **(b)** Representation of the host-guest complex 1,10-decanediammonium ion⊂**19** to illustrate the cavity of the host (MMFF, grey: C; blue: N, red: O; white: H). Adapted with permission from Ref. [68]. Copyright 2006 The American Chemical Society.

Dennis A. Dougherty's group demonstrated that cyclophanes recognize the amides of cationic amino acids by cation–π interactions.[72] The carboxylated derivative **20** of Dougherty's cyclophane[73] preferentially binds arginine amide (K_a = 4.6 × 10^3 L mol^{-1}) over lysine amide (K_a = 8.5 × 10^2 L mol^{-1}) at pD = 9 which is ascribed to the different binding modes of the two amino acid derivatives as evident by ^{1}H NMR shifts (Figure 19).[72] The results suggest that the guanidinium group of arginine amide is deeply buried within the cyclophane and hence stabilizing the host-guest complex with cation–π interactions. Lysine amide, on the other hand, most likely exhibits a coiled conformation which is not directed by cation–π interactions. No encapsulation was observed for the amino acids lysine and arginine.

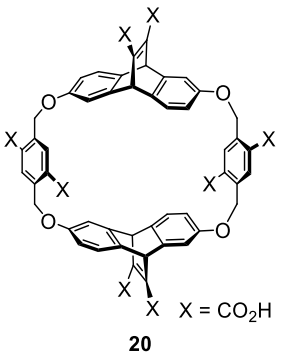

Figure 19. Chemical structure of host **20**.[72]

Synthetic hosts **21** – **23** by Marcey Waters's group, which are inspired by the structure of Dougherty's cyclophane,[73] recognize di- and trimethyl lysine[74] or dimethyl arginine residues[75] in post-translationally modified proteins by cation–π- and van der Waals-

interactions (Figure 20a, b). Each of these hosts is identified by a dynamic combinatorial library approach in which the macrocyclic host is constructed around a guest template by reversible bond formation under equilibrium conditions.[76] ITC experiments at pH = 8.5 and 299 K confirm binding of **21** to *N*-methylated lysine groups in histones, which are small proteins around which DNA strands are ordered in the formation of nucleosomes,[48a] with K_a in the order of 10^5 L mol^{-1} yet with a poor selectivity for trimethylated over dimethylated lysine.[74b] **22** with a deeper cavity (Figure 20c), however, displays a 14-fold improved selectivity for trimethyl lysine in histone 3 with $K_a \sim 10^6$ L mol^{-1} when compared to the dimethylated amino acid. This is ascribed to a decrease of entropic penalty for the binding of the higher methylated substrate to this receptor. Host **23**, on the other hand, shows selectivity for asymmetric dimethyl arginine with an affinity of 8.3×10^5 L mol^{-1} for a representative histone tail.[75b] Trimethyl lysine and symmetric dimethyl arginine, in contrast, are discriminated by a factor of ten. This selectivity is reasoned by the cuboid shape of the cavity, which mimics the geometry of the binding pocket for asymmetrically dimethylated arginines in proteins (Figure 20d). Further options to target post-translationally modified lysines are provided by sulfonated calixarenes.[77]

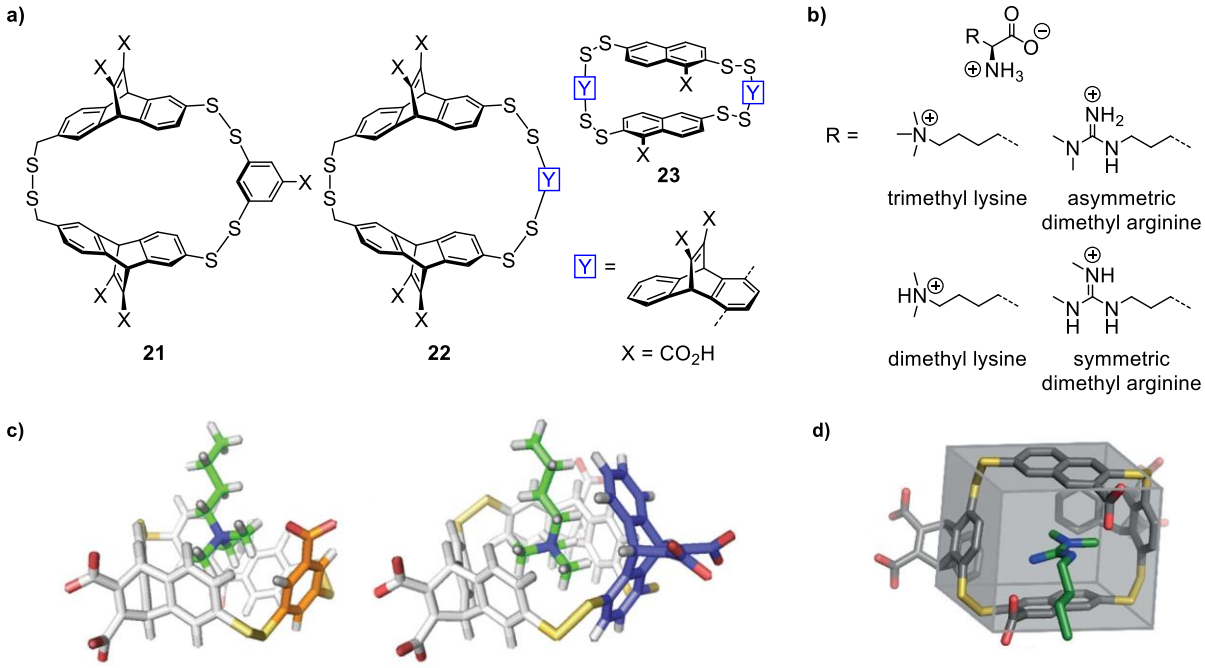

Figure 20. Chemical structures of **(a)** cyclophane hosts **21** – **23** and **(b)** methylated derivatives of the amino acids lysine and arginine. **(c)** Molecular models of the complexes Me_3-lysine⊂**21** (left) and Me_3-lysine⊂**22** (right) showing the deeper inclusion of the substrate for the latter. Only the specific rest of the amino acid (green) is shown. Adapted with permission from Ref. [74b]. Copyright 2014 The Royal Society of Chemistry. **(d)** Gas phase model of asymmetric Me_2-arginine⊂**23** illustrating the cuboid shape of the cavity. Adapted with permission from Ref. [75b]. Copyright 2019 Wiley VCH.

Another concept for selective amino acid recognition by cyclophanes relies on electrostatic interactions between the solubilizing functions of the host and specific amino acid guests.

Water-soluble pillar[5]arene **24** with carboxylate chains at both rims reveals selective recognition of the basic amino acids arginine, histidine and lysine in the order of 10^3 L mol^{-1} in ^{1}H NMR titrations at pD = 7.4 and 298 K (Figure 21a).[78] 2D NMR experiments suggest threading of the amino acid guest through the cavity of the host with coordination of the NH-groups to the carboxylate functions on the rims of the host. Other amino acids are bound with decreased affinity (< 20 L mol^{-1}). As electrostatic attraction is the driving force for complex formation, diamine cadaverine, which corresponds to decarboxylated lysine, is bound 30-times more strongly than lysine. Water-soluble pillar[6]arene **25**, on the other hand, is appended with protonable amine chains (Figure 21b).[79] Hence, host **25** displays selectivity for acidic amino acids glutamate and aspartate in fluorescence titration experiments at pH = 6.0 and 298 K with an association constant of approximately 1 × 10^6 L mol^{-1}. No encapsulation of other proteinogenic amino acids is observed.

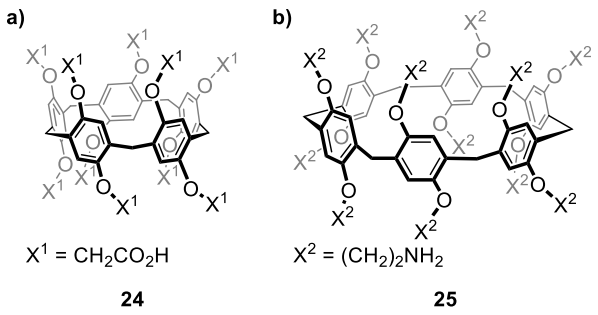

Figure 21. Chemical structures of **(a)** pillar[5]arene **24** for the recognition of basic α-amino acids and (**b**) pillar[6]arene **25** for the recognition of acidic α-amino acids.[78-79]

2.2.3 Neurotransmitters

Catecholamines are important neurotransmitters in signal transduction pathways which is the reason why synthetic receptors for this class of biomolecules are intensely investigated (Figure 22a).[80] Thomas Schrader's group, for example, designed several cyclophane hosts such as **26** which features a non-polar aromatic cavity with a *p*-xylylene bisphosphonate group as an amino alcohol binding site at one end and a catechol recognition element comprised of electron-poor nitroarenes and an isophthalimide moiety at the other (Figure 22b, c).[26, 81] ^{1}H NMR binding studies are performed in a solvent mixture CD_3OD/D_2O = 1/1 due to self-association of the host in pure water.[81b, 81c] Formation of 1:1 complexes with associations constants of approximately 10^2 L mol^{-1} are observed for adrenaline, noradrenaline and dopamine whereas no complexation is found in the case of aromatic amino acids. For non-aromatic ethanolamine, a decrease in

affinity is observed hinting at the presence of π–π-interactions in the host-guest complexes of **26** and the catecholamine substrates. Indication for hydrogen bonding between the cyclophane host and the catecholamine guest is derived from FT-IR experiments in which the P–O and amide carbonyl bands of **26** display shifts to smaller wavenumbers. Some improvement of selectivity for dopamine and noradrenaline as compared to adrenaline is achieved by replacing isophthalimide head group of **26** with pyridinedicarboximide.[81c] Interestingly, in a further evolved macrocyclic host decorated with phosphonic acid functions for selective adrenaline recognition in water, the aromatic ring of the substrate does not intercalate between the aromatic rings of the host.[81d]

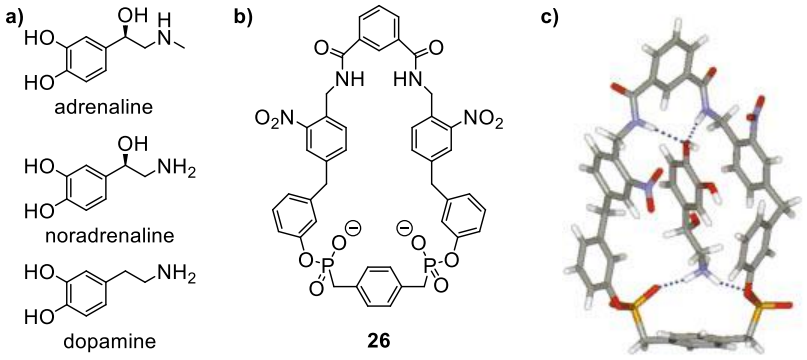

Figure 22. (a) Chemical structures of catecholamine guests adrenaline, noradrenaline and dopamine and **(b)** of the synthetic receptor **26**. **(c)** Optimized geometry of the complex noradrenaline⊂**26** in water according to Monte Carlo simulations (grey: C; blue: N; red: O, orange: P, white: H). Adapted with permission from Ref. [81b]. Copyright 2001 Wiley VCH.

Dougherty's cyclophane (**27**) was studied as a host for various methylated ammonium, iminium and sulfonium guests to gain fundamental insight into cation–π interactions (Figure 23).[73] Among those guests is the neurotransmitter acetylcholine which is bound with an association constant of 3.5×10^4 L mol^{-1} in aqueous borate buffer at 298 K.[82] Yet this host is not outstanding in terms of selectivity for the small neurotransmitter molecule when compared to the various cationic guests in this extensive study.[73] Moreover, the binding of acetylcholine to water-soluble calixarenes[83] and pillararenes[84] has been exploited in fluorescence indicator displacement assays for acetylcholine sensing.

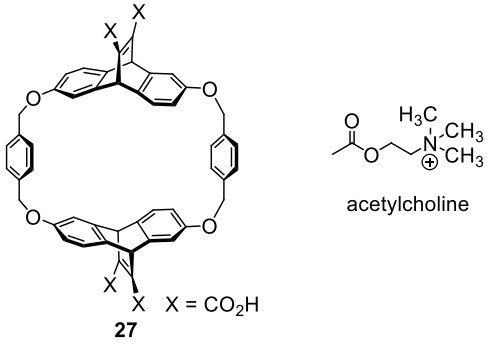

Figure 23. Chemical structures of the *R*,*R*,*R*,*R*-enantiomer of Dougherty's cyclophane (**27**) and one of its guest molecules, the neurotransmitter acetylcholine.[73, 82]

2.2.4 Carbohydrates

Carbohydrates are both hydrophilic and hydromimetic due to their numerous OH functionalities and show only minor structural differences between several derivatives[85] which is why the recognition of carbohydrates in water poses many challenges even for lectins, the carbohydrate binding proteins in living organisms.[86] Even though having focused on boronic acid receptors as covalent binders for sugar guests,[87] during the recent years supramolecular chemists have demonstrated that water-soluble cyclophanes are ideally suited to overcome these challenges and can indeed be highly efficient biomimetic receptors for the non-covalent binding of carbohydrates in water.[85]

In this regard, cyclophanes by A. P. Davis's group based on a so-called "temple design" show great potential (Figure 24a).[85a] This specific architecture of the cyclophane host is essential for efficient carbohydrate encapsulation in water: Aromatic units which can develop CH–π-interactions with a carbohydrate guest molecule represent the "roof" and the "floor" of the temple. Polar spacers keep the aromatic units at a defined distance and are involved in the formation of hydrogen bonds with the encapsulated saccharide derivative. Hydrophilic side chains provide solubility in water. Thus, the cavity of such a cyclophane host perfectly matches the polarity pattern of all-equatorial carbohydrates such as *β*-D-glucopyranose (Figure 24b). In a host-guest complex of the synthetic lectin with this guest molecule, all of the carbohydrate's axial H-atoms point towards the apolar aromatic subunits of the host and all equatorial OH-groups towards the polar spacers.

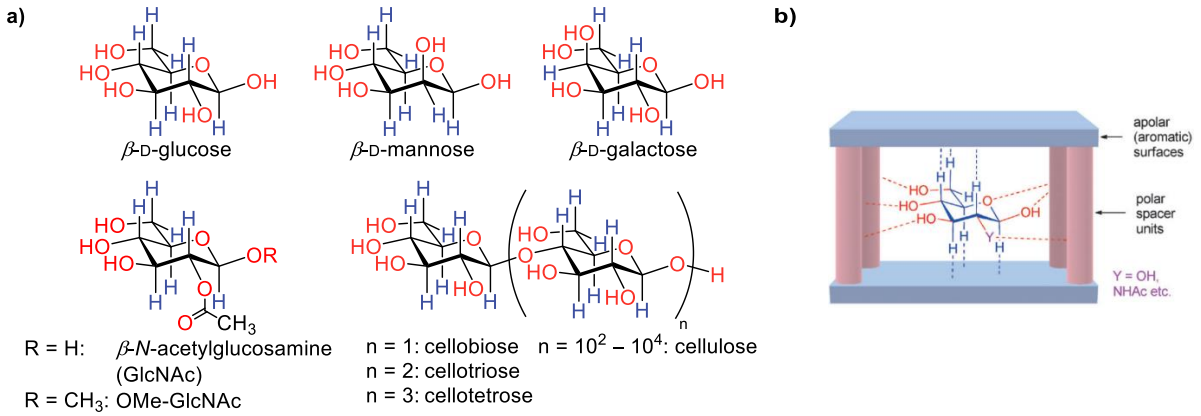

Figure 24. (a) Chemical structures of various carbohydrates. The functional groups are coloured according to polarity with regard to the synthetic lectins (red: polar, blue: apolar). **(b)** Schematic illustration depicting the design principle of the synthetic lectins by the Davis group. Adapted with permission from Ref. [88]. Copyright 2016 Wiley VCH.

In one of the first examples of a water-soluble cyclophane host for carbohydrates (**28**), biphenyl units were used as aromatic building blocks which were held apart by isophthalimide spacers with hydrophilic side chains (Figure 25).[60a] Even though good affinity is found in ^{1}H NMR titration experiments in $CDCl_3/CD_3OD$ (92:8) for a hydrophilic precursor of **28** towards octyl *β*-D-glucopyranoside (K_a = 600 L mol^{-1}, formation of 1:1 complex), in water at 296 K the binding propensity of D-glucose to **28** is as low as 9 L mol^{-1}. Monosaccharides with an axial OH-group such as D-galactose or D-mannose (Figure 24b) yield even smaller association constants. Showing clear preferences for *β*-glucosyl units, the disaccharide D-cellobiose is encapsulated by host **28** whereas D-lactose or D-maltose, which contain *α*-glucosyl units, are not. The highest affinity to **28**, however, is observed for *β*-*N*-acetylglucosamines (GlcNAc, Figure 24b) with binding constants of up to 630 L mol^{-1} for methylated GlcNAc in water at 298 K as confirmed by NMR studies and ITC.[89] GlcNAc is often involved in the posttranslational modification of proteins.[48a] Thus, cyclophane host shows selectivity for *β*-*N*-acetylglucosamine derivatives over other monosaccharides. Yet, as binding of aromatic guests such as nucleosides by **28** is also confirmed,[59] application of this synthetic lectin for selective carbohydrate binding in an *in vivo* environment is questioned by the Davis group.[90]

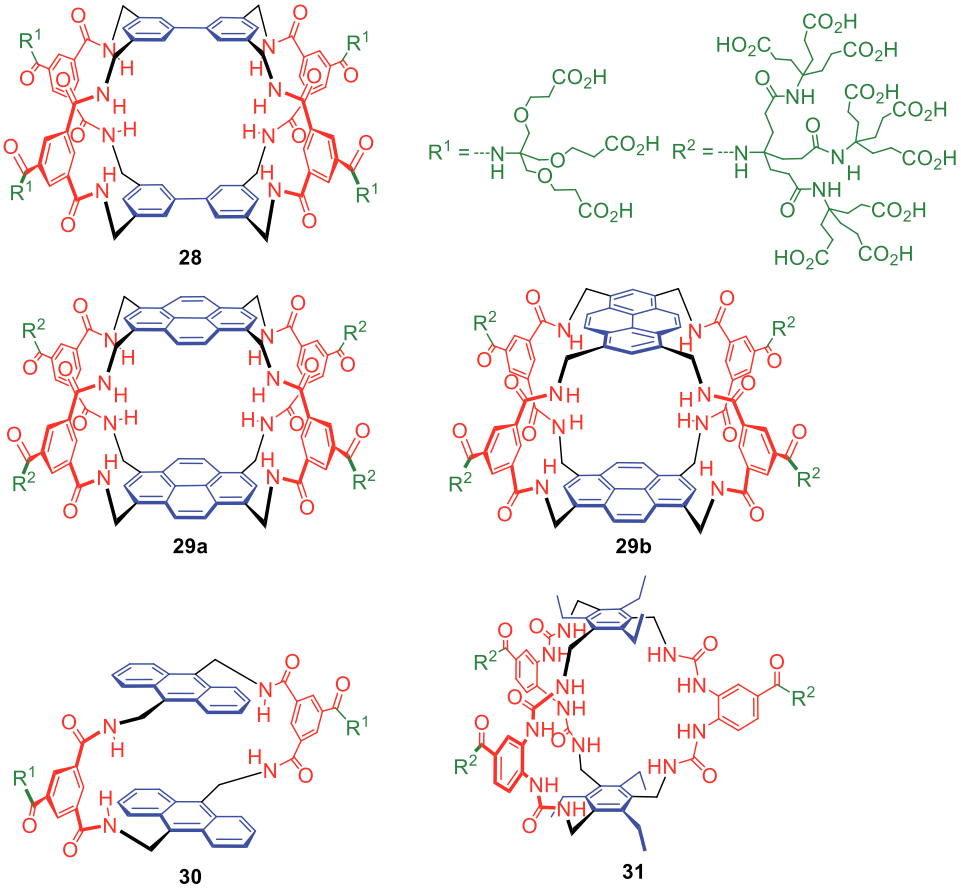

Figure 25. Chemical structures of the synthetic lectins **28** – **31**.[27b, 60a, 88, 90] The aromatic subunits are coloured in blue, the polar spacers in red and the solubilizing side chains in green.

Further optimizations, like extension of the aromatic subunits and use of larger solubilizing side chains, resulted in regioisomeric receptors **29a** and **29b** with pyrene subunits (Figure 25).[88] As confirmed by both ITC as well as NMR titration experiments at 298 K, staggered pyrenophane **29b** shows a remarkably high selectivity for methylated GlcNAc (Figure 24b). A binding constant of 1.8×10^4 L mol^{-1} in water is determined whereas binding of monosaccharides such as D-glucose, D-galactose or D-mannose is comparably weak. Eclipsed pyrenophane **29a**, on the other hand, binds extremely tightly to a GlcNAc-functionalized peptide ($K_a = 1.8 \times 10^4$ L mol^{-1}) as a model compound for a glycosylated protein. The interaction between staggered **29b** and the glycopeptide is not quantifiable due to broad signals in the ^{1}H NMR spectrum. The improved binding properties of macrocyclic bispyrenes **29a** and **29b** when compared to biphenyl cyclophane **28** could be due to a better interaction of the larger, more rigid pyrene subunits with the axial hydrogen atoms of the all-equatorial sugar substrate.

Moderately successful attempts to enhance the affinity of host **28** towards the biologically significant substrate D-glucose (Figure 24b), including variation of the cyclophane's spacer

units or substitution of the biphenyl core increase the low affinity by a maximum factor of approximately 7,[91] which illustrates once again the challenges of carbohydrate recognition in water. Exchange of the twisted biphenyl building blocks of **28** for more rigid anthracene subunits gave receptor **30** (Figure 25) with an association constant to D-glucose of 58 L mol^{-1} by ^{1}H NMR titration at 298 K which is comparable to the affinity of previous attempts. The clear advantage of **30** as compared to **28**, however, lies in a more convenient synthesis and the inclusion of fluorophore units.[27b] Moreover, the intercalation of glucose into the cavity of **30** is proven by crystal structure.[92] On the other hand, encapsulation of aromatic guest molecules was confirmed, as well.[20c] Substitution of the anthracene cores with four methoxy units and elongation of the solubilizing dendrimer chains could double the association strength towards D-glucose to 120 L mol^{-1}.[93]

Synthetic lectin **31** (Figure 25), for which the aromatic triethylmesitylene units are connected by three *N*,*N*-1,2-phenylenebisurea spacers, is the result of purposeful modifications in the receptor's structure to enhance affinity and selectivity for *β*-D-glucose (Figure 24b).[90] Interestingly, the cyclisation of cyclophane host **31** in the final step proves difficult unless a glycoside is added as template improving the yield to 50%. The stability constant for the host-guest complex D-glucose⊂**31** is as high as 1.8×10^4 L mol^{-1} at pH = 7.4 and 298 K which is rationalized by the cavity height of 8.4 Å being ideal for all-equatorial carbohydrates and by the formation of 10 hydrogen bonds between the linker units and *β*-D-glucose. This is illustrated by the optimized structure of the host-guest complex based on Monte Carlo simulations (Figure 26). Further binding studies demonstrate the selectivity of biomimetic receptor **31**. Monosaccharides with one axial OH group, for instance, such as D-galactose or D-mannose, are bound with an association constant as low as 10^2 L mol^{-1}. Moreover, unlike **28** (Figure 25),[59, 89] this receptor shows no affinity for GlcNAc or aromatic substrates. Encapsulation of D-glucose by **31** with comparable complex stability is confirmed even in biological environments such as human blood serum or cell culture media further elaborating the possible *in vivo* use of **31**.

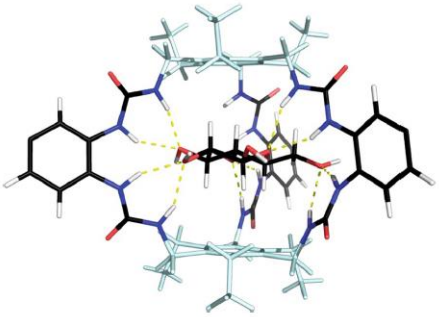

Figure 26. Structure of the host-guest complex β-D-glucose⊂**31** based on Monte-Carlo molecular mechanics (OPLS2005 force field). The yellow dashed lines indicate the ten hydrogen bonds in the complex as predicted by the simulation method.[90] Adapted with permission from Ref. [90]. Copyright 2019 Springer Nature.

The design of a receptor for enantioselective sugar recognition poses yet another challenge for saccharide binding. The asymmetric design of synthetic lectin **32** (Figure 27) with two different aromatic subunits, pyrene of D_2-symmetry and triethylmesitylene of C_3-symmetry, gives rise to planar chirality resulting in two possible enantiomers for **32**.[94] Separation of the enantiomers cannot be achieved. However, ^{1}H NMR titration studies with chiral D-GlcNAc (Figure 24b) gave two different stability constants, 1.3×10^3 L mol^{-1} and 81 L mol^{-1}, for the diastereomeric host-guest complexes D-GlcNAc⊂p*R*-**32** and D-GlcNAc⊂p*S*-**32** equalling an enantioselectivity of 16:1. Further 2D NMR studies identified p*R*-**32** as the tighter binding host enantiomer.

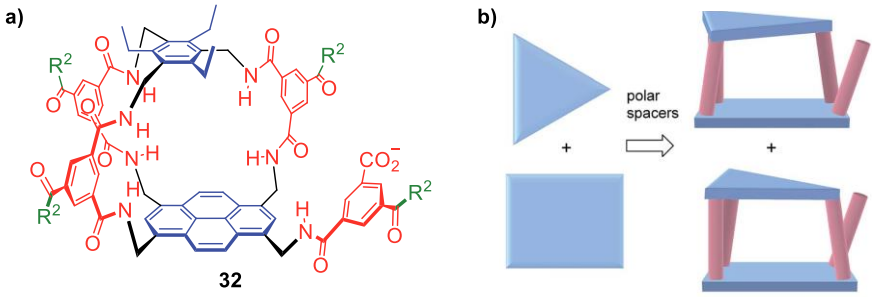

Figure 27. (a) Chemical structure of the p*S*-enantiomer of **32**. See Figure 25 for definition of R^2. The aromatic subunits are coloured in blue, the polar spacers in red. **(b)** Design principle and schematic representation of the synthetic lectin **32**. Adapted with permission from Ref. [94]. Copyright 2017 The Royal Society of Chemistry.

Cyclophane hosts of the "temple design" can not only be applied for the recognition of monosaccharides but also for di- and oligosaccharides. Introduction of two *meta*-terphenyl building blocks as aromatic cores gave synthetic lectin **33** (Figure 28), for example, which displays a strong binding propensity towards D-cellobiose (Figure 24b) in water of approximately 600 L mol^{-1} which is confirmed by ^{1}H NMR spectroscopy, fluorescence enhancement, induced circular dichroism (CD) and ITC.[27a] The association of **33** towards other disaccharides or monosaccharides such as GlcNAc is considerably weaker. The affinity

and selectivity for D-cellobiose was further improved to 3.3×10^3 L mol^{-1} by using dimethoxylated *para*-terphenyl moieties in the less preorganized host **34**.[60b]

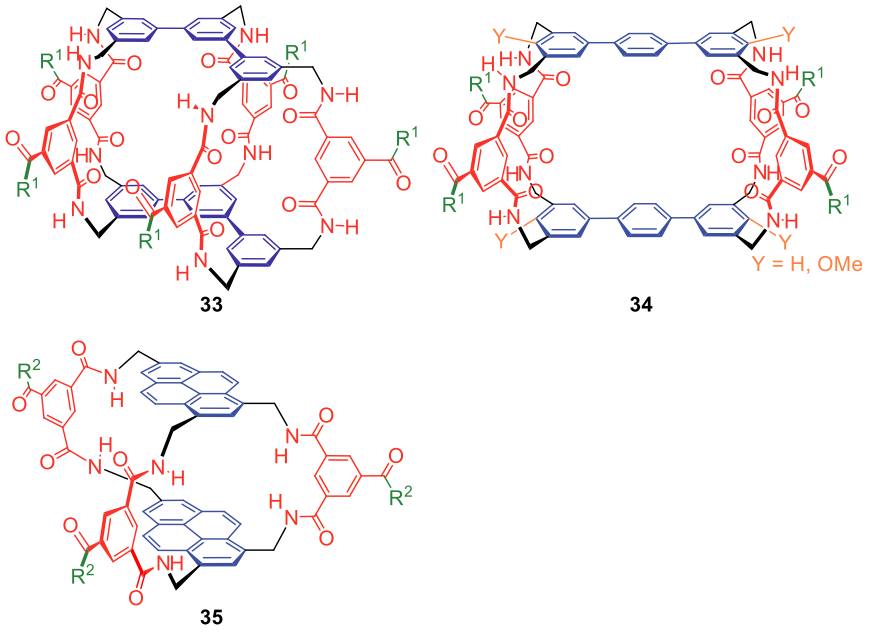

Figure 28. Chemical structures of the synthetic lectins **33** – **35**.[27a, 60b, 95] See Figure 25 for the definitions of R^1 and R^2. The aromatic subunits are coloured in blue, the polar spacers in red, the solubilizing side chains in green.

Synthetic lectin **35** (Figure 28) resembles **29a** and **29b** (Figure 25) but the pyrene cores are held by only three spacer units instead of four.[95] This more open structure turns cyclophane **35** into an efficient binder for small fragments of cellulose such as cellobiose ($K_a = 3.6 \times 10^3$ L mol^{-1}), cellotriose ($K_a = 5.0 \times 10^3$ L mol^{-1}) or cellotetraose ($K_a = 1.2 \times 10^4$ L mol^{-1}) as proven by ITC at 298 K. Monosaccharides, on the other hand, are comparably weakly encapsulated ($K_a \sim 10^2$ L mol^{-1}) demonstrating the selectivity of host **35** for longer sugar chains. The enhanced binding propensity for cellotetraose as compared to cellobiose is mainly due to entropic effects reflecting the greater translational freedom of the more extended substrates in the complex. The enthalpy of binding remains approximately constant for all cellulose fragments. A slight drop in association strength for even larger cellulose fragments is attributed to steric effects between the longer carbohydrates and the side chains of the receptor. No binding constant could be measured for polysaccharide cellulose, yet polyrotaxane formation between cyclophane **35** and cellulose was confirmed by induced CD effects as well as atomic force microscopy (AFM) images (Figure 29).

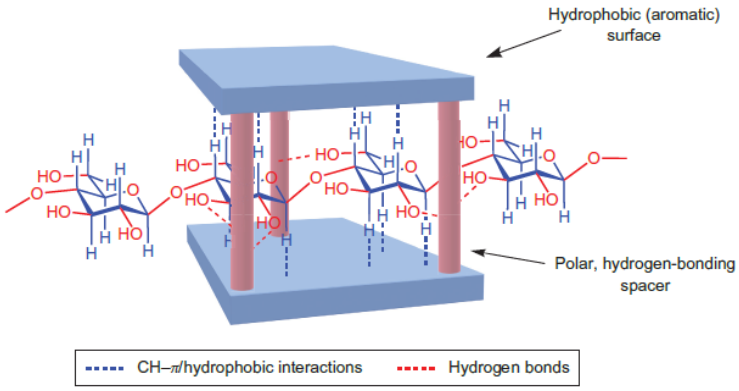

Figure 29. Schematic illustration of the threading of cellulose and its smaller fragments through the cavity of the pyrenophane **35**. Adapted with permission from Ref. [95]. Copyright 2015 Springer Nature.

In the host **36**, a hydrophobic cavity for saccharide binding is generated by linking the porphyrin subunits by quasi-tetrahedral amido-azonia cryptands (Figure 30a).[96] Encapsulation of several mono-, di and trisaccharides is confirmed by UV-vis titration experiments. D-Glucose, for example, is recognized with an association constant of 1.3×10^3 L mol^{-1} which clearly outperforms synthetic lectins **28** and **30** in terms of affinity. Yet regarding selectivity for monosaccharides, **36** cannot compare as it binds non-all-equatorial carbohydrate D-galactose as strongly as D-glucose. The highest affinity of **36**, however, is found for the α-1,4-linked glucose trimer maltotriose with $K_a = 5.2 \times 10^4$ L mol^{-1} (Figure 30b). A suggested structure for the host-guest complex maltotriose⊂**36** is obtained by molecular modelling (Figure 30c).

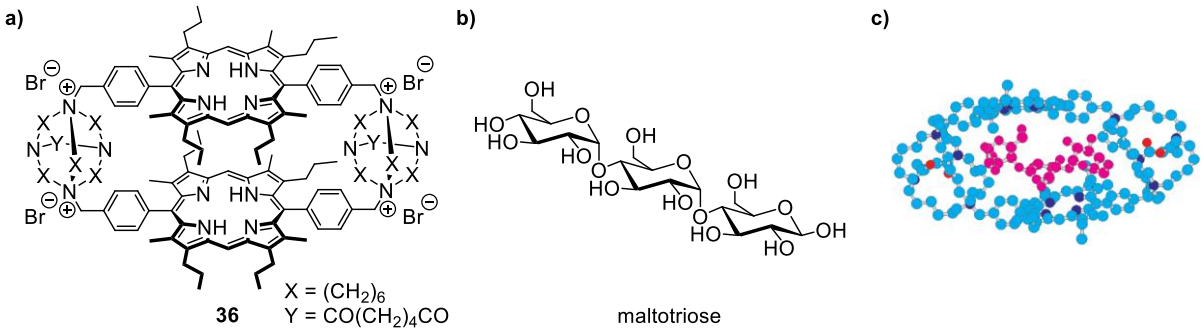

Figure 30. Chemical structures of **(a)** cyclic bisporphyrin host **36** and **(b)** carbohydrate guest maltotriose. **(c)** Energy-minimized structure of the host-guest complex maltotriose⊂**36** (Hyperchem). **36** is depicted in blue, maltotriose in magenta. Adapted with permission from Ref. [96]. Copyright 2001 The American Chemical Society.

Selectivity of a cyclophane host to a non-all-equatorial sugar derivative was observed by Francesconi *et al.*[97] In the cyclic anthracene dimer **37** the aromatic units for the formation of CH–π interactions towards a sugar guest are held apart by two 1,8-diaminocarbazole spacers which can develop hydrogen bonds with a substrate and which are functionalized with water-

solubilizing phosphonate groups (Figure 31a). In the analysis of ^{1}H NMR binding studies at pD = 11 ensuring full deprotonation of **37**, host self-aggregation to a supramolecular dimer has to be considerd. Thus, 1:1, 2:1 and 2:2 host-guest complex stoichiometries are included in the linear regression analysis and binding constants are defined as cumulative formation constants or intrinsic median binding concentration. The latter describes the total amount of receptor necessary to bind 50% of the substrate when the amount of formed complex is 0.[98] For a 1:1 host-guest complex, the intrinsic median binding concentration is identical to the dissociation constant K_d. Remarkably, receptor **37** binds carbohydrate derivatives with axial OH-groups such as methylated α-D-galactose as tightly as methylated α-D-glucose.[97] Yet the highest affinity in the range of 10^3 L mol^{-1} is observed for methylated α-L-fucose (Figure 31b) which was bound 30-times stronger than the corresponding β-anomer. A molecular mechanics analysis based on the intensity of nuclear Overhauser effect (NOE) signals between bound Me-α-L-fucose and cyclophane host **37** reveals hydrogen bonds involving both carbazolic NH and three aminic NH groups of the synthetic lectin and OH-2, OH-4 and the α-anomeric O of L-fucose (Figure 31c). Additional contributions to complex stability are provided by several CH−π interactions between the anthracene units of **37** and the axial hydrogen atoms of the carbohydrate guest molecule.

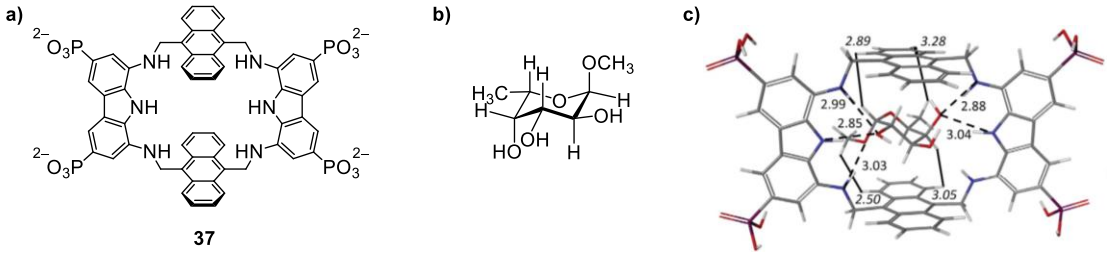

Figure 31. Chemical structures of **(a)** the biomimetic carbohydrate receptor **37** and **(b)** its substrate methylated α-L-fucose. **(c)** Global minimum structure of the host-guest complex α-L-fucose⊂**37** based on NOE signals. Solid lines correspond to the strongest intermolecular NOEs, dashed lines indicate hydrogen bonding interactions. The distances are given in Å. Adapted with permission from Ref. [97]. Copyright 2018 Wiley VCH.

2.2.5 Alkaloids

Alkaloids are a prominent class of ubiquitous nitrogen containing natural compounds with a great structural variety and diverse biological activity (Figure 32).[32] For example, the β-carboline alkaloid harmine was found to reversibly inhibit monoamine oxidase A and possesses anti-cancer and anti-inflammatory properties.[99] Thus, molecular detection and host-guest complexes of such alkaloids in aqueous environment are of general interest.[100] For aromatic

alkaloids, water-soluble cyclophane hosts should be especially efficient as they can stabilize the host-guest complex by π–π- and cation–π-interactions. However, only a few cases of host-guest complex formation between aromatic alkaloids and cyclophanes are reported.

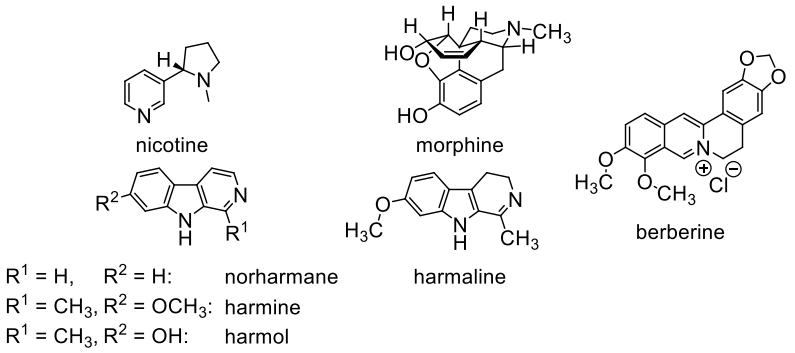

Figure 32. Chemical structures of selected exemplary alkaloids.

Dougherty's cyclophane (**27**) (Figure 33), for example, binds the protonated form of the well-known alkaloid nicotine in borate buffer at 298 K.[73] For the *S*,*S*,*S*,*S*-enantiomer of the host, the binding constant of 8.5×10^2 L mol^{-1} for the chiral alkaloid is slightly lower than that of the *R*,*R*,*R*,*R*-enantiomer with $K_a = 1.2 \times 10^3$ L mol^{-1}. Yet as this cyclophane binds a large variety of cationic guests, the recognition of nicotine by **27** is not selective. Nicotine as a template also amplified the formation of host **38** in a dynamic combinatory library.[101] The binding constants at pH = 6.9, at which the basic guest molecule is protonated, and at pH = 9.3, at which nicotine exists as free base, are both determined as approximately 3×10^3 L mol^{-1} at 298 K, suggesting that the host-guest complex is stabilized by dispersion rather than by cation–π-interaction. Morphine, on the other hand, templated the formation of cyclophane **21** (Figure 20a) as a racemate from a dynamic combinatory library.[102] The association constant of the host-guest complex morphine⊂**21** is 2.7×10^4 mol L^{-1} at pH = 9 and 298 K. However, **21** is also not selective towards the opiate. The water-soluble pillar[5]arene **24** (Figure 21) binds the alkaloid drug norharmane in water at pH = 7.0 and 298 K with an affinity of 3.4×10^4 L mol^{-1} for the 1:1 complex.[103] Interestingly, the cell toxicity of norharmane was reduced upon encapsulation. Moreover, protonation of the host by acidification triggered the reversible release of the alkaloid guest.

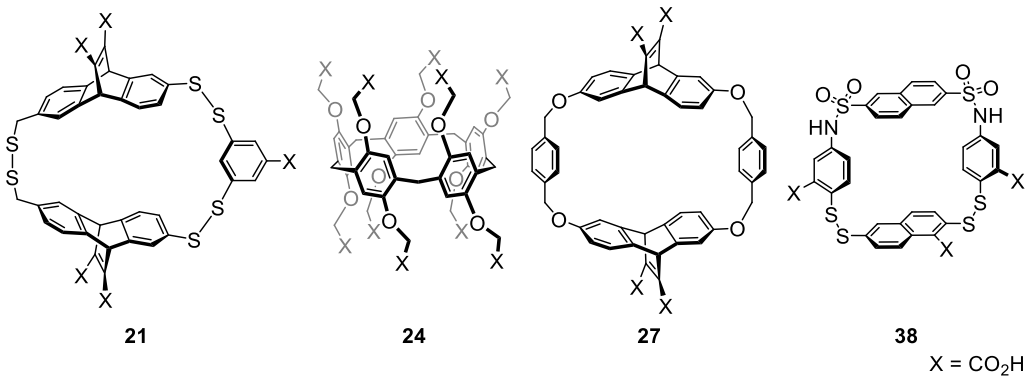

Figure 33. Chemical structures of known cyclophane hosts for alkaloids (**21** for morphine; **24** for norharmane; **27**, **38** for nicotine).[73, 101-103]

For other *harmala* alkaloids such as harmine, harmol or harmaline, and for benzylisoquinoline derivatives such as berberine, only inclusion complexes with the ubiquitous water-soluble macrocycle hosts cyclodextrins, cucurbiturils and calixarenes are reported.[100, 104] However, no chromophore-based macrocyclic hosts that exhibit absorption and emission in the visible spectral range have so far been applied for the recognition of these alkaloids. Moreover, no studies are reported on host-guest binding of a broad series of structurally different alkaloids with a particular host in comparative manner to explore a structure binding-property relationship.[100] Therefore, the design and investigation of a water-soluble cyclophane host for the recognition of such alkaloids in aqueous environment was one of the main aims of this thesis.

2.3 Conformational Selection and Induced Fit

Specific molecular recognition is ubiquitous in biological phenomena[105] including activation of enzymatic reactions by binding of the right substrate,[1] regulation of gene expression[106] or initiation of signal transduction cascades upon binding of a particular ligand to a receptor.[2] At the end of the 19th century in an early attempt to rationalize enzyme specificity, Emil Fischer compared the protein (P) to a lock in which the ligand (L) had to fit like a key (Figure 34a).[107] In this initial concept, biological macromolecules were defined as rigid systems neglecting their nowadays known structural flexibility. Hence, more refined binding models were developed involving conformational transitions[34] since knowledge of the binding mechanism of a specific receptor is advantageous for the rational design of effective drugs and therapeutics and often necessary to understand the functionality of biochemical pathways in cells.[108]

There are two limiting cases of binding models discussed in literature differing primarily in the order in which ligand binding and structural rearrangement of the protein occur. On the one hand, the induced fit concept, nowadays synonymous to the Koshland-Némethy-Filmer model,[34b] assumes that a ligand L first loosely associates with the protein P to the complex PL. Consecutively, structural rearrangements are induced in the protein until an optimal fit is achieved (P*L) (Figure 34b). The conformational selection model, on the other hand, which is based on an approach by Monod, Wyman and Changeux,[34a] states that the unbound protein exists in an equilibrium of various conformations (termed P and P* in Figure 34b). The ligand selectively binds to and stabilizes the best-fitting conformer shifting the whole equilibrium as a consequence. One way of differentiation between the two models is the analysis of relaxation experiments.[109] A chemically equilibrated system is disturbed by temperature jump or an increase in concentration of one of the species, for example, and the kinetic signature with which the system relaxes to the new equilibrium state is monitored.

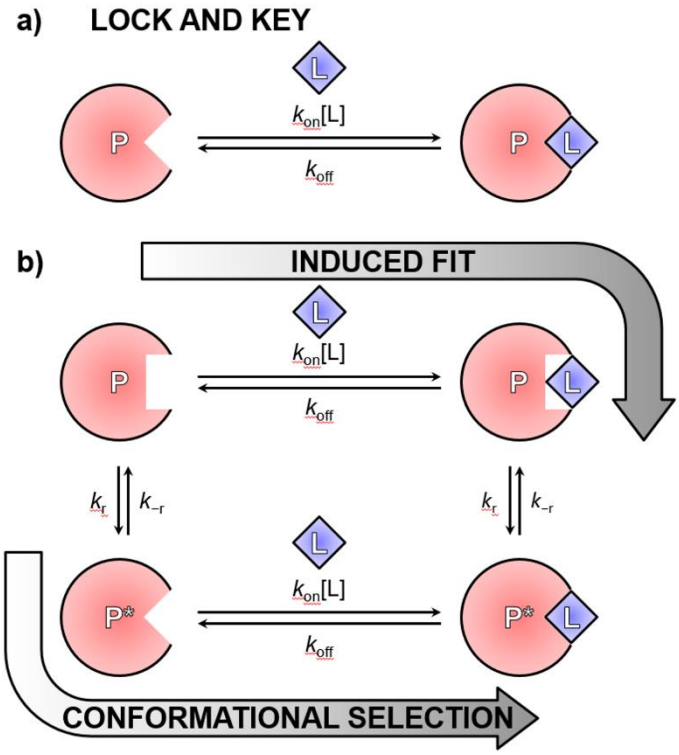

Figure 34. Schematic representation of a ligand (L) binding to a protein (P) according to **(a)** the lock and key model and **(b)** the induced fit and conformational selection models.

When [L] ≫ [P] in the experiment, the concentration of the ligand is considered constant and pseudo first order rate kinetics are assumed for the respective ligand binding step of both the induced fit and conformational selection model.[110] Thus, the mechanistic pathways can be

sufficiently described with two rate equations when considering the mass conservation relationships $[P]_0 = [P] + [PL] + [P^*L]$ or $[L]_0 = [L] + [PL] + [P^*L]$ with $[P]_0$ as total protein concentration and [P], [L], [PL] and [P*L] as the concentrations of protein, ligand and protein ligand complex at a given time *t*.

For the induced fit model, the rate equations

$$-\frac{d[P]}{dt} = k_{on}[L][P] - k_{off}[PL] \quad (1)$$

and

$$-\frac{d[P^*L]}{dt} = k_{-r}[P^*L] - k_r[PL] \quad (2)$$

are devised. The rate constants k_{on} and k_{off} refer to the ligand association and dissociation process, respectively. k_r and k_{-r} designate the rates of conformational change in the protein (Figure 34b). As the relaxation of the system to the equilibrium is monitored, the relationships between the concentrations of a species [P], [PL] or [P*L], respectively, at a given time *t* and in the equilibrium is defined as

$$[P] = [P]_e + \Delta[P], \quad (3)$$

$$[PL] = [PL]_e + \Delta[PL], \quad (4)$$

$$[P^*L] = [P^*L]_e + \Delta[P^*L]. \quad (5)$$

where the subscripted e refers to the concentration of the respective species in the equilibrium state and Δ indicates the deviation from equilibrium. When considering and $\Delta[P] + \Delta[PL] + \Delta[P^*L] = 0$ due to mass conservation and $k_{on}[L][P]_e = k_{off}[PL]_e$, equations (1) and (2) are expressed as

$$-\frac{d\Delta[P]}{dt} = (k_{on}[L] + k_{off})\Delta[P] + k_{off}\Delta[P^*L] \quad (6)$$

and

$$-\frac{d\Delta[P^*L]}{dt} = k_r\Delta[P] + (k_r + k_{-r})\Delta[P^*L] \quad (7)$$

or in the form of the matrix

$$\begin{pmatrix} -\frac{d\Delta[\mathrm{P}]}{dt} \\ -\frac{d\Delta[\mathrm{P*L}]}{dt} \end{pmatrix} = \begin{pmatrix} (k_{\mathrm{on}}[\mathrm{L}] + k_{\mathrm{off}}) & k_{\mathrm{off}} \\ k_{\mathrm{r}} & (k_{\mathrm{r}} + k_{\text{-r}}) \end{pmatrix} \begin{pmatrix} \Delta[\mathrm{P}] \\ \Delta[\mathrm{P*L}] \end{pmatrix}.$$

The non-zero eigenvalues λ of the matrix can be determined with

$$0 = (k_{\mathrm{on}}[\mathrm{L}] + k_{\mathrm{off}} - \lambda)(k_{\mathrm{r}} + k_{\text{-r}} - \lambda) - (k_{\mathrm{r}} k_{\mathrm{off}}) \tag{8}$$

which transforms to a quadratic equation with the solutions

$$\lambda_{1,2} = \frac{1}{2}\Big((k_{\mathrm{on}}[\mathrm{L}] + k_{\mathrm{off}} + k_{\mathrm{r}} + k_{\text{-r}}) \pm \sqrt{(k_{\mathrm{on}}[\mathrm{L}] + k_{\mathrm{off}} + k_{\mathrm{r}} + k_{\text{-r}})^2 - 4(k_{\mathrm{on}}[\mathrm{L}]k_{\text{-r}} + k_{\mathrm{on}}[\mathrm{L}]\mathrm{k_r} + k_{\mathrm{off}}k_{\text{-r}})}\Big) \tag{9}$$

with λ corresponding to the observed rate constant k_{obs}, with which the system relaxes to equilibrium. When applying the so-called rapid equilibrium approximation, which states that the bimolecular ligand binding step is much faster than the protein isomerization, i. e. $k_{\mathrm{on}}[\mathrm{L}] + k_{\mathrm{off}} \gg k_{\mathrm{r}} + k_{\text{-r}}$, equation (9) simplifies to

$$\lambda_1 = k_{\mathrm{obs},1} = k_{\mathrm{on}}[\mathrm{L}] + k_{\mathrm{off}} \tag{10}$$

for the larger k_{obs} and to

$$\lambda_2 = k_{\mathrm{obs},2} = k_{\mathrm{r}} \frac{k_{\mathrm{on}}[\mathrm{L}]}{k_{\mathrm{off}} + k_{\mathrm{on}}[\mathrm{L}]} + k_{\text{-r}} \tag{11}$$

for the smaller k_{obs} when approximating the term under the square root according to $\sqrt{1-x} \approx 1 - \frac{x}{2}$ for $x \ll 1$.[110-111]

The conformational selection model can be treated accordingly. The two necessary rate equations to describe the system are

$$-\frac{d[\mathrm{P}]}{dt} = k_{\mathrm{r}}[\mathrm{P}] - k_{\text{-r}}[\mathrm{P*}] \tag{12}$$

and

$$-\frac{d[\mathrm{P*L}]}{dt} = k_{\mathrm{off}}[\mathrm{P*L}] - k_{\mathrm{on}}[\mathrm{L}][\mathrm{P*}]. \tag{13}$$

Equations (12) and (13) are modified again with equations (3) − (5) to give the matrix

$$\begin{pmatrix} -\frac{d\Delta[\mathrm{P}]}{dt} \\ -\frac{d\Delta[\mathrm{P^*L}]}{dt} \end{pmatrix} = \begin{pmatrix} (k_\mathrm{r} + k_\mathrm{-r}) & k_\mathrm{-r} \\ k_\mathrm{on}[\mathrm{L}] & (k_\mathrm{on}[\mathrm{L}] + k_\mathrm{off}) \end{pmatrix} \begin{pmatrix} \Delta[\mathrm{P}] \\ \Delta[\mathrm{P^*L}] \end{pmatrix}.$$

The non-zero eigenvalues of this matrix are determined as

$$\lambda_{1,2} = \frac{1}{2}\Big((k_\mathrm{on}[\mathrm{L}] + k_\mathrm{off} + k_\mathrm{r} + k_\mathrm{-r}) \pm \sqrt{(k_\mathrm{on}[\mathrm{L}] + k_\mathrm{off} + k_\mathrm{r} + k_\mathrm{-r})^2 - 4(k_\mathrm{on}[\mathrm{L}]k_\mathrm{off} + k_\mathrm{off}k_\mathrm{r} + k_\mathrm{off}k_\mathrm{-r})} \Big). \quad (14)$$

Applying the rapid equilibrium approximation yields

$$\lambda_1 = k_{\mathrm{obs},1} = k_\mathrm{on}[\mathrm{L}] + k_\mathrm{off} \quad (15)$$

and

$$\lambda_2 = k_{\mathrm{obs},2} = k_\mathrm{r}\frac{k_\mathrm{off}}{k_\mathrm{off} + k_\mathrm{on}[\mathrm{L}]} + k_\mathrm{-r} \quad (16)$$

as the rate constants for the relaxation to equilibrium in case of conformational selection.[110-111]

The larger $k_{\mathrm{obs},1}$ values defined by equations (10) and (15) are identical for both the induced fit and the conformational selection model under the rapid equilibrium approximation. They describe the fast-equilibrating ligand-binding step and indeed are also identical to the equation for a rate constant of an isolated bimolecular reaction under pseudo-first order conditions such as the lock and key model (Figure 34).[110, 112] However, the contribution of this fast kinetic process to the overall relaxation is often hardly detectable by standard measurement techniques. The smaller $k_{\mathrm{obs},2}$ values defined by equations (11) and (16), on the other hand, are characteristic for induced fit or conformational selection, respectively, when the rapid equilibrium approximation is valid. The $k_{\mathrm{obs},2}$ values are accessible from experimental data as the slope of a plot of $\ln(\Delta[\mathrm{P^*L}])$ versus t. This relation is derived from the solution of the rate equations (2) and (13), which have the general shape

$$\Delta[\mathrm{P^*L}] = A_1 e^{-k_{\mathrm{obs},1}t} + A_2 e^{-k_{\mathrm{obs},2}t} \quad (17)$$

with constants A_1 and A_2 reflecting the respective boundary conditions.[110] Since $k_{obs,1} \gg k_{obs,2}$ as a result of the rapid equilibrium approximation, the first term of equation (17) is negligible. The corresponding linearization of this exponential equation, which is valid up to 10% from equilibrium, is given as

$$\ln(\Delta[\mathrm{P^*L}]) = -k_{obs,2}t + \ln(A_2). \tag{18}$$

With the help of equation (18), $k_{obs,2}$ values for the relaxation to equilibrium of a system can be determined for several concentrations of the ligand. Subsequently, these $k_{obs,2}$ values are plotted as a function of ligand concentration [L]. For induced fit, such a plot of $k_{obs,2}$ (equation (10)) increases hyperbolically with [L] with the asymptotic values of k_{-r} for [L] → 0 and $k_r + k_{-r}$ for [L] → ∞ (Figure 35a). On the other hand, for conformational selection a plot of $k_{obs,2}$ (equation ((15))) as a function of ligand concentration yields an inverse hyperbola decreasing with increasing [L] with the asymptotic values of $k_r + k_{-r}$ for [L] → 0 and k_{-r} for [L] → ∞ (Figure 35b).[112] In both cases, the focus of the hyperbola gives the dissociation constant $K_d = K_a^{-1}$. Hence, the dependence of $k_{obs,2}$ is indicative of whether the system follows the induced fit or the conformational selection model when the ligand association step is by far faster than the conformational changes in the protein.

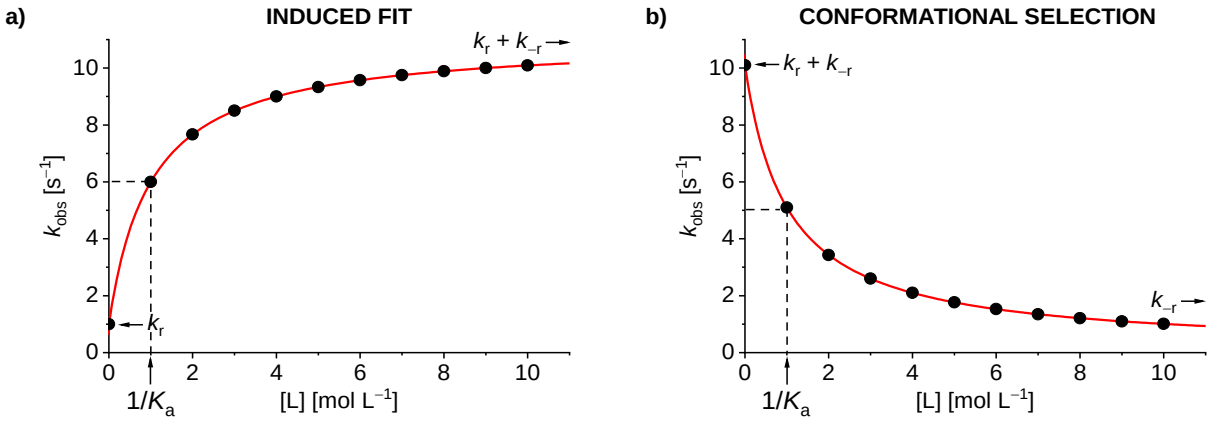

Figure 35. Representative plots for k_{obs} as a function of ligand concentration for **(a)** the induced fit and **(b)** the conformational selection model when the rapid equilibrium approximation is valid.[112]

Such differentiation becomes difficult, however, when the structural rearrangement of the protein is not the rate-determining step. For induced fit, $k_{obs,2}$ always increases as a function of [L]. Yet for conformational selection, such a plot can both decrease or increase depending on the relationships between the respective rate constants. Furthermore, the physical meanings of the asymptotes change. In other words, when $k_{obs,2}$ increases together with [L], conformational

selection can unambiguously be assumed. For the inverse case, a mechanistic assignment is not easily possible.[111b, 112-113] Moreover, it has to be noted that induced fit and conformational selection represent two limiting cases of ligand binding. The actual reality of ligand binding by proteins is by far more complex than the schematic representation in Figure 34b. For example, a binding event according to the conformational selection pathway may be followed by another structural adjustment of the protein ligand complex.[114] Additionally, induced fit and conformational selection are not necessarily mutually exclusive for a certain system. What mechanistic pathway the recognition event follows is mainly dependent on the ratio of rate constants for each step depicted in Figure 34b. Indeed, the mechanism of some systems can change from mainly conformational selection to mainly induced fit for high ligand concentration.[115]

Supramolecular host-guest chemistry has always been inspired by the selectivity and efficacy of substrate enzyme recognition. Like for proteins, structural rearrangements aiming for a more effective inclusion of a guest molecule is frequently observed for supramolecular hosts.[102, 116] The mechanistic duality between induced fit and conformational selection in a supramolecular system, however, has only recently been investigated with detailed kinetic studies by the groups of Bergman, Raymond and Toste.[116f] The free metallosupramolecular host **39** consisting of four Ga corners and four trianiline-linkers can adopt either a tetrahedral or a distorted conformation of S_4 symmetry (Figure 36a). Upon guest binding, the tetrahedral conformation is stabilized. The approach to guest encapsulation equilibrium of host **39** and NEt_4I was monitored by time-dependent ^1H NMR spectroscopy for different concentrations of NEt_4I showing decreasing relaxation rates k_{obs} with higher guest concentrations. Hence, guest recognition of host **39** occurs by conformational selection (Figure 36b).

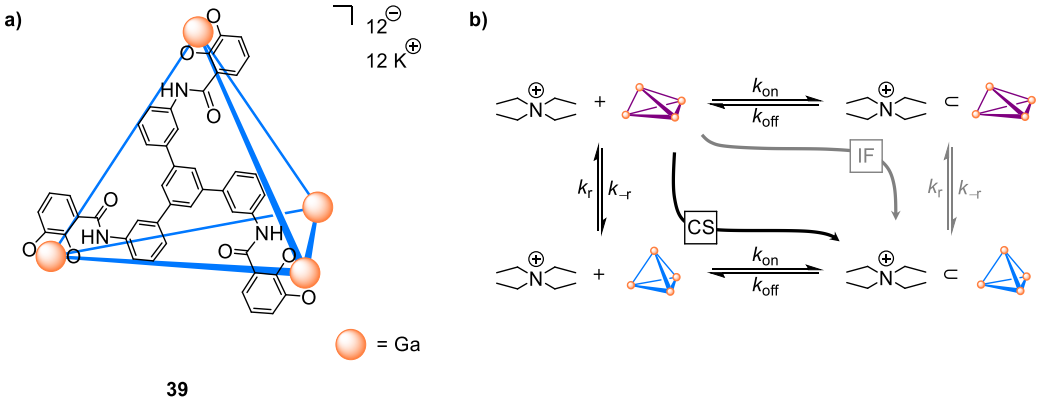

Figure 36. Schematic representations of **(a)** metallosupramolecular host **39** and **(b)** the mechanistic duality of induced fit (IF) and conformational selection (CS) for host **39** and guest NEt_4^+.[116f]

The group of Akine transferred the problem of induced fit vs. conformational selection, i.e. whether guest binding or host isomerization occurs first, to whether guest binding or ligand exchange reactions is faster for a cobalt(III) metallohost **40** (Figure 37a).[117] In methanol, host **40** both accommodates a guest cation in its 18-crown-6-like cavity and an exchange of the axial piperidine groups for a methoxo ligand occurs. Kinetic studies, which are similar to experiments for the differentiation between induced fit and conformational selection, were performed to determine in which order these steps take place. It was shown that the solvolytic ligand exchange was accelerated in the presence of Na^+ guest for both low and high amounts of Na^+ due to the coordination of solvent molecules to the alkali ion guest. As the ligand exchange, i. e. the step analogous to host isomerization, is the rate-determining step, the rapid equilibrium approximation is valid and it can be concluded that host binding precedes ligand exchange. However, kinetic studies with one equivalent of K^+ and Rb^+ as guests, respectively, suggested that for these alkali metal ions the ligand exchange occurs prior to guest recognition, i. e. the reaction first mechanism is observed under these conditions. Thus, cobalt(III) metallohost **40** represents an example for which the recognition pathway can be switched by variation of the cationic guests and their amount.

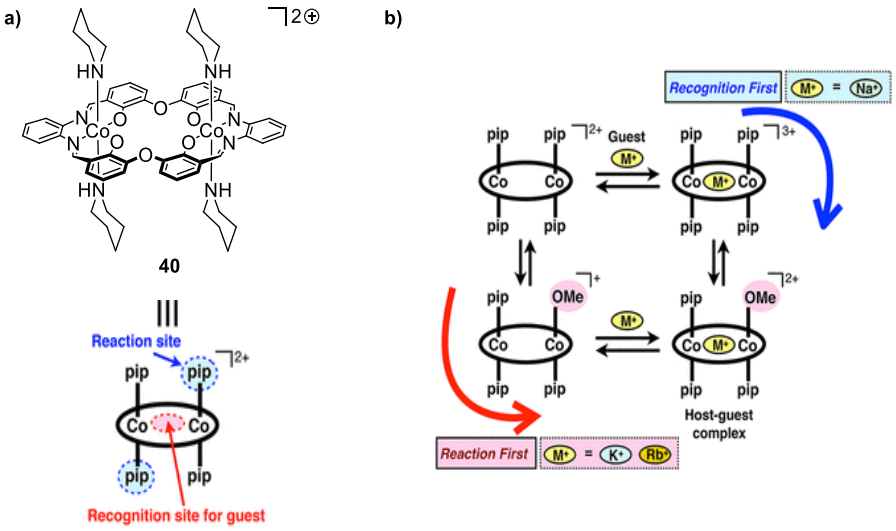

Figure 37. (a) Chemical structure of host **40** and schematic representation of its reactive sites. **(b)** Schematic illustration of the metal ion-dependent switch between the mechanisms recognition first and reaction first. Adapted with permission from Ref. [117]. Copyright 2019 The American Chemical Society.

Chapter 3

–

Results and Discussion

3.1 Synthesis

The target molecules, the macrocyclic dimers **[2PBI]-1m** and **[2PBI]-1p** as well as their reference monomers **ref-PBI-1m** and **ref-PBI-1p** were synthesized in a in a multistep approach according to the routes depicted in Scheme 1. In the first step, *N*,*N*′-dibutyl-1,6,7,12-tetrachloro-3,4:9,10-tetracarboxylic acid perylene bisimide[118] (**41**) was reacted with 4-iodophenole or 3-iodophenole in *N*-methylpyrrolidone (NMP) at 110 °C for 18 h to give literature-known PBI **42p**[119] and the new PBI derivative **42m**, respectively. In the next step, triisopropylsilyl (TIPS)-protected acetylene functionalities were introduced by Sonogashira coupling at the iodine atoms of the aryloxy substituents in the bay position.[120] The following saponification of the imide groups of **43m** and **p** with potassium hydroxide (KOH) in *tert*-butanol at 110 °C gave perylene bisanhydrides (PBA) **44m** and **p**. Subsequent imidization of PBAs **44m** and **p** with *para*-xylylenediamine according to Peter Spenst's procedure,[30a] in which the solvent toluene presumably templates the formation of cyclic PBI dimers, afforded the cyclophanes **[2PBI]-4m** and **p** in yields of 15%. Cleavage of the TIPS protecting groups of this precursor with tetra-*n*-butylammonium fluoride (TBAF) gave the instable intermediates **[2PBI]-4m** and **p**. Immediate Cu(I)-catalyzed alkyne-azide cycloaddition (CuAAC)[121] with OEG azide **45** using CuOAc as catalyst and tris(benzyltriazolylmethyl)amine (TBTA) as ligand[122] to stabilize the Cu(I) oxidation state gave **[2PBI]-1m** in the yield 50% and **[2PBI]-1p** in the yield of 75%. The reduced yield for the *meta*-cyclophane when compared to the *para*-cyclophane might be explained by the different orientation of the acetylene groups of the regioisomers. Close proximity of these Cu(I)-coordinating groups was reported to cause the removal of the CuAAC catalyst from the solution and thus impedes the reaction.[123]

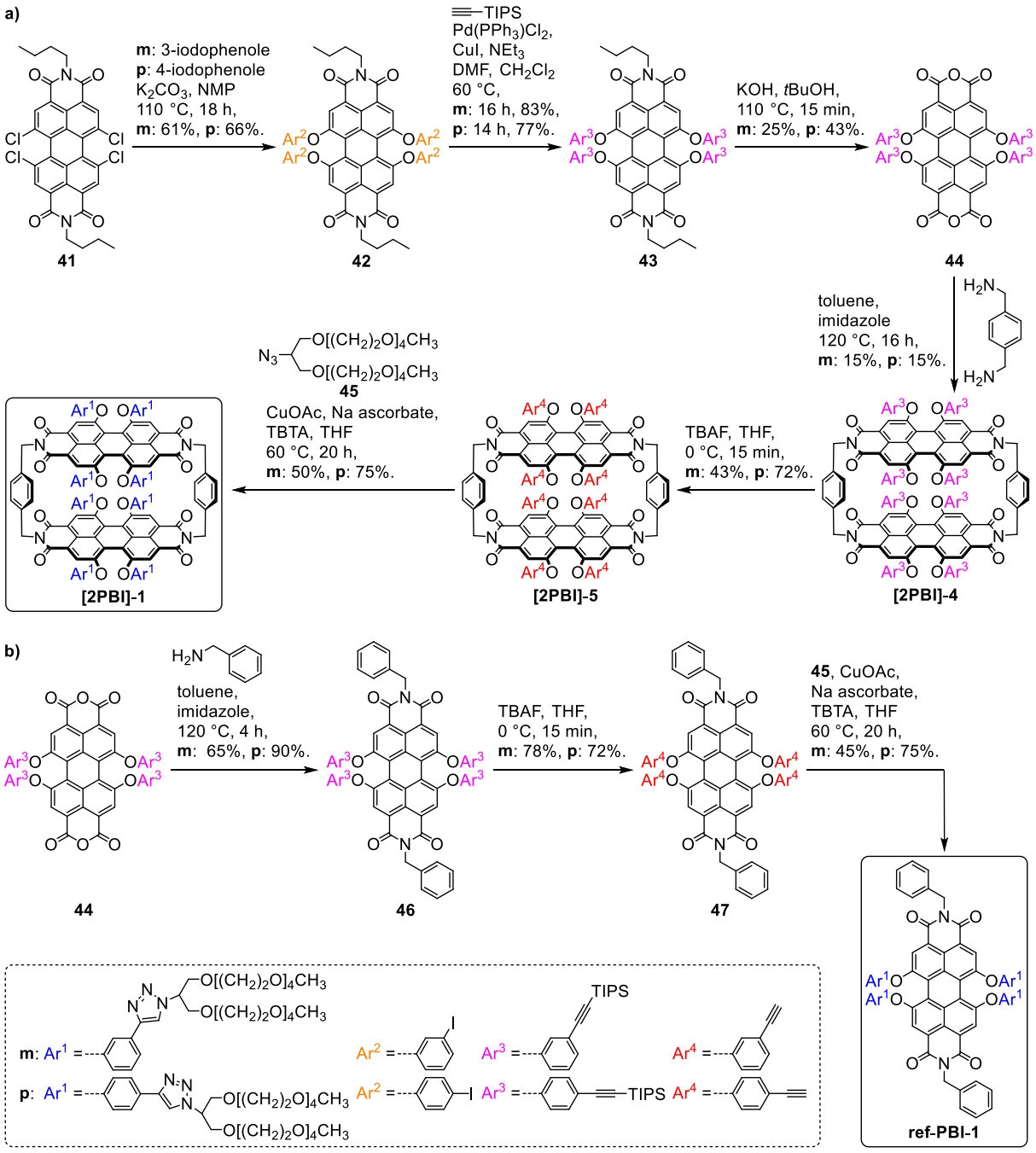

Scheme 1. Syntheses of **(a)** the target molecules of this work, the macrocyclic PBI dimers **[2PBI]-1m** and **p** and **(b)** the reference monomers **ref-PBI-1m** and **p**.

The respective water-soluble reference monomers **ref-PBI-1m** and **p** (Scheme 1b) were prepared in analogous fashion starting from PBAs **44m** or **p**. Imidization of the PBAs with benzyl amine in a solvent mixture of toluene and imidazole gave PBIs **46m** and **p** in yields of 65% and 90%, respectively. Deprotection of the TIPS groups with TBAF resulted in the instable intermediates **47m** and **p** which were immediately converted to **ref-PBI-1m** and **p** by CuAAC with azide **45**. Like in the case of the water-soluble cyclophanes **[2PBI]-1m** and **p**, a higher

yield of 75% was obtained for the *para*-substituted derivative **ref-PBI-1p** when compared to the yield of 45% for *meta*-functionalized **ref-PBI-1m**.

OEG azide **45**, which is used as a coupling partner in the final CuAAC, was prepared by tosylation of the literature known branched OEG precursor **48**[124] to OEG derivative **49** and subsequent nucleophilic substitution with NaN_3 (Scheme 2).

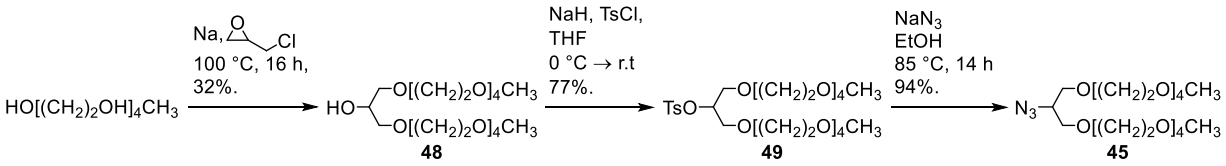

Scheme 2. Synthesis of glycerol azide **45**.

3.2 A Water-Soluble Perylene Bisimide Cyclophane as a Molecular Probe for the Recognition of Aromatic Alkaloids

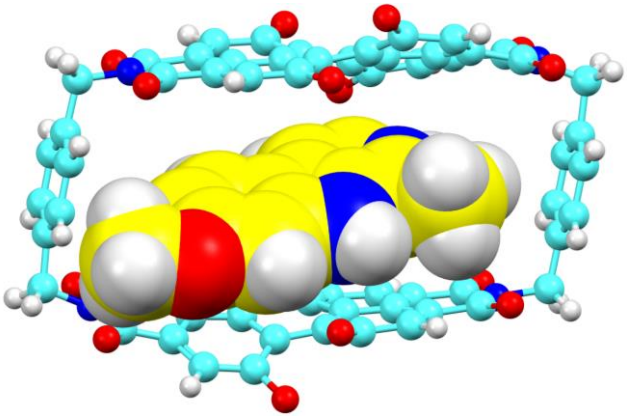

Abstract.[1] Here we report a water-soluble macrocyclic host based on perylene bisimide (PBI) chromophores which recognizes natural aromatic alkaloids in aqueous media by intercalating them into its hydrophobic cavity. The host-guest binding properties of our newly designed receptor with several alkaloids were studied by UV-vis and fluorescence titration experiments as the optical properties of the chromophoric host change significantly upon complexation of guests. Structural information on the host-guest complexes was obtained by 1D and 2D NMR spectroscopy and molecular modelling. Our studies reveal a structure binding-property relationship for a series of structurally diverse aromatic alkaloids with the new receptor and higher binding affinity for the class of harmala alkaloids. To our knowledge, this is the first example of a chromophoric macrocyclic host employed as a molecular probe for the recognition of aromatic alkaloids.

3.2.1 Introduction

About fifty years ago, the discovery of cation complexation by macrocyclic crown ethers marked the beginning of the field of supramolecular chemistry.[7a, 9] Since then encapsulation of a broad variety of organic substrates by macrocyclic hosts has been reported[62] and the research focus in this field has shifted towards water-soluble artificial receptors[125] due to their

[1] This chapter has been published: M. Sapotta, A. Hofmann, D. Bialas, F. Würthner, *Angew. Chem. Int. Ed.* **2019**, *58*, 3516 – 3520.

promising pharmaceutical and medical applications.[15] In this regard cyclodextrins and cucurbiturils as well as hydrophilic pillararenes and calixarenes evolved as universal hosts for the complexation of drugs, vitamins, fragrances, and other desirable guest molecules.[16-19, 71] For other applications, however, e.g. the detection and analysis of biomolecules, selectivity towards a specific analyte is required.[74d, 126] This holds in particular true for so-called molecular probes which, in addition to a high selectivity for the recognition of specific guest molecules, are required to show a specific response to the respective analyte such as a change in absorbance or fluorescence.[25, 127] Towards this goal, among macrocyclic receptors the class of cyclophanes appears to be highly promising. By additionally employing π-π- and C−H-π-interactions for guest encapsulation, cyclophanes are suitable hosts not only for biologically important aromatic molecules such as certain amino acids,[24] nucleotides,[20a, 25] the neurotransmitters epinephrine or dopamine,[26] but also for carbohydrates[128] in water.

However, the design of cyclophanes which possess larger cavities and are composed of dyes remains challenging.[25, 129] For instance, only recently Stoddart and co-workers have accomplished the extension of their famous viologen-based cyclophanes ("blue box")[130] by additional phenyl units to achieve the encapsulation of larger π-systems such as tetracene or corannulene.[14c] Likewise, our efforts to synthesize cyclophanes based on the large and strongly aggregating perylene bisimide (PBI) fluorophores[28] only recently succeeded in the complexation of a variety of polycyclic aromatic hydrocarbons (PAHs) in organic solvents.[30a]

Here we report on the refinement of this PBI cyclophane with hydrophilic oligoethylene glycol (OEG) groups to afford the first water-soluble macrocyclic PBI host **[2PBI]-1p** (Figure 38a) and demonstrate its successful application as a synthetic receptor for the aromatic alkaloids harmine and berberine. Alkaloids are a prominent class of ubiquitous nitrogen containing natural compounds with a great structural variety and diverse biological activity.[32b] Thus, comparable to the demonstration of the power of synthetic methodologies by successful natural product synthesis,[131] complexation of alkaloid natural products illustrates the advancement in supramolecular host design. Whereas the rather unspecific complexation of aromatic alkaloids in water by cyclodextrins and cucurbiturils as well as calixarene derivatives were already reported,[100, 104d] to the best of our knowledge **[2PBI]-1p** is the first chromophore-based macrocyclic host that monitors aromatic alkaloids by specific host-guest binding and concomitant changes in the optical properties of the host thus resembling a molecular probe.

3.2.2 Optical Properties of [2PBI]-1p

The newly designed macrocyclic receptor **[2PBI]-1p** was synthesized in a multistep approach according to the route depicted in Scheme 1. The synthetic details and characterization of **[2PBI]-1p** and all unknown intermediates are provided in the Experimental Section (Chapter 6.2). The alkaloid guests **G1** – **G10** (Figure 38b) used in this work are either commercially available or were prepared according to literature (see Chapter 6.1).

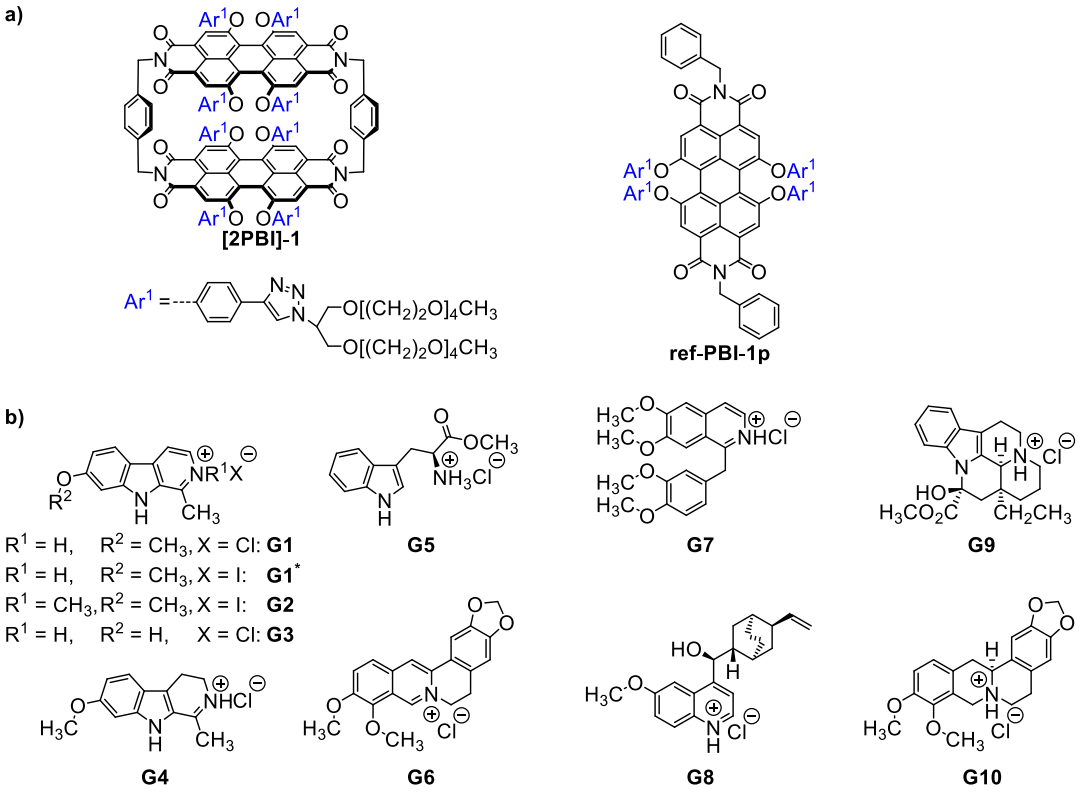

Figure 38. (a) Chemical structures of the newly developed receptor **[2PBI]-1p** and the monomeric reference compound **ref-PBI-1p**, and **(b)** of the investigated alkaloid guests **G1** – **G10**.

The optical properties of cyclophane **[2PBI]-1p** were investigated by UV-vis and fluorescence spectroscopy in different solvents (see Figure A1 in the Appendix I, Chapter 3.2.7). In $CHCl_3$, the absorption spectrum of **[2PBI]-1p** shows a regular vibronic progression with maxima at 581 and 542 nm and a ratio of the 0−0 and 0−1 vibronic transitions ($A_{0,0}/A_{0,1}$) of 1.27. In comparison, the $A_{0,0}/A_{0,1}$ ratio of the monomeric reference **ref-PBI-1p** with benzyl groups in the imide positions is 1.65 in the same solvent (Figure A2). Since the $A_{0,0}/A_{0,1}$ ratio is generally known to decrease significantly upon interchromophoric interaction in PBI cyclophanes[30, 132] and folda-dimers bearing rigid spacers,[133] it can be concluded that there is a considerable electronic coupling between the PBI subunits of **[2PBI]-1p**, compared to the respective

monomeric chromophore, yet the close contact to form a dimer aggregate is prohibited by the rigid xylylene spacer. **[2PBI]-1p** exhibits a fluorescence quantum yield (Φ_{fl}) of 8 % in $CHCl_3$, which is markedly lower than that for the previously reported *para*-xylylene-bridged PBI cyclophane (**[2PBI]-2**, see Chapter 2.1) bearing *tert*-butylphenoxy substituents in the bay positions (Φ_{fl} = 16 % in $CHCl_3$).[30a]

In H_2O, the absorption spectrum of **[2PBI]-1p** shows a slight redshift of 15 nm when compared to the spectrum in $CHCl_3$ and a considerable decrease in intensity of about 20 % which are known trends for PBIs in aqueous environment.[28, 31b] In H_2O, cyclophane **[2PBI]-1p** is virtually non-fluorescent (< 0.1%). Self-aggregation of **[2PBI]-1p** in H_2O is considered negligible as the spectral features in organic and aqueous media are similar to each other and as the concentration-dependent UV-vis spectra in H_2O are identical (Figure A3). Additionally, with regard to the host/guest titration studies, the absorption and emission spectra of **[2PBI]-1p** were measured in a mixture of H_2O/CH_3CN (1/1 vol%) and in pure CH_3CN. In these solvents the absorption spectra are nearly identical and the absorption maxima are a bit blue shifted (21 nm) compared to that in pure H_2O. The fluorescence quantum yield of **[2PBI]-1p** in the polar environments of CH_3CN as well as H_2O/CH_3CN is ~ 0.4 %.

3.2.3 Host-Guest Binding Studies of [2PBI]-1p with Aromatic Alkaloids

Host-guest binding studies of receptor **[2PBI]-1p** with the aromatic alkaloids **G1** – **G10** (Figure 38b) were performed in a solvent mixture of H_2O/CH_3CN (1/1 vol%). The advantage of this solvent system is the presence of a sufficiently strong emission which allowed fluorescence titration experiments.[2] Thus, we were able to determine the binding constants by two independent spectroscopic methods, UV-vis absorption and fluorescence, in order to obtain more credible data. All investigated alkaloids were used as salts for better solubility and stability in the applied solvent mixture. First, we have studied the *harmala* alkaloid harmine (**G1**) as a prime example. Upon addition of harmine hydrochloride to a solution of **[2PBI]-1p** in H_2O/CH_3CN (1/1), distinct changes in the absorption spectrum of the host are visible (Figure 39a). The decrease in intensity with increasing amount of **G1** in the region of the PBI S_0-S_1 transition is accompanied by a slight shift of the maxima from 575 nm and 539 nm to 577 nm and 540 nm, respectively. Also the $A_{0,0}/A_{0,1}$ ratio increased from 1.20 to 1.25 upon addition of

[2] In pure H_2O, a reliable data evaluation of our host/guest titration experiments was unfortunately not possible.

G1 indicating a disruption of the interchromophoric interaction between the PBI subunits of the host.

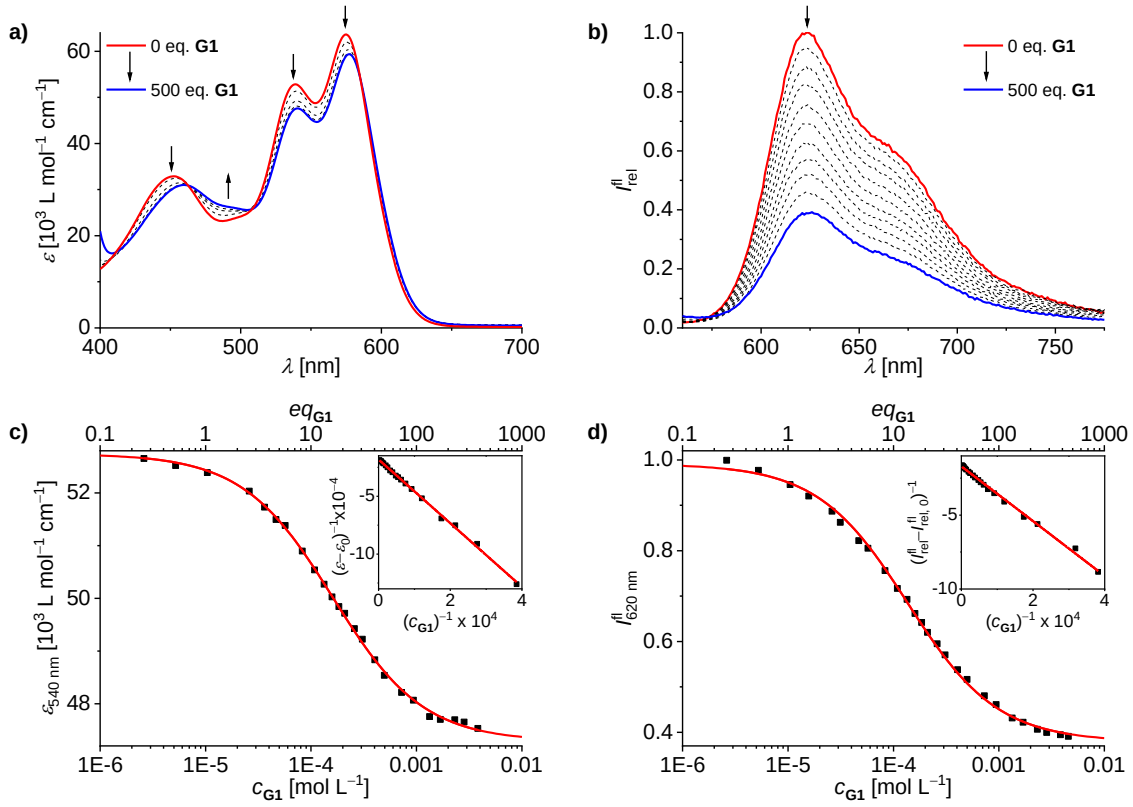

Figure 39. (a) UV-vis and **(b)** fluorescence titration (λ_{ex} = 520 nm) of **[2PBI]-1p** (c_0 = 1 × 10^{-5} mol L^{-1}) with **G1** in H_2O/CH_3CN (1/1 vol%) at 295 K. Arrows indicate changes upon increasing guest concentration. **(c)** Plots of UV-vis (540 nm) and **(d)** fluorescence (620 nm) titration data points as a function of guest concentration fitting with a 1:1 host guest binding model; insets: Benesi-Hildebrand plots showing a 1:1 stoichiometry of the host guest complex.

These observations suggest the formation of a host/guest complex between **[2PBI]-1p** and **G1** by intercalation of the aromatic alkaloid between the PBI π-surfaces of the host. The Benesi-Hildebrand plot[134] of the UV-vis titration data confirms a 1:1 stoichiometry of the host-guest complex **G1⊂[2PBI]-1p** (Figure 39c, inset). Correspondingly, the evaluation of the UV-vis titration data with a 1:1 binding model (see Experimental Section)[135] gave an association constant of K_a = 7.0 × 10^3 L mol^{-1} (Table 1).[3] A control titration experiment with the monomeric reference **ref-PBI-1p** in the same solvent mixture did not show any changes of the UV-vis spectrum of **ref-PBI-1p** upon addition of up to 1000 equivalents (eq.) of alkaloid **G1** (Figure A5). This corroborates our conclusion that the observed alterations in the absorption spectra of cyclophane **[2PBI]-1p** in the presence of **G1** are indeed due to complexation of the

[3] To exclude any influence of possible protonation eqilibria of the alklaoid guest on complex formation, control experiments were performed with **[2PBI]-1p** and **G1** in phosphate buffer (pH = 6.5). Yet the results did not differ significantly from those obtained in unbuffered H_2O/CH_3CN solution (K_a = 8.3 × 10^3 L mol^{-1}, see Figure A4).

guest molecule within the cavity, and not due to π-π-stacking of the aromatic alkaloid to the outside of the PBI macrocycle.

The recognition of **G1** by **[2PBI]-1p** could also be followed by fluorescence titration as strong quenching of the host emission was observed upon addition of the guest (Figure 39b, d). On the basis of our previously reported studies,[30a] the observed decrease in the fluorescence intensity can be explained in terms of a charge transfer complex formed by encapsulation of the electron-rich aromatic alkaloid **G1** in the cavity of the electron-poor PBI cyclophane. Evaluation of the fluorescence titration experiments gave comparable results to the UV-vis titrations in terms of the 1:1-stoichiometry of the host-guest complex and association constant (K_a = 7.6×10^3 L mol^{-1}).

Table 1. Comparison of the association constants K_a of **G1** – **G10** with **[2PBI]-1p** ($c_0 = 1 \times 10^{-5}$ mol L^{-1}) as determined based on UV-vis and fluorescence titration in H_2O/CH_3CN (1/1) at 295 K.

Guest	$K_a^{UV\text{-}vis}$ [L mol^{-1}]	K_a^{fl} [L mol^{-1}]	Ø (K_a) [L mol^{-1}][a]	$-\Delta G^0$ [kJ mol^{-1}][b]
G1	$(7.0 \pm 0.05) \times 10^3$	$(7.6 \pm 0.03) \times 10^3$	7.3×10^3	21.8
G1*	$(8.2 \pm 0.10) \times 10^3$	$(7.2 \pm 0.05) \times 10^3$	7.7×10^3	21.9
G2	$(2.5 \pm 0.01) \times 10^3$	$(2.2 \pm 0.01) \times 10^3$	2.4×10^3	19.1
G3	$(1.7 \pm 0.01) \times 10^3$	$(1.5 \pm 0.01) \times 10^3$	1.6×10^3	18.1
G4	$(1.2 \pm 0.01) \times 10^3$	$(1.2 \pm 0.01) \times 10^3$	1.2×10^3	17.4
G5	25.2 ± 0.83	19.6 ± 0.15	22.4	7.63
G6	$(8.4 \pm 0.04) \times 10^3$	$(7.1 \pm 0.03) \times 10^3$	7.8×10^3	22.0
G7	—[c]	21.6 ± 0.30	21.6	7.54
G8	< 5	—[c]	< 5	< 4
G9	—[d]	—[d]	—	—
G10	—[d]	—[d]	—	—

[a] Average from UV-vis and fluorescence titration experiments. [b] Gibbs free energies of complexation ΔG^0 determined from Ø (K_a) according to $\Delta G^0 = -RT\ln(K_a)$. [c] Reliable evaluation of data was not possible due to negligible spectral changes. [d] No binding.

We have continued our studies with the harmine derivative 2-methyl harmine iodide (**G2**) and harmol hydrochloride (**G3**), the *harmala* alkaloid harmaline hydrochloride (**G4**) and the amino acid derivative (*S*)-tryptophan methyl ester hydrochloride (**G5**), the latter as a model compound for the biosynthetic precursor of the important class of *harmala* alkaloids.[136] In addition, the study includes other naturally occurring alkaloids such as berberine chloride (**G6**), papaverine hydrochloride (**G7**), quinine hydrochloride (**G8**), vincamine hydrochloride (**G9**) and

tetrahydropalmatine hydrochloride (**G10**) to explore a structure-binding property relationship. The UV-vis and fluorescence titration experiments with these alkaloids are shown in Figure A6 − Figure A13. A 1:1 stoichiometry of the host-guest complexes was confirmed by Benesi-Hildebrand plots for all of these guests. Accordingly, the association constants were determined by fitting the titration data with a 1:1 binding model and the estimated binding constants are summarized in Table 1.

3.2.4 Structure Binding-Property Relationship

In the series of structurally related guests **G1** − **G5** the stability of the host-guest complexes decreases from the strongest binder **G1** (K_a = 7.3 × 10^3 L mol^{-1}, averaged value) over the moderate substrates **G2** (K_a = 2.4 × 10^3 L mol^{-1}), **G3** (K_a = 1.6 × 10^3 L mol^{-1}) and **G4** (K_a = 1.2 × 10^3 L mol^{-1}) to the weakest binder **G5** (K_a = 22.4 L mol^{-1}). The lowered association constant for **G2** compared to **G1** can be ascribed to steric effects of the additional methyl group at the 2-position which results in a reduced π-π-interaction between the binding partners in the complex. **G4** with a dihydropyridine ring also shows a reduced binding constant when compared to **G1**. This can be attributed to the smaller π-scaffold of **G4** (two fully conjugated rings) compared to **G1** and the increased steric demand of the sp^3 carbons in its 3- and 4-positions in contrast to the sp^2 carbons of **G1**. The declined binding constant of **G3** when compared to **G1** might be due to the solvation of the hydroxyl group. Tryptophan derivative **G5** is a very poor binder indicating that the annulation to the full *β*-carboline scaffold is necessary for an enhanced association constant with the receptor **[2PBI]-1p**. The binding propensity of the isoquinoline containing alkaloid **G6** (K_a = 7.8 × 10^3 L mol^{-1}) is as strong as for the indole alkaloid harmine (**G1**), while papaverine hydrochloride (**G7**) shows only a very weak (21.6 L mol^{-1}) and quinine hydrochloride (**G8**) a negligible interaction (< 5 L mol^{-1}). Vincamine (**G9**) and tetrahydropalmatine (**G10**), on the other hand, do not show any recognizable binding affinity. The poor binding affinities of **G4** and **G7** – **G10** can be ascribed, on the one hand, to a small π-scaffold of these guests with only up to two fused aromatic rings and, on the other hand, to steric hindrance as they contain bulky units.

To assess whether different counter ions have any influence on the binding propensity, harmine HI (**G1***) in comparison to harmine HCl (**G1**) was investigated as well (Figure A14). Since the association constants of **G1*** and **G1** are almost identical, it can be concluded that different

counter ions have no considerable effect on the host-guest binding of the alkaloids with **[2PBI]-1p**.

3.2.5 Structural Elucidation

To gain some insight into the structural features of the host-guest complexes, we have performed 1D and 2D ^{1}H NMR spectroscopic studies. NMR spectra were recorded in D_2O/CD_3CN (1/1 vol%) at 340 K to obtain intense and well resolved signals of **[2PBI]-1**. Harmine HCl (**G1**) was used as a guest since it showed a strong binding with the host. Upon addition of **G1** only the mean signals of free host, free guest and the complex are observed due to fast exchange taking place under the applied conditions. The signals of **[2PBI]-1p** show distinct changes in chemical shifts. This is seen most clearly for the aromatic linker protons (Figure 40a, signal b), which are shifted downfield from 7.17 ppm for the free host to 7.44 ppm after the addition of 20 equivalents of **G1**, and for the triazole protons (signal e), which are moved upfield from 7.80 to 7.69 ppm. These relocations are attributed to (de)shielding effects caused by the proximity of the guest to these protons in the host-guest complex. In addition, all protons of **G1** experience chemical shielding (upfield shift) to varying extents upon complexation with the host as can be seen by comparing the NMR spectra after the addition of 1 equivalent (eq.) and 20 eq. of **G1**, when almost all of **G1** is bound or free, respectively. The largest shifts are found for the protons in the 5 and 6 positions of **G1** as well as for the CH_3 group at the 1-position of the *β*-carboline scaffold.

The binding mode of **G1** to the receptor **[2PBI]-1p** was elucidated by ^{1}H, ^{1}H NMR NOESY experiments in D_2O/CD_3CN (1/1) at 340 K (Figure 40b). Correlations between the host and aromatic guest protons are not observed (Figure A15). However, cross peaks between the phenyl spacer protons (b) of **[2PBI]-1p** and the CH_3 (Figure 40b, cross signal i) as well as the OCH_3 group of G1 (cross signal ii) show the spatial proximity of these subunits in the host-guest complex. These findings prove once again that the alkaloid is indeed located inside of **[2PBI]-1p**. Alternative binding modes such as stacking of the guest on top of the chromophore scaffold of the host cannot give rise to cross signals to the aromatic linker protons of the host. Entanglement of the alkaloid hydrochloride by the OEG chains of the host, on the other hand, should generate additional correlations to the protons of the ethylene bridges which are, however, not observed. Based on the observed NOESY signals, the structure of the complex **G1⊂[2PBI]-1p** was modelled using the PM7 method (Figure 40c). The CH_3 and OCH_3 groups of guest **G1** are located next to the xylylene linkers of **[2PBI]-1p** on opposite sides of the host's

portal. That means, the aromatic **G1** immerges into the hydrophobic cavity of **[2PBI]-1p** with a parallel orientation to the long axes of the PBI subunits. This orientation may explain the lack of NOESY correlations for the aromatic protons (3, 4, 5, and 6) of **G1** as they are located within the cavity where no host protons are oriented to. This binding mode also explains why protons 5 and 6 of G1 are the most upfield shifted in the NMR titration as they are deeply buried in the host's interior.

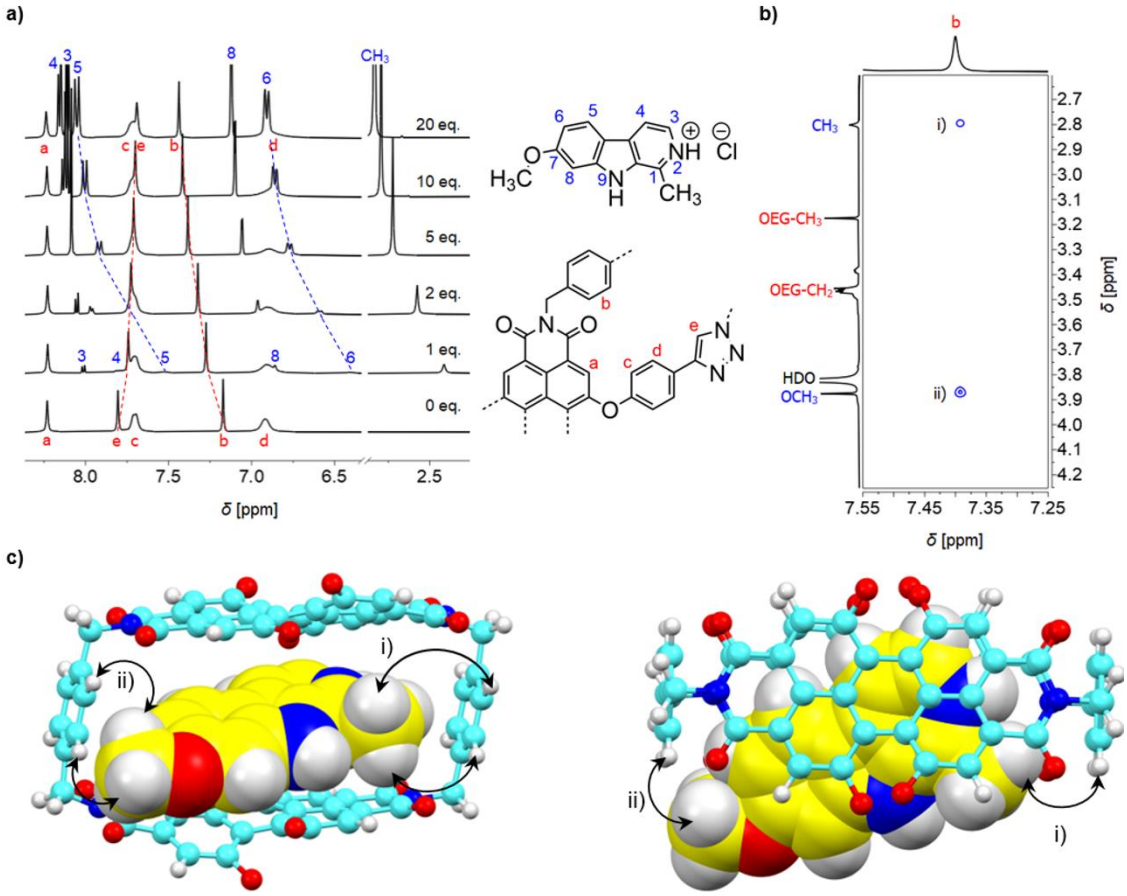

Figure 40. (a) ^{1}H NMR titration (400 MHz, 340 K) of **[2PBI]-1p** (c_0 = 5.0 × 10^{-4} mol L^{-1}) with **G1** in D_2O/CD_3CN (1/1 vol%). **(b)** Excerpt of the ^{1}H, ^{1}H NOESY NMR spectrum (600 MHz, 340 K) of **[2PBI]-1p** (c_0 = 5.0 × 10^{-4} mol L^{-1}) with **G1** in D_2O/CD_3CN (1/1 vol %). **(c)** Front (left) and top view (right) of the proposed structure of the complex **G1⊂[2PBI]-1p** modelled using the PM7 method. The curved arrows indicate the close proximity of protons giving rise to NOESY cross signals. The bay substituents of **[2PBI]-1p** are omitted for clarity. The full spectra of the complex and of free **[2PBI]-1p** are shown in the Figure A15 and Figure A16.

This proposed orientation of **G1**, especially with regard to the location of the CH_3 and OCH_3 substituents on the same side of the cavity, is further confirmed by the ^{1}H, ^{1}H NMR NOESY spectrum of the complex of **[2PBI]-1p** with 2-methyl harmine iodide (**G2**) (Figure A 17, Figure A18). According to the proposed structural model, the increased sterical demand in the 2-position of the *β*-carboline scaffold of **G2** should force this position out of the host interior resulting in a displacement of the CH_3 group in the 1-postion away from the xylylene wall.

However, the distance between the OCH_3 group in the 7-position of **G2** and the host xylylene linker should remain mostly unaffected by this structural modification of guest **G2**. Indeed, the ^1H, ^1H NMR NOESY spectrum of **G2⊂[2PBI]-1p** still shows the correlation of the spacer protons to OCH_3 but not to the CH_3 group in the 1-postion (Figure A18). In its place a new cross peak between NCH_3 of **G2** in the 2-postion and the linker protons of **[2PBI]-1p** can be seen. Hence, the overall overlap between the π-surfaces of host and guest is decreased which leads to a smaller binding constant for **G2** as compared to **G1**.

3.2.6 Conclusion

In summary, we accomplished the synthesis of a water-soluble PBI cyclophane supramolecular host **[2PBI]-1p**. This new synthetic receptor recognizes various natural aromatic alkaloids such as harmine, harmaline or berberine with good binding affinities. For efficient binding of alkaloids to the receptor three conjugated rings are beneficial and large substituents in alkaloids diminish the binding affinity. To our knowledge, **[2PBI]-1p** is the very first example of a chromophoric receptor that can be used for the recognition of aromatic alkaloids in aqueous media. Thus, our present study may encourage further research to develop more unique chromophore-based receptors for the detection and analysis of alkaloids.

3.2.7 Appendix I

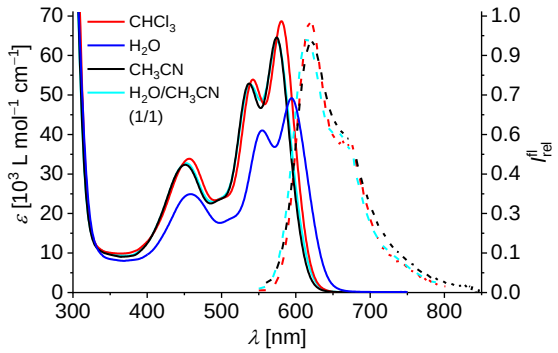

Figure A1. Solvent-dependent UV-vis ($c = 1 \times 10^{-5}$ L mol $^{-1}$) and fluorescence ($c = 7 \times 10^{-7}$ L mol $^{-1}$, λ_{ex} = 530 nm) spectra of **[2PBI]-1p** at 295 K. Fluorescence spectra are normalized to the corresponding UV-vis spectra.

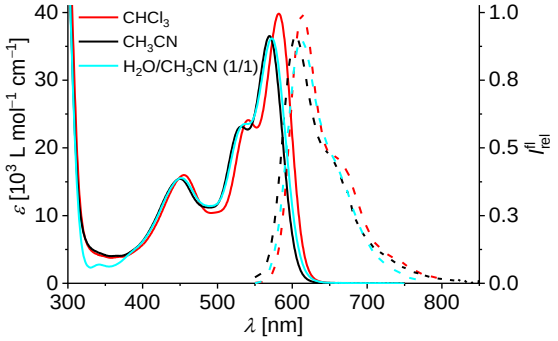

Figure A2. Solvent dependent UV-vis ($c = 2 \times 10^{-5}$ L mol $^{-1}$) and fluorescence ($c = 1 \times 10^{-6}$ L mol $^{-1}$, λ_{ex} = 530 nm) spectra of monomeric reference **ref-PBI-1p** at 295 K. Fluorescence spectra are normalized to the corresponding UV-vis spectra.

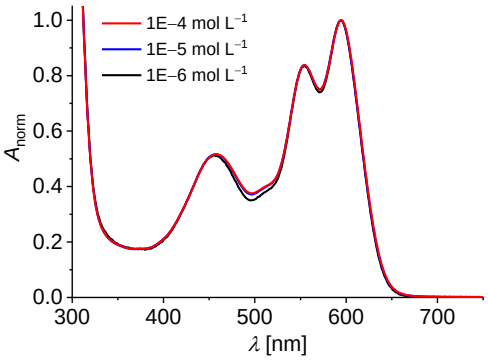

Figure A3. Concentration dependent UV-vis spectra of **[2PBI]-1p** in H_2O at 295 K.

Host-Guest Binding Studies

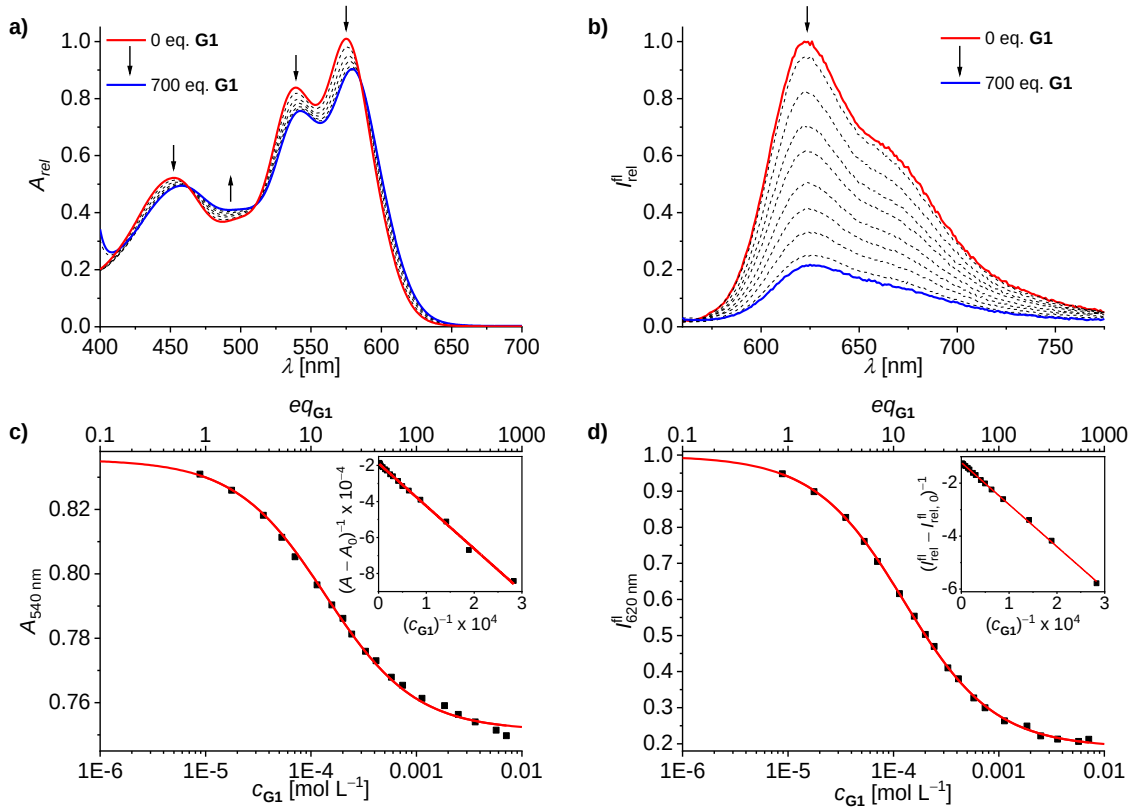

Figure A4. (a) UV-vis and **(b)** fluorescence titration (λ_{ex} = 520 nm) of **[2PBI]-1p** (c_0 = 1 × 10^{-5} mol L^{-1}) with **G1** in H_2O/CH_3CN (1/1 vol%) and phosphate buffer (pH = 6.5) at 295 K. Arrows indicate changes upon increasing guest concentration. **(c)** Plots of UV-vis (540 nm) and **(d)** fluorescence (620 nm) titration data points as a function of guest concentration and fitting with a 1:1 binding model; insets: Benesi-Hildebrand plots showing a 1:1 stoichiometry of the host-guest complex. K_a (UV) = 8.4 × 10^3 mol L^{-1}; K_a (fl) = 8.1 × 10^3 L mol^{-1}, Ø (K_a) = 8.3 × 10^3 mol L^{-1}; − ΔG^0 = 22.1 kJ mol^{-1}.

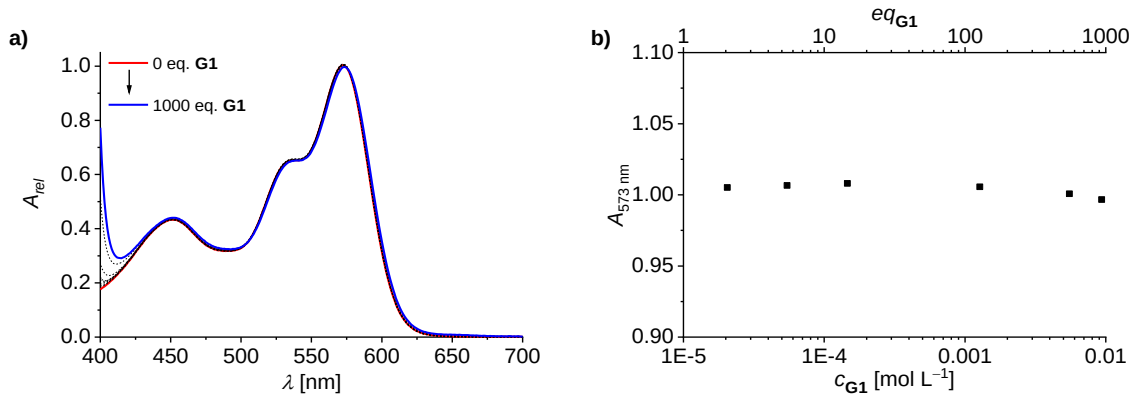

Figure A5. (a) UV-vis spectrum of reference **ref-PBI-1p** (c_0 = 1 × 10^{-5} mol L^{-1}) in H_2O/CH_3CN (1/1 vol%) upon addition of **G1** at 295 K. **(b)** Cross section at 573 nm.

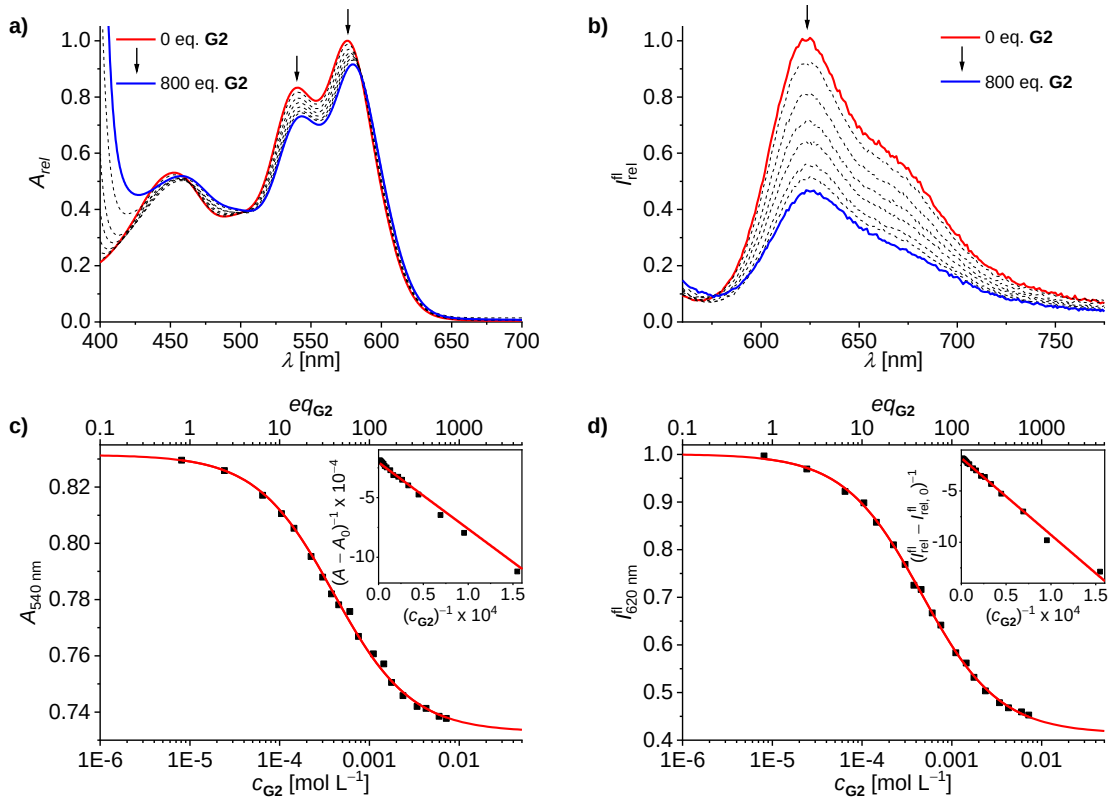

Figure A6. (a) UV-vis and **(b)** fluorescence titration (λ_{ex} = 520 nm) of **[2PBI]-1p** (c_0 = 1 × 10^{-5} mol L^{-1}) with **G2** in H_2O/CH_3CN (1/1 vol%) at 295 K. Arrows indicate changes upon increasing guest concentration. **(c)** Plots of UV-vis (540 nm) and **(d)** fluorescence (620 nm) titration data points as a function of guest concentration and fitting with a 1:1 binding model; insets: Benesi-Hildebrand plots showing a 1:1 stoichiometry of the host-guest complex.

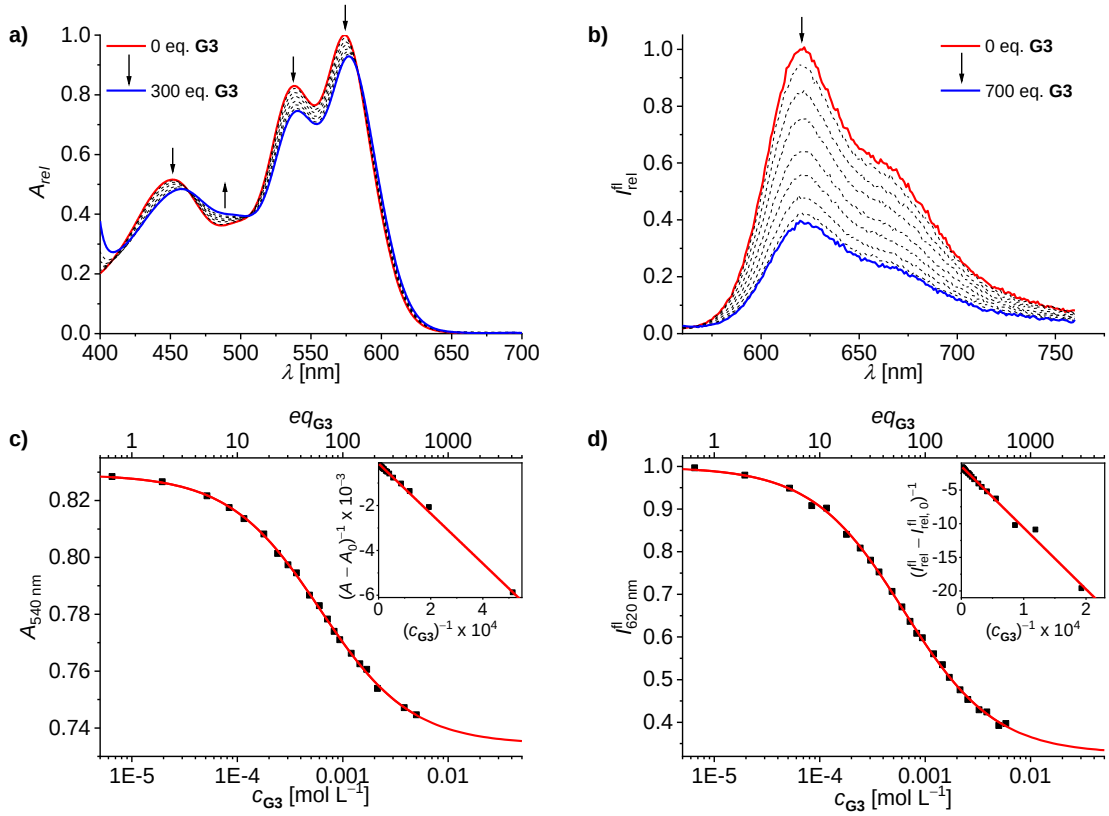

Figure A7. (a) UV-vis and **(b)** fluorescence titration (λ_{ex} = 520 nm) of **[2PBI]-1p** (c_0 = 1 × 10^{-5} mol L^{-1}) with **G3** in H_2O/CH_3CN (1/1 vol%) at 295 K. Arrows indicate changes upon increasing guest concentration. **(c)** Plots of UV-vis (540 nm) and **(d)** fluorescence (620 nm) titration data points as a function of guest concentration and fitting with a 1:1 binding model; insets: Benesi-Hildebrand plots showing a 1:1 stoichiometry of the host-guest complex.

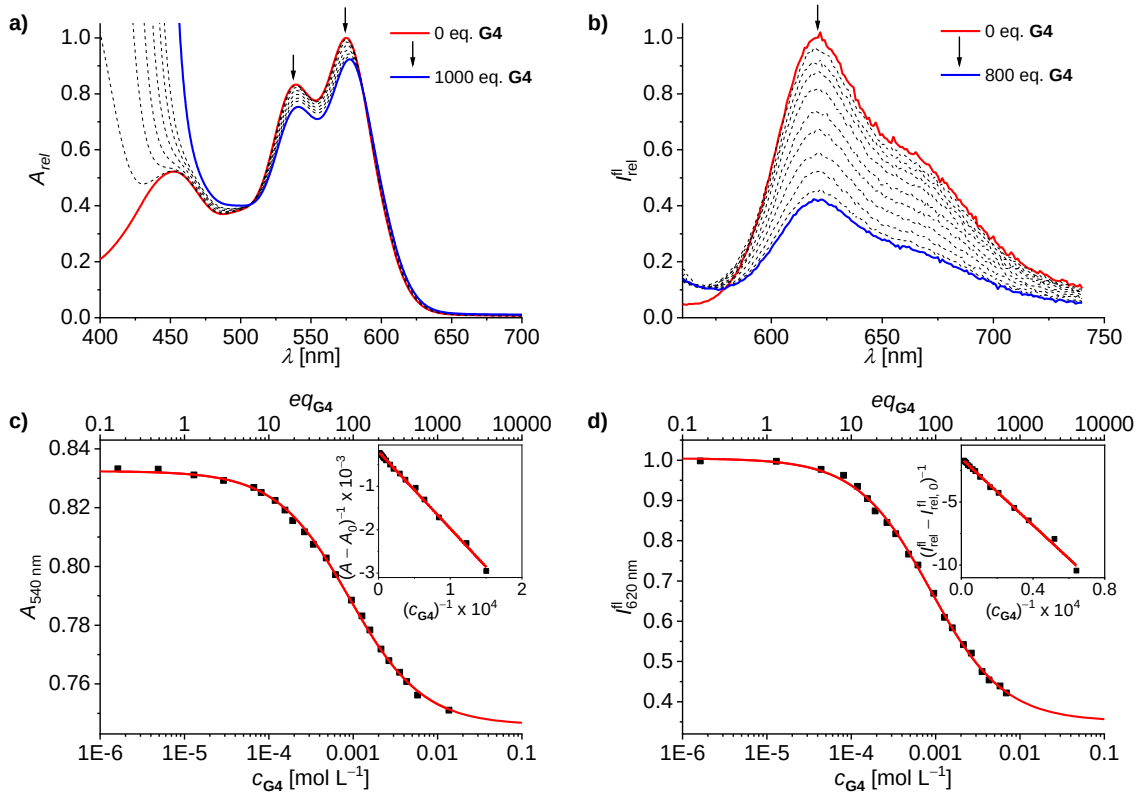

Figure A8. (a) UV-vis and **(b)** fluorescence titration (λ_{ex} = 520 nm) of **[2PBI]-1p** (c_0 = 1 × 10^{-5} mol L^{-1}) with **G4** in H_2O/CH_3CN (1/1 vol%) at 295 K. Arrows indicate changes upon increasing guest concentration. **(c)** Plots of UV-vis (540 nm) and **(d)** fluorescence (620 nm) titration data points as a function of guest concentration and fitting with a 1:1 binding model; insets: Benesi-Hildebrand plots showing a 1:1 stoichiometry of the host-guest complex.

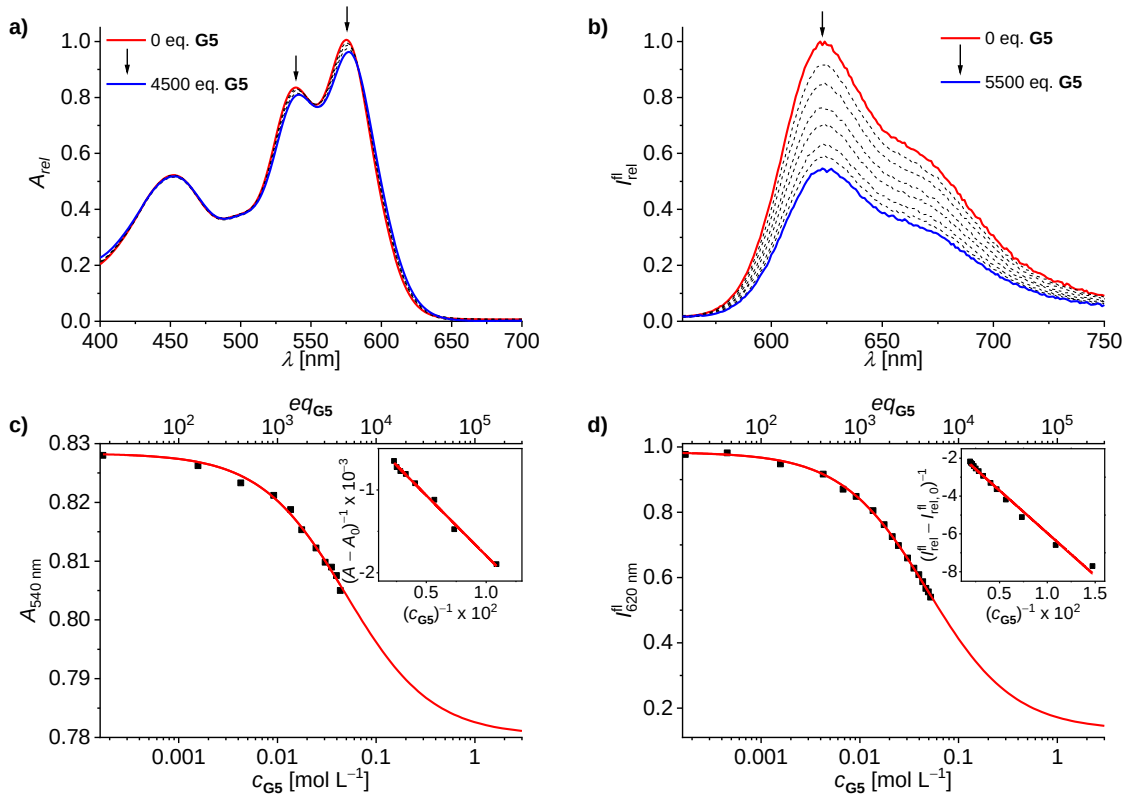

Figure A9. (a) UV-vis and **(b)** fluorescence titration (λ_{ex} = 520 nm) of **[2PBI]-1p** (c_0 = 1 × 10^{-5} mol L^{-1}) with **G5** in H_2O/CH_3CN (1/1 vol%) at 295 K. Arrows indicate changes upon increasing guest concentration. **(c)** Plots of UV-vis (540 nm) and **(d)** fluorescence (620 nm) titration data points as a function of guest concentration and fitting with a 1:1 binding model; insets: Benesi-Hildebrand plots showing a 1:1 stoichiometry of the host-guest complex.

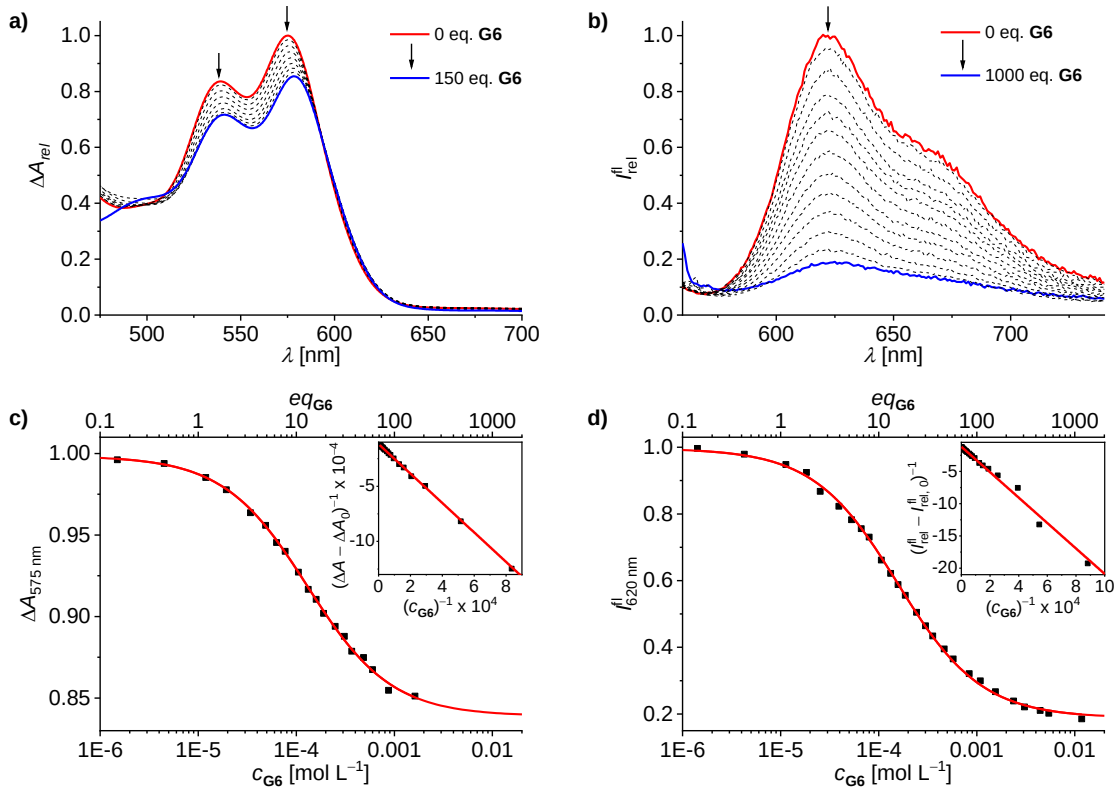

Figure A10. (a) UV-vis and **(b)** fluorescence titration (λ_{ex} = 520 nm) of **[2PBI]-1p** (c_0 = 1 × 10^{-5} mol L^{-1}) with **G6** in H_2O/CH_3CN (1/1 vol%) at 295 K. Arrows indicate changes upon increasing guest concentration. **(c)** Plots of UV-vis (540 nm) and **(d)** fluorescence (620 nm) titration data points as a function of guest concentration and fitting with a 1:1 binding model; insets: Benesi-Hildebrand plots showing a 1:1 stoichiometry of the host-guest complex.

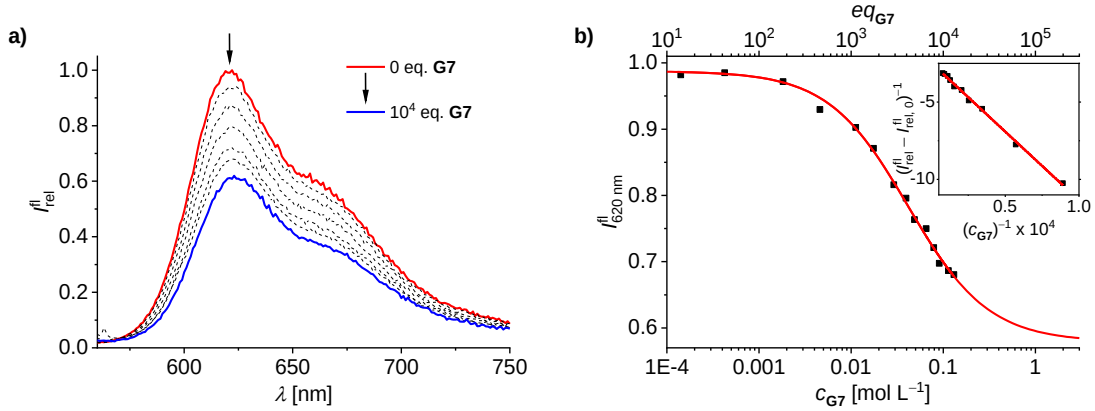

Figure A11. (a) Fluorescence titration (λ_{ex} = 520 nm) of **[2PBI]-1p** (c_0 = 1 × 10^{-5} mol L^{-1}) with **G7** in H_2O/CH_3CN (1/1 vol%) at 295 K. Arrows indicate changes upon increasing guest concentration. **(b)** Plot of the fluorescence (620 nm) titration data points with a 1:1 binding model fit; inset: Benesi-Hildebrand plot showing a 1:1 stoichiometry of the host-guest complex.

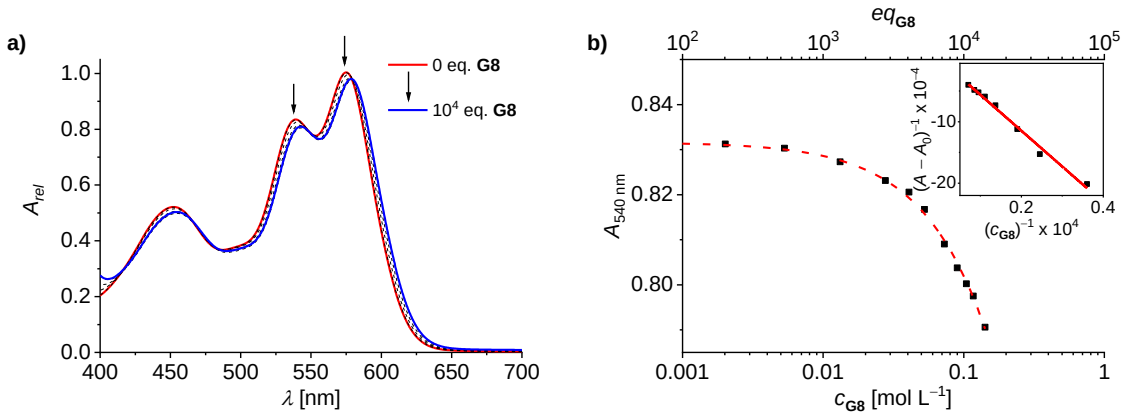

Figure A12. (a) UV-vis titration of **[2PBI]-1p** (c_0 = 1 × 10^{-5} mol L^{-1}) with **G7** in H_2O/CH_3CN (1/1 vol%) at 295 K. Arrows indicate changes upon increasing guest concentration. **(b)** UV-vis titration (540 nm) data points with a 1:1 binding model fit; inset: Benesi-Hildebrand plot a 1:1 stoichiometry of the host-guest complex.

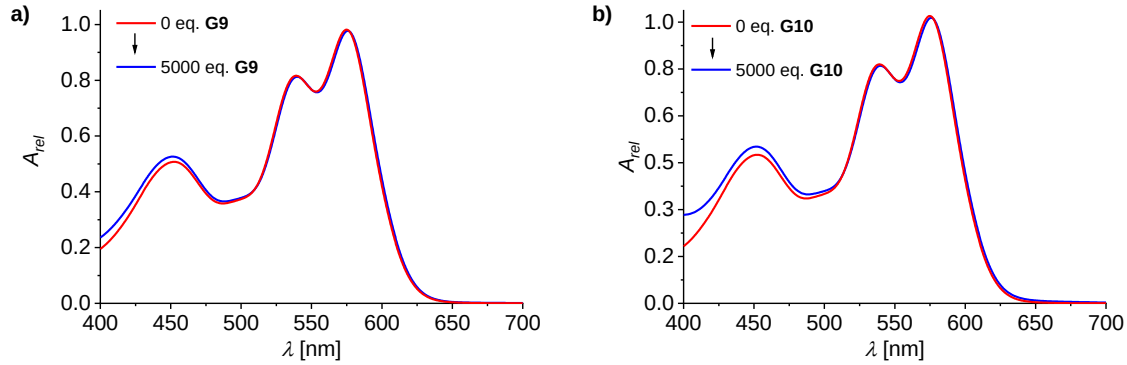

Figure A13. UV-vis spectra of **[2PBI]-1p** (c_0 = 1 × 10^{-5} mol L^{-1}) with **(a) G9** and **(b) G10** in H_2O/CH_3CN (1/1 vol%) at 295 K. No spectral changes indicating complexation were observed.

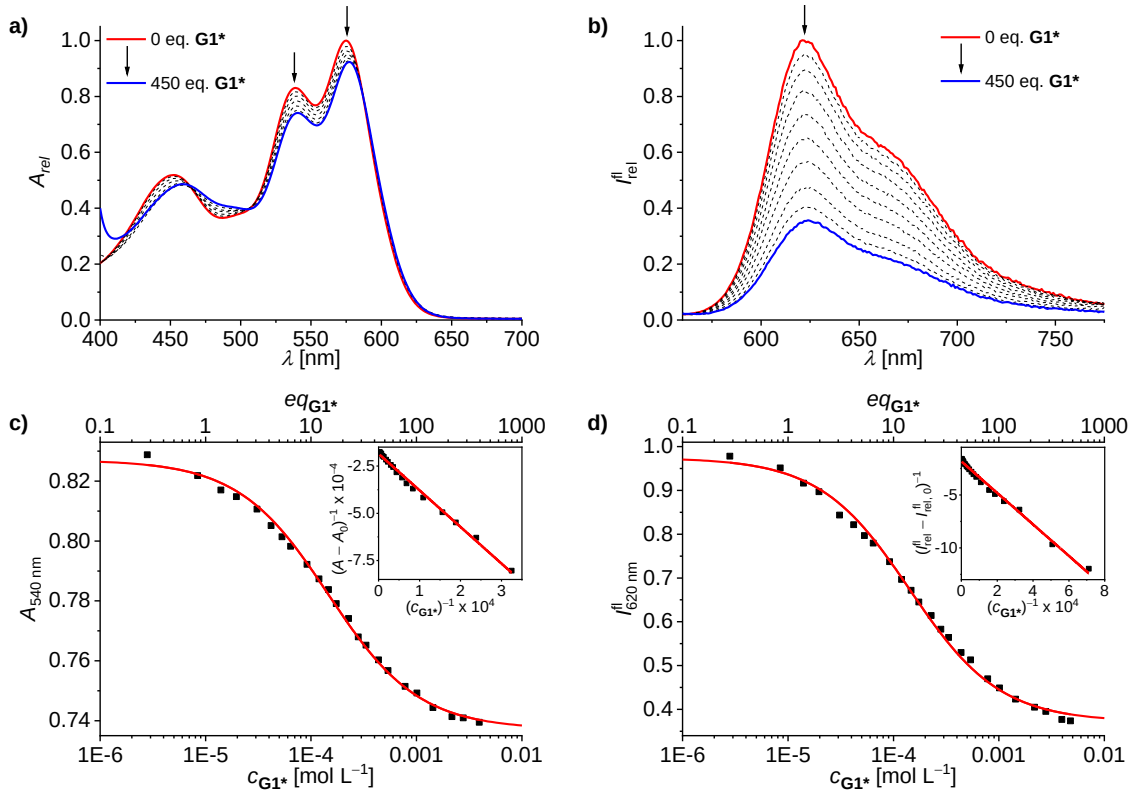

Figure A14. (a) UV-vis and **(b)** fluorescence titration (λ_{ex} = 520 nm) of **[2PBI]-1p** (c_0 = 1 × 10^{-5} mol L^{-1}) with **G1*** in H_2O/CH_3CN (1/1 vol%) at 295 K. Arrows indicate changes upon increasing guest concentration. **(c)** Plots of UV-vis (540 nm) and **(d)** fluorescence (620 nm) titration data points as a function of guest concentration and fitting with a 1:1 binding model; insets: Benesi-Hildebrand plots showing a 1:1 stoichiometry of the host-guest complex.

2D NMR Spectra

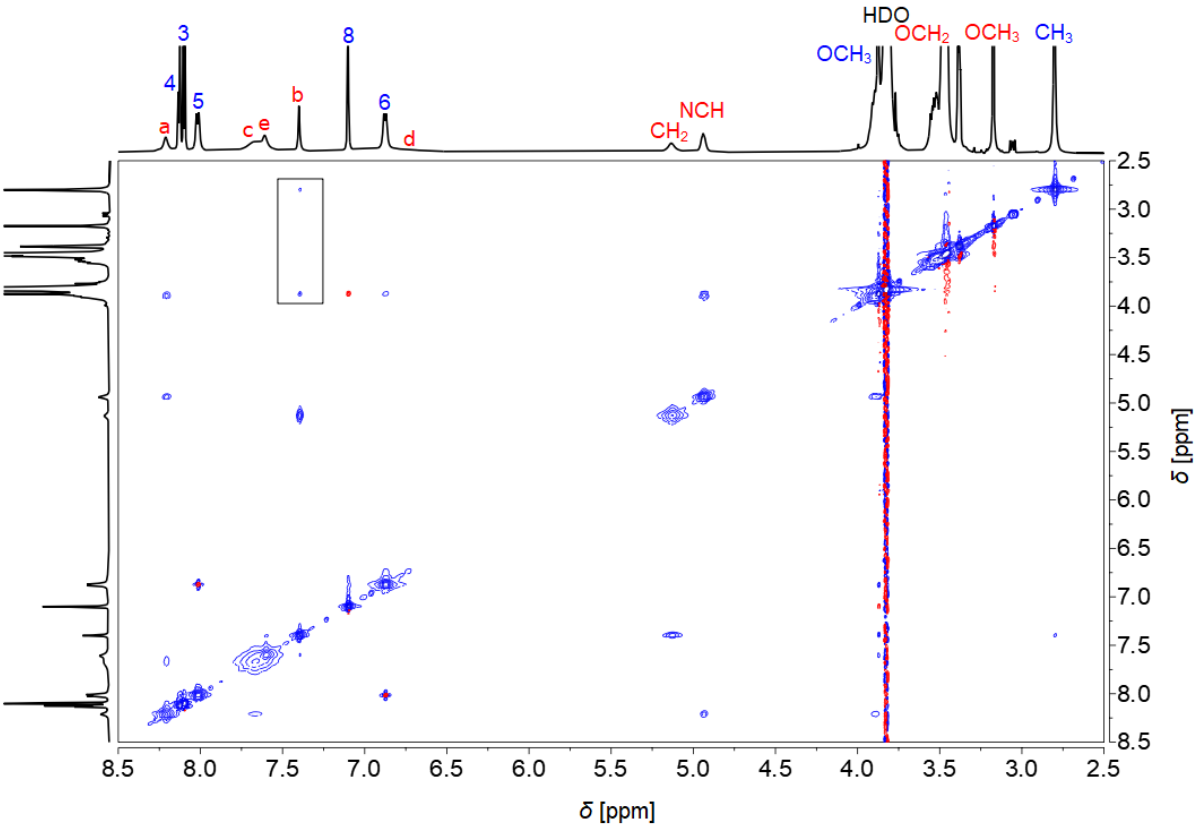

Figure A15. Full $^{1}H,^{1}H$ NOESY NMR spectrum (600 MHz, 340 K) of **[2PBI]-1p** (c = 5.0 × 10^{-4} mol L^{-1}) in the presence of **G1** (c = 7.5 × 10^{-3} mol L^{-1}) in D_2O/CD_3CN (1/1 vol%). For assignment of signals see Figure 40.

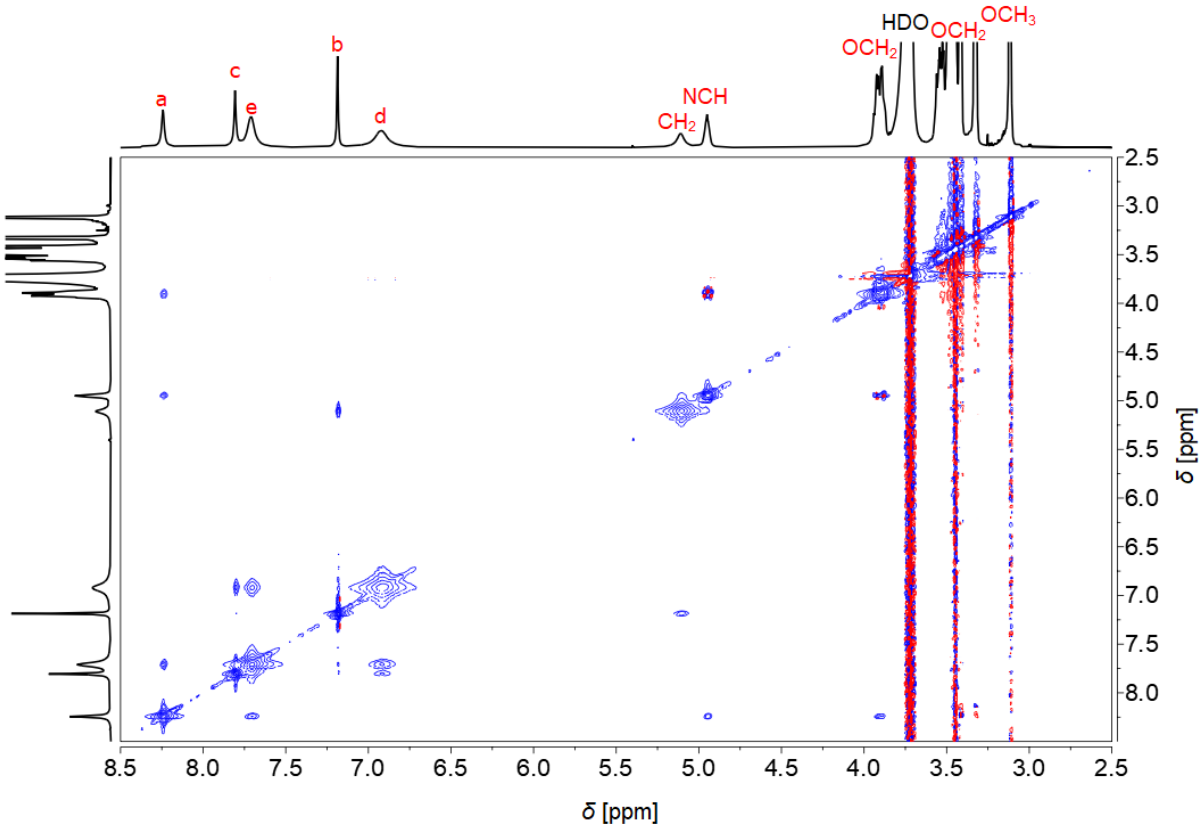

Figure A16. $^{1}H,^{1}H$ NOESY NMR spectrum (600 MHz, 340 K) of free **[2PBI]-1p** (c = 5.0 × 10^{-4} mol L^{-1}) in D_2O/CD_3CN (1/1 vol%). For assignment of signals see Figure 40.

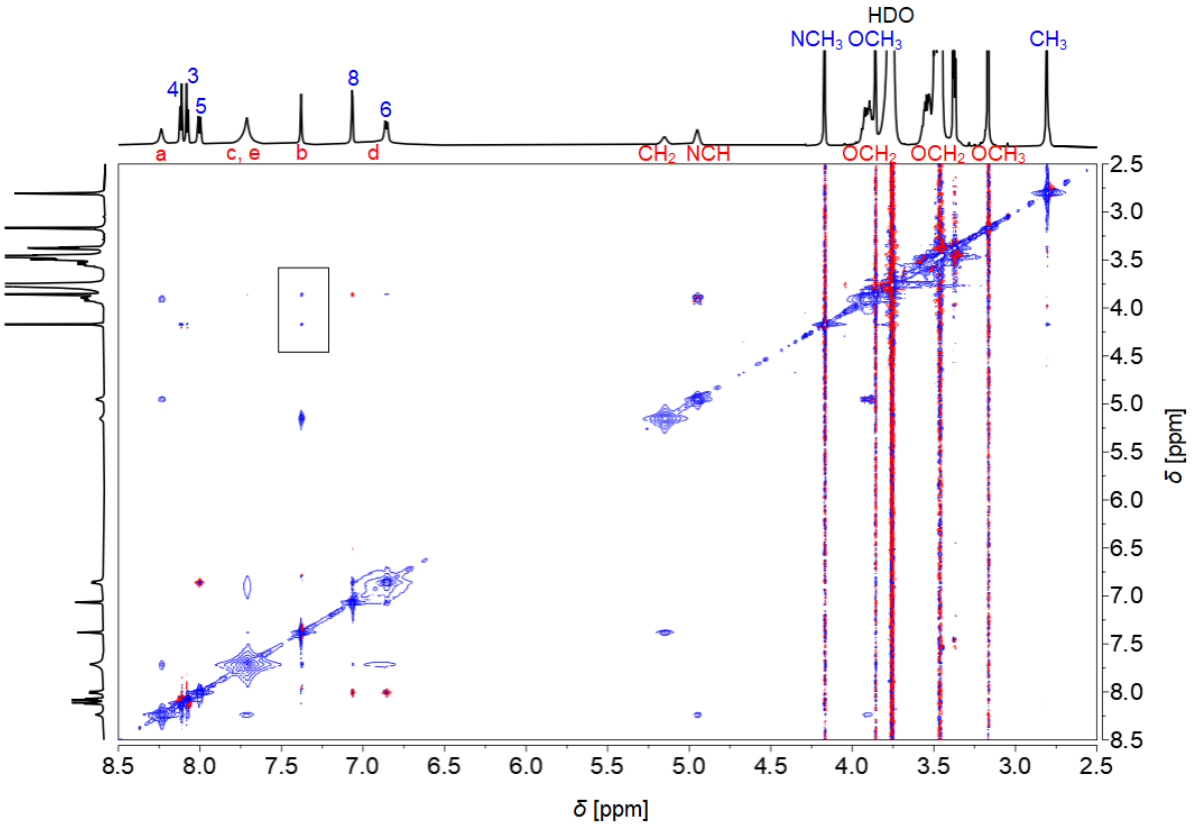

Figure A 17. Full ^{1}H,^{1}H NOESY NMR spectrum (600 MHz, 340 K) of **[2PBI]-1p** (c = 5.0 × 10^{-4} mol L^{-1}) upon complexation with **G2** (c = 7.5 × 10^{-3} mol L^{-1}) in D_2O/CD_3CN (1/1 vol%)

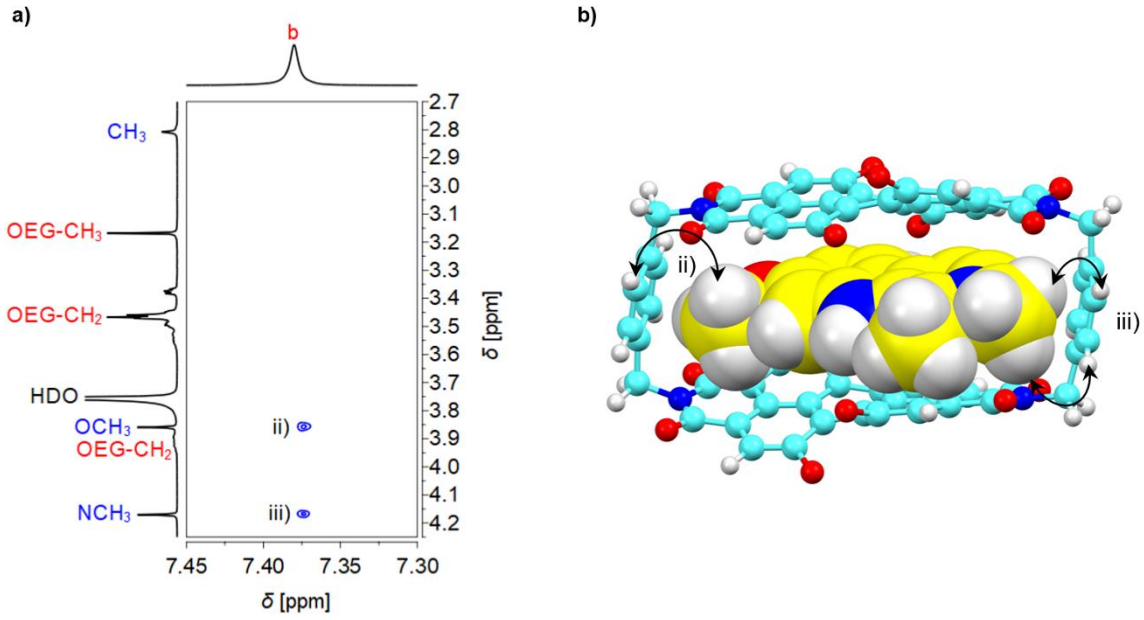

Figure A18. (a) Excerpt of the 2D spectrum with cross signals between **G2** and linker protons of **[2PBI]-1p**. For assignment of signals of **[2PBI]-1p** and the β-carboline scaffold see Figure 40. **(b)** Modelled structure of **G2⊂[2PBI]-1p** as calculated by the PM7 method. The curved arrows indicate the close proximity of protons giving rise to NOESY cross signals. The bay substituents of **[2PBI]-1p** are omitted for clarity.

3.3 Entropy-Driven Self-Assembly and Guest-Mediated Disassembly of a Perylene Bisimide Cyclophane in Water

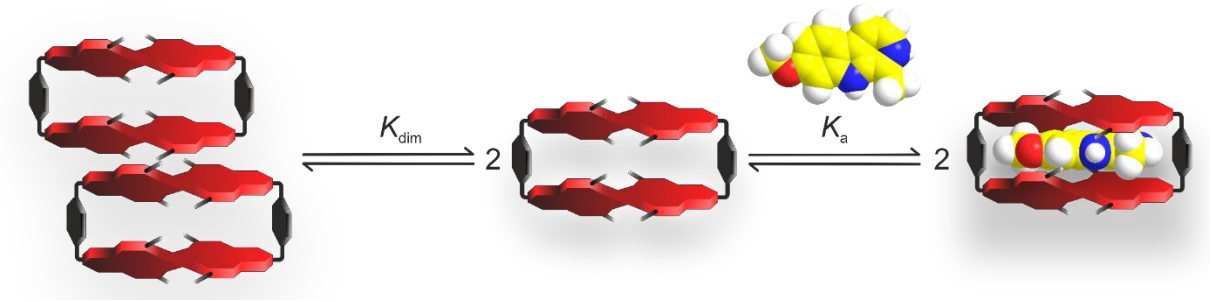

Abstract. Here we report on the thermodynamic bias for the self-assembly behavior of a perylene bisimide (PBI) cyclophane **[2PBI]-1m** appended with oligo ethylene glycol chains and its reference monomer **ref-PBI-1m** in aqueous environment. Concentration-dependent UV-vis studies as well as atomic force microscopy show that both PBIs form supramolecular dimers in aqueous solution with a *J*-type excitonic coupling. Temperature-dependent UV-vis studies in water revealed self-assembly of both PBI derivatives yet, interestingly, with opposing responses of their supramolecular structures to temperature variation. Upon heating, the reference monomer clearly deaggregates whereas enhanced aggregation was observed for the cyclophane. These observations unambiguously identify different thermodynamic driving forces behind the aggregation processes of the two structurally related PBI derivatives in water. Indeed, self-assembly of the reference monomer is enthalpy-driven whereas that of the PBI cyclophane is entropy-driven as confirmed by thermodynamic data. Our thorough investigations suggest different orientations of the solubilizing oligoethylene glycol chains around the hydrophobic core of the respective PBI as the possible reason for the observed inversion of the thermodynamic driving force for the PBI monomer and cyclophane. In addition, we demonstrate that the uptake of the alkaloid harmine as a guest molecule into the cavity of the aggregated PBI cyclophane host triggers its disassembly to monomeric host-guest complexes. As the formation of a host-guest complex with the alkaloid out of the dimer aggregate is accompanied by a color change from blue to purple, this PBI cyclophane represents a potential molecular probe for this class of natural products.

3.3.1 Introduction

Water as the solvent of life plays a pivotal role in directing self-assembly and recognition processes in biological systems.[6] The unique properties of this medium, resulting in the self-sorting phenomenon[43] referred to as the hydrophobic effect,[5] govern the self-assembly of lipids into biological membranes,[137] drive folding of peptides into functional proteins[138] or control receptor-ligand interactions.[139] Despite the omnipresent involvement of water and the hydrophobic effect in virtually all biological processes in living systems, our understanding of this effect is still unsatisfactory.

In this regard, the field of supramolecular chemistry[7a, 7b] is of great assistance and contributes invaluable complementary insight into the mysteries of the hydrophobic effect by purposeful design of artificial model systems which self-assemble and operate in aqueous solution.[140] Indeed, the growing knowledge on self-assembly processes in water increases the prospects for the development of promising aqua materials for different applications.[15b, 141] In particular, the way water effects thermodynamic driving forces behind self-assembly and recognition is of interest. A prominent example for this is the influence of water molecules solvating the cavity of macrocyclic hosts on the entropy and enthalpy of host-guest complex formation.[142]

Our group has recently contributed to the understanding of the delicate balance of the thermodynamic driving forces in water by reporting on the self-assembly behavior of an amphiphilic perylene bisimide (PBI) dye functionalized at the imide groups with hydrophilic oligoethylene glycol (OEG) chains. Interestingly, the aggregation process of this PBI derivative is driven by entropy and is enthalpically even disfavored in aqueous media as indicated by enhanced self-assembly at elevated temperature.[143] Such a phenomenon, even though it is known for the self-assembly of biological systems such as collagen fibrils or β-amyloids,[144] is rare for supramolecular systems,[145] which in general tend to aggregate in an enthalpically driven manner.[146] Our understanding in thermodynamics of the self-assembly of amphiphilic dyes in aqueous solution could be further improved by the very recent investigation of how modulation of the OEG chain length contributes to the entropic driving force of the aggregation of naphthalene bisimide (NBI) systems.[147] Furthermore, Syamala *et al*. could demonstrate the vital role of back-folding of the OEG-appended imide substituent over the π-core in the thermodynamic signature of self-assembly of amphiphilic NBI dyes in water.[147]

However, all the rylene dyes investigated so fare bear the solubilizing OEG chains in the imide position and are monomeric on a molecular level. Moreover, there is no report to date on the

self-assembly of macrocyclic PBI dyes in water. In order to gain further insight on the balance between entropy and enthalpy for aqueous self-assembly phenomena, we designed the water-soluble cyclic PBI dimer **[2PBI]-1m** (Figure 41), which bears the solubilizing OEG groups in the bay position, and its reference monomer **ref-PBI-m** that possesses the same substitution pattern like cyclophane **[2PBI]-1m** but lacks the second chromophore building block. Interestingly, our thorough investigation by temperature-dependent UV-vis spectroscopy in water revealed a thermodynamic bias in the self-assembly of these two PBI systems despite their structural similarities. Reference monomer **ref-PBI-m** shows a common temperature response, i. e. it deaggregates upon heating, indicating an enthalpy-driven self-assembly process. In the case of macrocycle **[2PBI]-1m**, on the other hand, stronger aggregation is induced by heating, suggesting an entropically favored self-assembly process which could be corroborated by thermodynamic data. Concentration-dependent UV-Vis studies as well as atomic force microscopy (AFM) confirmed formation of supramolecular dimers for both PBI derivatives, thus ruling out the effect of different aggregation mechanisms as the cause for the observed thermodynamic bias. We propose that the extend of back-folding of the OEG-chain over the hydrophobic PBI core is the source for the observed thermodynamic bias.

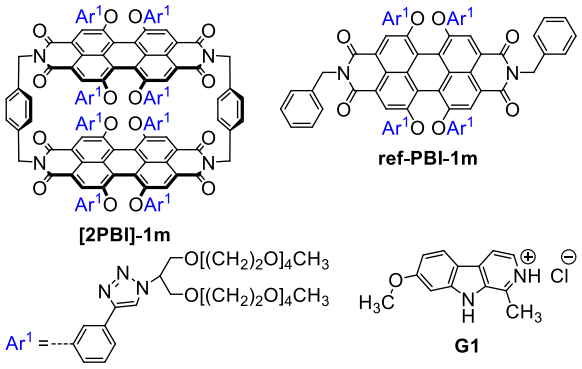

Figure 41. Chemical structures of water-soluble PBI cyclophane **[2PBI]-1m** and reference monomer **ref-PBI-1m** as well as *harmala* alkaloid guest harmine hydrochloride (**G1**).

3.3.2 Solvent-Dependent UV-vis Studies of [2PBI]-1m and ref-PBI-1m

The synthesis of PBI cyclophane **[2PBI]-1m** and monomeric reference **ref-PBI-1m** is presented in Chapter 3.1. For experimental details, see Chapter 6.

The optical properties of PBI cyclophane **[2PBI]-1m** and reference monomer **ref-PBI-1m** were probed by solvent-dependent UV-vis studies (Figure 42). In $CHCl_3$ at 298 K, **ref-PBI-1m** (c = 2.0×10^{-5} mol L^{-1}) shows the usual vibronic progression for PBIs with four bay-substituents

with maxima at 577 and 538 nm[148] and a regular ratio of the 0−0 and 0−1 vibronic transitions ($A_{0,0}/A_{0,1}$) of 1.62[149] suggesting the monomeric nature of **ref-PBI-1m** in this solvent (Figure 42a). In the more polar solvents acetone and acetonitrile, a blueshift of approximately 20 nm is observed along with a minimal loss in intensity. In $CHCl_3$ cyclophane **[2PBI]-1m** (c = 1.0 × 10^{-5} mol L^{-1}, T = 298 K) shows the common optical features of *para*-xylylene-bridged PBI cyclophanes, which were discussed previously (see Chapter 3.2), with absorption maxima at 574 and 538 nm and an $A_{0,0}/A_{0,1}$ ratio of 1.21 indicating the weak intramolecular interaction of the PBI cores within the cyclophane (Figure 42b).[30, 150] In acetone or acetonitrile, a drop in intensity of 12% and a hypsochromic shift of about 10 nm are observed. The minor change of $A_{0,0}/A_{0,1}$ from 1.21 in $CHCl_3$ to 1.17 in acetone can be ascribed to solvent effects. Most importantly, though, no spectral attributes are observed for both PBI derivatives hinting at the formation of aggregates under these conditions. In H_2O at 298 K, on the other hand, both PBI cyclophane **[2PBI]-1m** (1.0 × 10^{-5} mol L^{-1}) and reference monomer **ref-PBI-1m** (2.0 × 10^{-5} mol L^{-1}) display a hypochromic shift with prominent additional transitions at 651 and 638 nm, respectively, which strongly indicate aggregation in aqueous environment probably promoted by the hydrophobic effect (Figure 42).[5]

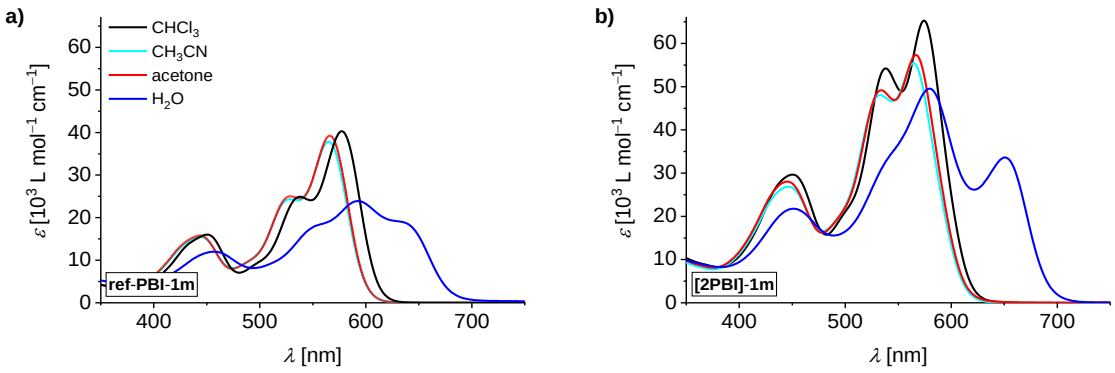

Figure 42. Solvent-dependent UV-vis spectra of **(a) ref-PBI-1m** (c = 2 × 10^{-5} mol L^{-1}) and **(b) [2PBI]-1m** (c = 1 × 10^{-5} mol L^{-1}) in $CHCl_3$ (black), CH_3CN (cyan), acetone (red) and H_2O (blue) at 298 K.

In order to get further insight into the self-assembly behavior of PBI cyclophane **[2PBI]-1m** and reference monomer **ref-PBI-1m** in aqueous environment, solvent composition-dependent spectra were recorded in different acetone/water mixtures at a concentration of 1.25 × 10^{4} mol L^{-1} at 298 K (Figure 43). For both compounds, the monomeric spectral features observed in pure acetone gradually change upon increasing water content. For PBI reference monomer **ref-PBI-1m**, the spectrum apparently shifts to higher wavelengths (Figure 43a) whereas for cyclophane **[2PBI]-1m** the emergence of a new band at 652 nm is observed (Figure

43b). Obviously, these changes can be ascribed to aggregation behavior of both PBI derivatives, which is exclusive to water or to aqueous mixtures with a high water content.

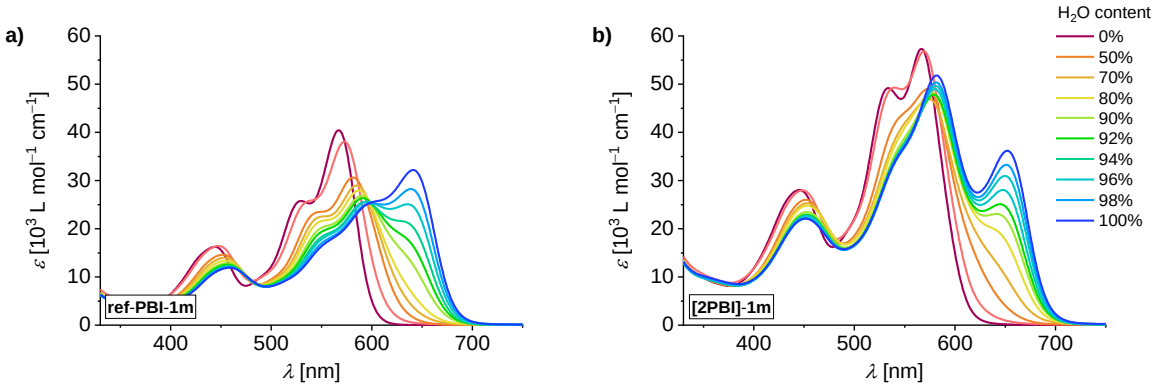

Figure 43. Solvent-dependent UV-vis spectra of **(a) ref-PBI-1m** and **(b) [2PBI]-1m** in water/acetone mixtures (c = 1.25 × 10^{-4} mol L^{-1}, T = 298 K) of varying vol%-compositions.

3.3.3 Temperature-Dependent Spectroscopic Studies of [2PBI]-1m and ref-PBI-1m in Water

The aggregation behavior of PBI cyclophane **[2PBI]-1m** and its monomeric reference **ref-PBI-1m** was investigated further by temperature-dependent UV-vis spectroscopy in H_2O. Upon increasing the temperature from 278 K to 333 K, the UV-vis spectrum of reference monomer **ref-PBI-1m** in H_2O (c = 4 × 10^{-5} mol L^{-1}) shows significant changes (Figure 44a). Upon heating from 278 K to 333 K, its spectral properties gradually become more monomer-like with the $A_{0,0}$ transition shifting from 645 nm to 590 nm and displaying isosbestic points at 486 nm and 458 nm. These observations confirm that **ref-PBI-1m** aggregates in H_2O at lower temperatures with a bathochromically shifted aggregate band indicating the *J*-type exciton coupling between the PBI chromophores in the aggregated species.[151] The plot of the degree of aggregation α_{agg} as a function of temperature shows that at a concentration of 4.0 × 10^{-5} mol L^{-1} at 278 K, the fully aggregated state of **ref-PBI-1m** is not reached (Figure 44a, inset). Performing temperature-dependent UV-vis studies at 5.0 × 10^{-4} mol L^{-1}, a higher degree of self-assembly is achieved as shown by the more intense $A_{0,0}$ band of the aggregate at 645 nm (see Figure A20 in Appendix II, Chapter 3.3.9). Yet at this concentration, the monomer state can no longer be observed due to precipitation at elevated temperature (*vide infra*).

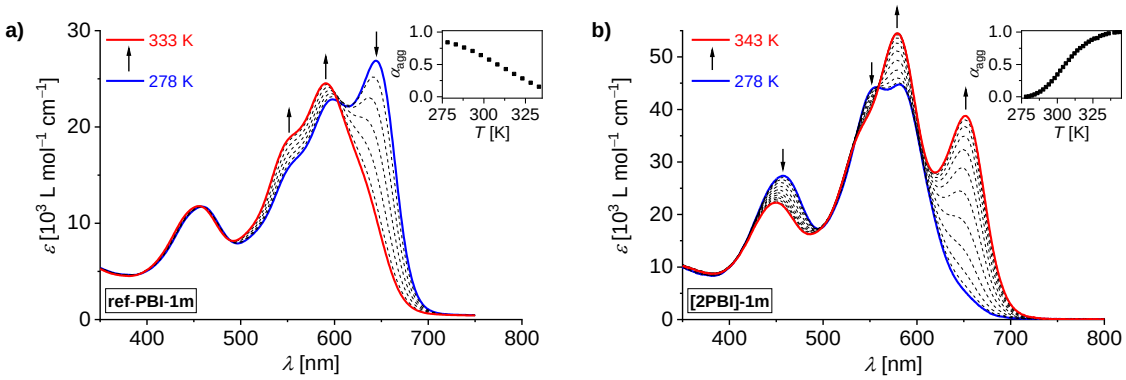

Figure 44. Temperature-dependent UV-vis spectra of **(a) ref-PBI-1m** (c = 4.0 × 10^{-5} mol L^{-1}) and **(b) [2PBI]-1m** (c = 5.0 × 10^{-6} mol L^{-1}) in pure H_2O. Arrows indicate spectral changes upon heating. Insets: Plots of the degree of aggregation (α_{agg}) as a function of temperature (see Figure A20 for the spectrum of the fully aggregated state of **ref-PBI-1m**).

Likewise, the UV-vis properties of cyclophane **[2PBI]-1m** (c = 5 × 10^{-6} mol L^{-1}) are subject to temperature-induced changes in H_2O upon increasing the temperature from 278 K to 343 K (Figure 44b). At 278 K, the $A_{0,0}$ and $A_{0,1}$ transitions of the cyclic PBI dimer at 580 nm and 555 nm, respectively, are well-resolved and of almost equal intensity, resembling the monomeric spectral features of para-xylylene-bridged PBI cyclophanes observed in $CHCl_3$ or acetone yet suggesting increased intramolecular coupling of the PBI subunits in **[2PBI]-1m** in H_2O. Interestingly, the band at 580 nm is enhanced upon heating to 343 K whereas the band at 555 nm decreases. Moreover, an additional transition emerges simultaneously at 652 nm. Isosbestic points are present at 559 nm, 533 nm and 498 nm. Clearly, these temperature-induced spectral changes indicate aggregation of cyclophane **[2PBI]-1m** at elevated temperatures with a *J*-type intermolecular excitonic coupling of the chromophores in the supramolecular assembly.[151] This uncommon temperature response contradicts that of conventional PBI aggregates and many other supramolecular assemblies in organic solvents.[146] However, it is in accordance with the self-assembly behavior of some PBI and naphthalene diimide (NDI) derivatives bearing OEG chains in water.[31b, 143, 147] Most notably, PBI cyclophane **[2PBI]-1m** shows the opposite temperature response compared to the structurally related reference monomer **ref-PBI-1m**, as the monomer deaggregates upon heating whereas the cyclophane aggregates upon heating. This observation suggests that, despite similarities in structure, the self-assembly of the PBI systems discussed here is driven by different thermodynamic parameters, that is enthalpy in the case of reference monomer **ref-PBI-1m** and entropy in the case of **[2PBI]-1m**.[143, 147]

As the spectral changes upon aggregation for both **[2PBI]-1m** and **ref-PBI-1m** hint at a *J*-type excitonic coupling of the chromophores in the supramolecular assembly, which typically enhances the fluorescence of the coupled chromophores,[152] the temperature response was additionally probed by fluorescence spectroscopy in a qualitative manner.[4] For cyclophane **[2PBI]-1m**, almost no fluorescence signal (λ_{ex} = 533 nm) is detectable in water at 278 K even at a large slit width of 12 nm (Figure A21a). Indeed, it has been shown previously that the fluorescence of a similar PBI cyclophane is strongly quenched in water.[150] Upon increasing the temperature gradually from 278 to 343 K to induce the aggregation process, the emission of **[2PBI]-1m** is enhanced by a factor of ~ 5 which is accompanied by a considerable sharpening of the spectrum and a redshift of the fluorescence maximum from 673 nm at 278 K to 691 nm at 343 K. Since **ref-PBI-1m** shows an inverted temperature response when compared to the cyclophane, its fluorescence intensity should accordingly exhibit the opposite response to the temperature change. This is indeed confirmed, i. e. a higher fluorescence is observed at lower temperature when **ref-PBI-1m** is aggregated compared to elevated temperature where **ref-PBI-1m** is present in a monomeric state (Figure A21b).

For both cyclophane **[2PBI]-1m** and for reference monomer **ref-PBI-1m** precipitation was observed above specific temperatures (also referred to as lower critical solution temperature (LCST) behavior) which can be ascribed to dehydration of the OEG chains due to weakening of the hydrogen bonds to solvent molecules at higher temperatures.[141a, 143] The LCST can be characterized by the onset of this behavior, the so-called cloud point. Reference monomer **ref-PBI-1m** shows a cloud point at 58 °C (Figure A22), whereas for cyclophane **[2PBI]-1m** a cloud point of 75 °C was determined. This trend does not surprise since the onset of the LCST behavior of a system is related to the extent of solvation of this system in H_2O. As PBI monomer **ref-PBI-1m** is appended with half the number of solubilizing OEG side chains per openly accessible π-surface when compared to the cyclophane **[2PBI]-1m**, the former is obviously less solvated in H_2O (*vide infra*) as reflected by its lower cloud point compared to the cyclophane.

[4] As the measurements were performed at concentrations of 5.0×10^{-6} mol L^{-1} and 2.5×10^{-5} mol $L^{-1}$for **[2PBI]-1m** and **ref-PBI-1m**, respectively, to monitor a significant part of the assembly process, the optical density of the sample was above 0.5. Thus, the spectral shape is likely influenced by inner filter effects.

3.3.4 Concentration-Dependent UV-vis Studies of [2PBI]-1m and ref-PBI-1m

To further explore the aggregation mechanism of the OEG-substituted **[2PBI]-1m** and **ref-PBI-1m**, concentration-dependent UV-vis studies were performed at 298 K. As the self-assembly of both PBI derivatives is too strong in pure water to monitor a significant range of the transition from monomer to aggregated species, a small amount of acetone (8 vol%) was added as cosolvent. For reference cyclophane **[2PBI]-1m**, an increase in concentration from 1.1×10^{-6} mol L^{-1} to 1.2×10^{-3} mol L^{-1} in H_2O/acetone (92/8 vol%) resulted in an enhancement of the $A_{0,0}$ band with a slight redshift from 570 nm to 581 nm (Figure 45a). Concomitantly, a new band at higher wavelengths (λ_{max} = 650 nm) emerged, which is in accordance with the temperature-dependent UV-vis studies in pure H_2O, indicating self-assembly of **[2PBI]-1m** in a *J*-type arrangement.[151] For the assignment of the aggregation process to either the isodesmic or the dimer model, the transformations in the absorption spectra as a function of concentration were fitted globally (Figure 45a, Figure A23) as well as locally at 650 and 620 nm (Figure A24) to the two aggregation models.[153] By comparison, the dimer model obviously describes the observed spectral changes more accurately than the isodesmic model, yielding a global dimerization constant (K_{dim}) of 2.7×10^4 L mol^{-1} for **[2PBI]-1m** in H_2O/acetone (92/8) at 298 K (Table 2).

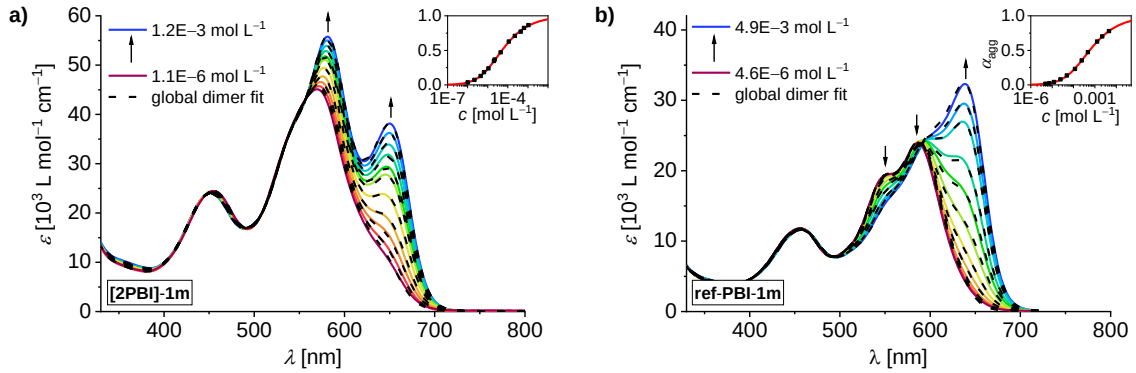

Figure 45. Concentration-dependent UV-vis spectra at 298 K of **(a) [2PBI]-1m** ($1.1 \times 10^{-6} - 1.2 \times 10^{-3}$ mol L^{-1}) and **(b) ref-PBI-1m** ($4.6 \times 10^{-6} - 4.9 \times 10^{-3}$ mol L^{-1}) in H_2O/acetone (92/8) (solid lines) and calculated spectra according to global fit analyses to the dimer model (dashed lines). Arrows indicate spectral changes upon increasing concentration. The insets show the analyses of the absorption data according to the dimer model at **(a)** 650 nm or **(b)** 640 nm.

When the concentration of reference monomer **ref-[2PBI]-1m** is increased from 4.6×10^{-6} mol L^{-1} to 4.9×10^{-3} mol L^{-1} in H_2O/acetone (92/8 vol%), a strong bathochromic shift of the $A_{0,0}$ transition from 587 nm to 637 nm was observed (Figure 45b). This indicates the formation of a *J*-type aggregate species as already suggested by the temperature-dependent UV-vis study of this PBI in pure H_2O.[151] In this solvent composition, however, an insufficient

range of the transition from monomer to aggregated species is covered for the differentiation between the aggregation models. Thus, an additional concentration-dependent UV-vis study in H_2O/acetone (97/3 vol%) was performed (Figure A25), where analogous changes in the optical properties of **ref-PBI-1m** were observed upon increasing the concentration ($2.2 \times 10^{-6} – 3.2 \times 10^{-3}$ mol L^{-1}). A comparison of a global fit analysis to both the isodesmic and the dimer model (Figure 45b and Figure A26) yielded better conformity with the latter which is also supported by the results of exemplary local fits at selected wavelengths (641 and 620 nm) (Figure A27). Thus, supramolecular dimerization was confirmed for the reference monomer. Conclusively, in H_2O/acetone (92/8) a global dimerization constant of 1.8×10^3 L mol^{-1} for **ref-PBI-1m** at 298 K was obtained (Table 2) which is one order of magnitude smaller than that of cyclophane **[2PBI]-1m** ($K_{dim} = 2.7 \times 10^4$ L mol^{-1}). The results from our concentration-dependent experiments clearly imply that the self-assembly processes of PBI monomer **ref-PBI-1m** and cyclophane **[2PBI]-1m** follow the same aggregation model yet with opposite temperature responses. The formation of supramolecular dimers for both PBIs instead of aggregates is also crucial for the explanation of the unusual band shape of the self-assembled structure for cyclophane **[2PBI]-1m**. Since only half of the PBI dyes in **[2PBI]-1m** are aggregated and thus experience *J*-type coupling, the *J*-band remains low with a similar extinction coefficient (~ 40 $\times 10^3$ L mol^{-1} cm^{-1}) and λ_{max} value (640 – 650 nm) as for **ref-PBI-1m** whereas the other half of the PBI dyes still absorbs at around 570 nm as expected for non-aggregated PBIs.

Table 2. Comparison of the thermodynamic data of PBI cyclophane **[2PBI]-1m** and reference monomer **ref-PBI-1m** in H_2O/acetone (92/8) at 298 K.

	K_{dim} [L mol^{-1}]	ΔG_{dim}^0 [kJ mol^{-1}][a]	ΔH_{dim} [kJ mol^{-1}]	ΔS_{dim} [J mol^{-1} K^{-1}]
[2PBI]-1m	2.7×10^4	− 25.3	21.2	155
ref-PBI-1m	1.8×10^3	− 18.6	− 35.8	− 58.5

[a] Gibbs free energies of dimerization ΔG_{dim}^0 determined from K_{dim} at 298 K according to $\Delta G_{dim}^0 = - RT \ln(K_{dim})$.

To characterize the thermodynamic parameters for the supramolecular dimerization of PBI cyclophane **[2PBI]-1m** and monomer **ref-PBI-1m**, concentration-dependent UV-vis studies were performed in H_2O/acetone (92/8 vol%) at variable temperatures from 288 − 313 K in steps of 5 K (Figure A28, Figure A29,). For **ref-PBI-1m**, which disassembles upon heating (Figure 44a), a van't Hoff analysis gave a dimerization enthalpy (ΔH_{dim}) of −35.8 kJ mol^{-1} and a dimerization entropy (ΔS_{dim}) of −58.5 J mol^{-1} K^{-1} (Figure A30a, Table 2). Thus, the enthalpically driven nature of the dimerization of **ref-PBI-1m**, which is governed mainly by intermolecular interaction between the hydrophobic π-scaffolds is confirmed.[154] In contrast,

for cyclophane **[2PBI]-1m** which self-assembles upon heating (Figure 44b), the dimerization process is endothermic as the ΔH_{dim} value is positive (21.2 kJ mol^{-1}). Due to the likewise positive entropy contribution (ΔS_{dim} = 155 J mol^{-1} K^{-1}), however, the overall process is energetically favored with a Gibbs free energy of dimerization (ΔG_{dim}^{0}) of −25.3 kJ mol^{-1} at 298 K (Figure A30b, Table 2). This is a clear thermodynamic signature for an entropy-driven self-assembly mechanism of **[2PBI]-1m** which is mainly directed by dehydration of the OEG chains at higher temperature.[143, 147]

3.3.5 Atomic Force Microscopy of [2PBI]-1m and ref-PBI-1m

For further confirmation of the supramolecular dimerization of PBI cyclophane **[2PBI]-1m** and monomer **ref-PBI-1m** in aqueous media, atomic force microscopy (AFM) studies were performed by spin-coating of the respective solution on the polar substrate mica.[5] Using solutions of **[2PBI]-1m** (H_2O/acetone = 92/8) and **ref-PBI-1m** (H_2O/acetone = 97/3) at a concentration of 2 × 10^{-6} mol L^{-1}, where both compounds are predominantly non-aggregated, the parameters of the monomeric units were obtained. Solutions of higher concentrations in the same solvents were employed for the estimation of the respective aggregate sizes. For **ref-PBI-1m** at 2 × 10^{-6} mol L^{-1}, the AFM image shows small nanoparticles with a height (*h*) of approximately 0.2 ± 0.02 nm and a diameter (*d*) of 3.6 – 4.5 nm (Figure A31), which can be ascribed to isolated molecules with the π-core lying flat on the surface.[155] The relatively large diameter is attributed to the extension of OEG chains on the AFM substrate as well as to contributions of the tip broadening effect. In contrast, at a higher concentration of 5 × 10^{-5} mol L^{-1} larger, spherical nanoparticles were observed with $h = d$ = 0.95 ± 0.15 nm (Figure 46a, c and Figure A32). The dimensions of these nanoparticles corroborate the presence of supramolecular dimers of **ref-PBI-1m** when considering that a dimer stack of **ref-PBI-1m** should have approximately twice the height of the monomeric unit in addition to at least 0.35 nm for the π–π-distance. The OEG chains are probably wrapped around the molecular assembly which explains the reduced diameter of the nanoparticles when compared to monomeric **ref-PBI-1m**. Most importantly, no larger structures were found, which precludes an isodesmic or a cooperative aggregation mechanism.[6] The height of the nanoparticles of

[5] AFM measurements were kindly performed by Dr. Vladimir Stepanenko.

[6] As the nanoparticles of **ref-PBI-1m** tend to agglomerate on the AFM substrate especially at higher concentrations (1 × 10^{-4} mol L^{-1}), a highly anti-cooperative aggregation mechanism cannot be ruled out under the conditions of the spin-coating process. As these conditions cannot be applied to monitor the self-assembly process by UV-vis studies, only the first step of

0.95 nm is further supported by a geometry-optimized structure of the supramolecular dimer of **ref-PBI-1m** in aqueous solution (PM6), where the distance between the lower PBI core, with which the dimer lies on the AFM substrate, and a triazole group of the upper PBI was determined as 0.88 nm (Figure A34a).

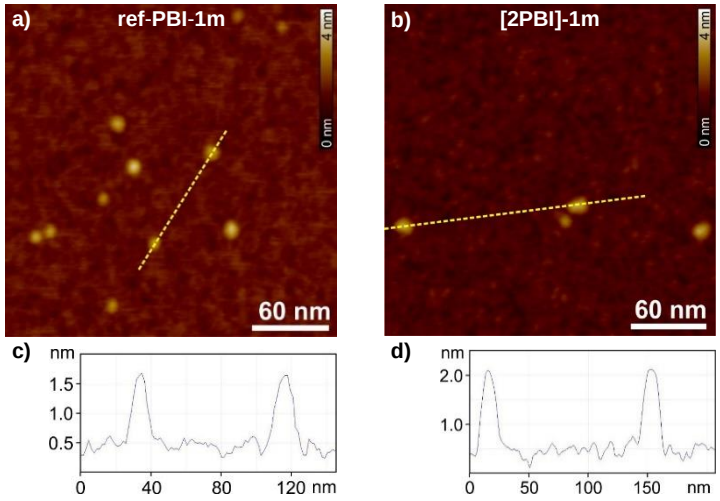

Figure 46. Height AFM images of a sample prepared by spin-coating of a solution of **(a)** reference monomer **ref-PBI-1m** in H_2O/acetone (97/3) and **(b)** PBI cyclophane **[2PBI]-1m** in H_2O/acetone (92/8) at $c = 5 \times 10^{-5}$ mol L^{-1} on mica. *Z* scale is 4 nm. **(c)** Cross-section analysis of the yellow dashed line in **(a)**. **(d)** Cross-section analysis of the yellow dashed line in **(b)**.

For cyclophane **[2PBI]-1m** at lower concentration (2×10^{-6} mol L^{-1}), small nanoparticles with $h = 0.46 \pm 0.02$ nm and $d = 4.6 – 5.6$ nm were observed by AFM (Figure A33). The height of a cyclophane similar to **[2PBI]-1m** was calculated as 0.65 nm.[30a] Correspondingly, and since the height of these nanoparticles is approximately twice the height of the nanoparticles of monomeric **ref-PBI-1m**, they likely represent isolated, slightly tilted **[2PBI]-1m** molecules with one π-surface lying flat on the substrate and the OEG chains spread around the molecule. At a concentration of 5×10^{-5} mol L^{-1}, the AFM image of **[2PBI]-1m** shows a thin film comprised of larger nanoparticles with a height and a diameter of 1.7 ± 0.2 nm (Figure 46c, d and Figure A35). These parameters are in accordance with the minimum dimensions of a stacked cyclophane dimer estimated based on twice the height of monomeric **[2PBI]-1m** in addition to the intermolecular π–π-distance, thus corroborating the supramolecular dimerization of **[2PBI]-1m**. No evidence of extended aggregate structures was found in the AFM images.[7] In a geometry-optimized structure of the dimer stack of **[2PBI]-1m** in water (PM6), the distance

this possible highly anti-cooperative aggregation can be analyzed, which corresponds to the supramolecular dimerization of **ref-PBI-1m** as proven previously by the UV-vis studies.

[7] At a higher concentration of 1×10^{-4} L mol^{-1} a thin film of nanoparticles of similar dimensions as at 5×10^{-5} L mol^{-1} is observed.

between the bottommost PBI core and one of the triazole rings lying over the topmost PBI core was determined as 1.8 nm further corroborating the results from the AFM measurement (Figure A34b).

3.3.6 Discussion of the Thermodynamic Bias

The preference of **ref-PBI-1m** and **[2PBI]-1m** to form supramolecular dimers instead of extended aggregates, as confirmed by both UV-vis and AFM studies, is in accordance with previous results obtained with a fourfold aryl bay-functionalized PBI derivative in cyclohexane and can be explained in terms of steric features.[156] Prior to dimerization, the bay-substituents including the solubilizing OEG chains are distributed uniformly around the hydrophobic π-surfaces of the corresponding monomeric unit, thereby screening the core from the aqueous environment. Upon formation of a supramolecular dimer, the substituents have to rearrange away from the core making one π-surface accessible to interact with the other monomer unit and most likely sterically shielding the second accessible π-surface impeding further aggregation. The aggregation processes of PBI monomer **ref-PBI-1m** and PBI cyclophane **[2PBI]-1m** can even be considered as limiting cases of anti-cooperative chain growth in which the dimerization step is favored over the elongation process to such a strong extent that the latter does not occur.[157]

In the following, the thermodynamic bias observed for the supramolecular dimerization of PBI monomer **ref-PBI-1m** and cyclophane **[2PBI]-1m** in water is discussed more elaborately. We assume that the OEG chains of both PBI systems are back-folded to a certain extent over the (outer) π-surfaces of the chromophores in the monomeric state screening the apolar PBI cores from the bulk water.[147, 158] Evidence for this back-folding is indeed found in a 2D NMR spectrum of **ref-PBI-1m** in the polar solvent CD_3CN, where this PBI does not aggregate as indicated by UV-vis spectroscopy (Figure 42) and sharp ^1H NMR signals. Cross signals are observed in the ^1H, ^1H ROESY spectrum of **ref-PBI-1m** indicating close proximity of the PBI core protons of the reference monomer and the protons of the OEG chain which are close to the triazole ring corroborating back-folding of these groups over the PBI moiety (Figure 47 and Figure A36). In the case of cyclophane **[2PBI]-1m**, ^1H NMR peaks at room temperature are broad due to the thermodynamic equilibrium between its stereoisomers (see Chapter 3.4).[159] Likewise, for both PBIs in water broad ^1H NMR signals are observed due to aggregation precluding performance of analogous studies in this solvent.

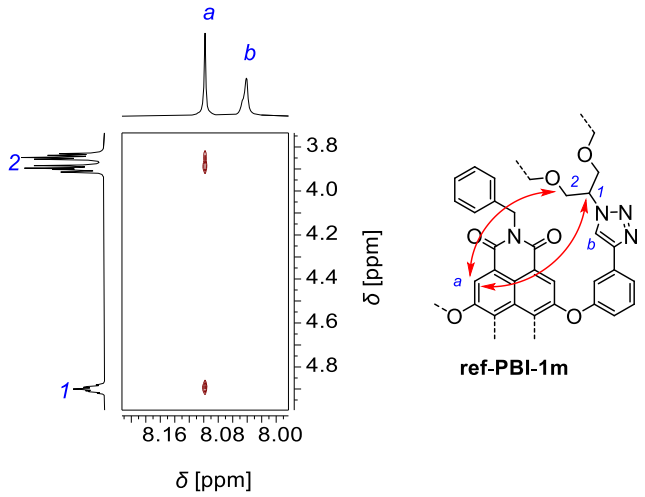

Figure 47. Excerpt of the ^{1}H, ^{1}H ROESY NMR spectrum (600 MHz, 295 K) of **ref-PBI-1m** in CD_3CN showing the cross signals (indicated by red arrows) between the PBI core proton *a* and the protons *1* and *2* of the OEG chain. See Figure A36 for the full spectrum.

Calculations[8] performed on the monomeric species with back-folded OEG-chains show in case of the reference monomer that the solubilizing groups do not suffice to cover all of the hydrophobic parts of the chromophore core, leaving some of them exposed to the bulk water (Figure 48a and b, see black arrow in Figure 48b). For the PBI cyclophane, which is appended with twice as many polar OEG chains per solvent-exposed π-surface when compared to reference monomer **ref-PBI-1m**, this screening from bulk water becomes more efficient burying the apolar building blocks of the PBI completely under hydrophilic residues (Figure 48c and d).

The shell of OEG chains around the chromophore cores forms hydrogen bonds with the solvent which have to be broken upon aggregation. The necessity to break these hydrogen bonds is reflected in the enthalpic cost for the aggregation of **[2PBI]-1m** which cannot be compensated by the gain of dispersion interaction between the chromophores in the aggregate. Hence, the driving force of the dimerization originates in the gain of entropy upon release of the hydrogen-bonded water molecules into the bulk solvent (Figure 49a).[143]

[8] Calculations were kindly performed by Dr. Joachim Lindner.

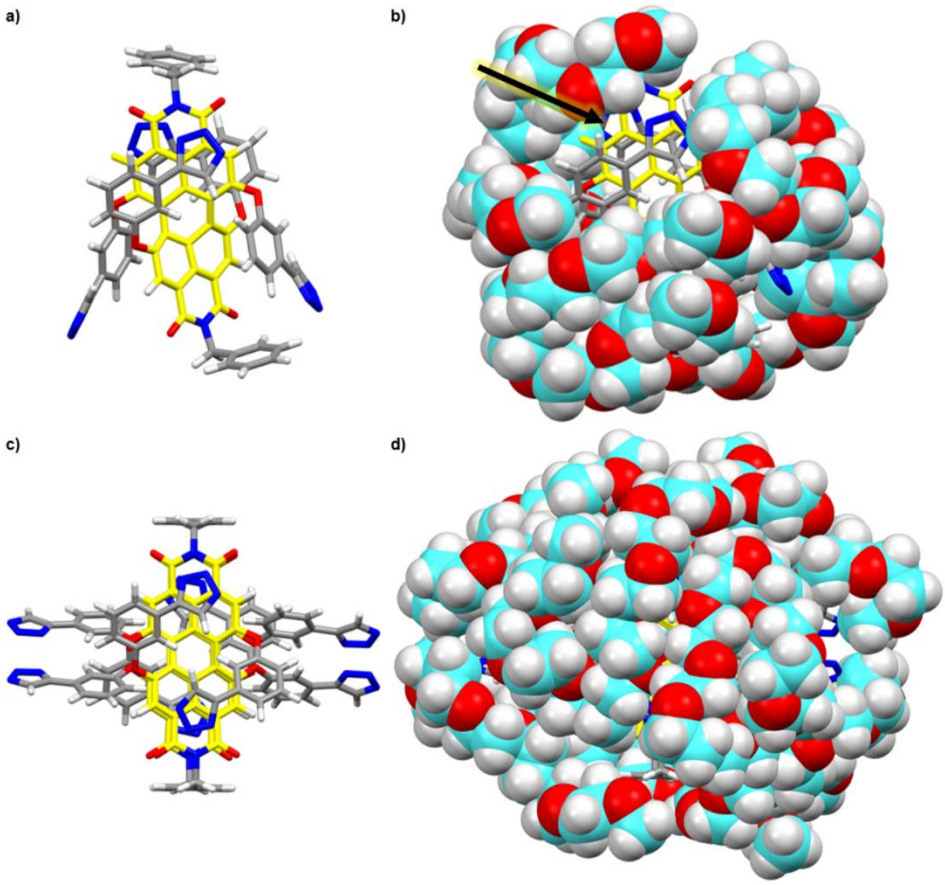

Figure 48. Top view on the calculated monomeric structures (PM6) with back-folded OEG-chains of **(a, b) ref-PBI-1m** and **(c, d) [2PBI]-1m**. The left-hand side shows only the mostly hydrophobic parts of the molecules (yellow carbon atoms: PBI core; grey carbon atoms: imide and bay substituents) and right-hand side includes the solubilizing OEG chains (cyan) to the same view of the molecules. See Chapter 6.1 for a detailed description of the calculations.

As **ref-PBI-1m** possesses half as many OEG chains less hydrogen bonds have to be broken upon dimerization reducing the enthalpic cost but also the entropic gain by water release declines. On the other hand, facilitated dispersion interaction between two monomeric units of **ref-PBI-1m** by less steric hindrance contributes to the enthalpic gain. Furthermore, the exposed hydrophobic core of monomeric **ref-PBI-1m** is surrounded by energetically frustrated water molecules with an unfavorable hydrogen-bond count.[43, 158] The release of this so-called "high energy water"[142a] to the bulk solvent upon self-assembly of **ref-PBI-1m** should be accompanied by an enthalpy gain, as well. As a result, the overall dimerization of **ref-PBI-1m** is an enthalpically driven process (Figure 49).

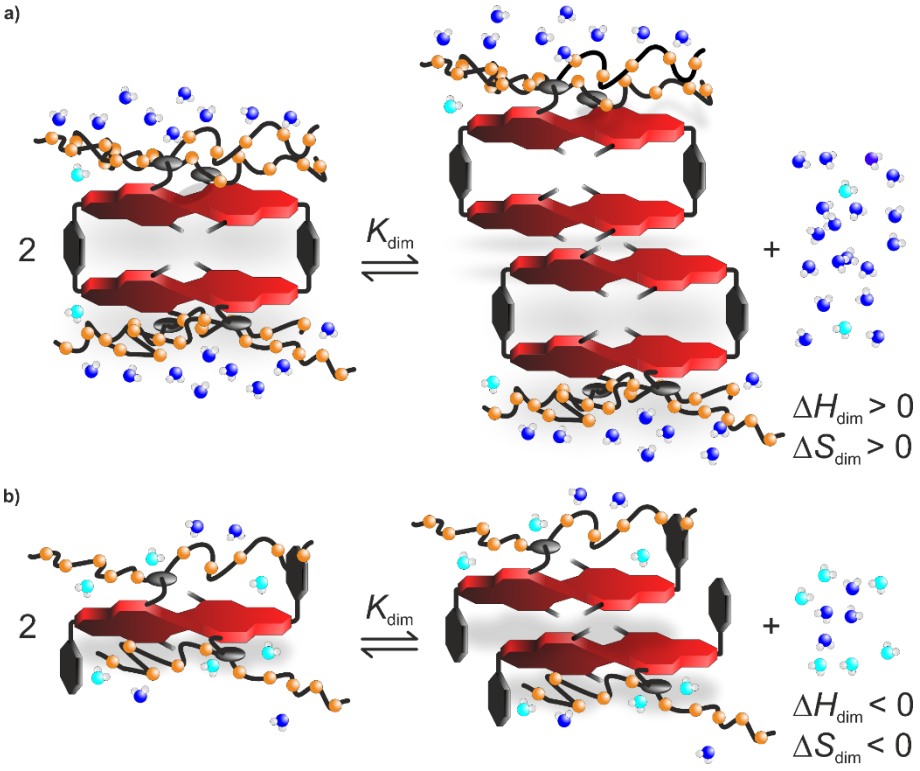

Figure 49. Schematic illustration of the proposed dimerization process of **(a) [2PBI]-1m** and **(b) ref-PBI-1m**. Only a representative number of OEG chains is shown, the rest is omitted for clarity. Water molecules which are hydrogen-bonded to the OEG chains are shown in dark blue, energetically frustrated water molecules in the proximity of hydrophobic surfaces are displayed in cyan. The implied homochiral conformation in the racemic dimer aggregates is a tentative assumption.[159-160]

Another factor influencing the self-assembly tendency of both PBI systems and the entropy of dimerization is the higher degree of preorganization in the cyclophane due to the proximity of the second PBI core within the cyclic bis-chromophore. PBIs with four bay functionalities are not planar but twisted and undergo a fast interconversion of the *P* and *M* atropisomers.[39] We have shown previously that the energy barrier for the interconversion is slightly higher for a PBI cyclophane than for a corresponding monomer.[159] Thus, we reason that in a supramolecular dimer of **ref-PBI-1m**, in which both PBI cores have a favored conformation to maximize dispersion forces,[160] it is energetically easier for one of the two molecules to interconvert and, consequently, weaken the intermolecular interaction. In a supramolecular assembly of **[2PBI]-1m**, on the other hand, such an interconversion (*P* ⇌ *M*) is more restricted resulting in a stabilization of the cyclophane dimer with respect to a stacked dimer of **ref-PBI-1m**, contributing to the higher stability of the supramolecular dimer when compared to the reference monomer.

3.3.7 Host-Guest Binding Properties of [2PBI]-1m in Water

In Chapter 3.2, it was shown by UV-vis and fluorescence titration experiments that cyclophane **[2PBI]-1p**, which is a regioisomer of **[2PBI]-1m**, acts as a molecular probe for naturally occurring aromatic alkaloids such as the *harmala* alkaloid harmine hydrochloride (**G1**, Figure 41).[150] Since the only structural difference between the two PBI cyclophane derivatives is the position of the solubilizing groups in the aryl substituents at the bay positions, the cavity of **[2PBI]-1m** is similar to the one of **[2PBI]-p**. It is, therefore, reasonable to assume comparable host-guest binding properties for the two regioisomers. Indeed, under the same conditions that were applied for **[2PBI]-1p** (H_2O/CH_3CN (1/1 vol%), $c_{host} = 1 \times 10^{-5}$ mol L^{-1}, $T = 295$ K), **[2PBI]-1m** binds **G1** with an almost identical binding strength of 5.6×10^3 mol L^{-1} (Figure A37) when compared to 7.3×10^3 mol L^{-1} for **[2PBI]-1p**. Yet, due to the self-assembly of **[2PBI]-1m** to discrete supramolecular dimers in aqueous solution, the interplay of aggregation and guest encapsulation of a PBI cyclophane can be investigated. Such studies have been performed before with molecular clips and tweezers or a calixarenes derivative indicating competitive disassembly of host aggregates upon guest encapsulation.[161] Harmine hydrochloride (**G1**), one of the best performing alkaloid guests for **[2PBI]-1p**,[150] was chosen as an exemplary guest for **[2PBI]-1m**.

Upon addition of **G1** (up to 200 equivalents (eq.)) to a highly diluted solution of essentially non-aggregated **[2PBI]-1m** ($c = 1.0 \times 10^{-6}$ mol L^{-1}) in H_2O/acetone (92/8 vol%) at 298 K (Figure 50a), distinct changes in the UV-vis properties of the cyclophane were observed which clearly hint at the formation of a host-guest complex between **G1** and **[2PBI]-1m**. For example, at 298 K, the $A_{0,0}$ (~ 573 nm) and $A_{0,1}$ (~ 553 nm) transitions for the free cyclophane host are not easily distinguishable from each other due to signal broadening. Yet with increasing concentration of guest **G1**, the vibronic structure of the S_0–S_1 absorption band of the host becomes clearly discernible. Moreover, this is accompanied by a prominent red shift of the $A_{0,0}$ band. The presence of several isosbestic points at 541 nm, 552 nm, 579 nm and 618 nm indicates the equilibrium between the free host and the host-guest complex. The 1:1 stoichiometry of the host-guest complex **G1⊂[2PBI]-1m** was assessed by a Benesi-Hildebrand plot (Figure A38).[134] Accordingly, fitting of the titration data to a 1:1 host-guest binding model[135] gave an estimated host-guest binding constant (K_a) of 2.2×10^4 L mol^{-1} (Figure 50a, inset and Figure A38b).[9] As a control experiment, the UV-vis titration of reference monomer

[9] As the fluorescence of non-aggregated **[2PBI]-1m** is strongly quenched in H_2O/acetone = 92/8, additional verification of the binding constant by fluorescence titration is not possible.

ref-PBI-1m with **G1** was performed (Figure A39a). At a concentration of 1.0×10^{-6} mol L^{-1} in H_2O/acetone (97/3) at 298 K, the UV-vis spectrum of **ref-PBI-1m** barely changes upon addition of **G1** (up to 400 eq.) confirming that there is virtually no specific interaction between monomer **ref-PBI-1m** and alkaloid **G1**.

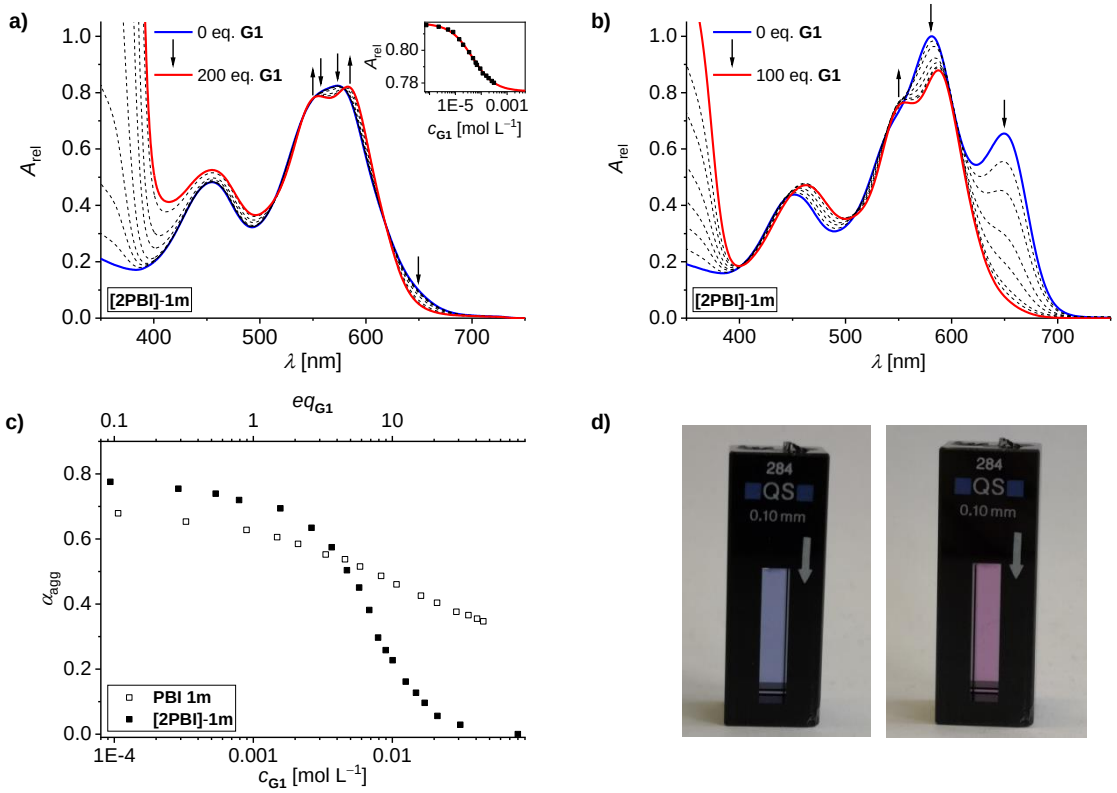

Figure 50. UV-vis titration of **[2PBI]-1m** at **(a)** $c_0 = 1 \times 10^{-6}$ mol L^{-1} and **(b)** $c_0 = 1 \times 10^{-3}$ mol L^{-1} with **G1** in H_2O/acetone (92/8 vol%) at 298 K. Spectra are normalized to the most intense band of the supramolecular dimer of **[2PBI]-1m**. Arrows indicate changes upon increasing guest concentration. The inset in **(a)** shows a plot of UV-vis titration data points at 565 nm as a function of guest concentration and fitting with a 1:1 host guest binding model. **(c)** Comparison of the degree of aggregation α_{agg} of PBI monomer **ref-PBI-1m** and PBI cyclophane **[2PBI]-1m** as a function of the concentration of alkaloid **G1** **[2PBI]-1m** ($c_0 = 1 \times 10^{-3}$ mol L^{-1}). **(d)** Representative photographs of solutions of **[2PBI]-1m** (1×10^{-3} mol L^{-1}) in 0.10 mm cuvettes without guest (left) and in the presence of 100 eq. of **G1** (right).

To explore the impact of guest addition on the dimer aggregate of the PBI cyclophane, UV-vis titration experiments with **[2PBI]-1m** ($c_0 = 1.0 \times 10^{-3}$ mol L^{-1}) in H_2O/acetone (92/8) were conducted (Figure 50b). Note that at high concentrations of a host H, smaller amounts of a guest G are needed to shift the equilibrium H + G ⇌ HG towards the host-guest complex HG than at low concentrations.[162] Prior to guest addition, **[2PBI]-1m** is strongly aggregated at this concentration ($\alpha_{agg} \approx 0.8$, see Figure 50c, black squares) and shows the distinct bathochromically shifted band of the supramolecular dimer at 650 nm. Upon addition of up to 100 eq. of guest **G1**, this band gradually disappears, which, as discussed previously, indicates disassembly of **[2PBI]-1m**. Moreover, the $A_{0,0}$ band at 582 nm decreases and redshifts to

587 nm while the $A_{0,1}$ band (552 nm) becomes more pronounced. Remarkably, the spectrum corresponding to the titration end point at high host concentration (1×10^{-3} mol L^{-1}, Figure 50b) strongly resembles the spectrum of the titration end point at lower concentration of **[2PBI]-1m** (1×10^{-6} mol L^{-1}, Figure 50a). Therefore, it can be concluded that the disassembly of the supramolecular host dimer of **[2PBI]-1m** upon addition of **G1** yields neither the free cyclophane monomer nor any aggregated host-guest complexes but monomeric **G1⊂[2PBI]-1m**. This transition from dimer-aggregate to monomeric host-guest complex can even be followed by the naked eye, as the solution of the supramolecular dimer of **[2PBI]-1m** is bluish whereas the solution of **G1⊂[2PBI]-1m** is purple (Figure 50d).

UV-vis titration experiments with the supramolecular dimer of reference monomer **ref-PBI1m** ($c_0 = 1 \times 10^{-3}$ mol L^{-1}) revealed that with increasing the concentration of **G1** the $A_{0,0}$ transition at 640 nm decreases and is hypsochromically shifted (Figure A39b). These spectral changes towards a more monomer-like spectrum of **ref-PBI-1m** indicate deaggregation upon addition of **G1** even though no specific host-guest interaction was observed for non-aggregated **ref-PBI-1m**. Yet for **ref-PBI-1m**, the full monomeric state is not reached even after the addition of 100 eq. of **G1**,[10] which led to a quantitative disassembly in the case of cyclophane **[2PBI]-1m**. A plot of the degree of aggregation (α_{agg}) as a function of the concentration of alkaloid **G1** for **[2PBI]-1m** and **ref-PBI-1m** shows that the effect of deaggregation is indeed more pronounced for the PBI cyclophane than for the PBI monomer (Figure 50c), especially when considering that the tendency to dimerize in the respective solvent mixtures is higher for **[2PBI]-1m** (K_{dim} $=2.7 \times 10^4$ mol L^{-1}) than for **ref-PBI-1m** ($K_{dim} = 8.3 \times 10^3$ mol L^{-1}).

Thus, we assume that in the case of **ref-PBI-1m** the disassembly of the supramolecular dimer is caused by disruption of the intermolecular dispersion attraction by unspecific association of the aromatic guest to the π-surface of the PBI, which should be more favorable for higher concentrations of both **ref-PBI-1m** and **G1**. Such effects apparently do not account for the deaggregation of cyclophane **[2PBI]-1m** upon addition of **G1**, particularly since the degree of deaggregation upon alkaloid addition is more pronounced even though its overall dimerization propensity is stronger than for **ref-PBI-1m**. It should be noted that the π-core of *tetra*-bay-functionalized PBIs such as **[2PBI]-1m** and **ref-PBI-1m** is not planar due to steric effects of the bay substituents.[39] For the supramolecular dimer of **[2PBI]-1m**, we reason that a specific twist angle of the naphthalene subunits of the chromophores is assumed in the aggregate to

[10] The addition of higher amounts of **G1** was not possible due to solubility issue.

maximize attractive intermolecular interactions. However, in the host-guest complex **G1⊂[2PBI]-1m**, this angle changes to effectively accommodate the guest molecule within the cyclophane cavity. Apparently, this conformational alteration of the PBI core is then no longer suited for the cohesion in a dimer aggregate. Interestingly, host self-association (K_{dim} = 2.7 × 10^4 mol L^{-1}) and guest uptake (K_a = 2.2 × 10^4 L mol^{-1}) are of comparable strength. At higher concentrations of **[2PBI]-1m** these two processes are in competition with each other (Figure 51), yet the increasing concentration of **G1** during the titration shifts the equilibrium from the dimerized host towards the monomeric host guest complex **G1⊂[2PBI]-1m**.[161]

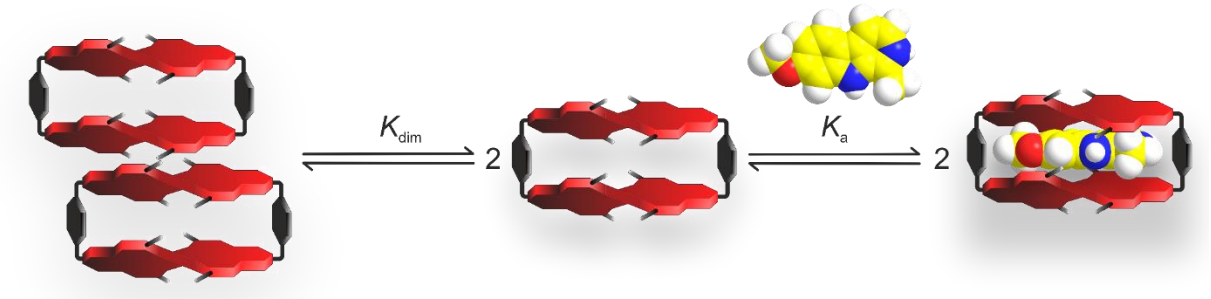

Figure 51. Schematic representation of the equilibrium of PBI cyclophane **[2PBI]-1m** between its dimer aggregate and the host-guest complex with alkaloid guest **G1**. The OEG chains are omitted for clarity. The implied homochiral conformation in the racemic dimer aggregate is a tentative assumption.[159-160]

3.3.8 Conclusion

In summary, by temperature-dependent UV-vis studies in water we demonstrated the thermodynamic bias behind the self-assembly process of PBI cyclophane **[2PBI]-1m** and its reference monomer **ref-PBI-1m**. For **ref-PBI-1m**, a common temperature response of the aggregate was observed leading to deaggregation at elevated temperature. In the case of the cyclophane, however, enhanced aggregation was observed upon increasing the temperature. These findings corroborate an enthalpically-favored self-assembly process for the reference monomer whereas for the PBI cyclophane this process is entropically driven and enthalpically even disfavored according to a van't Hoff plot in water/acetone (92/8 vol%). This thermodynamic bias reflects the higher extent of solubilization of the cyclophane which is caused by the doubled number of solubilizing OEG chains appended to the hydrophobic chromophore core. Indeed, our results support the notion that an entropy-driven self-assembly is observed for such cases where a high degree of back-folding of the solubilizing side chains occurs resulting in complete screening of the hydrophobic PBI core from the bulk water.[147, 158] Furthermore, UV-vis dilution experiments and AFM studies were performed to demonstrate

that the self-assembly process of both **ref-PBI-1m** and **[2PBI]-1m** follows the dimerization model. Interestingly, the dimerization tendency in H_2O/acetone (92/8 vol %) is approximately an order of magnitude higher for the cyclophane (K_{dim} = 2.7 × 10^4 mol L^{-1}) than for the reference monomer (K_{dim} = 1.8 × 10^3 mol L^{-1}) which can be rationalized based on a favorable statistics as well as on the higher conformational rigidity of cyclophane **[2PBI]-1m** when compared to **ref-PBI-1m**. Cyclophane host **[2PBI]-1m** in its monomeric state binds the *harmala* alkaloid harmine hydrochloride (**G1**) in water with a binding strength of 2.2 × 10^4 L mol^{-1}. When **[2PBI]-1m** is aggregated, host self-association and guest encapsulation become competing processes with the equilibrium being shifted towards the host-guest complex **G1⊂[2PBI]-1m** upon addition of higher amounts of **G1**. Due to the color change accompanying the host-guest complex formation out of the dimer aggregate from blue to purple, **[2PBI]-1m** represents a potential molecular probe for this class of natural products.

3.3.9 Appendix II

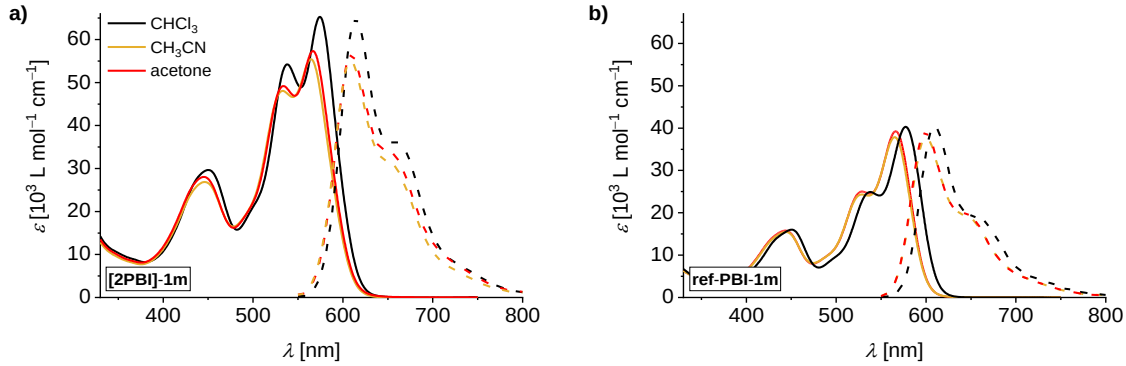

Figure A19. Solvent-dependent UV-vis (solid lines) and fluorescence spectra (dashed lines, λ_{ex} = 530 nm) of **(a) [2PBI]-1m** (c = 1 × 10^{-5} mol L^{-1}) and **(b) ref-PBI-1m** (c = 2 × 10^{-5} mol L^{-1}) in $CHCl_3$ (black), CH_3CN (orange) and acetone (red). The fluorescence spectra are normalized to the respective UV-vis spectra.

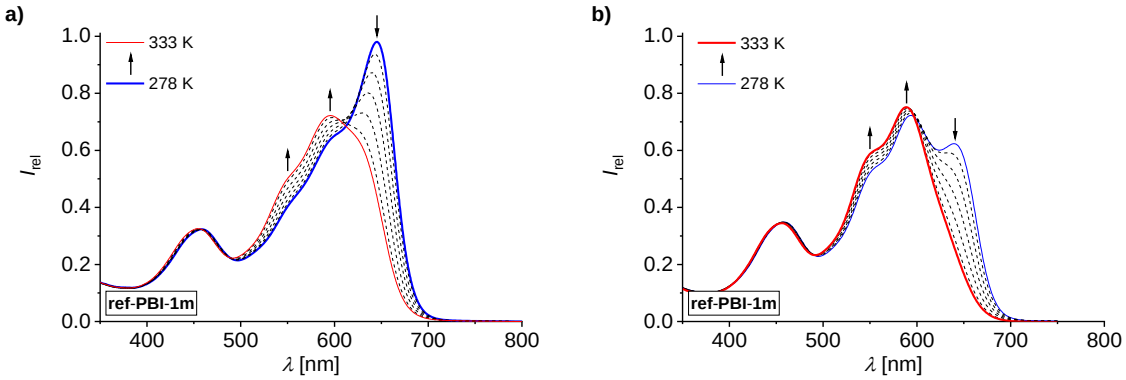

Figure A20. Temperature-dependent UV-vis spectra of **ref-PBI-1m** at a concentration of **(a)** 5.0 × 10^{-4} mol L^{-1} and **(b)** 1.5 × 10^{-5} mol L^{-1} in pure H_2O, heating rate = 0.5 K min^{-1}. Arrows indicate spectral changes upon heating.

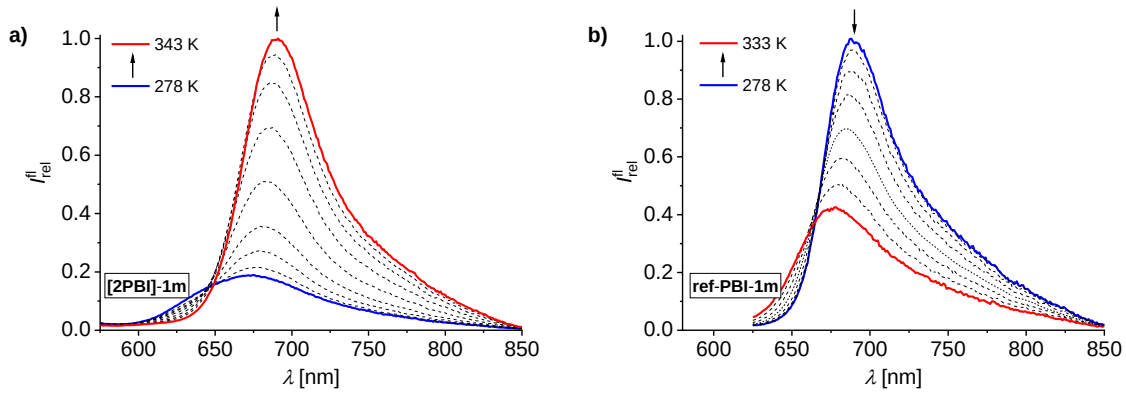

Figure A21. Temperature-dependent fluorescence spectra of **(a) [2PBI]-1m** (c = 5.0 × 10^{-6} mol L^{-1}, λ_{ex} = 533 nm) and **(b) ref-PBI-1m** (c = 2.5 × 10^{-5} mol L^{-1}, λ_{ex} = 597 nm) in H_2O. The spectra are normalized to the most intense spectrum. Arrows indicate spectral changes upon increasing temperature.

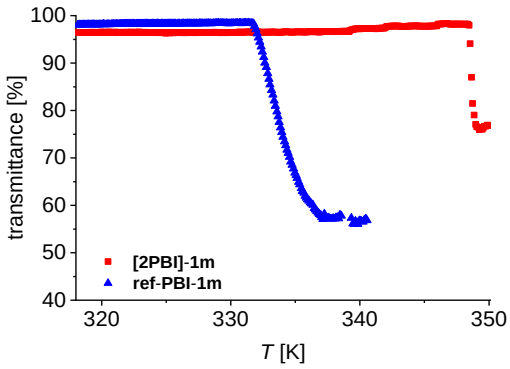

Figure A22. Comparison of the temperature-dependent transmittance of PBI cyclophane **[2PBI]-1m** and PBI monomer **ref-PBI-1m** in H_2O at 800 nm (c = 2.5 × 10^{-4} mol L^{-1}, heating rate 0.1 K min^{-1}).

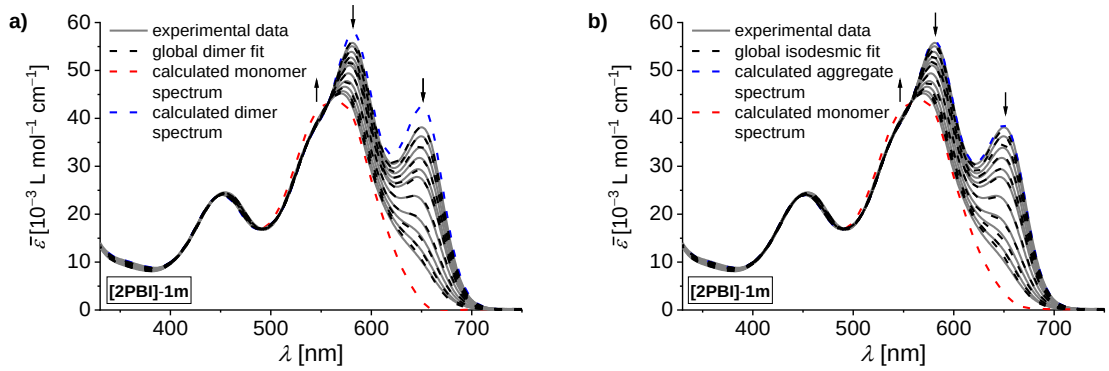

Figure A23. Comparison of the concentration-dependent UV-vis spectra of **[2PBI]-1m** (1.0 × 10^{-3} mol L^{-1} – 1.2 × 10^{-6} mol L^{-1}) in H_2O/acetone (92/8 vol%) at 298 K (grey solid lines) to calculated spectra obtained **(a)** by a global fit analysis to the dimer model (black dashed lines) and **(b)** by a global fit analysis to the isodesmic model (black dashed lines), respectively. The calculated monomer and dimer/aggregate spectra are displayed in red and blue dashed lines, respectively. Arrows indicate spectral changes upon increasing concentration.

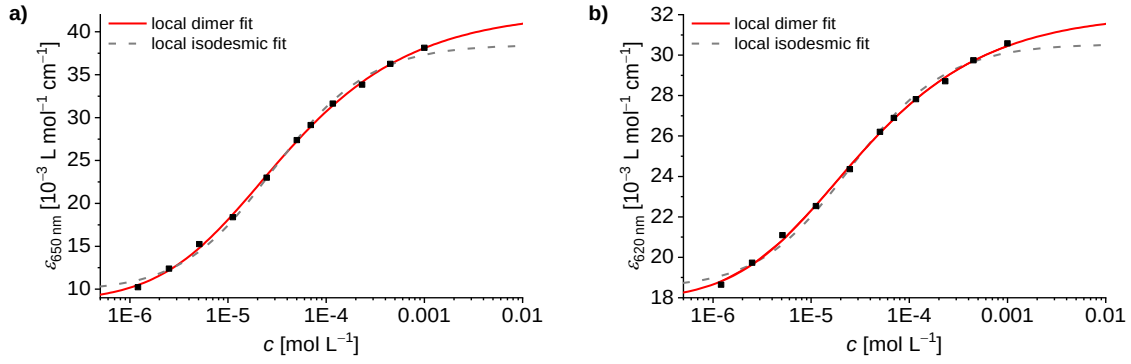

Figure A24. Extinction coefficients of **[2PBI]-1m** at **(a)** 650 nm and **(b)** 620 nm as a function of concentration in H_2O/acetone (92/8 vol%) at 298 K. The red solid lines represent a local fit to the dimer model, the grey dashed lines a local fit to the isodesmic model.

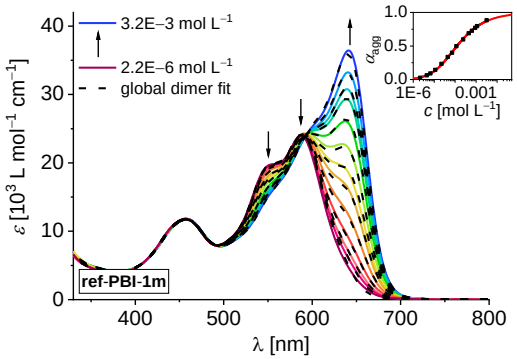

Figure A25. Concentration-dependent UV-vis spectra of **ref-PBI-1m** (2.2×10^{-6} – 3.2×10^{-3} mol L^{-1}) in H_2O/acetone (97/3) (solid lines) and calculated spectra according to global fit analyses to the dimer model (dashed lines) at 298 K. Arrows indicate spectral changes upon increasing concentration. The insets show the analyses of the absorption data according to the dimer model at 641 nm. The global dimerization constant is determined as 8.3×10^3 L mol^{-1} for **ref-PBI-1m** in H_2O/acetone (97/3) at 298 K.

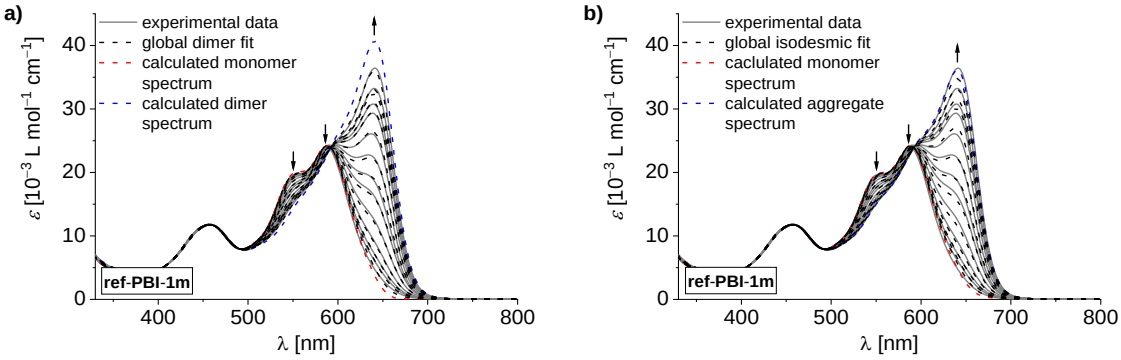

Figure A26. Comparison of the concentration-dependent UV-vis spectra of **ref-PBI-1m** (3.2×10^{-3} mol L^{-1} – 2.2×10^{-6} mol L^{-1}) in H_2O/acetone (97/3 vol%) at 298 K (grey solid lines) to calculated spectra obtained by **(a)** a global fit analysis to the dimer model (black dashed lines) and **(b)** a global fit analysis to the isodesmic model (black dashed lines). The calculated monomer and dimer/aggregate spectra are displayed in red and blue dashed lines, respectively. Arrows indicate spectral changes upon increasing concentration.

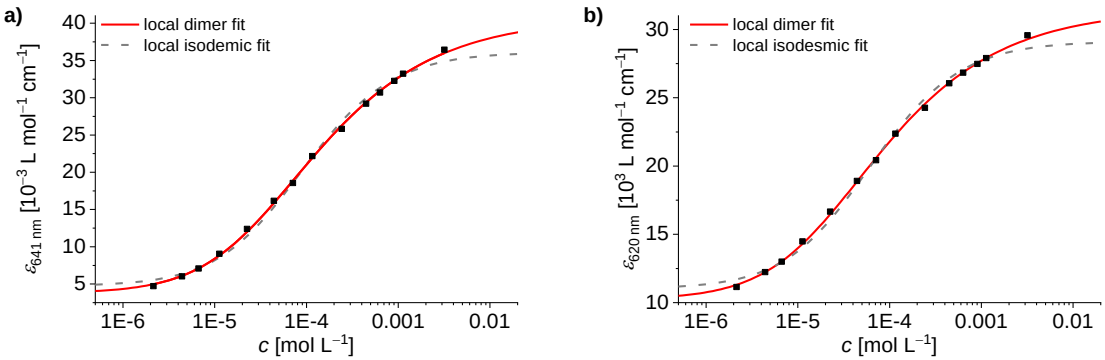

Figure A27. Extinction coefficients of **ref-PBI-1m** at **(a)** 641 nm and **(b)** 620 nm as a function of concentration in H_2O/acetone (97/3 vol%) at 298 K. The red solid lines represent a local fit to the dimer model, the grey dashed lines a local fit to the isodesmic model.

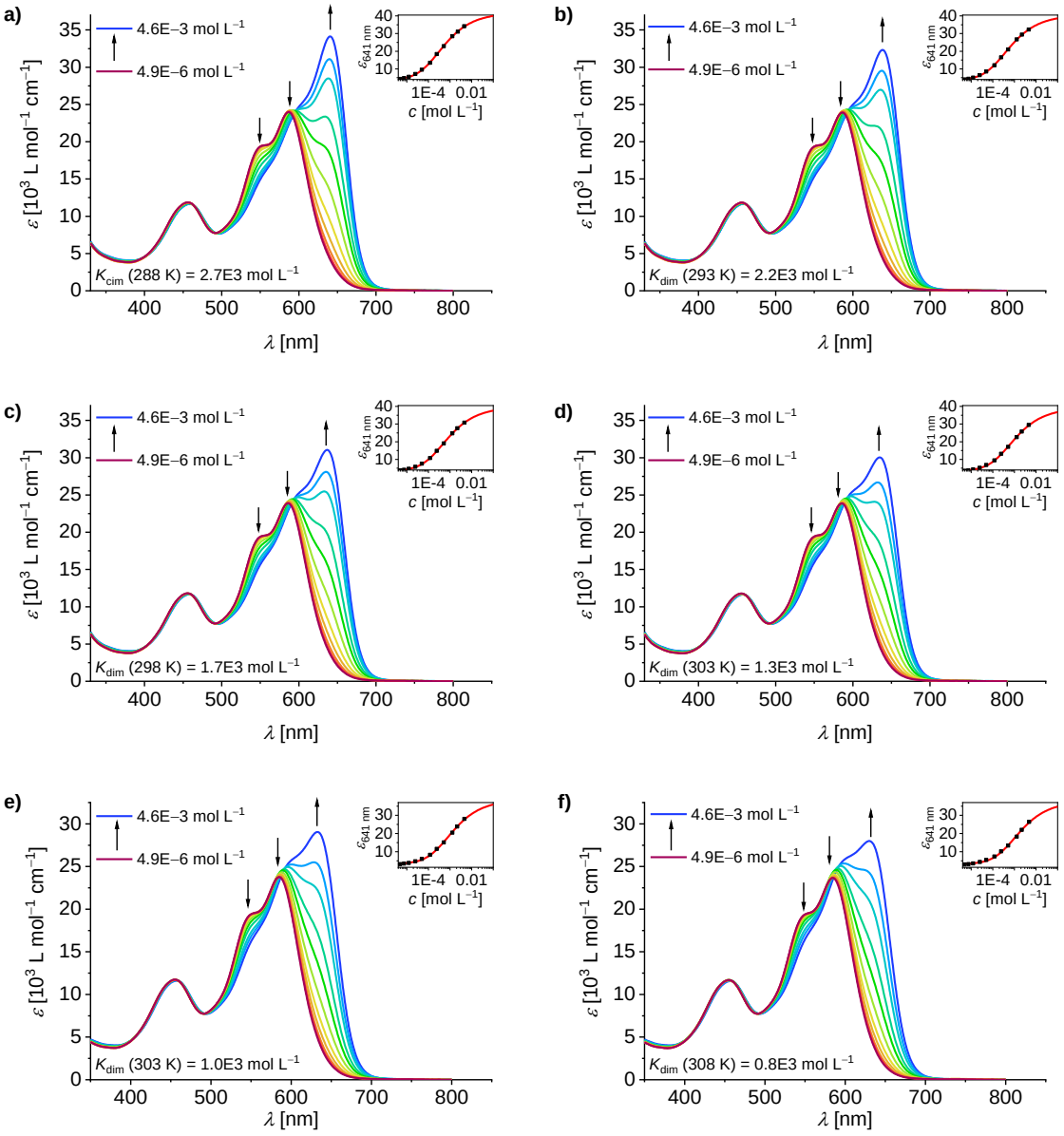

Figure A28. Concentration-dependent UV-vis spectra of **ref-PBI-1m** (4.6×10^{-3} mol L^{-1} – 4.9×10^{-6} mol L^{-1}) in H_2O/acetone (92/8 vol%) at **(a)** 288 K, **(b)** 293 K, **(c)** 298 K, **(d)** 303 K, **(e)** 308 K and **(f)** 313 K. The insets show the data points at 641 nm as a function of concentration and fitting to the dimer model. Arrows indicate changes upon increasing the concentration.

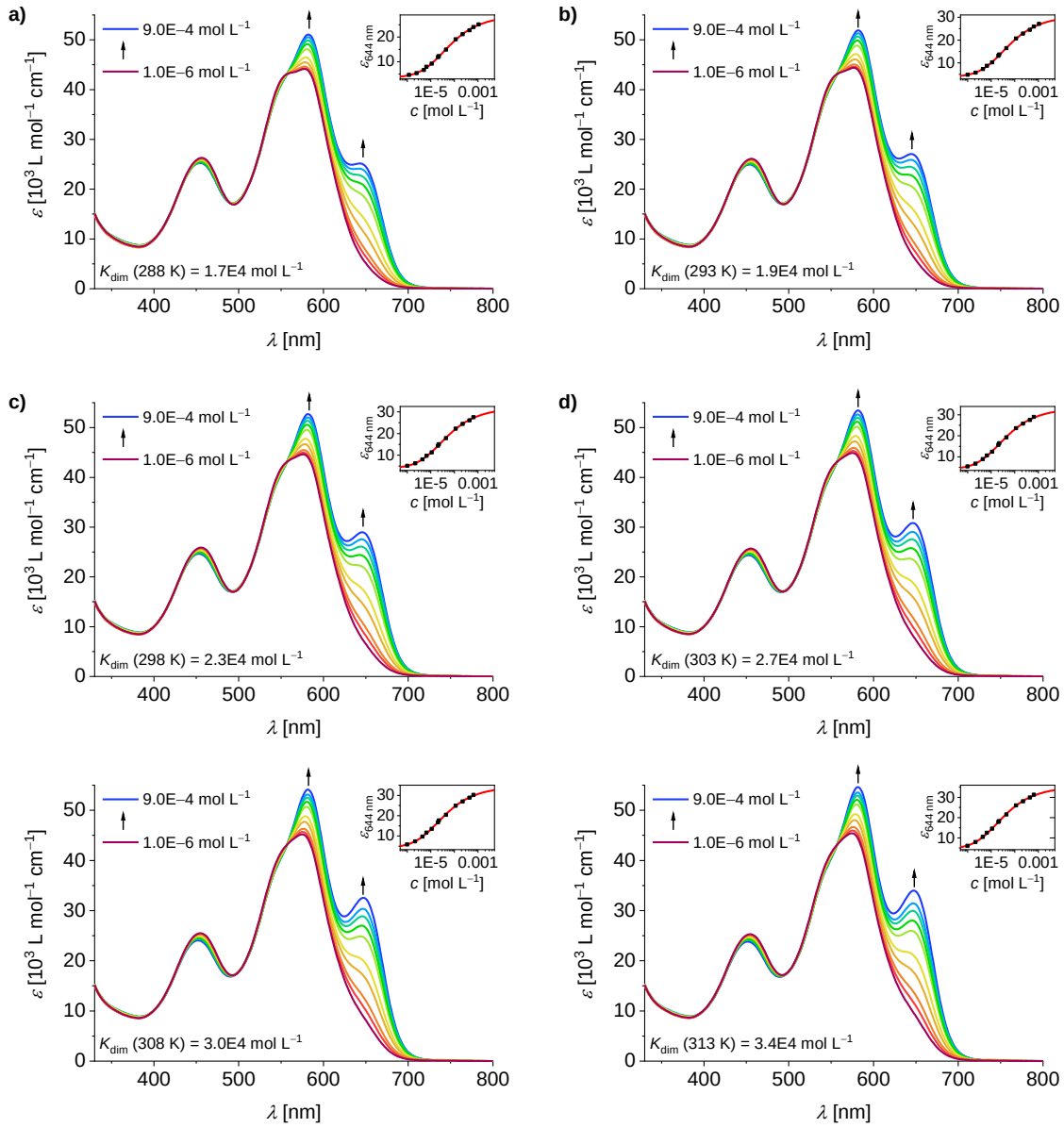

Figure A29. Concentration-dependent UV-vis spectra of **[2PBI]-1m** (1.0×10^{-6} mol L^{-1} – 9.0×10^{-4} mol L^{-1}) in H_2O/acetone (92/8 vol%) at **(a)** 218 K, **(b)** 293 K, **(c)** 298 K, **(d)** 303 K, **(e)** 308 K and **(f)** 313 K. Arrows indicate spectral changes upon increasing concentration. The insets show the absorption data at 644 nm as a function of concentration and fitting to the dimer model.

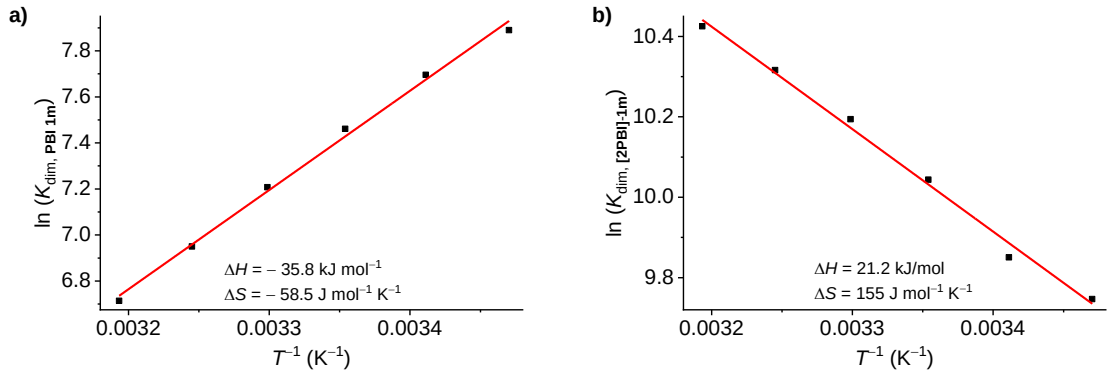

Figure A30. Van't Hoff analysis of **(a) ref-PBI-1m** and **(b) [2PBI]-1m** in H_2O/acetone (92/8 vol%).

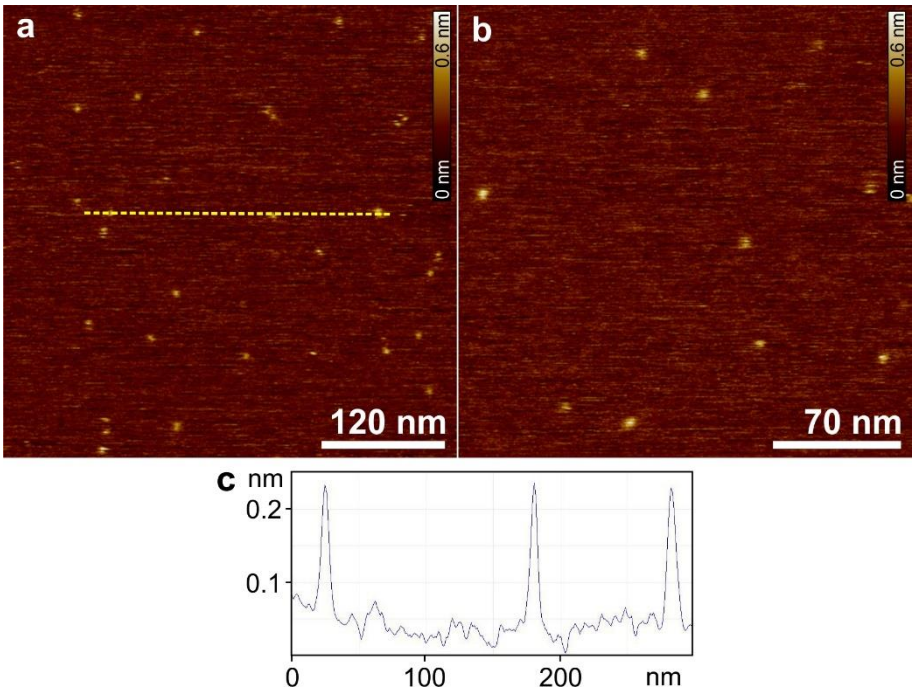

Figure A31. (a, b) Height AFM images of a sample prepared by spin-coating of a solution of PBI monomer **ref-PBI-1m** in H_2O/acetone (97/3) at $c = 2 \times 10^{-6}$ mol L^{-1} on mica. *Z* scale is 0.6 nm. **(c)** Cross-section analysis of the yellow dashed line in **(a)**.

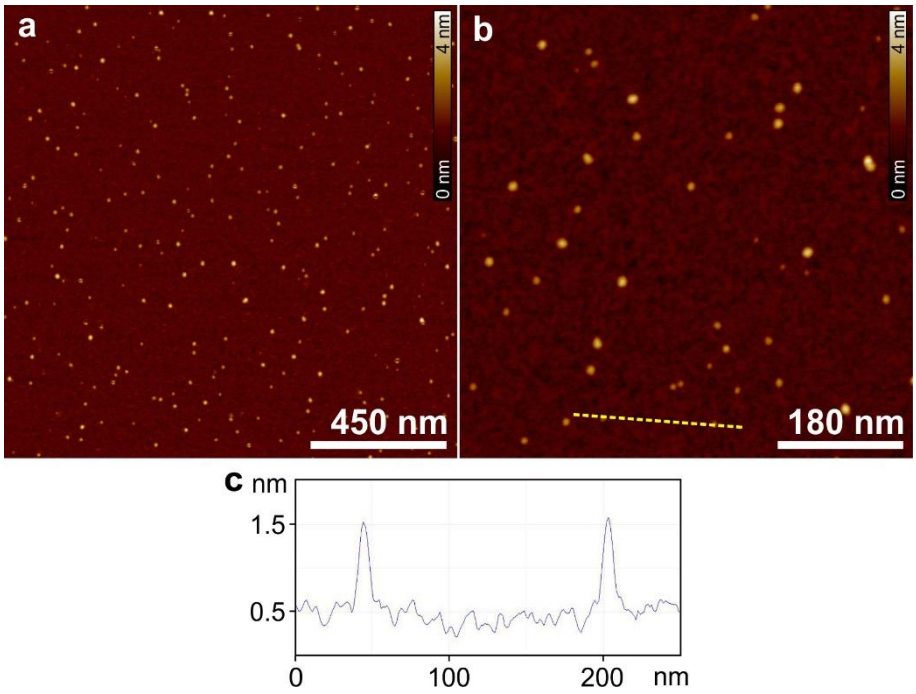

Figure A32. (a, b) Height AFM images of a sample prepared by spin-coating of a solution of PBI monomer **ref-PBI-1m** in H_2O/acetone (97/3) at $c = 5 \times 10^{-5}$ mol L^{-1} on mica. *Z* scale is 4 nm. **(c)** Cross-section analysis of the yellow dashed line in **(b)**.

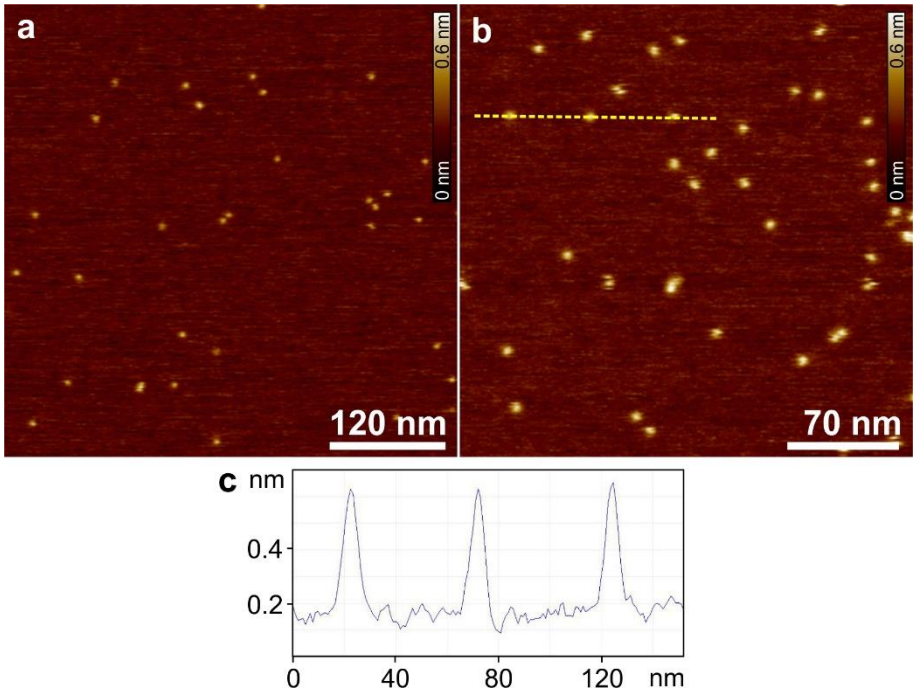

Figure A33. (a, b) Height AFM images of a sample prepared by spin-coating of a solution of PBI cyclophane **[2PBI]-1m** in H_2O/acetone (92/8) at $c = 2 \times 10^{-6}$ mol L^{-1} on mica. *Z* scale is 0.6 nm. **(c)** Cross-section analysis of the yellow dashed line in **(b)**.

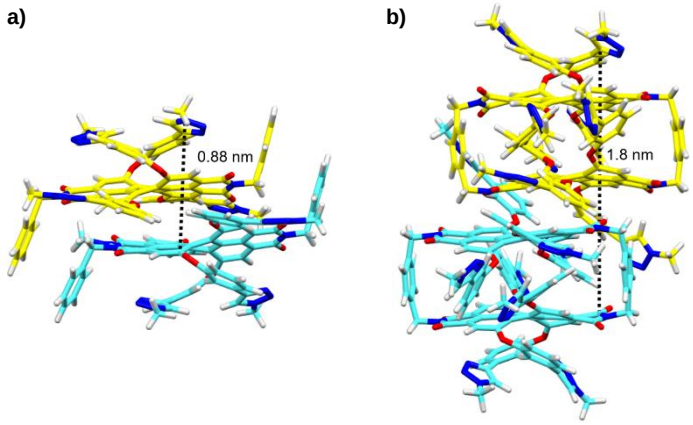

Figure A34. Geometry-optimized structures of the supramolecular dimers of **(e) ref-PBI-1m** and **(f) [2PBI]-1m**. The distance measurements between the PBI core at the bottom and a triazole group over the top-most PBI core should represent the height of the nanoparticles observed in the AFM measurements.

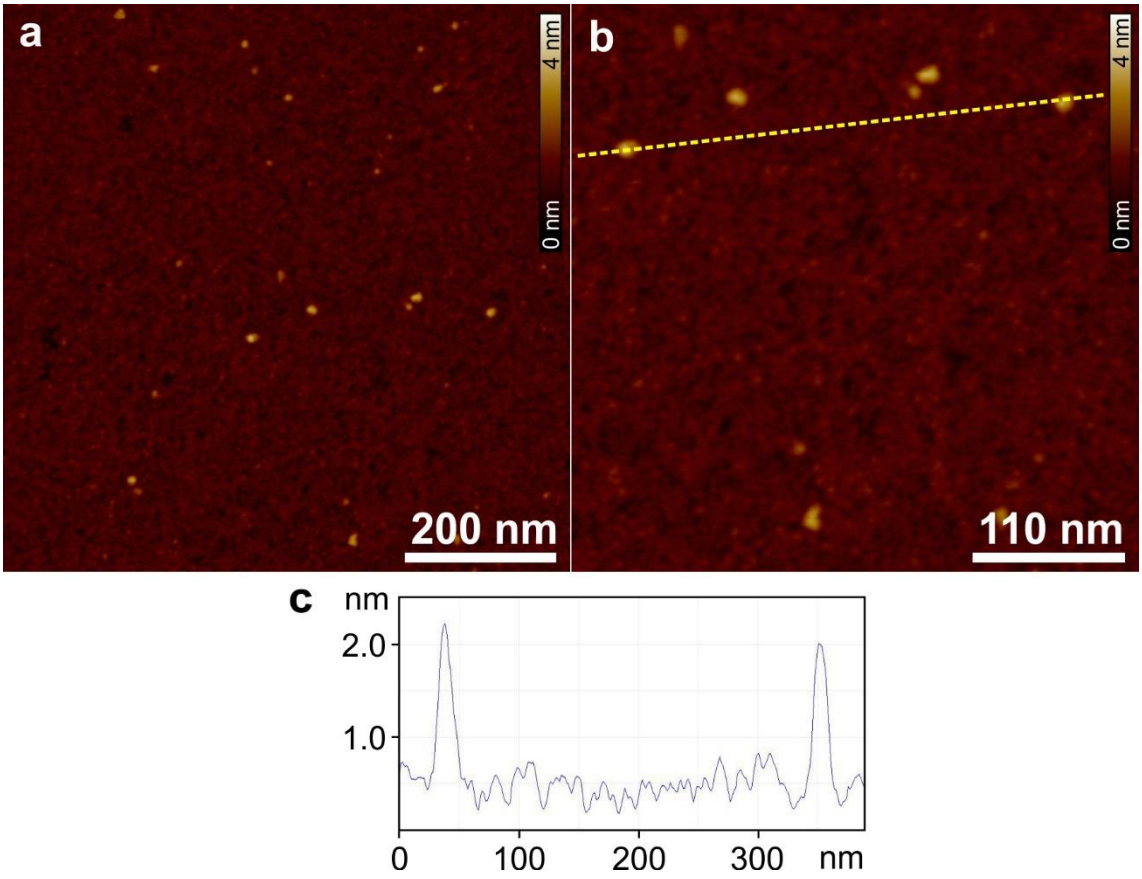

Figure A35. (a – **b)** Height AFM images of a sample prepared by spin-coating of a solution of PBI cyclophane **[2PBI]-1m** in H_2O/acetone (92/8) at $c = 5 \times 10^{-5}$ mol L^{-1} on mica. *Z* scale is 4 nm. **(c)** Cross-section analysis of the yellow dashed line in **(b)**.

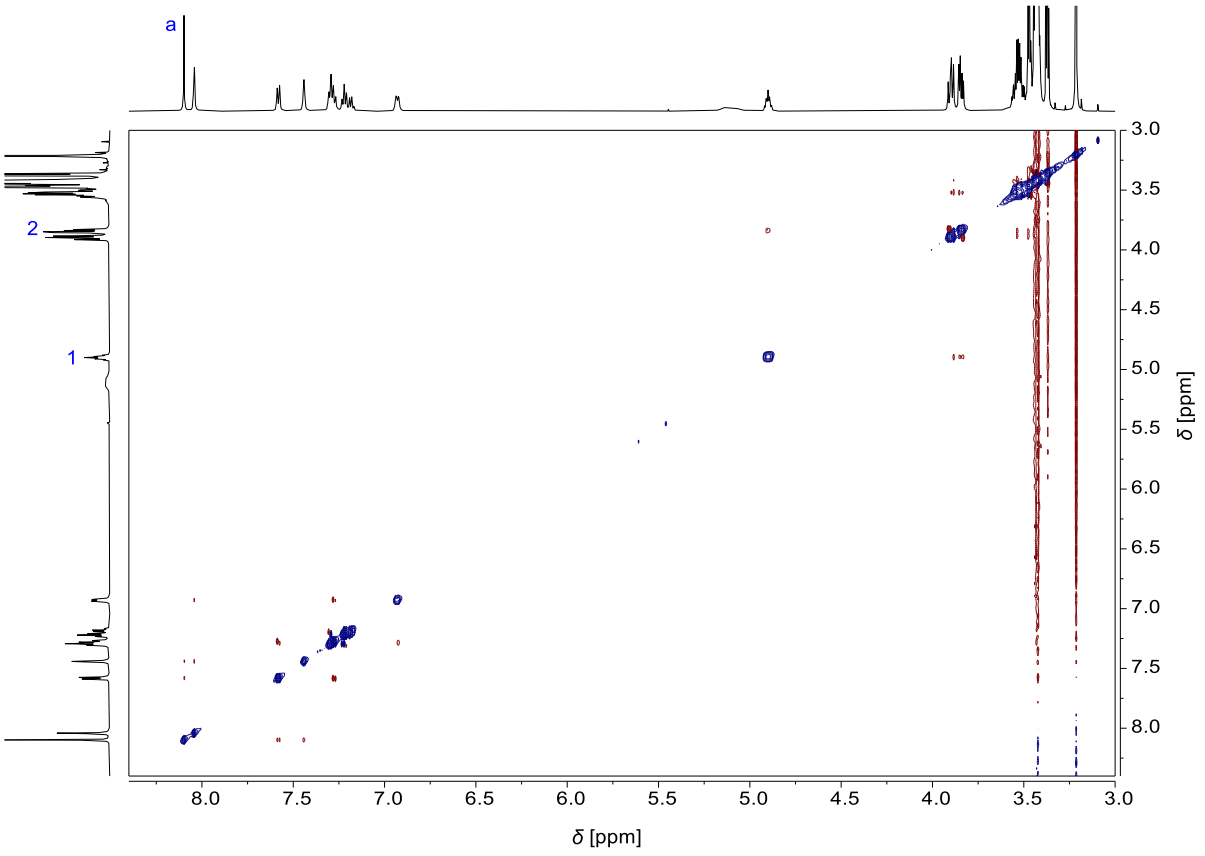

Figure A36. Full ^{1}H, ^{1}H ROESY NMR spectrum (600 MHz, 295 K) of **ref-PBI-1m** in CD_3CN showing the cross signals between the PBI core proton (a) and the protons 1 and 2 of the OEG chain.

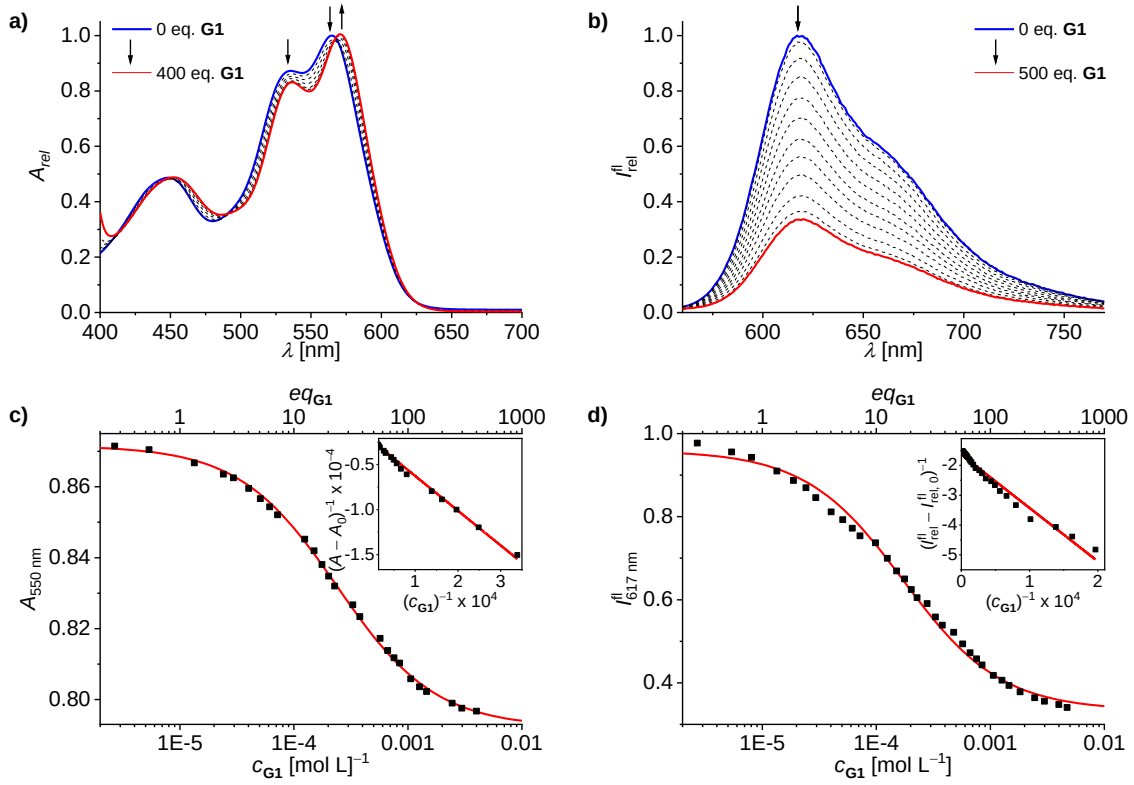

Figure A37. (a) UV-vis and **(b)** fluorescence titration (λ_{ex} = 520 nm) of **[2PBI]-1m** (c_0 = 1 × 10^{-5} mol L^{-1}) with **G1** in H_2O/CH_3CN (1/1 vol%) at 295 K. Arrows indicate changes upon increasing guest concentration. **(c)** Plots of UV-vis (540 nm) and **(d)** fluorescence (620 nm) titration data points as a function of guest concentration and fitting with a 1:1 host guest binding model; insets: Benesi-Hildebrand plots showing a 1:1 stoichiometry of the host-guest complex.

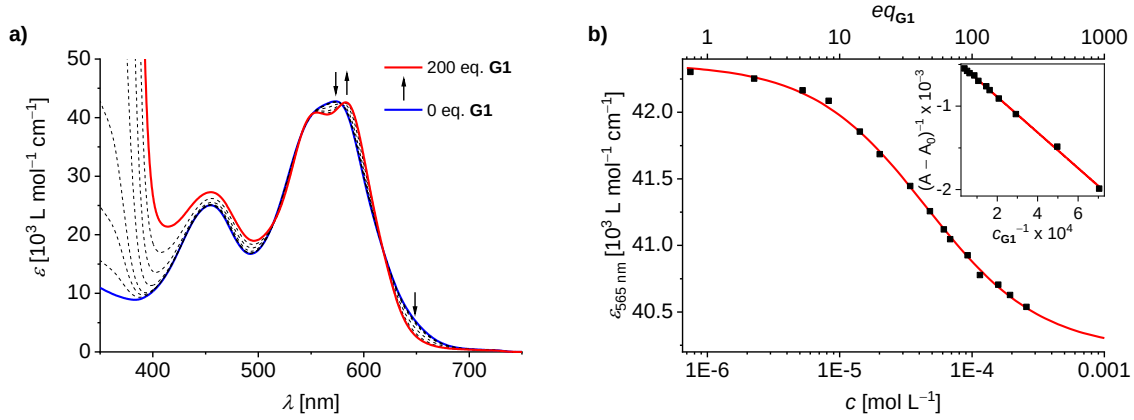

Figure A38. (a) UV-vis titration of **[2PBI]-1m** (c_0 = 1 × 10^{-6} mol L^{-1}) with **G1** in H_2O/acetone (92/8 vol%) at 298 K. Arrows indicate changes upon increasing guest concentration. **(b)** Plot of UV-vis titration data points (565 nm) as a function of guest concentration and fitting with a 1:1 host guest binding model; inset: Benesi-Hildebrand plot showing a 1:1 stoichiometry of the host-guest complex.

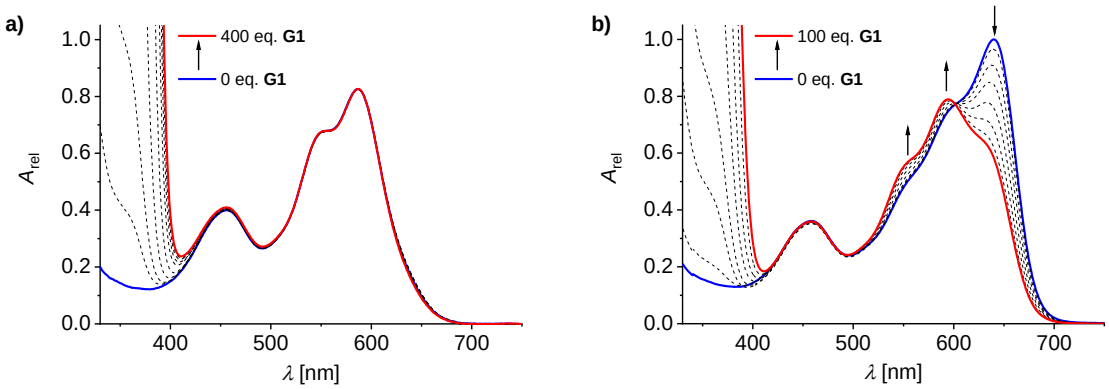

Figure A39. UV-vis spectrum of **ref-PBI-1m** at (a) $c_0 = 1 \times 10^{-6}$ mol L^{-1} and (b) $c_0 = 1 \times 10^{-3}$ mol L^{-1} in H_2O/acetone (97/3 vol%) upon addition of **G1** at 298 K.

3.4 Guest-Mediated Chirality Transfer in Host-Guest Complexes of an Atropisomeric Perylene Bisimide Cyclophane Host

Abstract.[11] The dynamic equilibrium of stereoisomers of a cyclophane, which is comprised of two atropisomeric perylene bisimide (PBI) subunits, and its host-guest binding with an achiral and a series of chiral guests have been studied. Temperature-dependent ^{1}H NMR spectroscopic studies have shown that at higher temperature all three stereoisomers ((*M*,*M*) and (*P*,*P*) enantiomers and mesomer (*M*,*P*)/(*P*,*M*)) of the cyclophane are in a dynamic equilibrium as only one set of proton signals was observed. However, at a lower temperature (260 K) two sets of signals in a ratio of 2:1, instead of the theoretically expected 1:1 ratio, were observed for the diastereomers (*M*,*M*)/(*P*,*P*) and (*M*,*P*)/(*P*,*M*) of the cyclophane presumably due to chiral recognition for the enantiomeric (*M*,*M*)/(*P*,*P*) conformers. The ^{1}H NMR studies further revealed that the achiral guest perylene mostly selects the (*M*,*M*)/(*P*,*P*) enantiomeric pair of the host for encapsulation. The induction of chirality in host-guest complexes of the cyclophane with chiral guests has been investigated by circular dichroism (CD) spectroscopy. A distinct CD effect was observed upon addition of chiral guests to the solution of racemic cyclophane host, indicating a pronounced preference of the chiral guests for one of the two homochiral stereoisomers, (*M*,*M*) and (*P*,*P*), for encapsulation. Kinetic studies by time-dependent NMR spectroscopy did not lead to conclusive results to assign the recognition process of chiral guests to either the induced fit or the conformational selection model.

[11] This chapter has been published: M. Sapotta, P. Spenst, C. R. Saha-Möller, F. Würthner, *Org. Chem. Front.* **2019**, *6*, 892–899.

3.4.1 Introduction

For over a century, Emil Fischer's lock-and-key principle has been a plausible and popular concept to describe protein-substrate interactions and to explain their high specificity.[107, 163] During the rapid development of supramolecular chemistry in the last decades,[7a] for which biological processes have always been a guiding inspiration, this seminal principle has been adapted in host-guest chemistry.[62] Even though molecular receptors and their substrates are nowadays known to be more flexible than the proverbial "lock" and "key" and, indeed, are subject to conformational changes upon guest recognition,[102, 116a-h] shape complementarity may still be considered as a basic requirement for substrate binding.[164] In this regard, cyclophanes, for example, which possess a well-defined cavity ideal for the encapsulation of geometrically compatible guests play an eminent role.[14c, 90, 129a, 130, 165] In this context, our group has demonstrated that a cyclophane based on bay-substituted perylene bisimide (PBI) dyes efficiently binds polyaromatic hydrocarbons (PAHs).[30] Interestingly, however, rigid flat PAHs such as pyrene showed a lower affinity (K_a = 1.1 × 10^2 L mol^{-1} in $CHCl_3$) compared to more flexible π-scaffolds such a phenylnaphthalene (K_a = 1.1 × 10^4 L mol^{-1} in $CHCl_3$) which is obviously a consequence of a better structural match of the latter to the core-twisted PBI cyclophane host. In our most recent work, this PBI cyclophane has been further elaborated towards a water-soluble receptor for alkaloids such as harmine or berberine.[150] Another complementary example of a cyclophane host, which is comprised of "blue box" derivatives, has been reported by Stoddart and Siegel *et al*.[166] Here, the flat cavity of this cyclophane does not provide an ideal fit for the bowl-shaped corannulene guest in its ground state but for the planarized transition state of the bowl-to-bowl inversion of corannulene. Thus, the inversion rate of the guest can be accelerated in a way that is reminiscent of the catalytic activity of an enzyme. These recent results suggest that meanwhile available larger cyclophane hosts are highly promising for research beyond the traditional host-guest chemistry. Here we elucidate new phenomena originating from the (*M*)/(*P*)-atropisomerism of bay-substituted PBI subunits of the cyclophane upon interaction with achiral and chiral guests.

The transmission of chiral information is considered as an essential step in the emergence of homochirality in nature[167] and is a key process in total synthesis.[131] The induction and transfer of chirality is also exemplified by supramolecular helical assemblies, where the chiral information stored in the asymmetric building blocks direct the overall helicity of the aggregate.[168] In smaller more defined systems such as host-guest complexes, chirality can also be relayed from the guest to the host.[169] Core-twisted PBIs bearing substituents in the bay

positions are a unique class of dyes which are equipped with inherent conformational chirality.[170] Accordingly, they are suitable recipients of chiral information, for instance, from homochiral side chains to create (*M*)- or (*P*)-handed assemblies.[160, 171] However, to date chirality transfer from homochiral guests to PBI cyclophane receptors has not been reported.

Herein we report for the first time on chirality transfer upon host-guest binding from homochiral guest molecules (*S*)-**G12** − (*S*)-**G14** to a PBI cyclophane host (**[2PBI]-2**), which is comprised of two atropisomeric PBI subunits (Figure 52a). Since each of the PBI subunits can display (*M*) or (*P*) conformation by core twist, this dimeric PBI cyclophane can have three stereoisomers, these are the homochiral enantiomeric pair (*M*,*M*) and (*P*,*P*) and heterochiral mesomer (*M*,*P*)/(*P*,*M*) (Figure 52b). As the equilibrium between the stereoisomers is fast at room temperature, **[2PBI]-2** is racemic. Our studies have shown that this conformational equilibrium can be shifted by addition of guest molecules and that host-guest binding either results in the enrichment of the homochiral enantiomeric pair for achiral guests or in the distinct preference for one specific homochiral enantiomer for chiral guests. The latter leads to circular dichroism (CD) active host-guest complexes by chirality transfer from the guest to the PBI cyclophane.

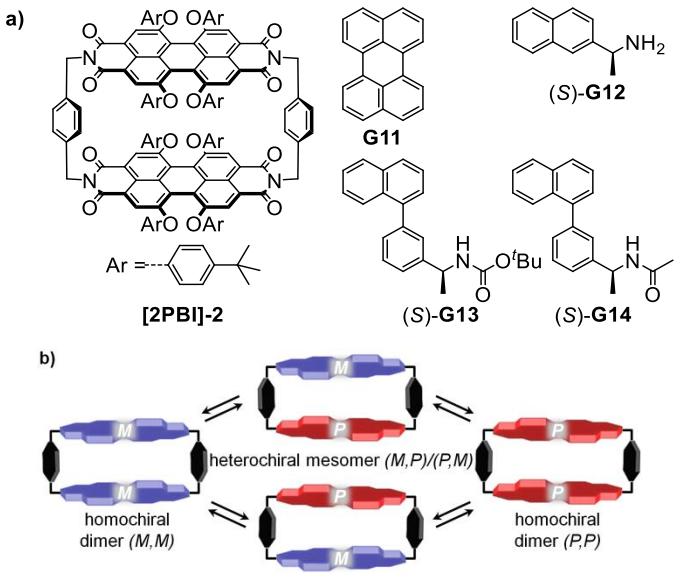

Figure 52. (a) Structures of perylene bisimide cyclophane **[2PBI]-2**, achiral guest perylene (**G11**) and homochiral guests (*S*)-**G12**, (*S*)-**G13** and (*S*)-**G14**. **(b)** Schematic representation of the conformational equilibrium between the (*M*,*M*), (*P*,*M*)/(*M*,*P*) and (*P*,*P*) stereoisomers of **[2PBI]-2**.

3.4.2 Synthesis of Chiral Guests (*S*)-G13 and (*S*)-G14

The atropisomeric cyclophane **[2PBI]-2** was synthesized according to the previously reported procedure.[30a] Chiral guest (*S*)-**G12** was obtained from a commercial source. For the guest

molecules (*S*)-**G13** and (*S*)-**G14,** the amino group of enantiomerically pure (*S*)-1-(3-bromophenyl)ethylamine, which is commercially available, was protected with di-*tert*-butyl dicarbonate or acetic anhydride, respectively, to give the homochiral bromophenyl derivatives **50** and **51** in excellent yields.[172] By subsequent Suzuki coupling[173] with (1-naphthyl)boronic acid, the target guest molecules (*S*)-**G13** and (*S*)-**G14** were obtained in yields of 69% and 56%, respectively (Scheme 3). (*R*)-**G14** was prepared applying the same procedure as for (*S*)-**G14**.

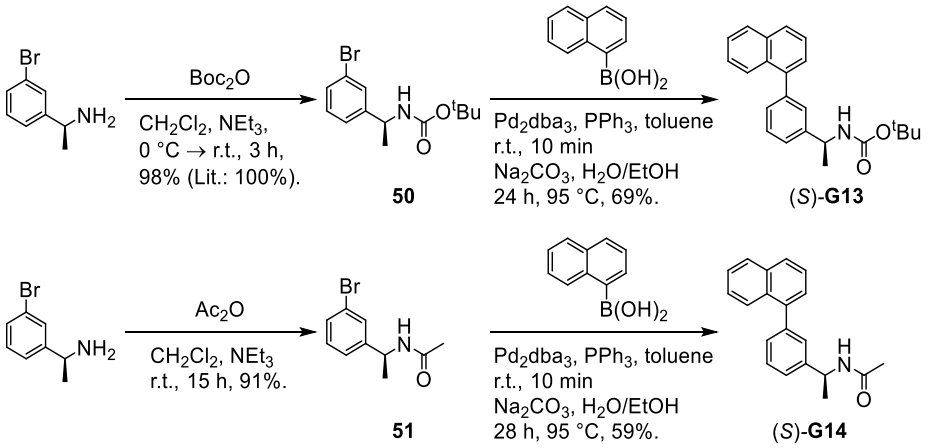

Scheme 3. Synthesis of the chiral guests **(a)** (*S*)-**G13** and **(b)** (*S*)-**G14**.

3.4.3 Temperature-dependent ^{1}H NMR studies of [2PBI]-2[12]

The conformational flexibility of cyclophane **[2PBI]-2** was probed by variable temperature (*T*) ^{1}H NMR spectroscopy from 360 K – 260 K in $C_2D_2Cl_4$ in steps of 10 K (Figure 53).[33] At 360 K, only one set of relatively sharp proton signals was observed. Upon decreasing *T*, the signals broadened and became less intense until a coalescence temperature (T_c) is reached at around 320 K. Upon cooling down further to 260 K, the proton resonances were split into two sets of signals with a ratio of 2:1. Within each set further splitting into two peaks occurs as the protons are no longer chemically equivalent in twisted PBI conformation which can be seen best for the protons *b*/*b*′ of the phenoxy substituents and the diastereotopic benzylic CH_2 protons *e*/*e*′ of the linker unit (Fig. 3a). The observed temperature-dependent changes of the ^{1}H NMR spectra can be rationalized based on the conformational equilibrium between the stereoisomers of cyclophane **[2PBI]** (Fig. 1b). At higher temperature (360 K), the dynamic interconversion process is fast when compared to the NMR time scale giving rise to a spectrum which shows

[12] These temperature-dependent ^{1}H NMR studies as well as data analysis and interpretation were performed by Dr. Peter Spenst: P. Spenst, *Xylylene-Bridged Perylene Bisimide Cyclophanes and Macrocycles*, doctoral thesis, Julius-Maximilians-Universität Würzburg, **2016**.

only the mean proton signals for all isomers. At T_c, the proton peaks are hardly visible since the rate of conformational exchange is reduced to values similar to the difference in the peak frequency. Below that temperature, the interconversion between the stereoisomers becomes sufficiently slow so that two separate sets of signals were observed for the diastereomers (*M*,*M*)/(*P*,*P*)-**[2PBI]** and (*M*,*P*)/(*P*,*M*)-**[2PBI]**.[13] Since a differentiation between the enantiomers (*M*,*M*)-**[2PBI]** and (*P*,*P*)-**[2PBI]** by NMR is naturally not possible, the additional signal splitting for each of the diastereomers is apparently caused by the twist in the PBI subunits as the protons are oriented either into the direction of the cavity or away from it and thus experience different shielding effects. Accordingly, in total four sets of signals were observed at lower temperature. Now the question arises why a 2:1 ratio for the diastereomers is observed at 260 K. If there were no transfer of chiral information between the subunits of **[2PBI]**, the signals for the homochiral (*M*,*M*)/(*P*,*P*) and mesomeric (*M*,*P*)/(*P*,*M*) diastereomers should appear in a theoretically expected 1:1 ratio. Instead, a ratio of 2:1 is found, indicating a clear preference for one conformation. Chiral self-recognition of core-twisted PBIs has been reported for the assembly of chiral PBI monomers,[160] and in preorganization of linear bis-PBI intermediates in cyclization into homochiral dimers.[174] Thus, we assume that the homochiral (*M*,*M*)/(*P*,*P*) conformations of **[2PBI]** prevail at lower temperature due to chiral recognition of one PBI subunit in the cyclophane by the other.

For the conformational interconversion of the diastereomers an activation energy $\Delta G^{\ddagger}$ of 68.7 kJ mol^{-1} was calculated according to the equation (19)[175] where R = universal gas constant, N_A = Avogadro constant, h = Planck constant, using the value for the coalescence temperature T_c = 320 K and the difference in frequencies $\Delta\nu$ = 18.1 Hz for the mean shifts of the PBI core proton *a* of the diastereomers at 260 K. This value is slightly higher than the activation energy of ~ 60 kJ mol^{-1} reported for the (*M*) ⇌ (*P*) interconversion of a core *tetra*-phenoxy substituted PBI monomer,[170a, 176] which could be explained by steric restrictions imposed by the cyclophane structure of **[2PBI]**-**2**.

[13] Note that the *meso*-isomers (*M*,*P*) and (*P*,*M*) are achiral and conformationally identical.

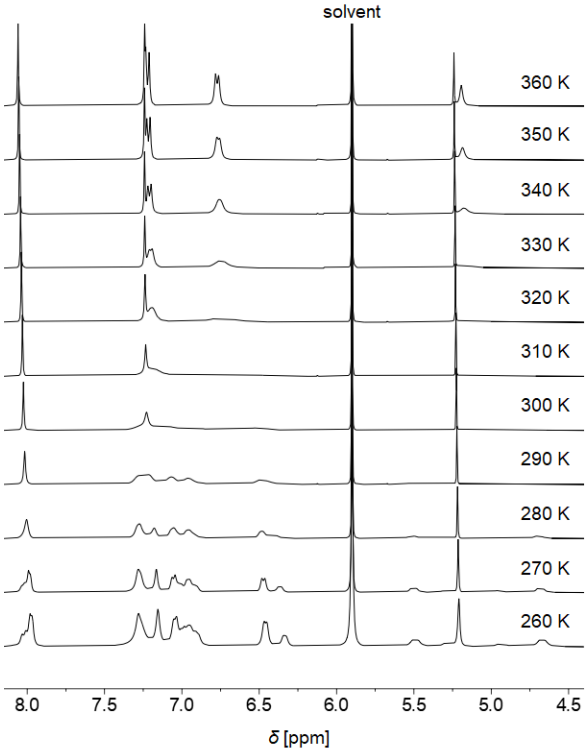

Figure 53. Temperature-dependent ^{1}H NMR spectra ($C_2D_2Cl_4$, 400 MHz) of **[2PBI]-2** (c = 1 × 10^{-4} mol L^{-1}) from 360 K to 260 K. See Figure 54 for signal assignments. The signal at 5.20 ppm originates from CH_2Cl_2.[33]

$$\Delta G^{\ddagger} = RT_c \cdot \ln\left(\frac{RT_c\sqrt{2}}{\pi N_A h \Delta\nu}\right) \tag{19}$$

As there is apparently some chiral recognition between the PBI subunits of free cyclophane **[2PBI]-2** across a fairly large interchromophoric distance of 6.5 Å,[30a] it is reasonable to ask what effect the bridging of this gap by an encapsulated aromatic guest molecule would have on this process. Therefore, we have performed temperature-dependent ^{1}H NMR studies in $C_2D_2Cl_4$ with **[2PBI]-2** in the presence of achiral guest perylene (**G11**) which was reported to bind strongly to **[2PBI]-2** (K_a = 4.6 × 10^4 L mol^{-1} in $CHCl_3$).[30a] For the purpose of comparability, we have determined the binding constant for **G11** in $C_2H_2Cl_4$ by UV-vis and fluorescence titration at 298 K (Figure A43 in Appendix III, Chapter 3.4.7). An average K_a value of 1.2 × 10^5 L mol^{-1} was obtained by fitting the titration data with a 1:1 binding model (for details see Chapter 6.1).

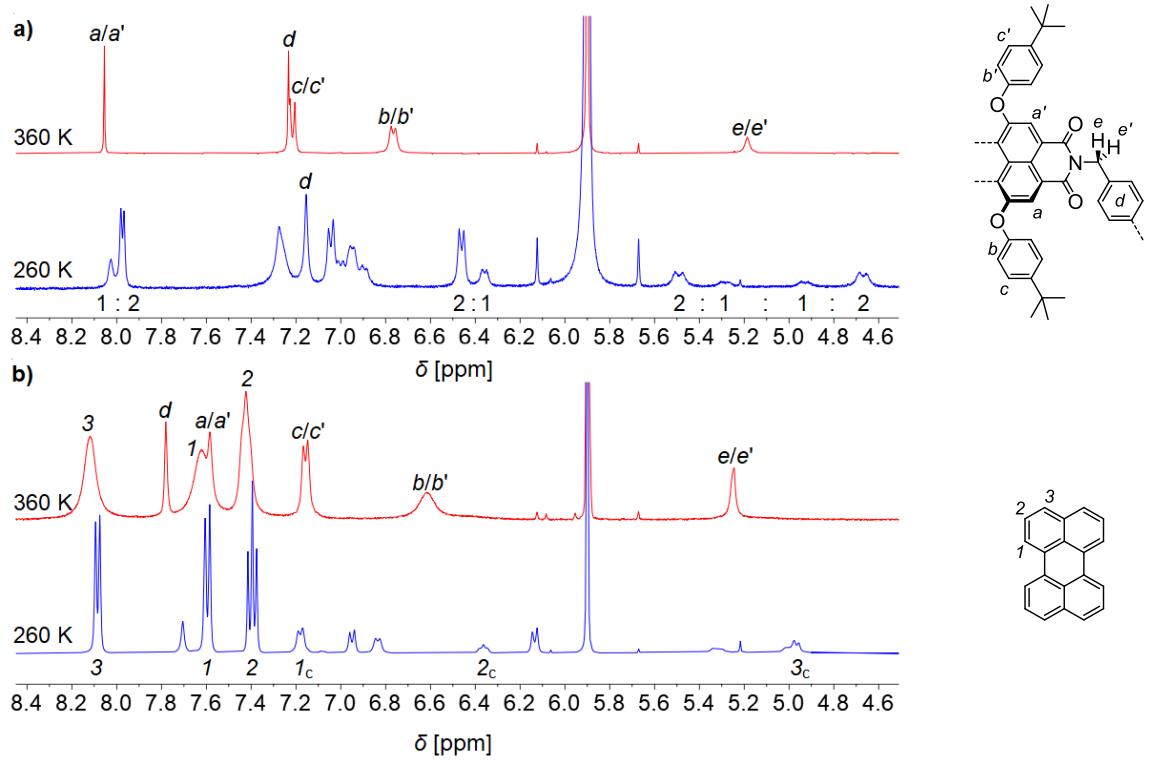

Figure 54. Excerpts of the temperature-dependent ^{1}H NMR spectra (400 MHz, $C_2D_2Cl_4$) of **(a) [2PBI]-2** (c = 1 × 10^{-4} mol L^{-1}) and **(b) [2PBI]-2** (c = 1 × 10^{-4} mol L^{-1}) in the presence of eight equivalents of achiral guest **G11** at 360 K (red spectra) and at 260 K (blue spectra). The signals of encapsulated guest **G11** at 260 K are assigned with 1_c, 2_c and 3_c.[33] For the full temperature range (360 K – 260 K) spectra in the presence of guest see Figure A40 in the Appendix.

Our temperature-dependent ^{1}H NMR studies in the presence of eight equivalents (eq.) of **G11** revealed only one set of signals for **[2PBI]-2** at 360 K like in the case of the pure host (Figure 54 and Figure A40). Both the signals of **G11** and of **[2PBI]-2** are broadened, suggesting a fast guest in-out exchange at this elevated temperature. Upon cooling down to 260 K, a sharpening of the protons of **G11** was observed since the guest in-out exchange slows down with decreasing temperature so that encapsulated guest molecules become distinguishable from the free ones in solution. Signal integration revealed the presence of a 1:1 host-guest complex. Due to chemical shielding by the cavity of **[2PBI]-2**, the signals of encapsulated **G11** experience a strong upfield shift of roughly 0.4 ppm for proton 1_c and 1 ppm for proton 2_c, respectively, and more than 3 ppm for proton 3_c. Moreover, each single signal of **[2PBI]-2** at 360 K splits in two signals when cooled down to 260 K as can be seen best for protons *b*/*b*′, *c*/*c*′ or *e*/*e*′ (Figure 54b). When compared to the pattern of signals observed for free **[2PBI]-2** at this temperature (Figure 54a), this indicates that the equilibrium between the stereoisomers of **[2PBI]-2** is shifted to one conformation of the host, either (*M*,*M*)/(*P*,*P*) or (*M*,*P*)/(*P*,*M*), which provides a better fit for **G11**. Due to geometrical restrictions imposed by the planar and rigid aromatic scaffold of **G11**, we assume that the homochiral (*M*,*M*)/(*P*,*P*) enantiomeric pair of host **[2PBI]-2** is favored.

Since **G11** is achiral, the racemic host-guest complexes **G11⊂**(*M*,*M*)-**[2PBI]-2** and **G11⊂**(*P*,*P*)-**[2PBI]-2** cannot be differentiated by NMR. Thus, the splitting of the signals of cyclophane **[2PBI]-2** in two sets at 260 K is again due to different shielding/deshielding effects of the cyclophane protons by the host cavity (*vide supra*).

3.4.4 Host-Guest Binding Studies of [2PBI]-2 with Chiral Guests

Since perylene is achiral, encapsulation of this guest by **[2PBI]-2** leads to a racemic mixture of the enantiomeric host-guest complexes **G11⊂**(*M*,*M*)-**[2PBI]-2** and **G11⊂**(*P*,*P*)-**[2PBI]-2**. Chiral guests, on the other hand, may differentiate between (*M*,*M*)-**[2PBI]-2** and (*P*,*P*)-**[2PBI]-2** for encapsulation. Thus, enantiomerically enriched host-guest complexes might be formed where chirality is transferred from the homochiral guest to the host.[169a] Therefore, we have investigated the binding behavior of **[2PBI]-2** towards the chiral guests (*S*)-**G12**,[14] (*S*)-**G13** and (*S*)-**G14** (for structures see Figure 52). First, UV-vis and fluorescence titration experiments were performed in $CHCl_3$ to estimate the binding constants (Figure 55 and Figure A44 − Figure A46). The homochiral naphthylethylamine (*S*)-**G12** showed only a weak binding strength of K_a = 15.1 L mol^{-1}, which is attributed to its small aromatic surface and steric hindrance imposed by the adjacent chiral group.[33] For (*S*)-**G13** and (*S*)-**G14** with a larger and flexible phenyl-naphthyl scaffold, more than ten times higher association constants of 167 L mol^{-1}and 247 L mol^{-1} were observed, respectively (Table 3).

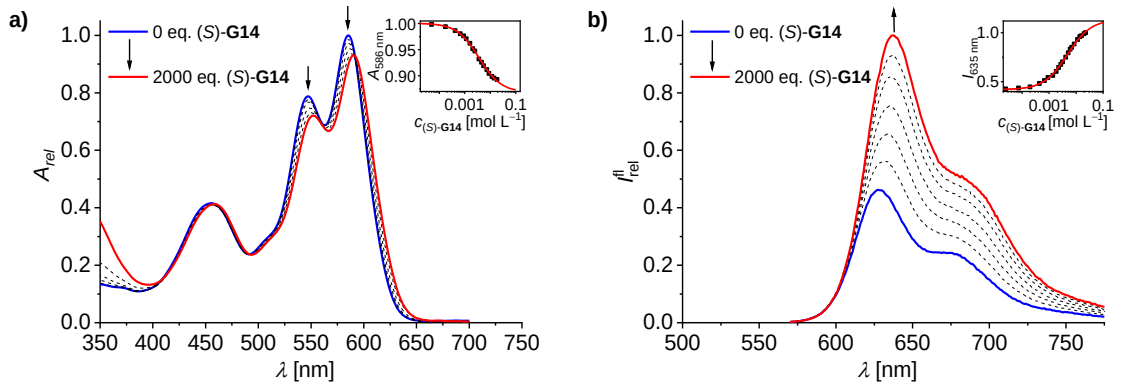

Figure 55. (a) UV-vis and **(b)** fluorescence titration (λ_{ex} = 530 nm) of **[2PBI]-2** ($c_0 = 1 \times 10^{-5}$ mol L^{-1}) with (*S*)-**G14** in $CHCl_3$ at 298 K. Insets: Plots of UV-vis (586 nm) and fluorescence (635 nm) titration data points as a function of guest concentration and fitting with a 1:1 binding model (for details see Experimental Section).

[14] The host-guest titration experiments of **[2PBI]-2** with (*S*)-**G12** as well as data analysis and interpretation were performed by Dr. Peter Spenst: P. Spenst, *Xylylene-Bridged Perylene Bisimide Cyclophanes and Macrocycles*, doctoral thesis, Julius-Maximilians-Universität Würzburg, **2016**.

Subsequently, CD spectroscopic studies were performed to explore the possible chirality induction by (*S*)-**G12** – (*S*)-**G14**. Indeed, upon addition of the chiral guests to a solution of **[2PBI]-2** in $CHCl_3$ at room temperature, the emergence of a CD signal for each of these guests was observed in the region of the optical transitions of the PBI cyclophane (Figure 56). As free **[2PBI]-2** is racemic, it does not display any CD activity. The host-guest complexes of **[2PBI]-2** with homochiral guests (*S*)-**G12** – (*S*)-**G14** show a small bisignate Cotton effect at higher wavelengths with a negative sign for the first couplet with zero crossings at around 600 nm and a positive CD signal for the S_0–S_1 transitions (480 – 600 nm) of the PBI chromophore. The latter results from the induced chirality to **[2PBI]-2** by the chiral guests rather than from excitonic coupling.[177] By comparison of the CD spectra of the host-guest complexes with those of literature-reported chiral PBI monomers[170a, 177] and homochiral dimers of conformationally fixed PBIs,[160] it can be assumed that chiral guests (*S*)-**G12** – (*S*)-**G14** prefer the (*P*,*P*) enantiomer of **[2PBI]-2**. The bisignate Cotton effect at higher wavelengths could originate from chiral exciton coupling due to a minor helical displacement of the chromophores.[178] Its negative sign is indicative of the left-handed helicity of the assumed supramolecular complex (*S*)-**G**⊂(*P*,*P*)-**[2PBI]-2**.[179]

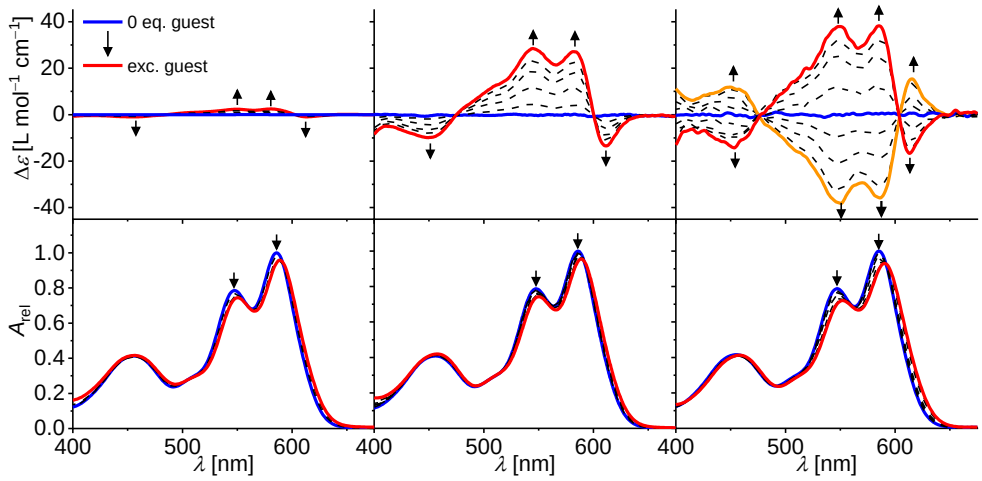

Figure 56. CD (top) and UV-vis titration (bottom) of **[2PBI]-2** ($c_0 = 5 \times 10^{-5}$ mol L^{-1}) with (left) (*S*)-**G12**[33] (excess (exc.) = 2×10^4 equivalents (eq.)), (middle) (*S*)-**G13** (exc. = 1×10^3 eq.), and (right) (*S*)-**G14** (red curve) and (*R*)-**G14** (orange curve) (exc. = 2×10^3 eq.) in $CHCl_3$ at 298 K. The arrows indicate changes upon increasing guest concentration.

For (*S*)-**G12** the extent of chirality induction is almost negligible with $\Delta\varepsilon$ = + 2 L mol^{-1} cm^{-1} at 580 nm, while an almost 15-fold signal increase was found for (*S*)-**G13** with $\Delta\varepsilon$ = + 27 L mol^{-1} cm^{-1} (581 nm) and (*S*)-**G14** conferred the strongest CD effect with $\Delta\varepsilon$ = + 38 L mol^{-1} cm^{-1} (585 nm). Interestingly, the increasing CD effect in the order of (*S*)-**G12** < (*S*)-**G13** < (*S*)-**G14** nicely correlates with the binding constant of these guests with **[2PBI]-2**

(Table 3). Thus, the distinctly stronger CD effect for (*S*)-**G14** can be ascribed to the higher host-guest complex stability and, to a certain extent, to the enhanced stereodifferentiation of (*S*)-**G14** when compared to (*S*)-**G12**.

Table 3. Comparison of the binding constants K_a and the CD effects of the chiral guests (*S*)-**G12** − (*S*)-**G14** towards host **[2PBI]-2** in $CHCl_3$ at 298 K.

guest	K_a^{UV} (L mol^{-1})	K_a^{fl} (L mol^{-1})	Ø K_a[a] (L mol^{-1})	$\Delta\varepsilon$ (L mol^{-1} cm^{-1})	g[b]
(*S*)-**G12**	14.7	15.4	15.1	+ 2 (580 nm)	+ 4.3 × 10^{-5}
(*S*)-**G13**	139	194	167	+ 27 (581 nm)	+ 3.7 × 10^{-4}
(*S*)-**G14**	285	208	247	+ 38 (585 nm)	+ 6.1 × 10^{-4}
(*R*)-**G14**	344	267	306	− 36 (585 nm)	− 5.7 × 10^{-4}

[a] Average from UV-vis and fluorescence titration experiments. [b] Dissymmetry factor $g = \Delta\varepsilon/\varepsilon$.

The stereodifferentiation of **[2PBI]-2** by (*R*)-enantiomers of the guest molecules should have the reversed CD effect in reference to the (*S*)-enantiomers. To verify this, CD titration experiments were conducted with (*R*)-**G14** as a representative example since its (*S*)-enantiomer showed the strongest CD effect. Indeed, mirror image CD spectra compared to those of (*S*)-**G14** were observed for (*R*)-**G14** implying that (*R*)-**G14** binds to the opposite enantiomer of **[2PBI]-2**. The observed $\Delta\varepsilon$ values for **G14**, even though it displayed the most pronounced CD effect among the investigated guest molecules, are slightly smaller than those of previously reported homochiral π-stacked dimers of conformationally fixed PBIs.[160] This might suggest that the encapsulation of **G14** can significantly, yet not fully, shift the equilibrium between (*M*,*M*)-**[2PBI]-2** and (*P*,*P*)-**[2PBI]-2**. However, it has to be taken into account that the amplitude of the bisignate CD spectrum of chromophores decreases with increasing interchromophoric distance and when the angle between the transition dipole moments of the chromophores approaches 0° or 180°.[179] Therefore, the lower $\Delta\varepsilon$ value of the host-complexes of chiral (*S*)-**G14** ($\Delta\varepsilon$ = + 38 L mol^{-1} cm^{-1}) and (*R*)-**G14** with the homochiral conformer of **[2PBI]-2** when compared to π-stacked dimers of conformationally fixed homochiral PBI monomers ($\Delta\varepsilon \approx$ + 55 L mol^{-1} cm^{-1})[180] could be ascribed to the geometrical features of cyclophane **[2PBI]-2**.

3.4.5 Kinetic Studies

For recognition processes in biological systems such as protein-ligand binding two different mechanistic models, namely induced fit (or Koshland-Némethy-Filmer model)[181] and

conformational selection (or Monod-Wyman-Changeux model),[34a] are discussed in literature.[111b, 114a, 182] Although there are a few reports on conformational changes of synthetic supramolecular receptors upon guest binding and for some of these systems induced fit has been implied,[102, 116a, 116d, 116e] only very recently the first detailed mechanistic investigation has been reported for host-guest encapsulation of a conformationally flexible metallo-supramolecular host for which a conformational selection was confirmed by kinetic studies.[116f] The host-guest binding process of **[2PBI]-2** with chiral guests (*S*)-**G12** – **G14** can in principle also follow one of these mechanistic models (Figure 57). According to the induced fit mechanism the guest would bind to any of the stereoisomers of **[2PBI]-2** ((*M*,*M*), (*P*,*P*) or (*M*,*P*)/(*P*,*M*)) and consecutively induce structural rearrangements in the cyclophane until the conformation is adopted which fits best to the chiral guest. On the other hand, for the conformational selection mechanism the guest would select the most compatible stereoisomer of **[2PBI]-2** out of the isomerization equilibrium for binding and thus shift the whole equilibrium. Hence, the difference between the two mechanisms is the order in which guest binding and host isomerization take place. A differentiation between these two mechanistic models is possible based on the rate constant k_{obs} with which the system approaches the equilibrium between free **[2PBI]-2**, unbound guest and the complex after the addition of the guest. When k_{obs} decreases with increasing guest concentration, the system follows the conformational selection model.[112, 116f] On the other hand, induced fit can be assumed when k_{obs} increases as a function of guest concentration but only under rapid equilibrium approximation, i. e. the isomerization of **[2PBI]-2** is the rate limiting step.[112] If in the latter case the rapid equilibrium approximation is not fulfilled, no unequivocal assignment of the mechanism is possible.

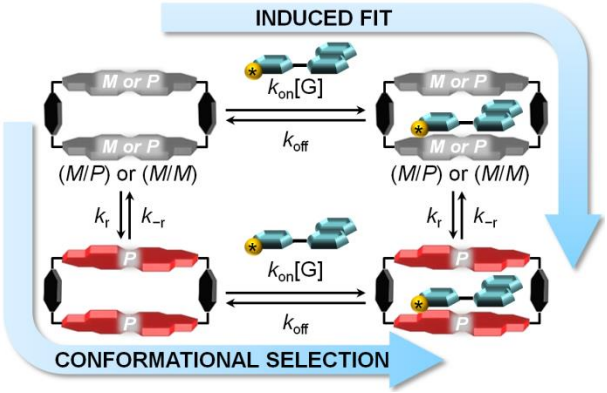

Figure 57. Schematic representation of the induced fit and the conformational selection model for **[2PBI]-2** and chiral guest (*S*)-**G14**.

To approach such mechanistic elucidation, time-dependent ^{1}H NMR measurements with **[2PBI]-2** and the strongest-binding guest (*S*)-**G14** were performed to estimate k_{obs} as a function of guest concentration. As the underlying kinetic processes are extremely fast at room temperature, the measurements were recorded in $CDCl_3$ at 217 K. Prior to the kinetic studies, ^{1}H NMR host-guest titration and ^{1}H-^{1}H ROESY studies were performed (Figure A48 − Figure A49) in $CDCl_3$ for signal assignment.[15] After the addition of (*S*)-**G14** to **[2PBI]-2** new proton signals appeared, besides those of free (*S*)-**G14**, which are attributed to the host-guest complex (*S*)-**G14**⊂(*P*,*P*)- **[2PBI]-2** (Figure A48). The intensity of the signals for the host-guest complex increased with increasing amounts of (*S*)-**G4** while the signals for the protons of free **[2PBI]-2** gradually vanished as the equilibrium is shifted towards the complex. As encapsulation of asymmetric guest (*S*)-**G14** reduces the symmetry of the cyclophane, a strong splitting of the signals of the complex occurs. The two signals for core protons of the free cyclophane at 8.18 ppm (*a*) and 8.02 ppm (*a′*) of the homochiral (*M*,*M*)/(*P*,*P*)-dimer, for example, each split into four separate signals at 8.20, 7.73, 7.24 and 6.85 ppm and at 7.89, 7.84, 7.68 and 7.57 ppm, respectively. Remarkably, all aromatic protons of (*S*)-**G14** experienced shielding to various extents upon complexation. Integration of the resonances for bound **[2PBI]-2** and bound (*S*)-**G14** confirmed the formation of a 1:1 complex.

For the kinetic ^{1}H NMR studies a particular amount (2 eq., 5 eq. or 10 eq.) of (*S*)-**G14** was added to a solution of free **[2PBI]-2** in $CDCl_3$ and the formation of signals corresponding to the host-guest complex was monitored as a function of time until the equilibrium between complex, unbound (*S*)-**G14** and free **[2PBI]-2** has been reached. Throughout this process, the proton peaks of the complex gradually increased while the proton peaks for the free host decreased. For signal integration dimethyl sulphone was added as internal standard. The first ^{1}H NMR spectrum of such a kinetic study, recorded 140 s after addition of 10 eq. of (*S*)-**G14** to a solution of **[2PBI]-2** in $CDCl_3$ at 217 K revealed that the host-guest complex has already been formed in significant amounts even after such a short time (Figure 58a and Figure A50). With progressing time, the concentration of free **[2PBI]-2** decreases as indicated by the reduced integral of the signals at 8.18 ppm (*a*) and 8.02 ppm (*a′*) with respect to the used integration standard dimethyl sulphone. Concomitantly, the concentration of the complex went up as indicated by the increase of the corresponding signals, for example at 8.20 ppm. With these

[15] The ^{1}H, ^{1}H ROESY NMR spectrum for signal assignment was recorded at 250 K. At 217 K, no distinct exchange peaks were observed, presumably because the underlying dynamic process is too slow at this temperature. For temperature-dependent shifts of the spectra, see Figure A42.

signals, the complex concentration was calculated[16] and plotted as a function of time (Figure 58b). This kinetic process is of pseudo first order, therefore the rate constant k_{obs} can be determined by evaluation of the slope of the linear part of a corresponding natural logarithm plot and a value of k_{obs} = 0.006 s^{-1} was obtained (Figure 58c). Similar measurements were performed after addition of 5 and 2 eq. of (*S*)-**G14** (Figure A52 – Figure A55) giving k_{obs} = 0.005 s^{-1} and k_{obs} = 0.003 s^{-1}, respectively. Thus, k_{obs} values are increased with increasing amounts of guest from 2 to 10 eq. for the present system (Figure 58d).

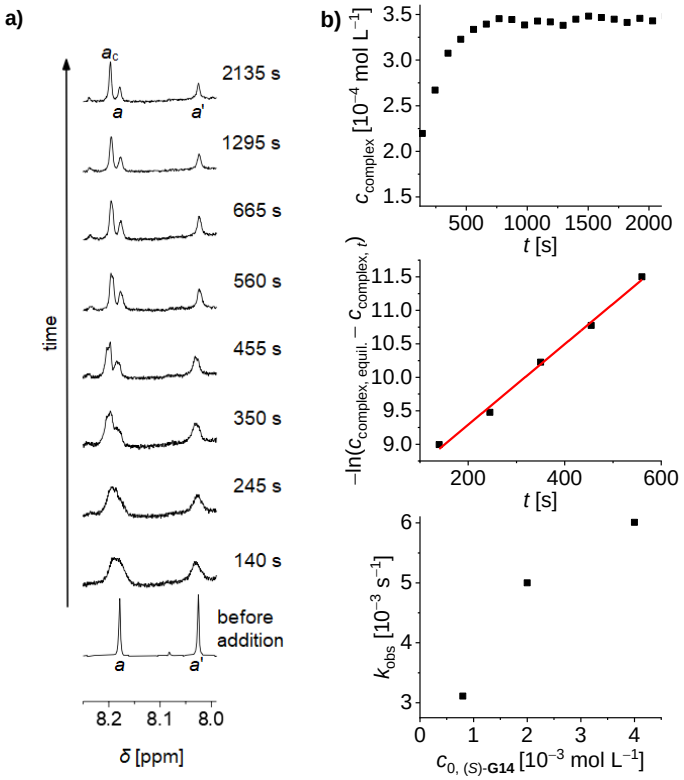

Figure 58. (a) Excerpts of the time-dependent ^{1}H NMR spectra (600 MHz, $CDCl_3$, 217 K, dimethyl sulphone as integration standard) of **[2PBI]-2** ($c_0 = 5 \times 10^{-4}$ mol L^{-1}) showing the development of the signals of PBI core protons *a* and *a′* (free host) and a_c (bound host) after the addition of 10 eq. of (*S*)-**G14**. **(b)** Plot of the complex concentration (*S*)-**G14⊂[2PBI]-2** as a function of time after addition of 10 eq. of (*S*)-**G14**. **(c)** Plot showing the first order kinetics for the approach to the complexation equilibrium as a function of time after addition of 10 eq. of (*S*)-**G14**. **(d)** Dependence of k_{obs} on the initial concentration of (*S*)-**G14**.

For the unequivocal assignment to a mechanistic model, either to induced fit or to conformational selection, the premise of the rapid equilibrium approximation must be fulfilled. Therefore, temperature-dependent ^{1}H NMR experiments in $CDCl_3$ of the free host (Figure A41) and in the presence of 5 eq. of (*S*)-**G14** (Figure A42) were performed to roughly estimate the rate constants of host isomerization k_{iso} and guest in-out exchange k_{ex}. In both experiments, T_c

[16] As the signals at 8.19 (1 proton of bound **[2PBI]**) and 8.18 ppm (4 protons of free **[2PBI]**) overlap significantly, they were integrated as one signal. The integral of the signal at 8.02 ppm (4 protons of free **[2PBI]**) was then substracted.

was observed at 295 K. Using equation (19) and the signal splitting $\Delta\nu$ = 94.5 Hz of the core protons of **[2PBI]-2** in $CDCl_3$ at 217 K the activation energy for the host isomerization was calculated as $\Delta G^{\ddagger}$ = 59.1 kJ mol^{-1}. Accordingly, the activation energy for guest in-out exchange was determined as 57.9 kJ mol^{-1}. For $\Delta\nu$, the difference between the free **[2PBI]-2** core proton at 8.03 ppm and the mean shifts of the corresponding four signals of the complex (7.89, 7.84, 7.68 and 7.57 ppm) as assigned by the ROESY spectrum (Figure A49) were used. With equation (20) the rate constants were determined as k_{iso} = 0.027 s^{-1} and k_{ex} = 0.053 s^{-1}.

$$k = \frac{k_b T}{h} e^{-\frac{\Delta G^{\ddagger}}{RT}} \tag{20}$$

Since k_{ex} is not significantly larger than k_{iso}, the rapid equilibrium approximation (i. e. $k_{iso} << k_{ex}$) is not sufficiently fulfilled by our system and thus no definite mechanistic conclusion can be made at this point. However, since **[2PBI]-2** shows conformational dynamics prior to guest binding, it is reasonable to propose the conformational selection model for the host-guest binding of cyclophane **[2PBI]-2**.

3.4.6 Conclusion

In summary, we could show by temperature-dependent ^{1}H NMR measurements in $C_2D_2Cl_4$ that the cyclic PBI dimer **[2PBI]-2** exhibits a dynamic equilibrium of its (*M*,*M*), (*P*,*P*) and (*M*,*P*)/(*P*,*M*) stereoisomers. Further investigations indicated that achiral guest perylene preferentially selects the enantiomeric pair (*M*,*M*)-**[2PBI]-2** and (*P*,*P*)-**[2PBI]-2** over the mesomer (*M*,*P*)/(*P*,*M*). For the first time, we could show that homochiral guests (*S*)-**G12** − (*S*)-**G14** induce chirality to a PBI cyclophane by host-guest binding. Chiral guests preferentially bind to one conformer of **[2PBI]-2** thus leading to a shift in the conformational equilibrium between the stereoisomers. Kinetic experiments to elucidate the underlying mechanism (conformational selection versus induced fit) for the host-guest binding did not yield unambiguous results as the rapid equilibrium approximation is not fulfilled by our system. However, owing to the conformational dynamics of the host **[2PBI]-2**, we assume that the conformational selection model is more reasonable for the present system.

3.4.7 Appendix III

Temperature-dependent ^{1}H NMR spectra

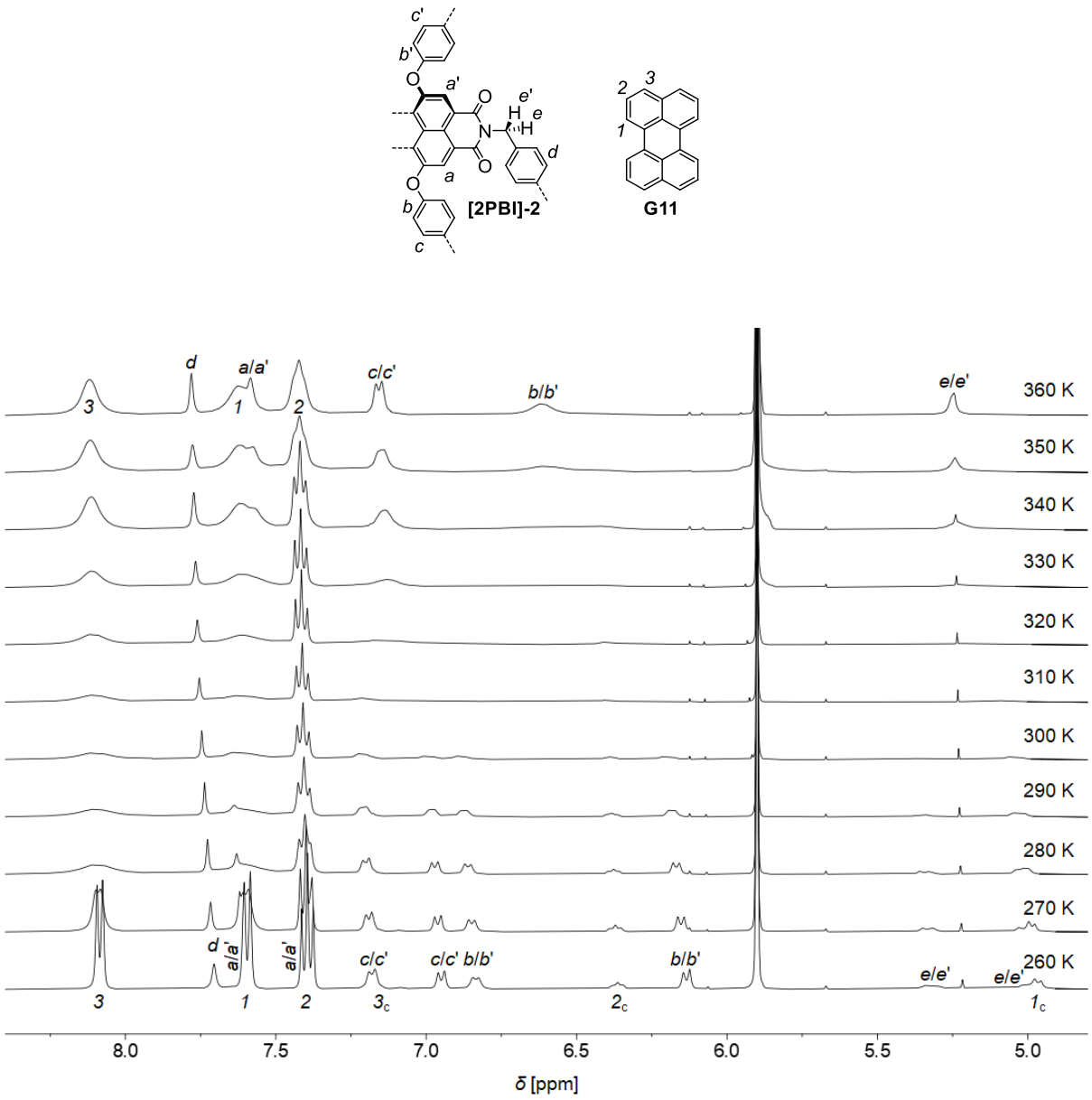

Figure A40. Temperature-dependent ^{1}H NMR spectra ($C_2D_2Cl_4$, 400 MHz) of **[2PBI]-2** (c = 1 × 10^{-4} mol L^{-1}) in the presence of 8 equivalents of **G11** from 360 K to 260 K in steps of 10 K. Signals of the encapsulated guest **G11** are assigned as 1_c, 2_c and 3_c.[33]

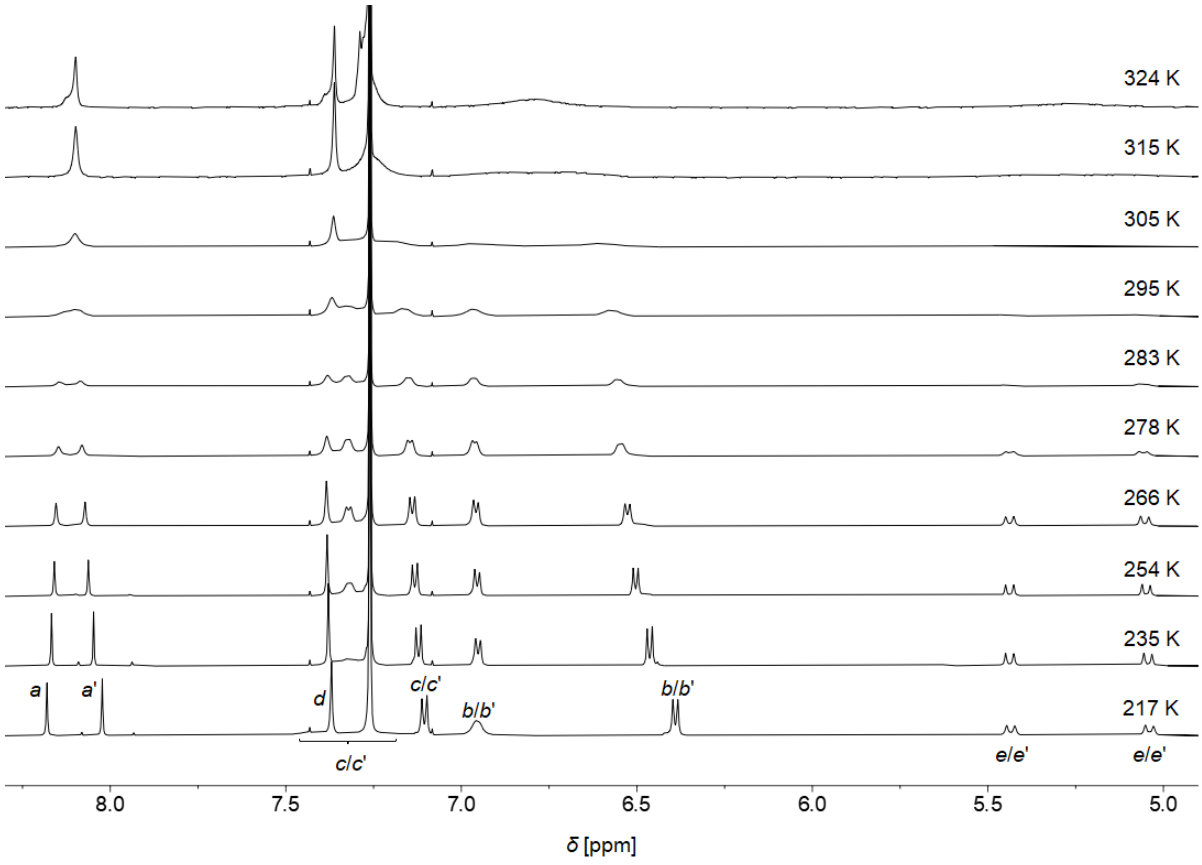

Figure A41. Temperature-dependent ^{1}H NMR spectra ($CDCl_3$, 600 MHz) of **[2PBI]-2** ($c = 5 \times 10^{-4}$ mol L^{-1}) from 324 K to 217 K.

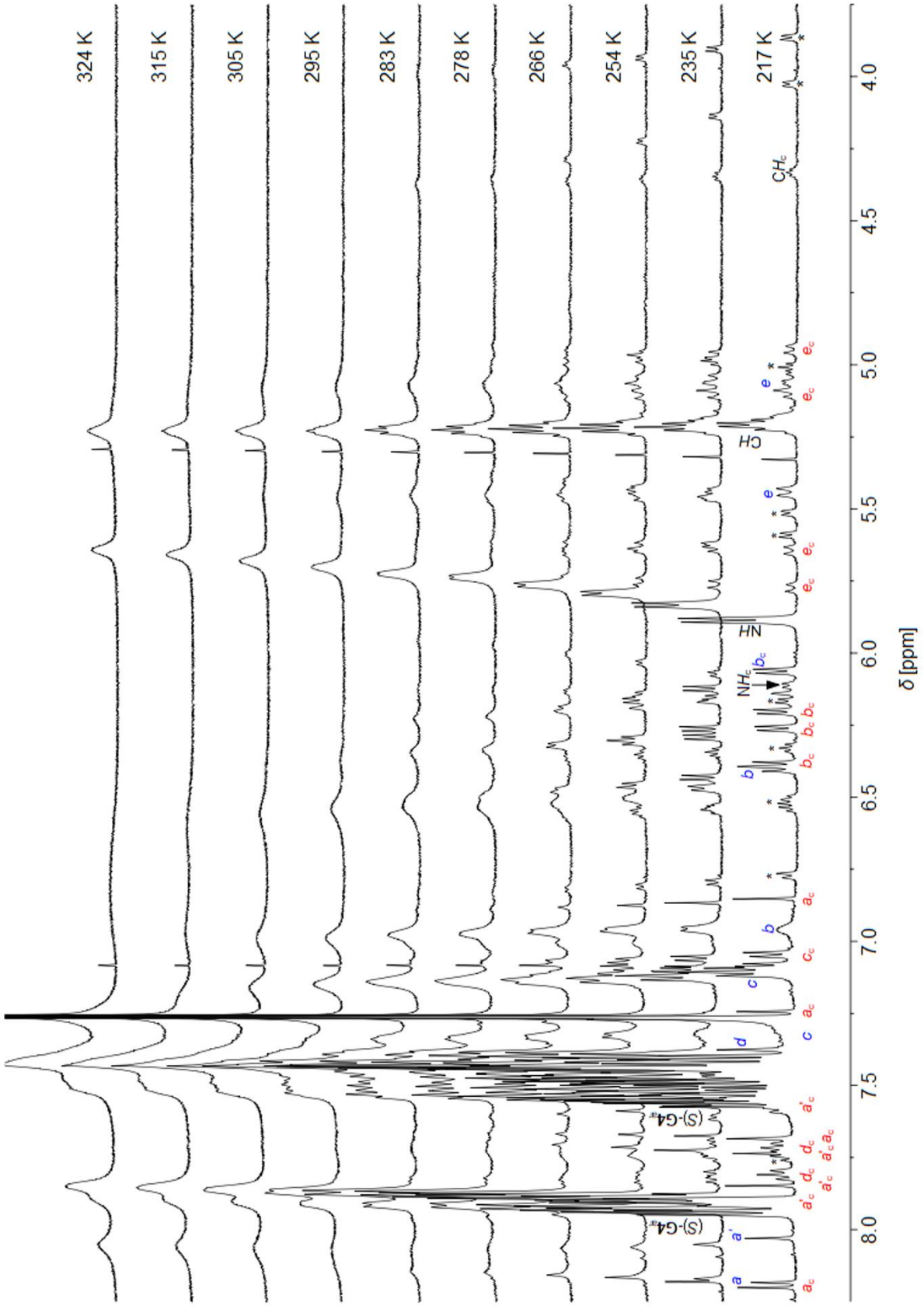

Figure A42. Excerpt of the temperature-dependent ^{1}H NMR spectra ($CDCl_3$, 600 MHz) of **[2PBI]-2** ($c = 5 \times 10^{-4}$ mol L^{-1}) in the presence of 5 eq. of (*S*)-**G14** from 324 K to 217 K. Signals of the host in the host-guest complex (*S*)-**G14⊂[2PBI]-2** are assigned with $a_c - e_c$. Peaks assigned with a * correspond to aromatic signals of bound (*S*)-**G14**.

Host-guest titration experiments

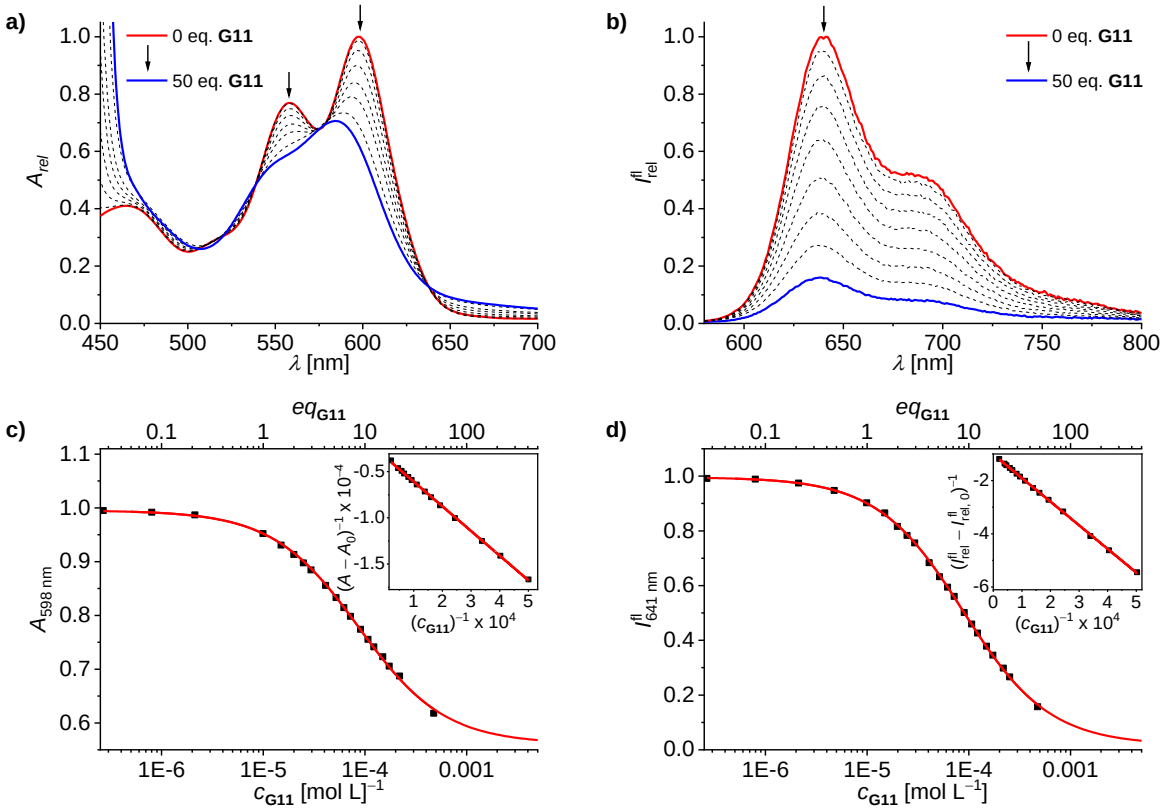

Figure A43. (a) UV-vis and **(b)** fluorescence titration (λ_{ex} = 530 nm) of **[2PBI]-2** ($c_0 = 1 \times 10^{-5}$ mol L^{-1}) with **G11** in $C_2H_2Cl_4$ at 298 K. **(c)** Plots of UV-vis (598 nm) and **(d)** fluorescence (641 nm) titration data points as a function of guest concentration and fitting with a 1:1 binding model; insets: Benesi-Hildebrand plots showing a 1:1 stoichiometry of the host-guest complex.

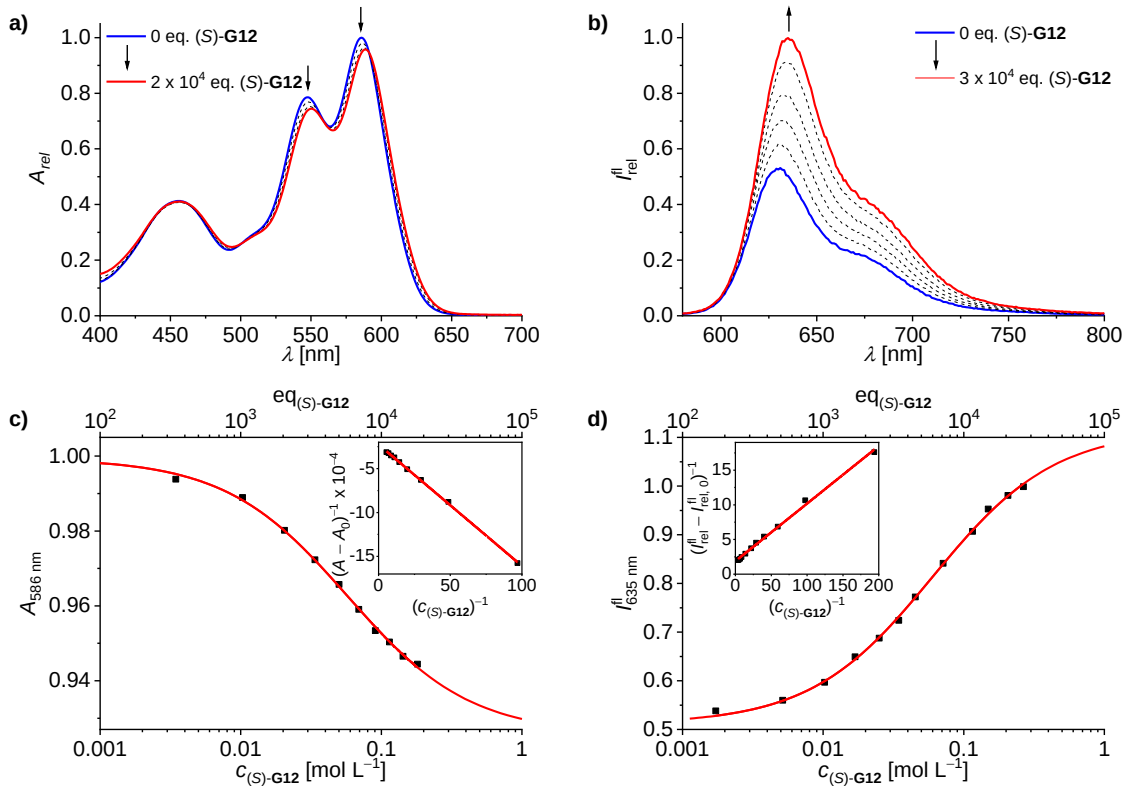

Figure A44. (a) UV-vis and **(b)** fluorescence titration (λ_{ex} = 530 nm) of **[2PBI]-2** ($c_0 = 1 \times 10^{-5}$ mol L^{-1}) with (*S*)-**G12** in $CHCl_3$ at 298 K. **(c)** Plots of UV-vis (586 nm) and **(d)** fluorescence (635 nm) titration data points as a function of guest concentration and fitting with a 1:1 binding model; insets: Benesi-Hildebrand plots showing a 1:1 stoichiometry of the host-guest complex.[33]

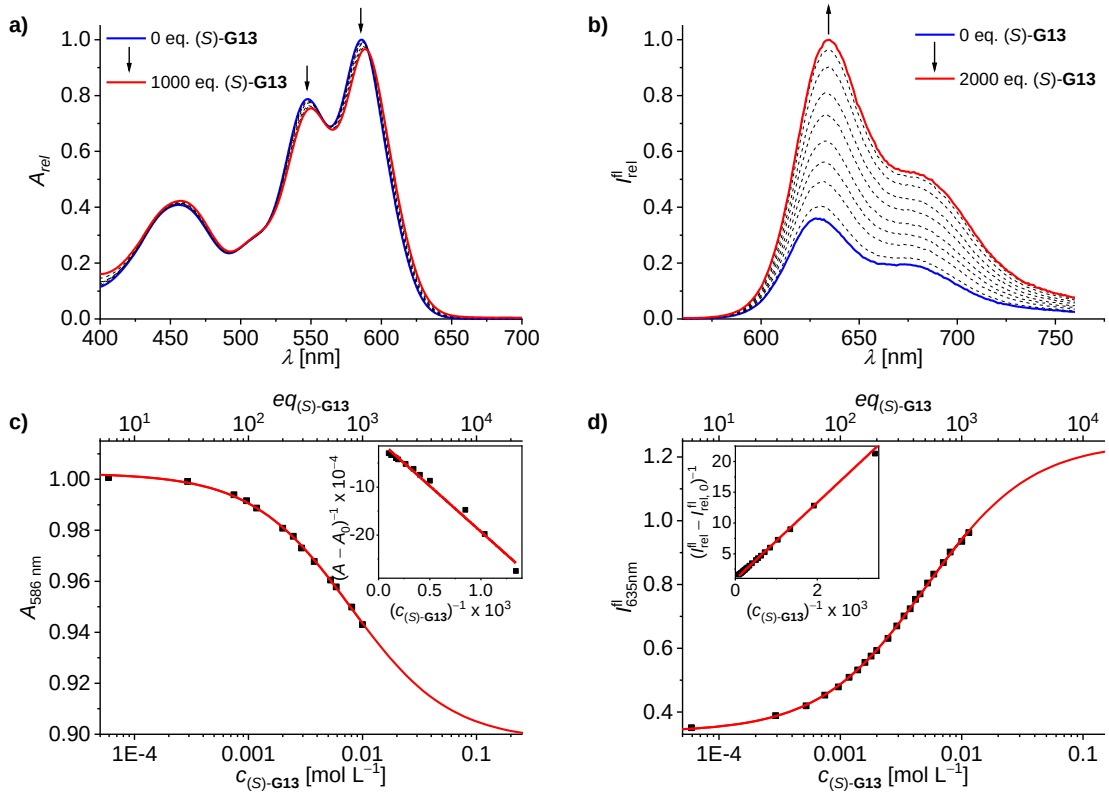

Figure A45. (a) UV-vis and **(b)** fluorescence titration (λ_{ex} = 530 nm) of **[2PBI]-2** ($c_0 = 1 \times 10^{-5}$ mol L^{-1}) with (*S*)-**G13** in $CHCl_3$ at 298 K. **(c)** Plots of UV-vis (586 nm) and **(d)** fluorescence (635 nm) titration data points as a function of guest concentration and fitting with a 1:1 binding model; insets: Benesi-Hildebrand plots showing a 1:1 stoichiometry of the host-guest complex.

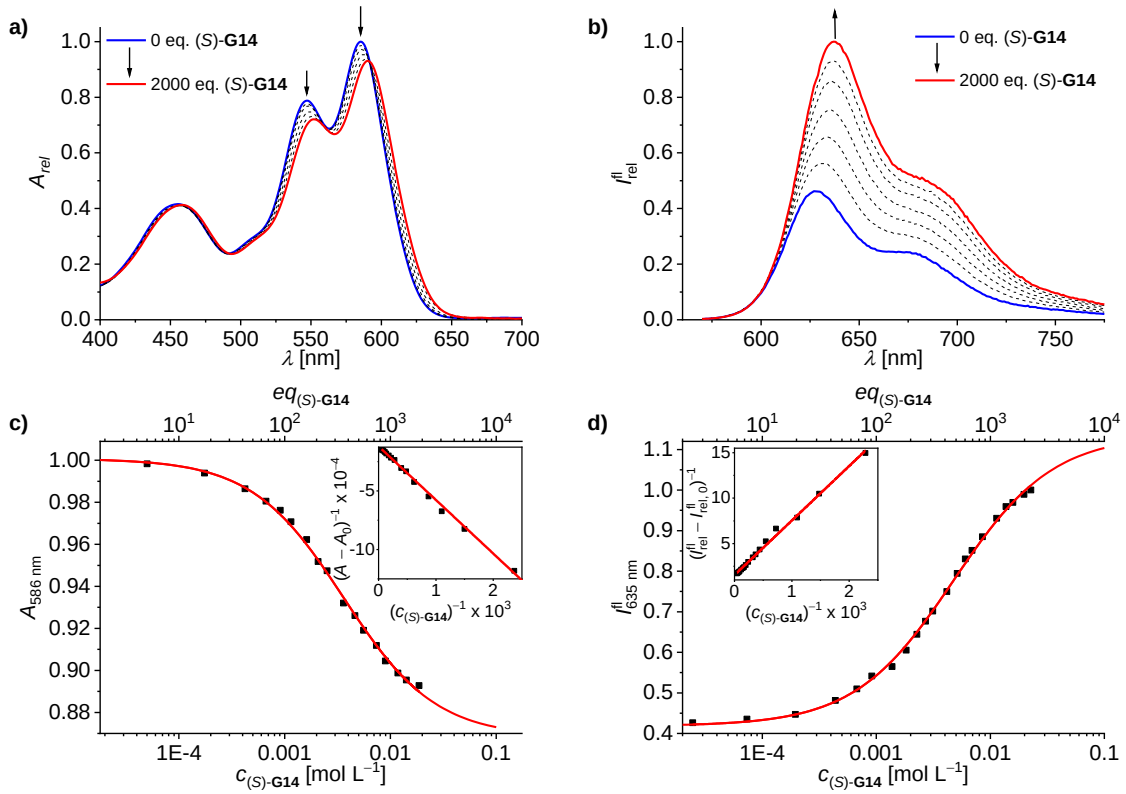

Figure A46. (a) UV-vis and **(b)** fluorescence titration (λ_{ex} = 530 nm) of **[2PBI]-2** (c_0 = 1 × 10^{-5} mol L^{-1}) with (*S*)-**G14** in $CHCl_3$ at 298 K. **(c)** Plots of UV-vis (586 nm) and **(d)** fluorescence (635 nm) titration data points as a function of guest concentration and fitting with a 1:1 binding model; insets: Benesi-Hildebrand plots showing a 1:1 stoichiometry of the host-guest complex.

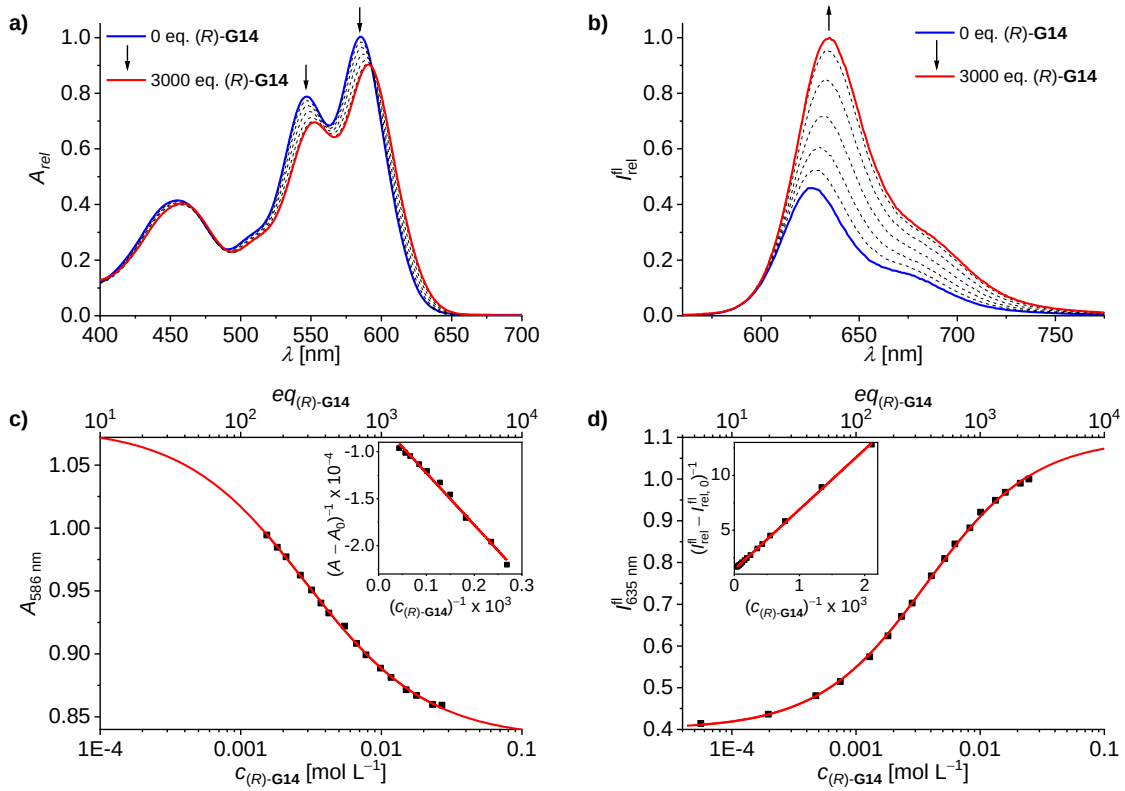

Figure A47. (a) UV-vis and **(b)** fluorescence titration (λ_{ex} = 530 nm) of **[2PBI]-2]** (c_0 = 1 × 10^{-5} mol L^{-1}) with (*R*)-**G14** in $CHCl_3$ at 298 K. **(c)** Plots of UV-vis (586 nm) and **(d)** fluorescence (635 nm) titration data points as a function of guest concentration and fitting with a 1:1 binding model; insets: Benesi-Hildebrand plots showing a 1:1 stoichiometry of the host-guest complex.

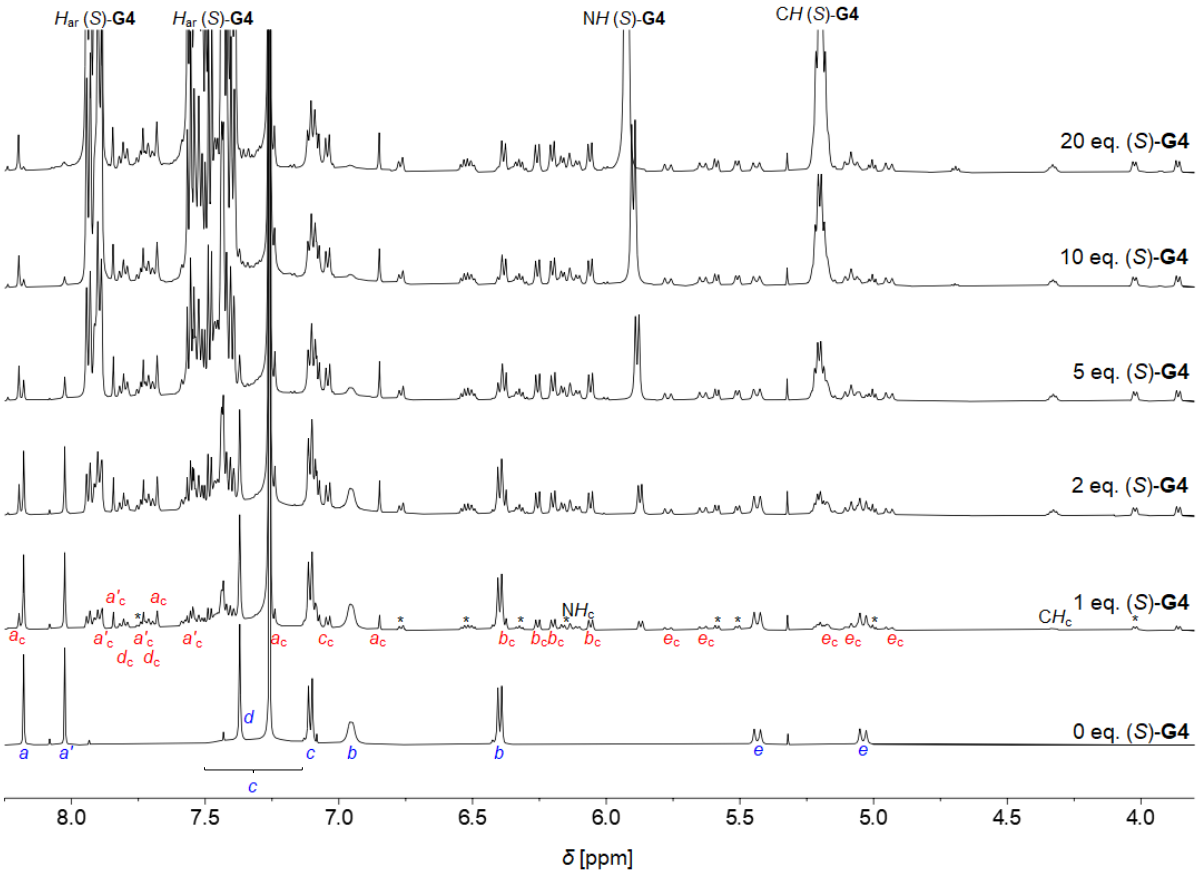

Figure A48. ^{1}H NMR titration ($CDCl_3$, 600 MHz, 217 K,) of **[2PBI]-2** ($c_0 = 5 \times 10^{-4}$ mol L^{-1}) with (*S*)-**G14**. Signals of the host in the host-guest complex (*S*)-**G14⊂[2PBI]-2** are assigned with $a_c - e_c$. Peaks assigned with a red * correspond to aromatic signals of bound (*S*)-**G14**.

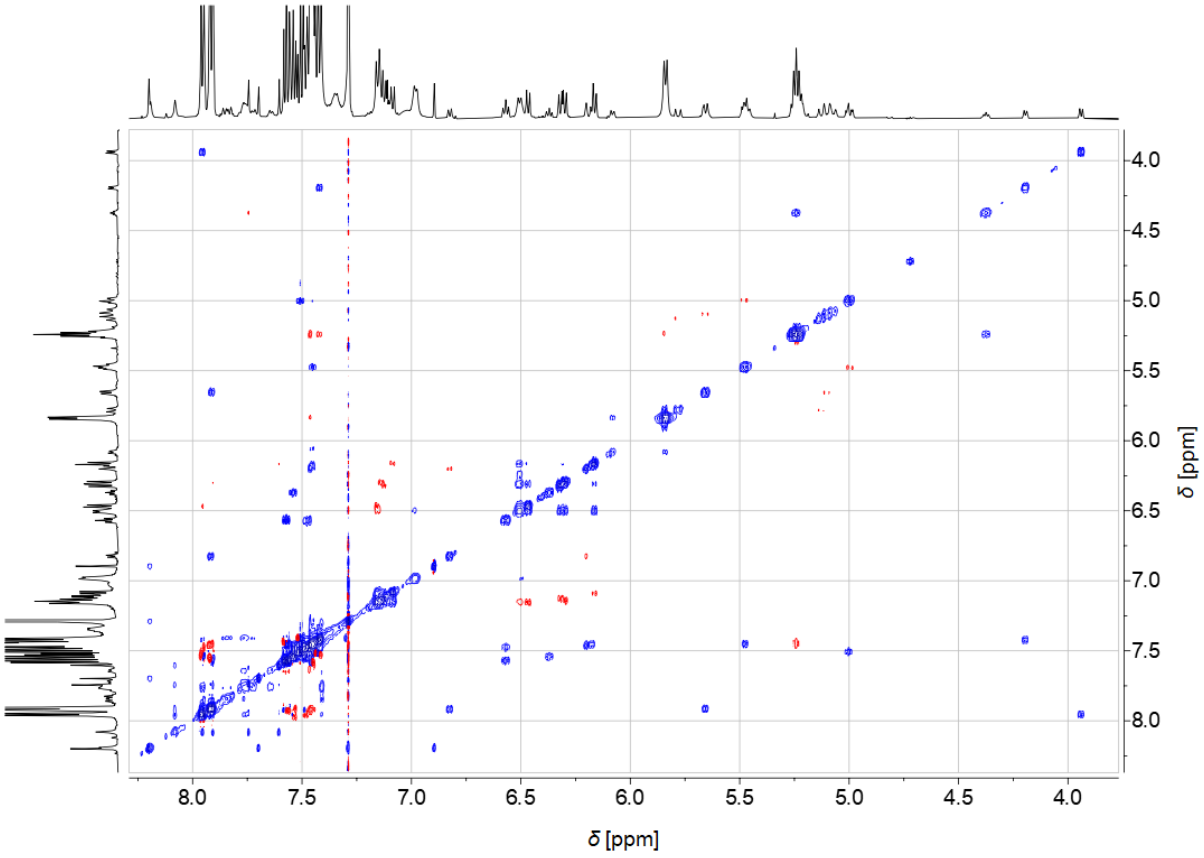

Figure A49. ^{1}H-^{1}H ROESY (600 MHz, $CDCl_3$, 250 K) of **[2PBI]-2** ($c = 5 \times 10^{-4}$ L mol^{-1}) in the presence of 5 eq. of (*S*)-**G14**.

Kinetic ^{1}H NMR studies

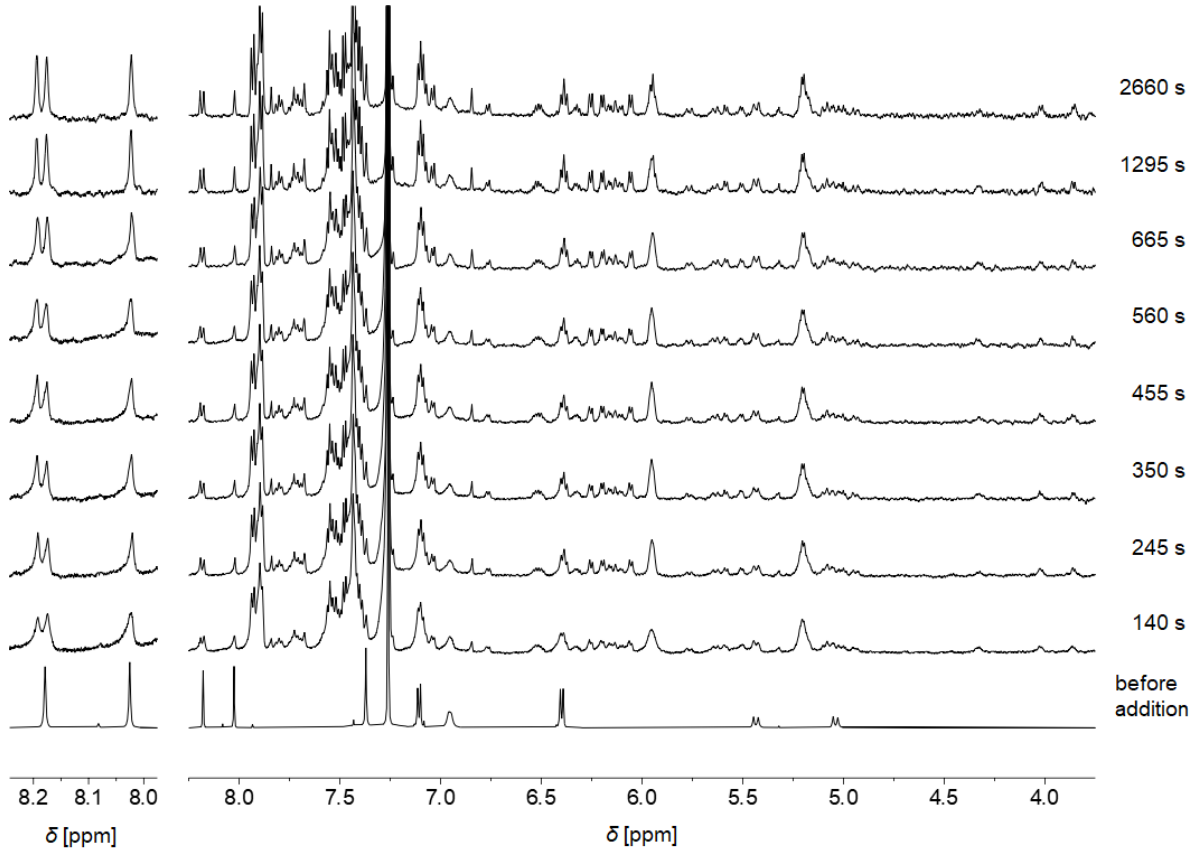

Figure A50. Time-dependent ^{1}H NMR spectra (600 MHz, $CDCl_3$, 217 K, dimethyl sulphone as integration standard) of **[2PBI]-2** ($c_0 = 5 \times 10^{-4}$ mol L^{-1}) after the addition of 10 eq. of (*S*)-**G14** (right). Excerpt thereof showing the PBI core protons (left).

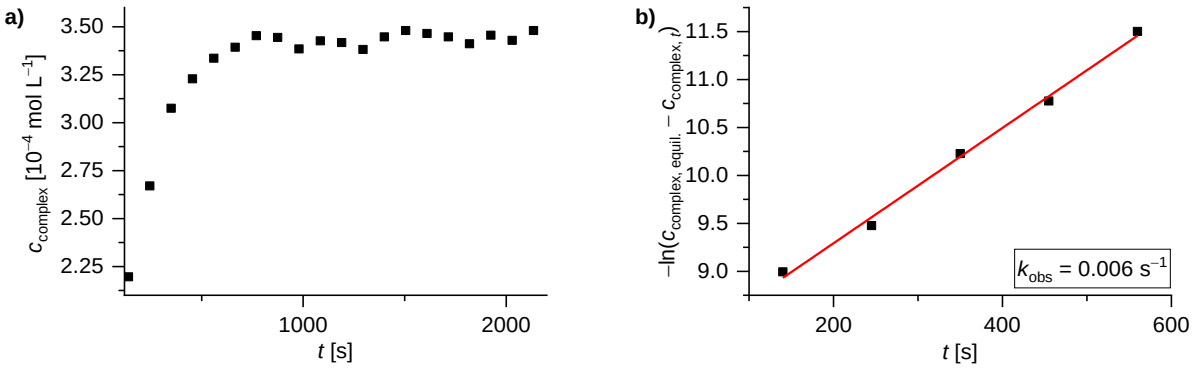

Figure A51. (a) Plot of the complex concentration (*S*)-**G14⊂[2PBI]-2** as a function of time after the addition of 10 eq. of (*S*)-**G14**. **(b)** Plot showing the first order kinetics for the approach to the complexation equilibrium after the addition of 10 eq. of (*S*)-**G14**.

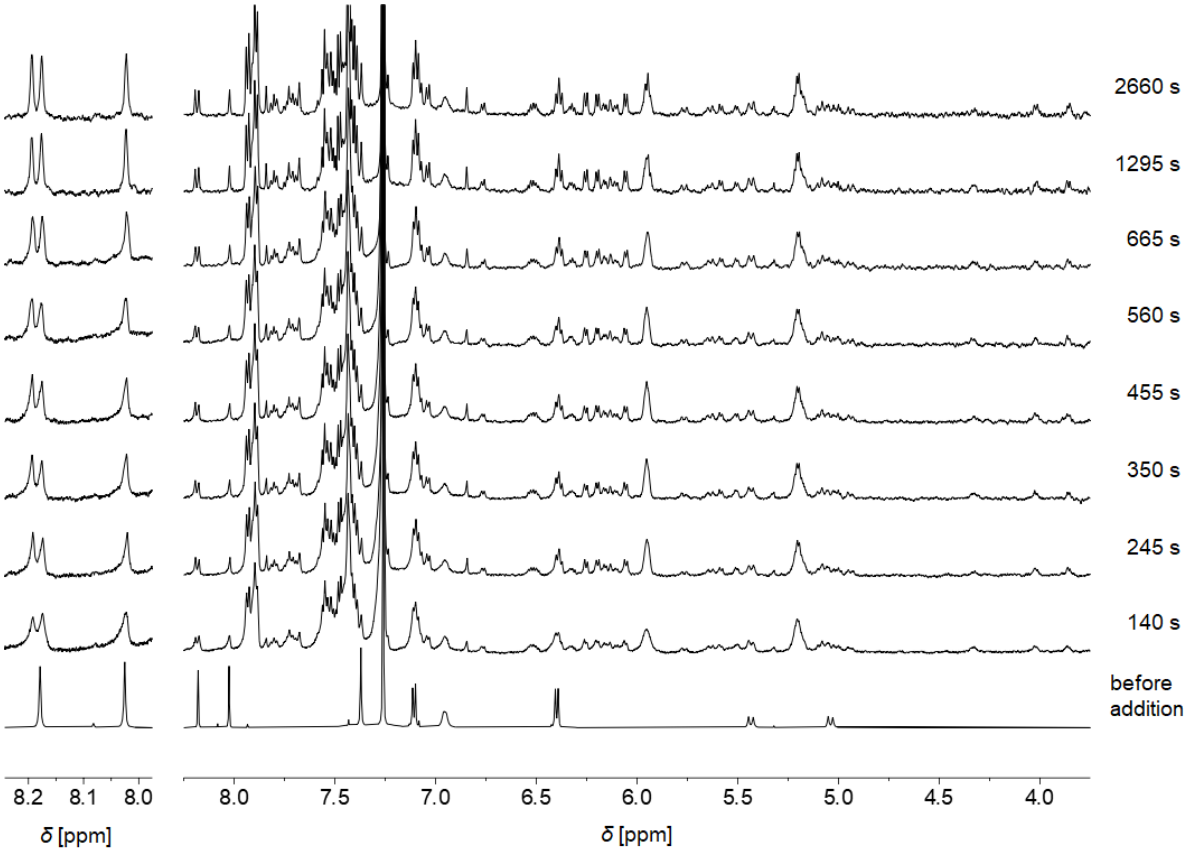

Figure A52. Time-dependent ^{1}H NMR spectra (600 MHz, $CDCl_3$, 217 K, dimethyl sulphone as integration standard) of **[2PBI]-2** ($c_0 = 5 \times 10^{-4}$ mol L^{-1}) after the addition of 5 eq. of (*S*)-**G14** (right). Excerpt thereof showing the PBI core protons (left).

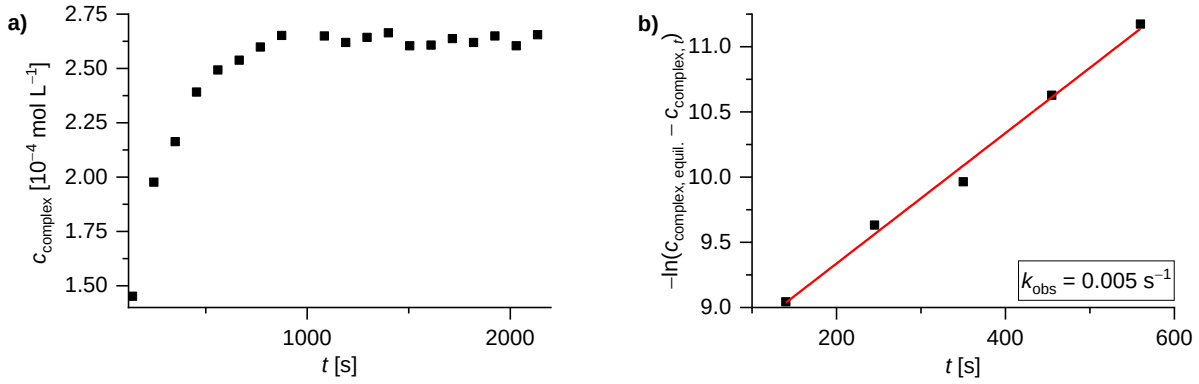

Figure A53. (a) Plot of the complex concentration (*S*)-**G14⊂[2PBI]-2** as a function of time after the addition of 5 eq. of (*S*)-**G14**. **(b)** Plot showing the first order kinetics for the approach to the complexation equilibrium after the addition of 5 eq. of (*S*)-**G14**.

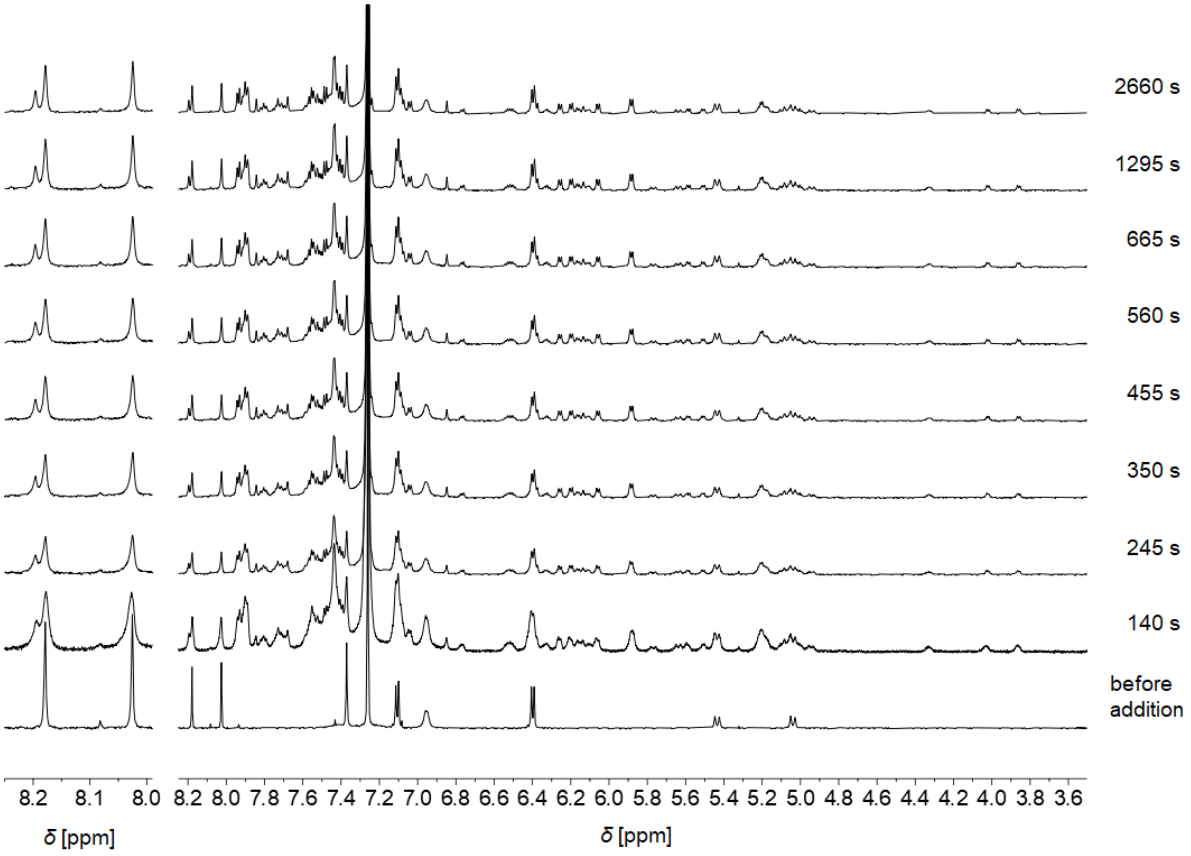

Figure A54. Time-dependent ^{1}H NMR spectra (600 MHz, $CDCl_3$, 217 K, dimethyl sulphone as integration standard) of **[2PBI]-2** ($c_0 = 5 \times 10^{-4}$ mol L^{-1}) after the addition of 2 eq. of (*S*)-**G14** (right). Excerpt thereof showing the PBI core protons (left).

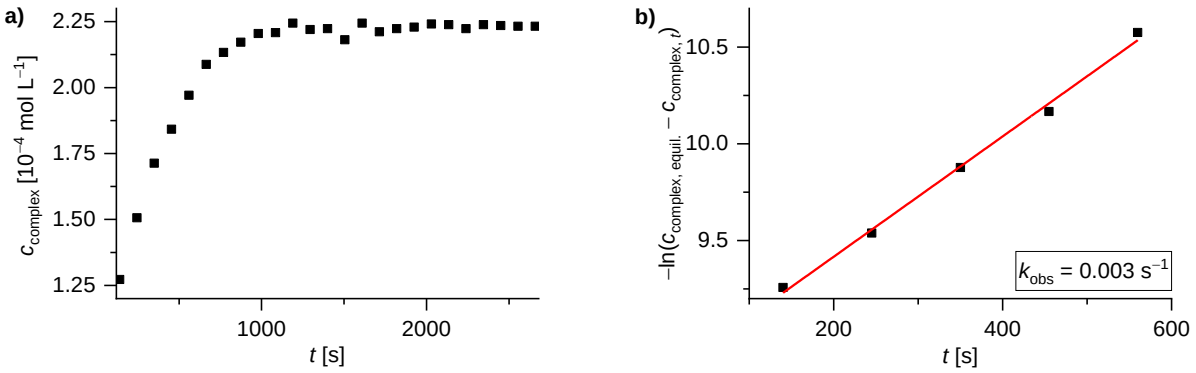

Figure A55. (a) Plot of the complex concentration (*S*)-**G14⊂[2PBI]-2** as a function of time after the addition of 2 eq. of (*S*)-**G14**. **(b)** Plot showing the first order kinetics for the approach to the complexation equilibrium after the addition of 2 eq. of (*S*)-**G14**.

Chapter 4

–

Summary

In this thesis, several new properties of perylene bisimide cyclophane hosts were elucidated such as guest recognition in aqueous environment (Chapter 3.2) or the self-assembly process of one of these hosts in water (Chapter 3.3). Furthermore, the chirality transfer upon guest recognition and the mechanistic model behind host-guest complex formation were investigated (Chapter 3.4).

The synthesis of the first water-soluble PBI cyclophanes **[2PBI]-1m** and **[2PBI]-1p** as well as their reference monomers, **ref-PBI-1m** and **ref-PBI-1p** was presented (Figure 59). Solubility of the hydrophobic chromophores in aqueous environment is provided by four branched oligoethylene glycol chains per PBI core which were attached by copper(I)-catalyzed alkyne-azide cycloaddition.

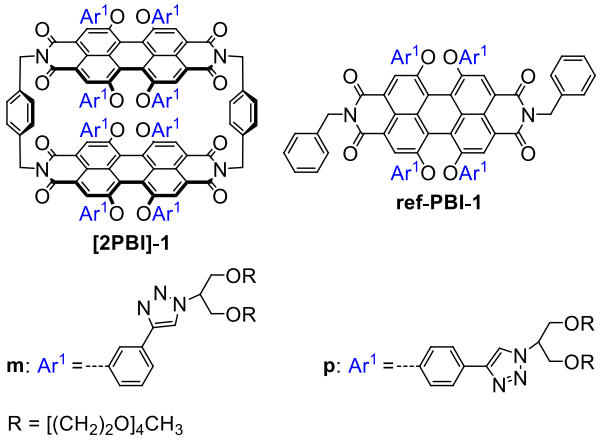

Figure 59. Molecular structures of water-soluble PBI cyclophane hosts **[2PBI]-1m** and **[2PBI]-1p** and their reference monomers **ref-PBI-1m** and **ref-PBI-1p**.

The property of water-soluble cyclophane host **[2PBI]-1p** to recognize natural aromatic alkaloids such as harmine, harmaline or berberine by intercalation into the hydrophobic cavity of the cyclic PBI dimer was investigated in detail (Figure 60). UV-vis and fluorescence titration studies confirmed good binding affinities in the order of 10^3 L mol^{-1} in H_2O/acetonitrile (1/1 vol%). A structure-binding property relationship for host **[2PBI]-1p** was devised showing that three conjugated rings in the π-skeleton of the alkaloid guests are beneficial and large substituents in alkaloids diminish the binding affinity. **[2PBI]-1p** represents the very first example of a chromophore macrocyclic receptor that can be used for the recognition of aromatic alkaloids in aqueous media.

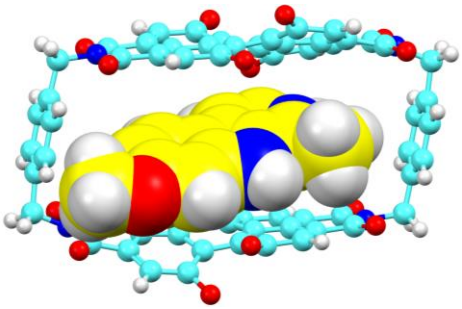

Figure 60. Calculated structure of the host-guest complex harmine⊂**[2PBI]-1m** (PM7).

The thermodynamic bias of the supramolecular dimerization of PBI cyclophane **[2PBI]-1m** and its reference monomer **ref-PBI-1m** in water was explored by temperature dependent UV-vis spectroscopy. For **ref-PBI-1m**, a common temperature response of the self-assembled structure was observed leading to deaggregation at elevated temperature. In the case of the cyclophane, however, enhanced aggregation was observed upon increasing the temperature. These findings corroborate an enthalpically-favored self-assembly process for the reference monomer whereas for the PBI cyclophane this process is entropically driven and enthalpically even disfavored (Figure 61). The inversion of the thermodynamic driving force for the supramolecular dimerization processes of **[2PBI]-1m** and **ref-PBI-1m** is ascribed to the higher degree of solvation of the cyclophane in water when compared to the reference monomer as the former is appended with twice as many polar OEG side chains per openly accessible, hydrophobic π-surface. In its monomeric state cyclophane host **[2PBI]-1m** binds the *harmala* alkaloid harmine (**G1**) in water with good affinity. As for **[2PBI]-1m** in the aggregated state, host self-association and guest encapsulation become competing processes with the equilibrium being shifted towards the host-guest complex **G1⊂[2PBI]-1m** upon addition of higher amounts of **G1**.

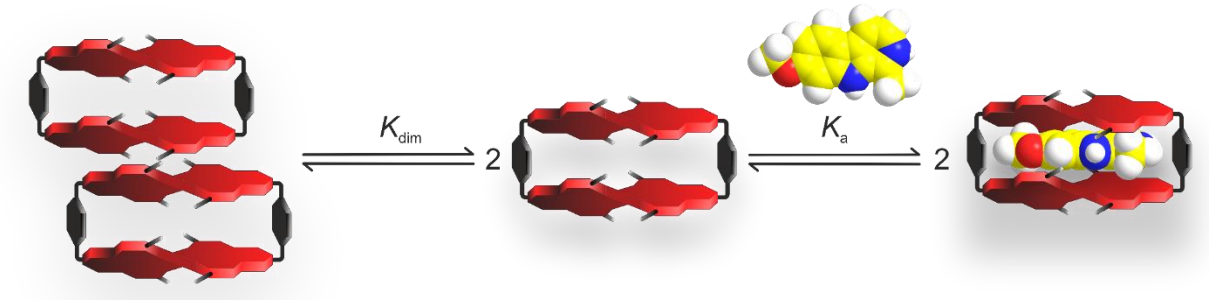

Figure 61. Schematic representation of the equilibrium of PBI cyclophane **[2PBI]-1m** between its dimer aggregate and the host-guest complex with alkaloid guest harmine in water.

The dynamic equilibrium of the (*M*,*M*), (*P*,*P*) and (*M*,*P*)/(*P*,*M*) stereoisomers of the cyclic PBI dimer **[2PBI]-2** which was observed previously by Dr. Peter Spenst was elucidated further. The greater stability of the homochiral (*M*,*M*)/(*P*,*P*)-enantiomeric pair when compared to the (*M*,*P*)/(*P*,*M*)-mesomer and the fact that achiral guest molecule perylene preferentially selects the enantiomeric pair (*M*,*M*)-**[2PBI]-2** and (*P*,*P*)-**[2PBI]-2** over the mesomer for formation of host-guest-complexes were reported previously.[33] In this work, it was proven that the induced CD-effect observed upon addition of homochiral guests is considerably enhanced when compared to initial studies by new guest molecules (*S*)-**G13** and (*S*)-**G14** with increased affinity for **[2PBI]-2**. Due to a more stable host-guest-binding to preferentially one conformer of **[2PBI]-2** the conformational equilibrium between the stereoisomers is shifted more efficiently to the host-guest complex of this conformer with (*S*)-**G13** and (*S*)-**G14** (Figure 62). Kinetic experiments to elucidate the underlying mechanism (conformational selection versus induced fit) for the host-guest binding process did not yield unambiguous results as the rapid equilibrium approximation is not fulfilled by the present system. However, owing to the conformational dynamics of cyclophane **[2PBI]-2**, conformational selection is assumed to be the more reasonable model.

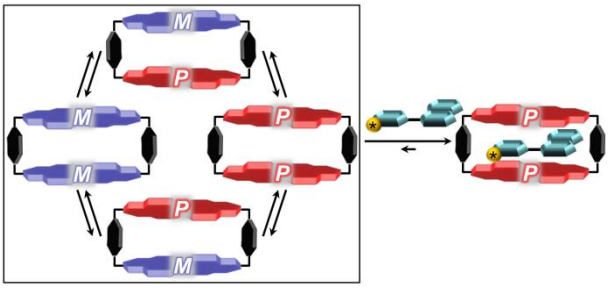

Figure 62. Schematic representation of the dynamic equilibrium of the (*M*,*M*), (*P*,*P*) and (*M*,*P*)/(*P*,*M*) stereoisomers of the cyclophane **[2PBI]-2** which can be shifted to one specific stereoisomer by encapsulation of a chiral guest within the cavity of the host.

In conclusion, in this thesis a broad range of properties of perylene bisimide cyclophane hosts, which are also of great relevance for molecular recognition processes in biological systems, was discussed. The investigations covered host-guest binding properties of a water-soluble PBI cyclophane in aqueous environment, the role of water in self-association processes of an amphiphilic PBI cyclophane in comparison to its reference monomer, chirality transfer and mechanistic studies on the formation of host-guest complexes. Hence, some of these insights can help to further our understanding of highly complex molecular recognition phenomena in living systems.

Chapter 5

–

Zusammenfassung

Diese Arbeit befasste sich mit der Erforschung neuer Eigenschaften von Perylenbisimid-cyclophanwirten, zum Beispiel der Gast-Komplexierung in wässriger Umgebung (Kapitel 3.2) oder dem Einfluss von Wasser beim Selbstassemblierungsprozess einer dieser Wirte in Wasser (Kapitel 3.3). Weiterhin wurden der Chiralitätstransfer durch Gasterkennung und das der Wirt-Gast-Komplexbildung zugrunde liegende mechanistische Modell untersucht (Kapitel 3.4).

Die Synthese der ersten wasserlöslichen PBI-Cyclophane **[2PBI]-1m** und **[2PBI]-1p** sowie deren Referenzmonomere **ref-PBI-1m** und **ref-PBI-1p** wurde vorgestellt (Abbildung 1). Die Löslichkeit der unpolaren Chromophore im wässrigen Medium wird von vier verzweigten OEG-Substituenten pro PBI-Einheit sichergestellt, die mittels Kupfer(I)-katalysierter Alkin-Azid-Cycloaddition am PBI-Gerüst eingeführt wurden.

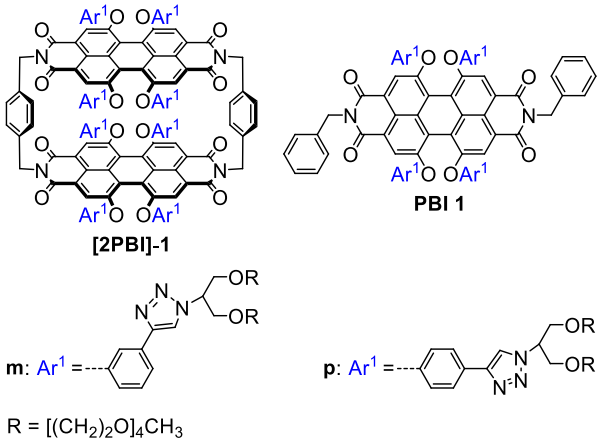

Abbildung 1. Molekülstrukturen der wasserlöslichen PBI-Cyclophanwirte **[2PBI]-1m** und **[2PBI]-1p** und deren monomeren Referenzverbindungen **ref-PBI-1m** und **ref-PBI-1p**.

Die Fähigkeit des wasserlöslichen Cyclophanwirts **[2PBI]-1p**, natürlich vorkommende aromatische Alkaloide, wie zum Beispiel Harmin, Harmalin oder Berberin, im wässrigen

Medium durch Einlagerung in seine hydrophobe Kavität zu erkennen, wurde ausführlich untersucht. Mittels UV-Vis- und Fluoreszenztitrationsstudien konnten gute Affinitäten im Bereich von 10^3 L mol^{-1} zu den oben aufgeführten Alkaloidgästen in H_2O/Acetonitril (1/1 vol%) nachgewiesen werden. Dabei wurde eine Struktur-Bindungseigenschaftsbeziehung abgeleitet, die besagt, dass sich drei konjugierte Ringe im Molekülskelett der Alkaloide positiv auf die Bindung zu **[2PBI]-1p** auswirken und dass große Substituenten am Alkaloidmolekül die Komplexstabilität verringern. **[2PBI]-1p** stellt das erste Beispiel eines farbstoffbasierten Makrozyklus' zur Erkennung aromatischer Alkaloide in wässriger Umgebung dar.

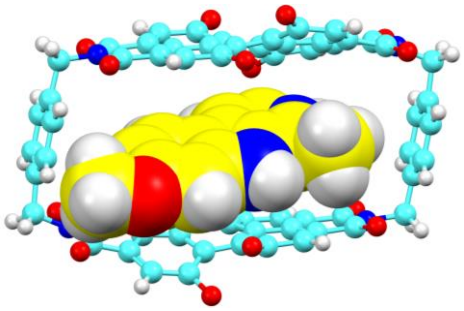

Abbildung 2. Berechnete Struktur des Wirt-Gast-Komplexes Harmin⊂**[2PBI]-1m** (PM7).

Die gegensätzlichen thermodynamischen Triebkräfte hinter den supramolekularen Dimerisierungen des PBI-Cyclophans **[2PBI]-1m** und dessen Referenzmonomers **ref-PBI-1m** in Wasser wurden mittels temperaturabhängiger UV-Vis-Studien untersucht. Bei **ref-PBI-1m** wurde das übliche Temperaturverhalten von selbstassemblierten Strukturen festgestellt, für die Deaggregation bei erhöhter Temperatur verzeichnet wird (Abbildung 3). Im Fall des Cyclophans **[2PBI]-1m** wurde jedoch verstärkte Aggregation bei höheren Temperaturen nachgewiesen. Diese Beobachtungen deuten darauf hin, dass beim Referenzmonomer ein von der Enthalpie begünstigter Selbstassemblierungsprozess vorliegt wohingegen dieser Prozess für das Cyclophan entropiegetrieben ist und enthalpisch nicht bevorzugt wird. Die Umkehr der thermodynamischen Triebkräfte für die supramolekularen Dimerisierungsprozesse von **[2PBI]-1m** und **ref-PBI-1m** wird dem erhöhten Grad der Solvatisierung des Cyclophans verglichen mit dem Referenzmonomer in Wasser zugeschrieben, da ersteres mit der doppelten Anzahl an polaren OEG-Ketten je frei zugänglicher hydrophober π-Oberfläche ausgestattet ist. Im monomeren Zustand bindet das Cyclophan **[2PBI]-1m** das Alkaloid Harmin (**G1**) in seiner Kavität in Wasser. Im aggregierten Zustand befinden sich Wirt-Selbsterkennung und Gasterkennung in Konkurrenz, wobei das Gleichgewicht auf die Seite des Wirt-Gast-Komplexes **G1⊂[2PBI]-1m** durch erhöhte Gastzugabe verschoben werden kann.

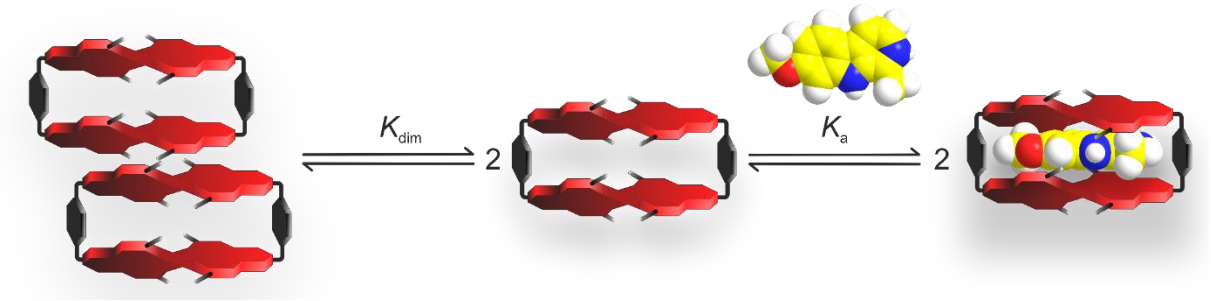

Abbildung 3. Schematische Darstellung des Geleichgewichts des PBI-Cyclophans **[2PBI]-1m** zwischen dem Dimeraggregat und dem Wirt-Gast-Komplex mit dem Alkaloidgast Harmin in Wasser.

Das von Dr. Peter Spenst beobachtete dynamische Gleichgewicht zwischen den (*M*,*M*)-, (*P*,*P*)- und (*M*,*P*)/(*P*,*M*)-Stereoisomeren des zyklischen PBI-Dimers **[2PBI]-2** wurde weiter untersucht. Dass das thermodynamische Gleichgewicht aufseiten des homochiralen (*M*,*M*)/(*P*,*P*)-Enantiomerenpaars liegt und dass der achirale Gast Perylen das homochirale Enantiomerenpaar (*M*,*M*)-**[2PBI]-2** und (*P*,*P*)-**[2PBI]-2** dem (*M*,*P*)/(*P*,*M*)-Mesomer zur Wirt-Gast-Komplexbildung vorzieht, war bereits aus vorangegangenen Arbeiten bekannt.[33] In dieser Arbeit wurde nachgewiesen, dass der durch Zugabe homochiraler Gäste zum Racemat von **[2PBI]-2** hervorgerufene induzierte CD-Effekt, im Vergleich zu früheren Studien, durch die neuen Gastmoleküle (*S*)-**G13** und (*S*)-**G14** mit erhöhter Affinität zu **[2PBI]-2** deutlich verstärkt wird. Durch die stabilere Wirt-Gast-Bindung mit bevorzugt einem Konformer von **[2PBI]-2** lässt sich das konformative Gleichgewicht zwischen den Stereoisomeren effektiver zum Wirt-Gast-Komplex dieses einen Konformers mit (*S*)-**G13** und (*S*)-**G14** verschieben. Weiterhin wurden zeitabhängige ^{1}H NMR-Studien zur Ermittlung des der Wirt-Gast-Erkennung zu Grunde liegenden Mechanismus' (induzierte Anpassung oder konformative Auslese) durchgeführt, die jedoch keine eindeutige Aussage zuließen, da die Annahme des schnellen Gleichgewichts für dieses System keine Gültigkeit besitzt. Jedoch wird aufgrund der konformativen Flexibilität des Cyclophans **[2PBI]-2** die konformative Auslese als der wahrscheinlichere Mechanismus angenommen.

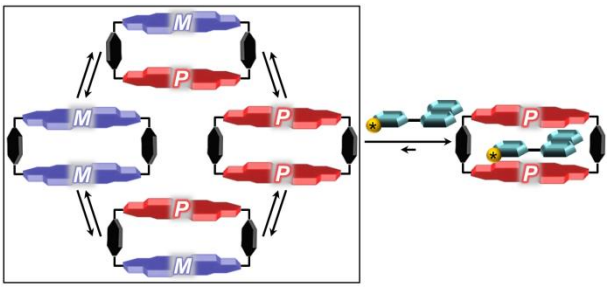

Abbildung 4. Schematische Darstellung der Verschiebung des konformativen Gleichgewichts zwischen den (*M*,*M*)-, (*P*,*P*)- und (*M*,*P*)/(*P*,*M*)-Stereoisomeren von Cyclophan **[2PBI]-2p** durch Einlagerung eines chiralen Gasts in die Kavität.

Zusammenfassend wurden in dieser These eine breite Vielfalt von Eigenschaften von Perylenbisimidcyclophanwirten erläutert, die auch für molekulare Erkennungsprozesse in biologischen Systemen von großer Bedeutung sind. Die Untersuchungen deckten Wirt-Gast-Bindungsstudien eines PBI-Cyclophanwirts in wässriger Umgebung, die Rolle von Wasser im Selbstassoziationsprozess eines PBI-Cyclophans im Vergleich zu dessen Referenzmonomer, Chiralitätstransfer und mechanistische Studien zur Bildung der Wirt-Gast-Komplexe ab. Somit können einige dieser Erkenntnisse zu einem tiefgreifenderen Verständnis von hochkomplexen molekularen Erkennungsphänomenen in lebenden Organismen beitragen.

Chapter 6

–

Experimental Section

6.1 Materials and Methods

Melting points. Melting points were determined with an Olympus BX41 polarization microscope (Linkam Scientific) with a TP-94-heating stage and are uncorrected.

NMR spectroscopy. NMR spectra were recorded on a Bruker Avance III HD 400 or 600 MHz spectrometer in deuterated solvents. Chemical shifts (δ) are internally referenced to the residual proton solvent resonances or to natural abundance carbon resonances. The abbreviations for signal multiplicities are s = singlet, d = doublet, t = triplet, q = quartet, quint = quintet, sext = sextet, m = multiplet.

Mass spectrometry. MALDI-TOF mass spectrometry was performed on a Bruker Daltonic Autoflex II mass spectrometer using *trans*-2-[3-(4-*tert*-butylphenyl)-2-methyl-2-propenylidene]malononitrile (DCTB) as matrix. High resolution ESI-TOF mass spectrometry was performed on a Bruker Daltonic microTOF focus spectrometer.

UV-vis spectroscopy. UV-vis absorption spectra were recorded on a JASCO V670 or V770 or a Perkin Elmer Lambda 950 spectrometer. The temperature was controlled by an NCP-706 thermostat (JASCO) or a PTP-1 Peltier element (Perkin Elmer). Either solvents of spectroscopic grade or Millipore water (ELGA Purelab Classic system (ρ = 18.2 MΩcm) was used. The measurements in organic solvents were performed in conventional quartz cells (Hellma Analytics). For measurements in aqueous media, these cuvettes were silanized (see procedure below) to minimize errors in sample concentrations due to adsorption of the compounds to the glass walls.

Fluorescence spectroscopy. Fluorescence spectra for titration experiments were recorded on a PTI QM4-2003 spectrometer. Quantum yields were determined on an Edinburgh Instruments FLS 980 spectrometer by optical dilution method ($OD_{max} < 0.05$) as the average value of four different excitation wavelengths using *N,N'*-di(2,6-di*iso*propylphenyl)-1,6,7,12-tetraphenoxy-perylen-3,4:9,10-tetracarboxylic acid bisimide (Φ_{fl} = 0.96 in $CHCl_3$)[183] as reference. Conventional quartz cells (10 mm, Hellma Analytics) and solvents of spectroscopic grade were used.

Circular dichroism spectroscopy. CD spectra were recorded on a JASCO J-810 spectrometer equipped with a CDF-242 Peltier element using conventional quartz cells and solvents of spectroscopic grade.

Atomic force microscopy. AFM measurements were performed under ambient conditions using a Bruker Multimode 8 SPM system operating in tapping mode. Silica cantilevers (OMCL-AC200TS, Olympus) with a resonance frequency of ~ 150 kHz and a spring constant of ~ 10 N m^{-1} were used. The samples were prepared by spin-coating of a sample solution in a given solvent onto mica.

Chromatography. Column chromatography was performed with glass columns using silica gel (Silica 60, particle size 0.04 – 0.063 mm, Macherey Nagel) as stationary phase. CH_2Cl_2 and ethyl acetate were distilled prior to use. Thin layer chromatography for reaction monitoring was carried out on pre-coated silica gel plates 60 with fluorescence indicator UV_{254} (Macherey Nagel or Merck). For preparative thin layer chromatography, pre-coated plates without fluorescence indicator were used. Recycling gel permeation chromatography was performed on a Shimadzu chromatography system (LC-20AD Prominence Pump, SPD-MA20A Prominence diode array detector) with three preparative JAIGEL columns (Japan Analytical Industries, 2 × 2H, 1 × 2.5H) in a row using $CHCl_3$ stabilized with ethanol and of HPLC grade as eluent. Flash chromatography was performed on a PuriFlash-XS 420+ (Interchim) using SilicaHP F0040 (30 μm) columns.

Silanization of cuvettes and glass vials. In the following, the procedure for the silanization of one commercial 1 cm cuvette in an unsilanized 250 mL flask is described.[184] Under nitrogen atmosphere, the cuvette was immersed into a mixture of freshly distilled trimethylsilylchloride (4.6 mL, 50.0 mmol) and NaI (7.50 g, 50.0 mmol) in dry acetonitrile (200 mL) and heated to 90 °C overnight. After cooling down, the cuvette was washed thoroughly with distilled water,

acetone and CH_2Cl_2. For silanization of other glassware, the amounts in this procedure were adapted by taking into account the approximated outer and inner surfaces of the respective cuvettes and glass vials as well as the inner sphere volume of the reaction flask.

Guest molecules. The alkaloid guests **G1**, **G4** – **G8** as well as **G11** and (*S*)-**G12** are commercially available and were used without further purification. **G2** was prepared by methylation of harmine with CH_3I,[185] **G3** was prepared according to literature[186] and **G9** and **G10** were obtained by precipitation of the corresponding, commercially available free base from CH_3OH with concentrated hydrochloric acid. (*S*)-**G13** and (*S*)-**G14** were synthesized in two steps as described in Chapter 6.2.

Host-guest titration experiments. For the titration experiments, a solution of both the respective PBI cyclophane ($c = 1.0 \times 10^{-5}$ mol L^{-1}) and the guest in excess in the corresponding solvent was titrated to a solution of pure PBI cyclophane of the same concentration in the same solvent keeping the host concentration constant during the experiment. The UV-vis and fluorescence titration data were fitted globally (**[2PBI]-1p**: 575 – 530 nm (UV-vis) and 610 – 680 nm (fluorescence). **[2PBI]-2**: 540 – 588 nm (UV-vis) and 625 – 685 nm (fluorescence)) to equation (21)[135] with ε_h, ε_{hg} and ε_{obs} as extinction coefficients at a given wavelength of the free host, the host-guest complex and the measured extinction coefficient, c_h^0 and c_g^0 as total concentrations of the host and the guest and K_a as binding constant. K_a was treated as shared variable.

$$\varepsilon_{obs} = \varepsilon_h + \frac{\varepsilon_{hg} - \varepsilon_h}{2c_h^0}\left(c_h^0 + c_g^0 + \frac{1}{K_a} \pm \sqrt{\left(c_h^0 + c_g^0 + \frac{1}{K_a}\right)^2 - 4c_h^0 c_g^0}\right) \qquad (21)$$

UV-vis dilution studies. For the concentration-dependent aggregation studies, stock solutions in the respective solvent mixture of Millipore water and spectroscopic grade acetone were prepared in silanized glassware and allowed to equilibrate at room temperature overnight. The stock solutions were diluted with the solvent mixture to the desired concentration and again equilibrated overnight. Data were fitted locally at three different wavelengths to either the dimerization (22) or the isodesmic growth model (23).[153a] Here, ε_{mon}, ε_{dim}, ε_{agg} and ε_{obs} represent the extinction coefficient of the monomer, the dimer, the aggregate or measured extinction coefficient, respectively. K_{dim} and K_{agg} are the dimerization and the aggregation constant and c_T is the total concentration of the sample.

$$\varepsilon_{obs} = \frac{4K_{dim}c_T + 1 - \sqrt{8K_{dim}c_T + 1}}{4K_{dim}c_T}(\varepsilon_{dim} - \varepsilon_{mon}) + \varepsilon_{mon} \quad (22)$$

$$\varepsilon_{obs} = \left(1 - \frac{2K_{agg}c_T + 1 - \sqrt{4K_{agg} + 1}}{2{K_{agg}}^2{c_T}^2}\right)(\varepsilon_{agg} - \varepsilon_{mon}) + \varepsilon_{mon} \quad (23)$$

For further confirmation of the aggregation mechanism and for obtaining the dimer or aggregate and the monomer spectrum, the data were also fitted to these models in a global fitting routine.[153b]

Time-dependent host-guest ^{1}H NMR studies. For the-time dependent NMR studies, an NMR tube with a solution of free **[2PBI]** in $CDCl_3$ (0.5 mL) with the integration standard dimethyl sulphone as well as a solution of (*S*)-**G14** of the desired concentration in $CDCl_3$ were cooled to 217 K in an acetone/dried ice bath. Directly before the measurement the guest solution (0.2 mL) was added to the NMR tube with the host, so that in the measured samples the concentrations were c_0 (**[2PBI]**) = 5×10^{-4} mol L^{-1} and c_0 ((*S*)-**G14**) = 1.0×10^{-3} mol L^{-1}, 2.5×10^{-3} mol L^{-1} or 5.0×10^{-3} mol L^{-1}, respectively. The sample was immediately placed in a cooled and shimmed NMR spectrometer where consecutive proton spectra were measured automatically (number of scans: 40, acquisition time: 2.5 s). Data treatment was carried out according to literature.[116f]

Molecular Modelling. Geometry optimization for the host-guest complexes of cyclophane **[2PBI]-1p** was performed by employing the semi-empirical Hamiltonian PM7[187] as implemented in the MOPAC program,[188] which also accounts for dispersion interactions. Geometries for **[2PBI]-1m** and **ref-PBI-1m** have been optimized employing the semi-empirical PM6 Hamiltonian[189] with D3H4 correction[190] for dispersion interactions and hydrogen bonding as implemented in MOPAC2016.[191] Solvent effects have been included implicitly using the COSMO model for water.[192]

6.2 Synthesis and Characterization

Synthesis of *N*,*N*′-dibutyl-1,6,7,12-tetra(3-iodophenoxy)-3,4:9,10-tetracarboxylic acid perylene bisimide (42m)

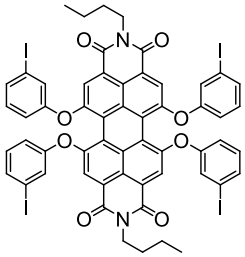

42m

Under nitrogen atmosphere, anhydrous K_2CO_3 (1.94 g, 14.1 mmol) and 3-iodophenole (6.18 g, 28.1 mmol) were dissolved in freshly distilled NMP (390 ml). After the addition of *N*,*N*-dibutyl-1,6,7,12-tetrachloro-3,4:9,10-tetracarboxylic acid perylene bisimide[118] (3.00 g, 4.69 mmol) the reaction was stirred at 110 °C for 18 h The crude product was precipitated by addition of 2 N HCl, filtered and washed with 2 N HCl and distilled water. Purification by column chromatography (silica gel, CH_2Cl_2/cyclohexane = 7/3) and subsequent precipitation from CH_2Cl_2 solution with CH_3OH yielded 3.94 g (2.87 mmol, 61%) of a red solid. **Mp**: > 350 °C. **^{1}H NMR** ($CDCl_3$, 400 MHz): δ = 8.21 (s, 4 H, CH_{PBI}), 7.45 (ddd, 4 H, ^3J = 7.8 Hz, ^4J = 1.6 Hz, ^4J = 1.0 Hz, CH_{aryl}), 7.22 (dd, 4 H, ^4J = 2.3 Hz, ^4J = 1.6 Hz, CH_{aryl}), 7.01 (t, 4 H, , ^3J = 8.1 Hz, CH_{aryl}), 6.91 (ddd, 4 H, ^3J = 8.2 Hz, ^4J = 2.4 Hz, ^4J = 1.0 , CH_{aryl}), 4.11 (t, 4 H, ^3J = 7.5 Hz, NCH_2), 1.67 (quint, 4 H, ^3J = 7.3 Hz, NCH$_2$CH_2), 1.41 (sext, 4 H, ^3J = 7.3 Hz CH_2CH$_3$), 0.95 (t, 6 H, ^3J = 7.2 Hz CH_3) ppm. **^{13}C NMR** ($CDCl_3$, 100 MHz): δ = 163.1, 155.9, 155.2, 133.8, 132.9, 131.3, 129.0, 123.3, 120.8 8 (2 signals), 120.24, 119.0, 94.7, 40.6, 30.3, 20.5, 13.9 ppm. **HRMS** (ESI, pos. mode, CH_3CN/CH_3Cl): *m/z* 1396.86942 $[M+Na]^+$, calculated for $C_{100}H_{122}N_2NaO_8Si_4$: 1396.86993. **UV-vis** ($CHCl_3$), λ_{max} (ε_{max}): 564 nm (43 × 10^3 L mol^{-1} cm^{-1}), 525 nm (28 × 10^3 L mol^{-1} cm^{-1}). **Fluorescence** ($CHCl_3$), λ_{max} (λ_{ex}): 599 nm (530 nm), Φ_{fl} = 94%.

Synthesis of *N,N′*-dibutyl-1,6,7,12-tetra[3-(triisopropylsilylethinyl)phenoxy]-3,4:9,10-tetracarboxylic acid perylene bisimide (43m)

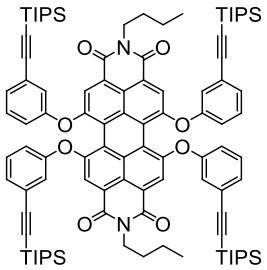

43m

Under nitrogen atmosphere, a degassed solution of triisopropylsilyl acetylene (1.43 mL, 1.16 g, 6.27 mmol) in NEt_3 (52.5 mL) was added to a mixture of *N,N′*-dibutyl-1,6,7,12-tetra(3-iodophenoxy)-3,4:9,10-tetracarboxylic acid perylene bisimide (**42m**) (875 mg, 637 μmol), $Pd(PPh_3)_2Cl_2$ (44.7 mg, 63.7 μmol) and CuI (24.3 mg, 127 μmol) in dry DMF (85.0 mL) and CH_2Cl_2 (44.0 mL) at room temperature. The reaction mixture was stirred at 55 °C for 16 h. After being cooled down to room temperature, the organic phase was washed successively with 2 N HCl, concentrated NH_4Cl solution and H_2O and dried over Na_2SO_4. Purification by column chromatography (silica gel, CH_2Cl_2/cyclohexane = 6/4) and precipitation from CH_2Cl_2 solution with CH_3OH yielded 839 mg (527 μmol, 83%) of a violet solid. **Mp**: 285 – 287 °C. **^{1}H NMR** (CD_2Cl_2, 400 MHz): δ = 8.12 (s, 4 H, C*H*$_{PBI}$), 7.28 – 7.23 (m, 8 H, C*H*$_{aryl}$), 6.97 – 6.92 (m, 8 H, C*H*$_{aryl}$), 4.08 (t, 4 H, ^3J = 7.3 Hz NC*H*$_2$), 1.64 (quint, 4 H, ^3J = 7.3 Hz, NCH$_2$C*H*$_2$), 1.38 (sext, 4 H, ^3J = 7.4 Hz, C*H*$_2$CH$_3$), 1.10 (s, 84 H, SiC*H*(C*H*$_3$)$_3$), 0.93 (t, 6 H, ^3J = 7.4 Hz C*H*$_3$) ppm. **^{13}C NMR** (CD_2Cl_2, 100 MHz): δ = 163.3, 155.8, 155.7, 133.1, 13.2, 128.6, 125.7, 123.6, 123.5, 120.9, 120.7, 120.5, 120.3, 106.3, 92.0, 40.7, 30.5, 20.7, 18.8, 14.0, 11.7 ppm. **HRMS** (ESI, pos. mode, CH_3CN/CH_3Cl): *m/z* 1613.80951 $[M+Na]^+$, calculated for $C_{100}H_{122}N_2NaO_8Si_4$: 1613.81705. **UV-vis** ($CHCl_3$), λ_{max} (ε_{max}): 571 nm (38×10^3 L mol^{-1} cm^{-1}), 533 nm (25×10^3 L mol^{-1} cm^{-1}). **Fluorescence** ($CHCl_3$), λ_{max} (λ_{ex}): 605 nm (530 nm), Φ_{fl} = 92%.

Synthesis of *N*,*N*′-dibutyl-1,6,7,12-tetra[4-(triisopropylsilylethinyl)phenoxy]-3,4:9,10-tetracarboxylic acid perylene bisimide (43p)

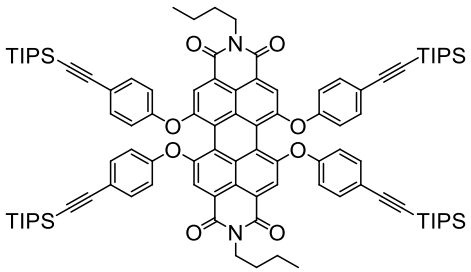

43p

Under nitrogen atmosphere, a degassed solution of triisopropylsilyl acetylene (1.63 mL, 1.33 g, 7.28 mmol) in NEt_3 (60.0 mL) was added to a mixture of *N*,*N*-dibutyl-1,6,7,12-tetra(4-iodophenoxy)-3,4:9,10-tetracarboxylic acid perylene bisimide (**42p**)[119] (1.00 g, 728 μmol), $Pd(PPh_3)_2Cl_2$ (51.1 mg, 72.8 μmol) and CuI (27.7 mg, 146 μmol) in dry DMF (100 mL) and CH_2Cl_2 (50.0 mL) at room temperature. The reaction mixture was stirred at 55 °C for 16 h. After being cooled down to room temperature, the organic phase was washed successively with 2 N HCl, concentrated NH_4Cl solution and H_2O and dried over Na_2SO_4. Purification by column chromatography (silica gel, CH_2Cl_2/cyclohexane = 7/3) and precipitation from CH_2Cl_2 solution with CH_3OH yielded 893 mg (560 μmol, 77%) of a violet solid. **Mp**: 326 – 328 °C. **^{1}H NMR** ($CDCl_3$, 400 MHz): δ = 8.13 (s, 4 H, C*H*$_{PBI}$), 7.44 – 7.41 (m, 8 H, C*H*$_{aryl}$), 6.86 – 6.83 (m, 8 H, C*H*$_{aryl}$), 4.11 (t, 4 H, NC*H*$_2$), 1.64 (quint, 4 H, NCH_2CH_2), 1.39 (sext, 4 H, CH_2CH_3), 1.15 (s, 84 H, $SiCH(CH_3)_3$), 0.94 (t, 6 H, CH_3) ppm. **^{13}C NMR** ($CDCl_3$, 100 MHz): δ = 163.1, 155.6, 155.3, 134.1, 132.8, 123.1, 120.4, 120.4, 120.2, 120.0, 119.9, 106.2, 91.0, 40.6, 30.2, 20.4, 18.8, 13.9, 11.4 ppm. **HRMS** (ESI, pos. mode, CH_3CN/CH_3Cl): *m/z* 1613.8161 $[M+Na]^+$, calculated for $C_{100}H_{122}N_2NaO_8Si_4$: 1613.8171. **UV-vis** ($CHCl_3$), λ_{max} (ε_{max}): 573 nm (44×10^3 L mol^{-1} cm^{-1}), 534 nm (28×10^3 L mol^{-1} cm^{-1}). **Fluorescence** ($CHCl_3$), λ_{max} (λ_{ex}): 605 nm (530 nm), Φ_{fl} = 92%.

Synthesis of 1,6,7,12-tetra[3-(triisopropylsilylethinyl)phenoxy]-3,4:9,10-tetracarboxylic acid perylene bisanhydride (44m)

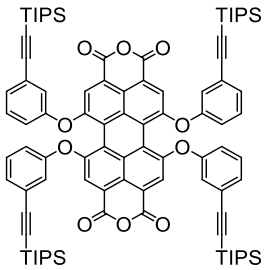

44m

A solution of *N*,*N*′-dibutyl-1,6,7,12-tetra[3-(triisopropylsilylethinyl)phenoxy]-3,4:9,10-tetracarboxylic acid perylene bisimide (**43m**) (1.21 g, 760 μmol) in *tert*-butylalcohol (90 mL) was heated to 110 °C. Finely ground KOH (852 mg, 15.2 mmol) was added and the reaction mixture was stirred at 110 °C for 15 min. The crude product was precipitated from the warm reaction mixture by addition of 2 N HCl, filtered, washed with H_2O and dried in vacuo. Purification by column chromatography (silica gel, CH_2Cl_2/cyclohexane = 6/4) and precipitation from CH_2Cl_2 solution with CH_3OH yielded 285 mg (192 μmol, 25%) of a violet solid. **Mp**.: 274 – 276 °C. **^{1}H NMR** (CD_2Cl_2, 400 MHz): δ = 8.14 (s, 4 H, CH_{PBI}), 7.30 – 7.26 (m, 8 H, CH_{aryl}), 6.99 – 6.93 (m, 8 H, CH_{aryl}), 1.10 (s, 84 H, SiCH(CH_3)$_3$) ppm. **^{13}C NMR** (CD_2Cl_2, 100 MHz): δ = 159.9, 156.3, 155.1, 133.7, 130.5, 129.2, 126.0, 123.7, 122.2, 122.1, 121.8, 120.6, 119.6, 106.0, 92.5, 18.8, 11.6 ppm. **HRMS** (ESI, pos. mode, CH_3CN/CH_3Cl): *m/z* 1503.65318 $[M+Na]^+$, calculated for $C_{92}H_{104}NaO_{10}Si_4$: 1503.65988. **UV-vis** ($CHCl_3$), λ_{max} (ε_{max}): 573 nm (35×10^3 L mol^{-1} cm^{-1}), 533 nm (21×10^3 L mol^{-1} cm^{-1}). **Fluorescence** ($CHCl_3$), λ_{max} (λ_{ex}): 603 nm (530 nm), Φ_{fl} = 93%.

Synthesis of 1,6,7,12-tetra[4-(triisopropylsilylethinyl)phenoxy]-3,4:9,10-tetracarboxylic acid perylene bisanhydride (44p)

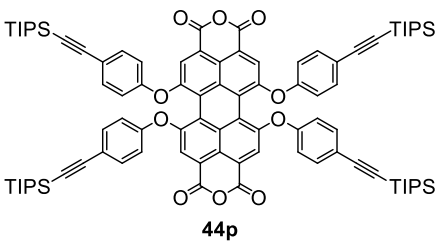

44p

A solution of *N*,*N*′-dibutyl-1,6,7,12-tetra[4-(triisopropylsilylethinyl)phenoxy]-3,4:9,10-tetracarboxylic acid perylene bisimide (**43p**) (100 mg, 62.8 μmol) in *tert*-butylalcohol (6.0 mL) was

heated to 110 °C. Finely ground KOH (70.5 mg, 1.26 mmol) was added and the reaction mixture was stirred at 110 °C for 15 min. The crude product was precipitated from the warm reaction mixture by addition of 2 N HCl, filtered, washed with H_2O and dried in vacuo. Purification by column chromatography (silica gel, CH_2Cl_2/cyclohexane = 7/3) and precipitation from CH_2Cl_2 solution with CH_3OH yielded 40.0 mg (27.0 μmol, 43%) of a violet solid. **Mp**.: 311 – 312 °C. **^{1}H NMR** ($CDCl_3$, 400 MHz): δ = 8.12 (s, 4 H, CH_{PBI}), 7.47 – 7.44 (m, 8 H, CH_{aryl}), 6.88 – 6.84 (m, 8 H, CH_{aryl}), 1.14 (s, 84 H, SiCH(CH_3)$_3$) ppm. **^{13}C NMR** ($CDCl_3$, 100 MHz): δ = 159.4, 156.2, 154.6, 134.4, 133.4, 121.9, 121.7, 121.3, 121.0, 120.1, 119.3, 105.9, 91.7, 18.8, 11.4 ppm. **HRMS** (ESI, pos. mode, CH_3CN/CH_3Cl): *m/z* 1503.6652 $[M+Na]^+$, calculated for $C_{92}H_{104}NaO_{10}Si_4$: 1503.6499. **UV-vis** ($CHCl_3$), λ_{max} (ε_{max}): 576 nm (35 × 10^3 L mol^{-1} cm^{-1}), 535 nm (21 × 10^3 L mol^{-1} cm^{-1}). **Fluorescence** ($CHCl_3$), λ_{max} (λ_{ex}): 605 nm (530 nm), Φ_{fl} = 85%.

Glycerolether azide 45

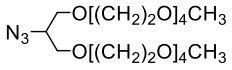

45

Under nitrogen atmosphere, a mixture of tosylate **49** (200 mg, 320 μmol) and NaN_3 (104 mg, 1.60 mmol) in ethanol (1.00 mL) was heated to 85 °C for 14 h. The salts were separated by filtration and the solvent was evaporated under reduced pressure. The residue was purified by column chromatography (silica gel, CH_2Cl_2/CH_3OH = 100/10) to obtain 156 mg (314 μmol, 94%) of a pale yellow oil. **^{1}H NMR** (400 MHz, $CDCl_3$): δ = 3.77 – 3.72 (m, 1 H, CHN$_3$), 3.67 – 3.52 (m, 36 H, OCH_2), 3.38 (s, 6 H, OCH_3) ppm. **^{13}C NMR** (100 MHz, $CDCl_3$): δ = 72.1, 71.1 (2 signals), 70.8, 70.7 (3 signals), 70.6, 70.5, 69.8, 60.7, 59.2 ppm. **HRMS** (ESI, pos. mode, CH_3CN/CH_3Cl): *m/z* 520.28549 $[M+Na]^+$, calculated for $C_{21}H_{43}N_3NaO_{10}$: 520.28407.

Synthesis of *N,N′*-dibenzyl-1,6,7,12-tetra[3-(triisopropylsilylethinyl)phenoxy]-3,4:9,10-tetracarboxylic acid perylene bisimide (46m)

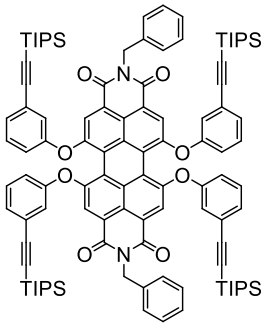

46m

Under nitrogen atmosphere, 1,6,7,12-tetra[3-(triisopropylsilylethinyl)phenoxy]-3,4:9,10-tetracarboxylic acid perylene bisanhydride (**44m**) (80.0 mg, 54.0 μmol) was reacted with benzylamine (224 μL, 221 mg, 1.62 mmol) in imidazole (170 mg) and toluene (4 mL) at 120 °C for 4 h. The crude product was precipitated by addition of 2 N HCl, collected by filtration and washed with H_2O. Further purification by column chromatography (CH_2Cl_2/hexane = 7/3) and precipitation from CH_2Cl_2 with CH_3OH yielded 70.3 mg (35.1 μmol, 65%) of a red solid. **Mp**.: 275 – 277 °C. **^{1}H NMR** (CD_2Cl_2, 400 MHz): δ = 8.13 (s, 4 H, C*H*$_{PBI}$), 7.42 – 7.39 (m, 4 H, C*H*$_{aryl}$), 7.28 – 7.19 (m, 14 H, C*H*$_{aryl}$), 6.96 – 6.91 (m, 8 H, C*H*$_{aryl}$), 5.27 (br s, 4 H C*H*$_2$), 1.09 (s, 84 H, SiC*H*(C*H*$_3$)$_3$) ppm. **^{13}C NMR** (CD_2Cl_2, 100 MHz): δ = 163.3, 155.9, 155.6, 137.6, 133.2, 130.2, 129.0, 128.7 (2 signals), 127.8, 123.7, 123.4, 121.0, 120.8, 120.6, 120.4, 120.3, 106.2, 92.1, 44.0, 18.8, 11.6 ppm. **HRMS** (ESI, pos. mode, CH_3CN/CH_3Cl): *m/z* 1681.78174 $[M+Na]^+$, calculated for $C_{106}H_{118}NNaO_8Si_4$: 1681.78575. **UV-vis** ($CHCl_3$), λ_{max} (ε_{max}): 575 nm (46×10^3 L mol^{-1} cm^{-1}), 536 nm (28×10^3 L mol^{-1} cm^{-1}). **Fluorescence** ($CHCl_3$), λ_{max} (λ_{ex}): 608 nm (530 nm), Φ_{fl} = 93%.

Synthesis of *N,N′*-dibenzyl-1,6,7,12-tetra[4-(triisopropylsilylethinyl)phenoxy]-3,4:9,10-tetracarboxylic acid perylene bisimide (46p)

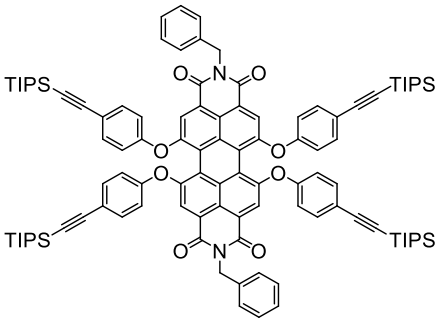

46p

Under nitrogen atmosphere, 1,6,7,12-tetra[4-(triisopropylsilylethinyl)phenoxy]-3,4:9,10-tetracarboxylic acid perylene bisanhydride (**44p**) (30.0 mg, 20.2 μmol) was reacted with benzylamine (66.2 μL, 65.1 mg, 607 μmol) in imidazole (300 mg) and toluene (15 mL) at 120 °C for 4 h. The crude product was precipitated by addition of 2 N HCl, collected by filtration and washed with H_2O. Further purification by column chromatography (CH_2Cl_2/hexane = 7/3) and precipitation from CH_2Cl_2 with CH_3OH yielded 30.5 mg (18.4 μmol, 90%) of a red solid. **Mp**.: > 350 °C. **^{1}H NMR** (CD_2Cl_2, 400 MHz): δ = 8.13 (s, 4 H, C*H*$_{PBI}$), 7.43 – 7.40 (m, 12 H, C*H*$_{aryl}$), 7.29 – 7.20 (m, 6 H, C*H*$_{aryl}$), 6.87 – 6.85 (m, 8 H, C*H*$_{aryl}$), 5.27 (br s, 4 H C*H*$_2$), 1.14 (s, 84 H, SiC*H*(C*H*$_3$)$_3$) ppm. **^{13}C NMR** (CD_2Cl_2, 100 MHz): δ = 163.3, 155.9, 155.7, 137.6, 134.2, 133.1, 129.0, 128.7, 127.8, 123.4, 121.1, 120.4, 120.2, 120.1, 106.2, 91.1, 44.0, 18.8, 11.4 ppm. **HRMS** (ESI, pos. mode, CH_3CN/CH_3Cl): *m/z* 1681.7817 $[M+Na]^+$, calculated for $C_{106}H_{118}NNaO_8Si_4$: 1681.7858. **UV-vis** ($CHCl_3$), λ_{max} (ε_{max}): 576 nm (42 × 10^3 L mol^{-1} cm^{-1}), 537 nm (26 × 10^3 L mol^{-1} cm^{-1}). **Fluorescence** ($CHCl_3$), λ_{max} (λ_{ex}): 607 nm (530 nm), Φ_{fl} = 92%.

Synthesis of glycerolether 48

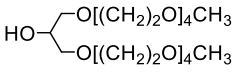

48

This literature-known compound was prepared according to a modified procedure.[124b] Under nitrogen atmosphere sodium (0.19 g, 8.07 mmol) was dissolved in tetraethylene glycol monomethyl ether (5.00 g, 24.3 mmol) at 100 °C. After cooling to 80 °C epichlorohydrin (0.63 mL, 0.75 g, 8.85 mmol) was added dropwise. The reaction mixture was heated overnight

at 100 °C. Precipitated salts were removed by filtration and the crude product was purified by column chromatography (ethyl acetate/CH_3OH = 100/10) to obtain 1.25 g (2.64 mmol, 32%) of the product as a colorless oil. **^{1}H-NMR** (400 MHz, $CDCl_3$): 4.00 – 3.94 (m, 1 H, C*H*OH), 3.67 – 3.63 (m, 30 H, OCH_2), 3.56 – 3.53 (m, 6 H, OCH_2), 3.38 (s, 6 H, OCH_3), 2.44 (br s, 1 H, O*H*). **HRMS** (ESI, pos. mode, CH_3OH): *m/z* 495.27782 $[M+Na]^+$, calculated for $C_{21}H_{44}NaO_{11}$: 495.27758. The characterization data are in accordance with literature.[124a]

Synthesis of glycerolether tosylate 49

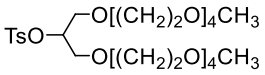

49

This unknown compound was prepared according to a modified literature procedure.[124b] Under nitrogen atmosphere, NaH (60% dispersion in mineral oil, 0.08 g, 3.15 mmol) was added to a solution of alcohol **48** (1.24 g, 2.62 mmol) in dry THF (20 mL) at room temperature. After the hydrogen evolution ceased, the reaction mixture was cooled to 0 °C and a solution of tosyl chloride (0.75 g, 3.94 mmol) in dry THF (10 mL) was added dropwise. After stirring at room temperature for 16 h, the solvent was evaporated and the residue was purified by column chromatography (silica gel, CH_2Cl_2/CH_3OH = 100/10). The product (1.28 g, 2.03 mmol, 77%) was obtained as a colorless oil. **^{1}H NMR** (400 MHz, $CDCl_3$): δ = 7.82 – 7.79 (m, 2 H, CH_{Ts}), 7.33 – 7.31 (m, 2 H, CH_{Ts}), 4.68 (pent, 1 H, C*H*OTs), 3.65 – 3.58 (m, 24 H, OCH_2), 3.55 – 3.49 (m, 12 H, OCH_2), 3.37 (s, 6 H, OCH_3), 2.44 (s, 3 H, CH_3) ppm. **^{13}C NMR** (100 MHz, $CDCl_3$): δ = 144.7, 134.2, 129.7, 128.2, 79.8, 72.1, 71.0, 70.7 (3 signals), 70.5, 69.8, 59.2, 21.8 ppm. **HRMS** (ESI, pos. mode, CH_3OH): *m/z* 649.28619 $[M+Na]^+$, calculated for $C_{28}H_{50}NaO_{13}S$: 649.28643.

Synthesis of acetyl-protected (*S*)-1-(3-bromophenyl)ethylamine (51)

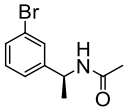

The reaction conditions were adopted from literature.[172b] Under nitrogen atmosphere, (*S*)-1-(3-bromophenyl)ethylamine (714 μL, 1.00 g, 5.00 mmol, 1 eq.) was dissolved in dry CH_2Cl_2 (5 mL). After the addition of Ac_2O (708 μL, 765 mg, 7.50 mmol, 1.5 eq) and NEt_3 (1.04 mL,

759 mg, 7.50 mmol, 1.5 eq.) the reaction was stirred overnight at room temperature. Then it was successively washed with 2 N HCl (1x), saturated aqueous $NaHCO_3$ solution (1x) and brine (1x). The organic phase was dried over Na_2SO_4. After removal of the solvent the crude product was purified by column chromatography (silica gel, CH_2Cl_2/CH_3OH = 100/5) to give 1.10 g (453 mmol, 91%) of a colorless oil. **^{1}H NMR** (CD_2Cl_2, 400 MHz): δ = 7.46 – 7.35 (m, 1H, CH_{aryl}), 7.40 – 7.38 (m, 1H, CH_{aryl}), 7.27 – 7.20 (m, 2H, CH_{aryl}), 5.83 (br s, 1H, N*H*), 4.99 (quint, 1H, , ^3J = 7.1 Hz, C*H*), 1.94 (s, 3H, CH_3) 1.43 (d, ^3J = 7.0 Hz, 3H, CH_3) ppm. **^{13}C NMR** (CD_2Cl_2, 100 MHz): δ = 169.3, 146.8, 130.6, 130.5, 129.4, 125.3, 122.9, 48.8, 23.5, 22.2 ppm. **HRMS** (ESI, pos. mode, CH_3CN/CH_3Cl): *m/z* 264.00005 $[M+Na]^+$, calculated for $C_{10}H_{12}BrNNaO^+$: 263.99945.

Synthesis of Cyclophane [2PBI]-1m via [2PBI]-5m

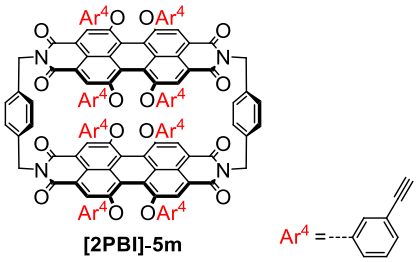

[2PBI]-5m: Under nitrogen atmosphere, cyclophane **[2PBI]-4m** (30.0 mg, 9.48 μmol) was dissolved in dry THF (5 mL) and cooled to 0 °C. Tetrabutyl ammonium fluoride was added as 1 M solution in THF (950 μmol in 950 μL). After 10 min, the reaction was quenched by addition of 2 N HCl (5 mL) upon which the crude product precipitated. The precipitate was collected by filtration, washed with H_2O and further purified by column chromatography (silica gel, $CHCl_3$). Precipitation from $CHCl_3$ solution with CH_3OH yielded 8.30 mg (4.34 μmol, 43%) of a red solid. Some of the starting material could be recovered (2.50 mg, 790 nmol). As **[2PBI]-5m** is instable it was immediately converted. **MS** (MALDI, pos. mode, DCTB 1:3 in $CHCl_3$): 1913.526 $[M]^+$, calculated for $C_{128}H_{64}N_4O_{16}$: 1913.932.

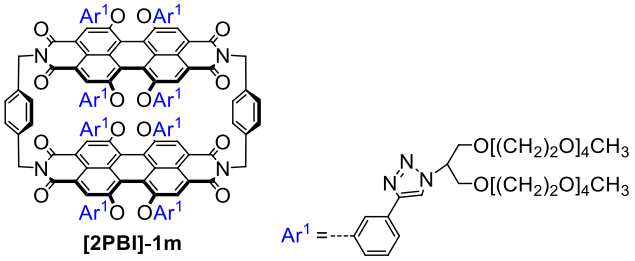

[2PBI]-1m: **[2PBI]-5m** (8.3 mg, 4.34 μmol) and azide **45** (38.8 mg, 78.1 μmol) were dissolved in dry THF (2 mL) and degassed by the freeze pump thaw procedure. Under nitrogen atmosphere, a mixture of CuOAc (213 μg, 1.73 μmol) and sodium ascorbate (6.87 mg, 34.7 μmol) in dry THF (0.5 mL) and tris(benzyltriazolylmethyl)amine (1.84 mg, 3.47 μmol) were added. The reaction was stirred for 20 h at 60 °C. The solvent was evaporated under reduced pressure and the residue was redissolved in $CHCl_3$. The organic phase was washed successively with 10 % NH_3 aqueous solution, concentrated NH_4Cl solution and H_2O. The crude product was purified first by gravity coloumn chromatography (silica gel, $CH_2Cl_2/CHCl_3/CH_3OH$ = 5/5/1) and then by preparative thin layer chromatography (silica gel, CH_2Cl_2/CH_3OH = 92/8). Slow precipitation from $CHCl_3$ with cyclohexane yielded 12.7 mg (2.15 μmol, 50 %) of a soft violet solid. **Mp**.: > 100 °C (decomposition). **^{1}H NMR** ($(CD_3)_2CO$), 400 MHz):[17] δ = 8.29 (s, 4 H, CH_{PBI}), 8.27 (s, 4 H, CH_{PBI}), 8.07 (s, 4 H, C$H_{triazol}$), 7.97 (s, 4 H, C$H_{triazol}$), 7.76 – 7.69 (m, 16 H, CH_{aryl}), 7.34 (s, 8 H, CH_{aryl} + 8 H, CH_{linker}), 7.05 (br s, 8 H, CH_{aryl}), 6.83 (br s, 8 H, CH_{aryl}), 5.31 (br s, 4 H, C$H_{2\ linker}$), 5.05 (br s, 4 H, C$H_{2\ linker}$), 4.99 (br s, 8 H, NC*H*), 4.00 – 3.99 (m, 32 H, NCHCH_2), 3.61 – 3.35 (m, 224 H, OCH_2), 3.35 (m, 32 H, OCH_2), 3.19 (2 s, 48 H, OCH_3) ppm. **^{13}C NMR** (CD_3CN, 150 MHz, 340 K): δ = 163.9, 157.3, 156.5, 147.1, 139.0, 134.7, 133.6, 131.6, 131.0, 124.3, 122.8, 122.2, 121.0, 118.1, 73.0, 72.1, 71.7, 71.6 (3 signals), 71.5 (2 signals), 71.4, 71.3 (2 signals), 62.5, 59.2, 43.6 ppm. **HRMS** (ESI, pos. mode, CH_3CN/CH_3Cl): *m/z* 1495.69096 $[M+4Na]^{4+}$, calculated for $C_{296}H_{408}N_{28}Na_4O_{96}^{4+}$: 1495.68684. **UV-vis** λ_{max} (ε_{max}): $CHCl_3$: 574 nm (65 × 10^3 L mol^{-1} cm^{-1}), 538 nm (54 × 10^3 L mol^{-1} cm^{-1}); CH_3CN: 574 nm (65 × 10^3 L mol^{-1} cm^{-1}), 537 nm (53 × 10^3 L mol^{-1} cm^{-1}). **Fluorescence** λ_{max} (λ_{ex}): $CHCl_3$: 614 nm (530 nm), Φ_{fl} = 15%; CH_3CN: 609 nm (530 nm), Φ_{fl} = 1%.

[17] The dynamic equilibrium caused by the inversion of the PBI core twist of **[1PBI]-1m** as discussed in chapter 3.4 is considerably slowed down at room temperature. Thus, signal splitting is observed between the protons oriented either into the direction of the cavity or away from it as they experience different shielding effects.

Synthesis of Cyclophane [2PBI]-1p via [2PBI]-4p

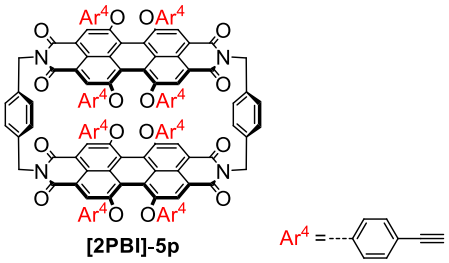

[2PBI]-5p: Under nitrogen atmosphere, cyclophane **[2PBI]-4p** (45.0 mg, 14.2 μmol) was dissolved in dry THF (5 mL) and cooled to 0 °C. Tetrabutyl ammonium fluoride was added as 1 M solution in THF (142 μmol in 142 μL). After 10 min, the reaction was quenched by addition of 2 N HCl (5 mL) upon which the crude product precipitated. The precipitate was collected by filtration, washed with H_2O and further purified by column chromatography (silica gel, $CHCl_3$). Precipitation from $CHCl_3$ solution with CH_3OH yielded 20.1 mg (10.7 μmol, 75%) of a red solid. As **[2PBI]-5p** is instable it was immediately converted. **MS** (MALDI, neg. mode, DCTB 1:3 in $CHCl_3$): 1913.436 $[M]^-$, calculated for $C_{128}H_{64}N_4O_{16}$: 1913.432.

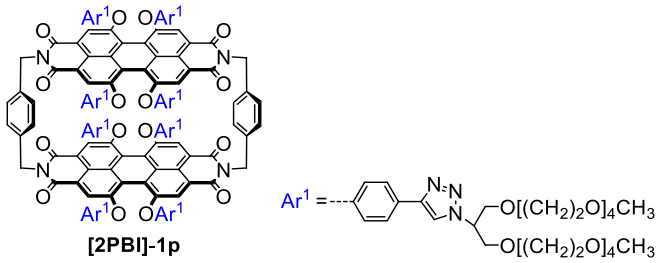

[2PBI]-1p: **[2PBI]-5p** (20.1 mg, 10.7 μmol) and azide **45** (95.9 mg, 193 μmol) were dissolved in dry THF (5 mL) and degassed by the freeze pump thaw procedure. Under nitrogen atmosphere, a mixture of CuOAc (525 μg, 4.28 μmol) and sodium ascorbate (17.0 mg, 85.7 μmol) in dry THF (0.5 mL) and tris(benzyltriazolylmethyl)amine (4.55 mg, 8.57 μmol) were added. The reaction was stirred for 20 h at 50 °C. The solvent was evaporated under reduced pressure and the residue was redissolved in $CHCl_3$. The organic phase was washed successively with 10 % NH_3 aqueous solution, concentrated NH_4Cl solution and H_2O. The crude product was purified first by gravity column chromatography (silica gel, $CH_2Cl_2/CHCl_3/CH_3OH$ = 5/5/1) and then by preparative thin layer chromatography (silica gel, CH_2Cl_2/CH_3OH = 92/8). Slow precipitation from $CHCl_3$ with cyclohexane yielded 45.1 mg (7.65 μmol, 75%) of a soft violet solid. **Mp**.: > 100 °C (decomposition). **^{1}H NMR** (CD_3CN, 600 MHz, 340 K): δ = 8.28 (s, 8 H, CH_{PBI}), 7.95 (s, 8 H, C$H_{triazol}$), 7.86 (br s, 16 H, CH_{aryl}),

7.31 (s, 8 H, C*H*linker), 7.06 (br s, 16 H, C*H*aryl), 5.22 (br s, 8 H, C*H*2 linker), 5.02 – 5.00 (m, 8 H, NC*H*), 4.04 – 3.97 (m, 32 H, NCHC*H*2), 3.63 – 3.53 (m, 192 H, OC*H*2), 3.50 – 3.48 (m, 32 H, OC*H*2), 3.40 – 3.38 (m, 32 H, OC*H*2), 3.21 (2 s, 2 × 24 H, OC*H*3) ppm. **^{13}C NMR** (CD_3CN, 150 MHz, 340 K): δ = 163.8, 156.2, 147.3, 138.9, 133.8, 131.0, 129.5, 128.5, 124.2, 122.0, 121.3, 120.8, 73.0, 72.1, 71.7, 71.6 (4 signals), 71.4 (2 signals), 71.3 (2 signals), 62.4, 59.2, 43.6 ppm. **HRMS** (ESI, pos. mode, CH_3CN/CH_3Cl): *m/z* 1964.5889 $[M+3H]^{3+}$, calculated for $C_{296}H_{411}N_{28}O_{96}^{3+}$: 1964.6041. **UV-vis** λ_{max} (ε_{max}): $CHCl_3$: 581 nm (69 × 10^3 L mol^{-1} cm^{-1}), 542 nm (54 × 10^3 L mol^{-1} cm^{-1}); CH_3CN: 575 nm (64 × 10^3 L mol^{-1} cm^{-1}), 537 nm (53 × 10^3 L mol^{-1} cm^{-1}); H_2O: 596 nm (49 × 10^3 L mol^{-1} cm^{-1}), 555 nm (41 × 10^3 L mol^{-1} cm^{-1}). **Fluorescence** λ_{max} (λ_{ex}): $CHCl_3$: 620 nm (530 nm), Φ_{fl} = 8%; CH_3CN: 615 nm (530 nm), Φ_{fl} < 1%.

Synthesis of Cyclophane [2PBI]-4m

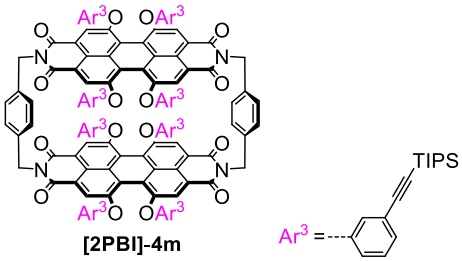

Under nitrogen atmosphere, 1,6,7,12-tetra[3-(triisopropylsilylethinyl)phenoxy]-3,4:9,10-tetra-carboxylic acid perylene bisanhydride (**44m**) (350 mg, 236 μmol), *para*-xylylenediamine (32.2 mg, 236 μmol) and imidazole (3.50 g) were dissolved in toluene (650 mL). The reaction was heated to 120 °C for 17 h. Toluene was removed by evaporation and the residue was dissolved in $CHCl_3$. The organic phase was washed with 2 N HCl (2x) and with H_2O (1x) and dried over Na_2SO_4. After evaporation of the solvent, the crude product was purified by column chromatography (silica gel, CH_2Cl_2/cyclohexane = 6/4) and recycling gel permeation chromatography ($CHCl_3$). Precipitation from $CHCl_3$ with CH_3OH yielded 56.4 mg (17.8 μmol, 15%) of a red solid. **Mp**.: > 350 °C. **^{1}H NMR** ($C_2D_2Cl_4$, 600 MHz, 360 K): δ = 8.08 (s, 8 H, C*H*PBI), 7.37 (s, 8 H, C*H*linker), 7.29 – 7.24 (m, 16 H, C*H*aryl), 6.94 (br s, 8 H, C*H*aryl), 6.85 (br s, 8 H, C*H*aryl), 5.29 (br s, 8 H, C*H*2), 1.24 (s, 168 H, SiC*H*(C*H*3)3) ppm. **^{13}C NMR** ($C_2D_2Cl_4$, 150 MHz, 360 K): δ = 162.4, 155.3, 154.7, 136.8, 131.9, 129.7, 129.5, 128.5, 125.6, 122.7, 120.6, 120.2, 119.8, 119.4, 105.9, 99.5, 91.9, 42.6, 18.5, 11.3 ppm. **HRMS** (ESI, pos. mode, CH_3CN/CH_3Cl): *m/z* 1603.73654 $[M+2Na]^{2+}$, calculated for $C_{200}H_{224}N_4Na_2O_{16}Si_8^{2+}$:

1603.73880. **UV-vis** ($CHCl_3$), λ_{max} (ε_{max}): 571 nm (60 × 10^3 L mol^{-1} cm^{-1}), 534 nm (50 × 10^3 L mol^{-1} cm^{-1}). **Fluorescence** ($CHCl_3$) λ_{max} (λ_{ex}): 612 nm (530 nm), Φ_{fl} = 22%.

Synthesis of Cyclophane [2PBI]-4p

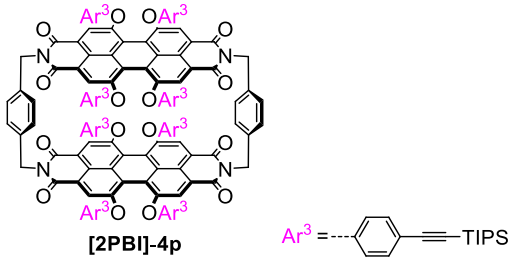

Under nitrogen atmosphere, 1,6,7,12-tetra[4-(triisopropylsilylethinyl)phenoxy]-3,4:9,10-tetra-carboxylic acid perylene bisanhydride (**44p**) (261 mg, 176 μmol), *para*-xylylenediamine (23.9 mg, 176 μmol) and imidazole (2.60 g) were dissolved in toluene (485 mL). The reaction was heated to 120 °C for 16 h. Toluene was removed by evaporation and the residue was dissolved in $CHCl_3$. The organic phase was washed with 2 N HCl (2x) and with H_2O (1x) and dried over Na_2SO_4. After evaporation of the solvent, the crude product was purified by column chromatography (silica gel, CH_2Cl_2/cyclohexane = 6/4) and recycling gel permeation chromatography ($CHCl_3$). Precipitation from $CHCl_3$ with CH_3OH yielded 42.0 mg (13.3 μmol, 15%) of a red solid. **Mp**.: > 350 °C. **^{1}H NMR** ($C_2D_2Cl_4$, 600 MHz, 360 K): δ = 8.09 (s, 8 H, C*H*$_{PBI}$), 7.48 – 7.46 (m, 16 H, C*H*$_{aryl}$), 7.38 (s, 8 H, C*H*$_{linker}$), 6.84 – 6.82 (m, 16 H, C*H*$_{aryl}$), 5.29 (br s, 8 H, C*H*$_2$), 1.24 (s, 168 H, SiC*H*(C*H*$_3$)$_3$) ppm. **^{13}C NMR** ($C_2D_2Cl_4$, 150 MHz, 360 K): δ = 162.3, 154.9, 136.8, 133.7, 131.7, 129.8, 122.7, 120.7, 120.3, 120.2, 119.4, 119.3, 106.1, 91.2, 42.6, 18.5, 11.3 ppm. **HRMS** (ESI, pos. mode, CH_3CN/CH_3Cl): *m/z* 1603.7345 $[M+2Na]^{2+}$, calculated for $C_{200}H_{224}N_4Na_2O_{16}Si_8^{2+}$: 1603.7388. **UV-vis** ($CHCl_3$), λ_{max} (ε_{max}): 575 nm (69 × 10^3 L mol^{-1} cm^{-1}), 537 nm (55 × 10^3 L mol^{-1} cm^{-1}). **Fluorescence** ($CHCl_3$) λ_{max} (λ_{ex}): 613 nm (530 nm), Φ_{fl} = 16%.

Synthesis of ref-PBI-1m via PBI 47m

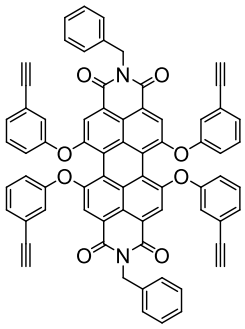

47m

PBI 47m: Under nitrogen atmosphere, PBI **46m** (32.3 mg, 19.5 μmol) was dissolved in dry THF (6 mL) and cooled to 0 °C. Tetrabutyl ammonium fluoride was added as 1 M solution in THF (117 μmol in 117 μL). After 15 min, the reaction was quenched by addition of 2 N HCl (6 mL), upon which the crude product precipitated. The precipitate was collected by filtration, washed with H_2O and further purified by column chromatography (silica gel, CH_2Cl_2/cyclohexane = 8/2). Precipitation from CH_2Cl_2 solution with CH_3OH yielded 14.9 mg (14.3 μmol, 78%) of a red solid. Intermediate **47m** is instable and was immediately converted. **^{1}H-NMR** (CD_2Cl_2, 400 MHz): δ = 8.16 (s, 4 H, CH_{PBI}), 7.43 – 7.41 (m, 4 H, CH_{aryl}), 7.29 – 7.22 (m, 14 H, CH_{aryl}), 7.03 – 7.02 (m, 4 H, CH_{aryl}), 6.97 – 6.92 (m, 4 H, CH_{aryl}), 5.27 (br s, 4 H CH_2), 3.12 (s, 4 H, C≡CH) ppm. **HRMS** (ESI, pos. mode, CH_3CN/CH_3Cl): *m/z* 1034.25625 $[M]^+$, calculated for $C_{70}H_{38}N_2O_8$: 1034.26282.

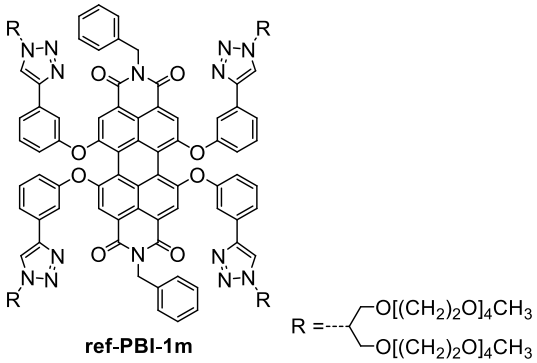

ref-PBI-1m

ref-PBI-1m: **PBI 47m** (14.9 mg, 14.4 μmol) and azide **45** (43.0 mg, 86.3 μmol) were dissolved in dry THF (3 mL) and degassed by the freeze pump thaw procedure. Under nitrogen atmosphere, a mixture of CuOAc (353 μg, 2.88 μmol) and sodium ascorbate (5.70 mg, 28.8 μmol) in dry THF (0.5 mL) and tris(benzyltriazolylmethyl)amine (1.53 mg, 2.88 μmol) were added. The reaction was stirred for 20 h at 60 °C. The solvent was evaporated and the

residue was redissolved in $CHCl_3$. The organic phase was washed successively with 10 % NH_3 aqueous solution, concentrated NH_4Cl solution and H_2O. The crude product was purified first by gravity coloumn chromatography (silica gel, CH_2Cl_2/CH_3OH = 100/6) and then by preparative thin layer chromatography (silica gel, CH_2Cl_2/CH_3OH = 100/6). Slow precipitation from $CHCl_3$ solution with cyclohexane yielded 19.5 mg (14.4 μmol, 45%) of a soft violet solid. **Mp**.: > 100 °C (decomposition). **^{1}H NMR** ($(CD3)_2CO$, 400 MHz): δ = 8.31 (s, 4 H, CH_{PBI}), 8.20 (s, 4 H, C$H_{triazol}$), 7.73 – 7.71 (m, 4 H, CH_{aryl}), 7.62 – 7.61 (m, 4 H, CH_{aryl}), 7.41 – 7.37 (m, 8 H, CH$_{aryl}$), 7.26 – 7.16 (m, 6 H, CH_{aryl}), 7.08 – 7.05 (m, 4 H, CH_{aryl}), 5.21 (br s, 4 H, NCH_2), 5.00 – 4.94 (m, 4 H, NCH), 4.02 – 3.92 (m, 16 H, NCHCH_2), 3.62 – 3.59 (m, 16 H, OCH_2), 3.56 – 3.53 (m, 16 H, OCH_2), 3.50 – 3.49 (m, 80 H, OCH_2), 3.41 – 3.38 (m, 16 H, OCH_2), 3.22 (s, 24 H, OCH_3) ppm. **^{13}C NMR** (CD_3CN, 150 MHz): δ = 163.8, 156.8, 156.4, 146.6, 138.2, 134.1, 133.6, 131.4, 129.3, 128.9, 128.9, 123.7, 122.4, 121.9, 121.3, 120.8, 120.6, 119.9, 117.6, 72.5, 71.4, 71.0 (3 signals), 70.8 (2 signals), 70.7, 61.7, 58.8, 44.3 ppm. **HRMS** (ESI, pos. mode, CH_3CN/CH_3Cl): *m/z* 1512.73436 $[M+2H]^{2+}$, calculated for $C_{154}H_{212}N_{14}O_{48}^{2+}$: 1512.72837. **UV-vis** λ_{max} (ε_{max}): $CHCl_3$: 577 nm (40 × 10^3 L mol^{-1} cm^{-1}), 538 nm (25 × 10^3 L mol^{-1} cm^{-1}); CH_3CN: 565 nm (38 × 10^3 L mol^{-1} cm^{-1}), 529 nm (24 × 10^3 L mol^{-1} cm^{-1}), acetone: 566 nm (38 × 10^3 L mol^{-1} cm^{-1}), 529 nm (25 × 10^3 L mol^{-1} cm^{-1}). **Fluorescence** λ_{max} (λ_{ex}): $CHCl_3$: 609 nm (530 nm), Φ_{fl} = 93%; CH_3CN: 600 nm (530 nm), Φ_{fl} = 87%; acetone: 599 nm (530 nm), Φ_{fl} = 90%.

Synthesis of ref-PBI-1p via PBI 47p

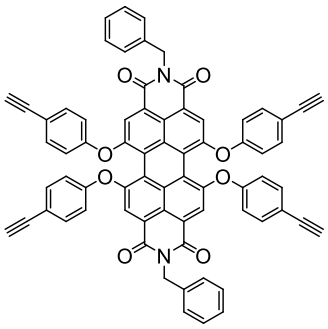

47p

PBI 47p: Under nitrogen atmosphere, PBI **46p** (24.0 mg, 14.5 μmol) was dissolved in dry THF (4 mL) and cooled to 0 °C. Tetrabutyl ammonium fluoride was added as 1 M solution in THF (90 μmol in 90 μL). After 15 min, the reaction was quenched by addition of 2 N HCl (4 mL), upon which the crude product precipitated. The precipitate was collected by filtration, washed

with H_2O and further purified by column chromatography (silica gel, CH_2Cl_2/hexane = 9/1). Precipitation from CH_2Cl_2 solution with CH_3OH yielded 9.70 mg (9.37 μmol, 65%) of a red solid. Intermediate **47p** is instable and was immediately converted. **^{1}H-NMR** (CD_2Cl_2, 400 MHz): δ = 8.15 (s, 4 H, C*H*$_{PBI}$), 7.41 – 7.39 (m, 12 H, C*H*$_{aryl}$), 7.28 – 7.20 (m, 6 H, C*H*$_{aryl}$), 6.88 – 6.86 (m, 8 H, C*H*$_{aryl}$), 5.25 (br s, 4 H C*H*$_2$), 3.14 (s, 4 H, C≡C*H*) ppm. **HRMS** (ESI, pos. mode, CH_3CN/CH_3Cl): *m/z* 1034.2582 $[M]^+$, calculated for $C_{70}H_{38}N_2O_8$: 1034.2623.

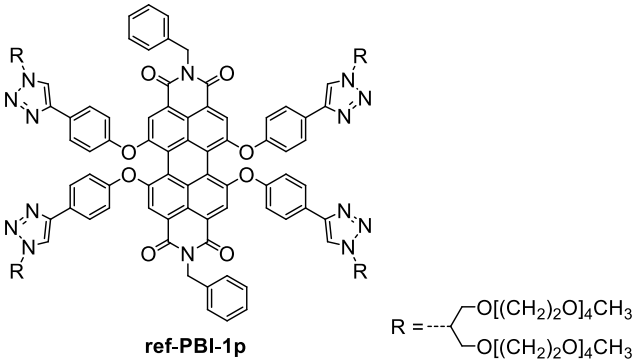

ref-PBI-1p

ref-PBI-1p: PBI **47p** (9.70 mg, 9.37 μmol) and azide **45** (28.8 mg, 57.9 μmol) were dissolved in dry THF (5 mL) and degassed by the freeze pump thaw procedure. Under nitrogen atmosphere, a mixture of CuOAc (236 μg, 1.93 μmol) and sodium ascorbate (3.83 mg, 19.3 μmol) in dry THF (0.5 mL) and tris(benzyltriazolylmethyl)amine (1.00 mg, 1.93 μmol) were added. The reaction was stirred for 20 h at 50 °C. The solvent was evaporated and the residue was redissolved in $CHCl_3$. The organic phase was washed successively with 10 % NH_3 aqueous solution, concentrated NH_4Cl solution and H_2O. The crude product was purified first by gravity coloumn chromatography (silica gel, CH_2Cl_2/CH_3OH = 100/5) and then by preparative thin layer chromatography (silica gel, CH_2Cl_2/CH_3OH = 100/6). Slow precipitation from $CHCl_3$ solution with cyclohexane yielded 11.3 mg (3.71 μmol, 38%) of a soft violet solid. **Mp**.: > 100 °C (decomposition). **^{1}H NMR** (CD_3CN, 400 MHz): δ = 8.19 (s, 4 H, C*H*$_{PBI}$), 7.99 (s, 4 H, C*H*$_{triazol}$), 7.75 – 7.73 (m, 8 H, C*H*$_{aryl}$), 7.31 – 7.30 (m, 4 H, CH$_{aryl}$), 7.26 – 7.17 (m, 6 H, C*H*$_{aryl}$), 7.01 – 6.99 (m, 8 H, C*H*$_{aryl}$), 5.14 – 5.11 (m, 4 H, NC*H*$_2$), 4.97 – 4.91 (m, 4 H, NC*H*), 3.96 – 3.85 (m, 16 H, NCHC*H*$_2$), 3.59 – 3.54 (m, 16 H, OC*H*$_2$), 3.51 – 3.45 (m, 96 H, OC*H*$_2$), 3.39 – 3.37 (m, 16 H, OC*H*$_2$), 3.21 (s, 24 H, OC*H*$_3$) ppm. **^{13}C NMR** (CD_3CN, 100 MHz): δ = 163.8, 156.4, 156.0, 146.8, 138.2, 133.6, 129.4, 128.9, 128.8, 128.3, 128.0, 123.7, 121.5, 121.3, 120.7, 120.6, 72.5, 71.5, 71.1 (3 signals), 70.9, 70.8, 61.8, 58.9 ppm. **HRMS** (ESI, pos. mode, CH_3CN/CH_3Cl): *m/z* 1512.7269 $[M+2H]^{2+}$, calculated for $C_{154}H_{212}N_{14}O_{48}^{2+}$: 1512.7284. **UV-vis** λ_{max} (ε_{max}): $CHCl_3$: 582 nm (40×10^3 L mol^{-1} cm^{-1}), 541 nm (24×10^3 L mol^{-1} cm^{-1});

CH_3CN: 569 nm (37×10^3 L mol^{-1} cm^{-1}), 531 nm (23×10^3 L mol^{-1} cm^{-1}). **Fluorescence** λ_{max} (λ_{ex}): $CHCl_3$: 614 nm (530 nm), Φ_{fl} = 53%; CH_3CN: 604 nm (530 nm), Φ_{fl} = 1%.

Synthesis of (*S*)-G13

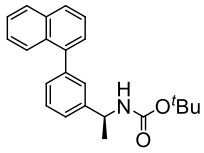

(*S*)-**G13**

The reaction conditions were adopted from literature.[173] Under nitrogen atmosphere, **51**[172a] (800 mg, 2.66 mmol, 1 eq.), 1-naphthylboronic acid (550 mg, 3.20 mmol, 1.2 eq.), Pd_2dba_3 (11.8 mg, 12.9 μmol, 0.5 mol%) and PPh_3 (140 mg, 532 μmol, 0.2 eq.) were dissolved in dry toluene (10.8 mL). The mixture was stirred at room temperature. After 10 min, Na_2CO_3 (1.13 g, 10.7 mmol, 4 eq.) and a mixture (1/1 vol%) of H_2O/EtOH (3 mL) were added and the reaction was heated to 95 °C for 24 h. After cooling down to room temperature, the mixture was extracted with CH_2Cl_2 (3x). The organic extracts were combined, washed with H_2O (1x) and dried over Na_2SO_4. After evaporation of the solvent, the crude product was purified by column chromatography (silica gel, CH_2Cl_2) and flash chromatography (silica gel, CH_2Cl_2/pentane 80/20 → 100/0). The product (638 mg, 1.84 mmol, 69%) was obtained as a colorless, glassy solid. **Mp**: 44 – 45 °C. **^{1}H NMR** ($CDCl_3$, 400 MHz): δ = 7.93 – 7.86 (m, 3H, CH_{aryl}), 7.55 – 7.37 (m, 8H, CH_{aryl}), 5.06 – 4.56 (br m, 2H, N*H*, C*H*), 1.51 (d, ^3J = 6.2 Hz, 3H, CH_3), 1.44 (s, 9H, (CH_3)$_3$) ppm. **^{13}C NMR** ($CDCl_3$, 100 MHz): δ = 155.2, 144.2, 141.1, 140.3, 133.9, 131.7, 129.0, 128.6, 128.4, 127.8, 127.5, 127.1, 126.2, 126.1, 125.9, 125.5, 125.0, 79.6, 50.3, 28.5, 23.0 ppm. **HRMS** (ESI, pos. mode, CH_3CN/CH_3Cl): *m/z* 370.17736 $[M+Na]^+$, calculated for $C_{23}H_{25}NNaO_2^+$: 370.17775.

Synthesis of (*S*)-G14

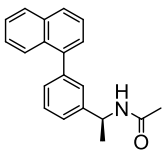

(*S*)-**G14**

The reaction conditions were adopted from literature.[173] Under nitrogen atmosphere, **51** (1.00 g, 4.13 mmol, 1 eq.), 1-naphthylboronic acid (852 mg, 4.96 mmol, 1.2 eq.), Pd_2dba_3

(19 mg, 20.7 μmol, 0.5 mol%) and PPh_3 (21.7 mg, 82.6 μmol, 0.02 eq.) were dissolved in dry toluene (12.0 mL). The mixture was stirred at room temperature. After 10 min, Na_2CO_3 (876 g, 8.26 mmol, 2 eq.) and a mixture (1/1 vol%) of H_2O/EtOH (4 mL) were added and the reaction was heated to 95 °C for 24 h. After cooling down to room temperature, the mixture was extracted with CH_2Cl_2 (3x). The organic extracts were combined, washed with H_2O (1x) and dried over Na_2SO_4. After evaporation of the solvent, the crude product was purified by column chromatography (silica gel, CH_2Cl_2) and flash chromatography (silica gel, CH_2Cl_2/pentane 80/20 → 100/0). The product (705 mg, 2.44 mmol, 59%) was obtained as a colorless, glassy solid. **Mp**: 52 – 54 °C. **^{1}H NMR** ($CDCl_3$, 400 MHz): δ = 7.92 – 7.86 (m, 3H, CH_{aryl}), 7.55 – 7.36 (m, 8H, CH_{aryl}), 5.92 (d, 1H, ^3J = 7.3 Hz, N*H*), 5.22 (quint, 1H, , ^3J = 7.3 Hz, C*H*), 1.98 (s, 3H, CH_3) 1.53 (d, ^3J = 6.9 Hz, 3H, CH_3) ppm. **^{13}C NMR** ($CDCl_3$, 100 MHz): δ = 169.3, 143.4, 141.2, 140.1, 133.9, 131.6, 129.2, 128.7, 128.4, 127.9, 127.8, 127.1, 126.2, 126.0, 125.9, 125.5, 125.3, 48.9, 28.5, 23.6, 22.1 ppm. **HRMS** (ESI, pos. mode, CH_3CN/CH_3Cl): *m/z* 312.13575 $[M+Na]^+$, calculated for $C_{20}H_{19}NNaO^+$: 312.13588.

References

[1] a) G. G. Hammes, *Enzyme Catalysis and Regulation*, Academic Press, Cambridge, **1982**; b) E. A. MacGregor, Š. Janeček, B. Svensson, *Biochim. Biophys. Acta* **2001**, *1546*, 1-20; c) M. Welin, P. Nordlund, *Biochem. Biophys. Res. Commun.* **2010**, *396*, 157-163; d) T. L. Amyes, J. P. Richard, *Biochemistry* **2013**, *52*, 2021-2035.

[2] a) E. Li, K. Hristova, *Biochemistry* **2006**, *45*, 6241-6251; b) B. Gomperts, I. Kramer, P. Tatham, *Signal Transduction*, Academic Press, Cambridge, **2009**; c) G. Krauss, *Biochemistry of Signal Transduction and Regulation*, 5th Edition ed., Wiley-VCH, Weinheim, **2014**; d) W. I. Weis, B. K. Kobilka, *Annu. Rev. Biochem.* **2018**, *87*, 897-919.

[3] a) R. A. Mariuzza, S. E. V. Phillips, R. J. Poljak, *Ann. Rev. Biophys. Biophys. Chem.* **1987**, *16*, 139-159; b) E. A. Greenfield, *Antibodies: A Laboratorial Manual*, Cold Spring Harbor Laboratory Press, U.S., Cold Spring Harbor, **2014**.

[4] a) E. A. Meyer, R. K. Castellano, F. Diederich, *Angew. Chem. Int. Ed.* **2003**, *42*, 1210-1250; b) S. R. J. Hoare, *Drug Discov. Today* **2005**, *10*, 417-427; c) M. G. Savelieff, G. Nam, J. Kang, H. J. Lee, M. Lee, M. H. Lim, *Chem. Rev.* **2019**, *119*, 1221-1322; d) F. M. Ferguson, N. S. Gray, *Nat. Rev. Drug Discov.* **2018**, *17*, 353-377.

[5] a) D. Chandler, *Nature* **2007**, *445*, 831-832; b) H. J. Bakker, *Nature* **2012**, *491*, 533-535; c) D. Ben-Amotz, *Annu. Rev. Phys. Chem.* **2016**, *67*, 617-638.

[6] P. Ball, *Chem. Rev.* **2008**, *108*, 74-108.

[7] a) J.-M. Lehn, *Supramolecular Chemistry: Concepts and Perspectives*, Wiley-VCH, Weinheim, **1995**; b) J. W. Steed, J. L. Atwood, *Supramolecular Chemistry*, 2nd ed., John Wiley & Sons, Chichester, **2009**; c) D. B. Amabilino, P. A. Gale, *Chem. Soc. Rev.* **2017**, *46*, 2376-2377.

[8] K. Ariga, T. Kunitake, *Supramolecular Chemistry - Fundamentals and Applications*, Springer-Verlag, Heidelberg, **2006**.

[9] C. J. Pedersen, *J. Am. Chem. Soc.* **1967**, *89*, 7017-7036.

[10] a) G. W. Gokel, *Comprehensive Supramolecular Chemistry, Vol. I. Molecular Recognition: Receptors for Cationic Guests*, Elsevier, London, **1996**; b) F. Vögtle, *Comprehensive Supramolecular Chemistry, Vol. II. Molecular Recognition: Receptors*

for Molecular Guests, Elsevier, London, **1996**; c) B. D. Smith, *Synthetic Receptors for Biomolecules: Design Principles and Applications*, Royal Society of Chemistry, Cambridge, **2015**.

[11] a) F. Zhang, G. Götz, H. D. F. Winkler, C. A. Schalley, P. Bäuerle, *Angew. Chem. Int. Ed.* **2009**, *48*, 6632-6635; b) M. C. O'Sullivan, J. K. Sprafke, D. V. Kondratuk, C. Rinfray, T. D. W. Claridge, A. Saywell, M. O. Blunt, J. N. O'Shea, P. H. Beton, M. Malfois, H. L. Anderson, *Nature* **2011**, *469*, 72-75.

[12] a) M. Ball, B. Fowler, P. Li, L. A. Joyce, F. Li, T. Liu, D. Paley, Y. Zhong, H. Li, S. Xiao, F. Ng, M. L. Steigerwald, C. Nuckolls, *J. Am. Chem. Soc.* **2015**, *137*, 9982-9987; b) D. J. Kim, K. R. Hermann, A. Prokofjevs, M. T. Otley, C. Pezzato, M. Owczarek, J. F. Stoddart, *J. Am. Chem. Soc.* **2017**, *139*, 6635-6643.

[13] J. Rebek Jr., *Proc. Natl. Acad. Sci. U.S.A.* **2009**, *106*, 10423-10424.

[14] a) H. Abe, Y. Chida, H. Kurokawa, M. Inouye, *J. Org. Chem.* **2011**, *76*, 3366-3371; b) Y. Sun, F. Guo, T. Zuo, J. Hua, G. Diao, *Nat. Commun.* **2016**, *7*, 12042; c) E. J. Dale, N. A. Vermeulen, M. Juríček, J. C. Barnes, R. M. Young, M. R. Wasielewski, J. F. Stoddart, *Acc. Chem. Res.* **2016**, *49*, 262-273; d) G.-W. Zhang, P.-F. Li, Z. Meng, H.-X. Wang, Y. Han, C.-F. Chen, *Angew. Chem. Int. Ed.* **2016**, *55*, 5304-5308; e) K. Yazaki, M. Akita, S. Prusty, D. K. Chand, T. Kikuchi, H. Sato, M. Yoshizawa, *Nat. Commun.* **2017**, *8*, 15914.

[15] a) H.-J. Schneider, *Supramolecular Systems in Biomedical Fields*, Royal Society of Chemistry, Cambridge, **2013**; b) X. Ma, Y. Zhao, *Chem. Rev.* **2015**, *115*, 7794-7839; c) M. J. Webber, R. Langer, *Chem. Soc. Rev.* **2017**, *46*, 6600-6620; d) J. Zhou, G. Yu, F. Huang, *Chem. Soc. Rev.* **2017**, *46*, 7021-7053.

[16] G. Crini, *Chem. Rev.* **2014**, *114*, 10940-10975.

[17] S. J. Barrow, S. Kasera, M. J. Rowland, J. del Barrio, O. A. Scherman, *Chem. Rev.* **2015**, *115*, 12320-12406.

[18] C. Sathiyajith, R. R. Shaikh, Q. Han, Y. Zhang, K. Meguellati, Y.-W. Yang, *Chem. Commun.* **2017**, *53*, 677-696.

[19] S. B. Nimse, T. Kim, *Chem. Soc. Rev.* **2013**, *42*, 366-386.

[20] a) D. Ramaiah, P. P. Neelakandan, A. K. Nair, R. R. Avirah, *Chem. Soc. Rev.* **2010**, *39*, 4158-4168; b) K. Hagiwara, M. Akita, M. Yoshizawa, *Chem. Sci.* **2015**, *6*, 259-263; c) E. M. Peck, W. Liu, G. T. Spence, S. K. Shaw, A. P. Davis, H. Destecroix, B. D. Smith,

J. Am. Chem. Soc. **2015**, *137*, 8668-8671; d) G. Wu, C.-Y. Wang, T. Jiao, H. Zhu, F. Huang, H. Li, *J. Am. Chem. Soc.* **2018**, *140*, 5955-5961.

[21] a) C. A. Hunter, *Chem. Soc. Rev.* **1994**, *23*, 101-109; b) S. Grimme, *Angew. Chem. Int. Ed.* **2008**, *47*, 3430-3434.

[22] D. A. Dougherty, *Acc. Chem. Res.* **2013**, *46*, 885-893.

[23] S. Tsuzuki, *Annu. Rep. Prog. Chem., Sect. C: Phys. Chem.* **2012**, *108*, 69-95.

[24] T. T. Goodnow, M. V. Reddington, J. F. Stoddart, A. E. Kaifer, *J. Am. Chem. Soc.* **1991**, *113*, 4335-4337.

[25] P. P. Neelakandan, P. C. Nandajan, B. Subymol, D. Ramaiah, *Org. Biomol. Chem.* **2011**, *9*, 1021-1029.

[26] M. Herm, O. Molt, T. Schrader, *Chem. Eur. J.* **2001**, *8*, 1485-1499.

[27] a) Y. Ferrand, M. P. Crump, A. P. Davis, *Science* **2007**, *318*, 619-622; b) C. Ke, H. Destecroix, M. P. Crump, A. P. Davis, *Nat. Chem.* **2012**, *4*, 718-723.

[28] F. Würthner, C. R. Saha-Möller, B. Fimmel, S. Ogi, P. Leowanawat, D. Schmidt, *Chem. Rev.* **2016**, *116*, 962-1052.

[29] a) D. Görl, X. Zhang, F. Würthner, *Angew. Chem. Int. Ed.* **2012**, *51*, 6328-6348; b) M. Sun, K. Müllen, M. Yin, *Chem. Soc. Rev.* **2016**, *45*, 1513-1528.

[30] a) P. Spenst, F. Würthner, *Angew. Chem. Int. Ed.* **2015**, *54*, 10165-10168; b) P. Spenst, R. M. Young, M. R. Wasielewski, F. Würthner, *Chem. Sci.* **2016**, *7*, 5428-5434.

[31] a) D. Görl, X. Zhang, V. Stepanenko, F. Würthner, *Nat. Commun.* **2015**, *6*, 7009; b) V. Grande, B. Soberats, S. Herbst, V. Stepanenko, F. Würthner, *Chem. Sci.* **2018**, *9*, 6904-6911.

[32] a) P. M. Dewick, *Medicinal Natural Products: A Biosynthetic Approach*, John Wiley & Sons, Chichester, **2009**; b) M. F. Roberts, *Alkaloids: Biochemistry, Ecology, and Medicinal Applications*, Springer US, New York, **2013**.

[33] P. Spenst, *Xylylene-Bridged Perylene Bisimide Cyclophanes and Macrocycles*, Julius-Maximilians-Universität Würzburg, **2016**.

[34] a) J. Monod, J. Wyman, J.-P. Changeux, *J. Mol. Biol.* **1965**, *12*, 88-118; b) D. E. Koshland, G. Némethy, D. Filmer, *Biochemistry* **1966**, *5*, 365-385.

[35] P. Spenst, F. Würthner, *J. Photochem. Photobiol. C* **2017**, *31*, 114-138.

[36] a) H. Langhals, R. Ismael, *Eur. J. Org. Chem.* **1998**, *1998*, 1915-1917; b) F. Schlosser, M. Moos, C. Lambert, F. Würthner, *Adv. Mater.* **2013**, *25*, 410-414.

[37] P. Spenst, A. Sieblist, F. Würthner, *Chem. Eur. J.* **2017**, *23*, 1667-1675.

[38] P. A. Gale, J. W. Steed, *Supramolecular Chemistry: From Molecules to Nanomaterials. Vol. 1: Concepts*, John Wiley & Sons, Chichester, **2012**.

[39] P. Osswald, F. Würthner, *J. Am. Chem. Soc.* **2007**, *129*, 14319-14326.

[40] J. Sung, A. Nowak-Król, F. Schlosser, B. Fimmel, W. Kim, D. Kim, F. Würthner, *J. Am. Chem. Soc.* **2016**, *138*, 9029-9032.

[41] N. Banerji, G. Angulo, I. Barabanov, E. Vauthey, *J. Phys. Chem. A* **2008**, *112*, 9665-9674.

[42] R. A. Marcus, *Angew. Chem. Int. Ed. Engl.* **1993**, *32*, 1111-1121.

[43] P. S. Cremer, A. H. Flood, B. C. Gibb, D. L. Mobley, *Nat. Chem.* **2017**, *10*, 8.

[44] Y. Chen, Y. Liu, *Chem. Soc. Rev.* **2010**, *39*, 495-505.

[45] M. Giuliani, I. Morbioli, F. Sansone, A. Casnati, *Chem. Commun.* **2015**, *51*, 14140-14159.

[46] T. Ogoshi, T. Yamagishi, Y. Nakamoto, *Chem. Rev.* **2016**, *116*, 7937-8002.

[47] a) N. Ahmed, B. Shirinfar, I. S. Youn, M. Yousuf, K. S. Kim, *Org. Biomol. Chem.* **2013**, *11*, 6407-6413; b) A. M. Agafontsev, T. A. Shumilova, T. Rüffer, H. Lang, E. A. Kataev, *Chem. Eur. J.* **2019**, *25*, 3541-3549.

[48] a) L. Stryer, *Biochemistry*, W.H. Freeman, New York, **1995**; b) S. Doonan, *Nucleic Acids*, The Royal Society of Chemistry, Cambridge, **2004**.

[49] A. M. Agafontsev, A. Ravi, T. A. Shumilova, A. S. Oshchepkov, E. A. Kataev, *Chem. Eur. J.* **2019**, *25*, 2684-2694.

[50] H. Sigel, R. Griesser, *Chem. Soc. Rev.* **2005**, *34*, 875-900.

[51] a) M. Dhaenens, J.-M. Lehn, J.-P. Vigneron, *J. Chem. Soc., Perkin Trans. 2* **1993**, 1379-1381; b) P. Čudić, M. Žinić, V. Tomišić, V. Simeon, J.-P. Vigneron, J.-M. Lehn, *J. Chem. Soc., Chem. Commun.* **1995**, 1073-1075; c) M.-P. Teulade-Fichou, J.-P. Vigneron, J.-M. Lehn, *Supramol. Chem.* **1995**, *5*, 139-147; d) O. Baudoin, F. Gonnet, M.-P. Teulade-Fichou, J. P. Vigneron, J.-C. Tabet, J.-M. Lehn, *Chem. Eur. J.* **1999**, *5*, 2762-2771.

[52] C. Nakai, W. Glinsmann, *Biochemistry* **1977**, *16*, 5636-5641.

[53] P. Cudic, J.-P. Vigneron, J.-M. Lehn, M. Cesario, T. Prangé, *Eur. J. Org. Chem.* **1999**, *1999*, 2479-2484.

[54] N. Berthet, J. Michon, J. Lhomme, M.-P. Teulade-Fichou, J. P. Vigneron, J.-M. Lehn, *Chem. Eur. J.* **1999**, *5*, 3625-3630.

[55] a) I. Piantanida, B. S. Palm, P. Cudic, M. Zinic, H.-J. Schneider, *Tetrahedron Lett.* **2001**, *42*, 6779-6783; b) H. Abe, Y. Mawatari, H. Teraoka, K. Fujimoto, M. Inouye, *J. Org. Chem.* **2004**, *69*, 495-504.

[56] a) P. P. Neelakandan, M. Hariharan, D. Ramaiah, *Org. Lett.* **2005**, *7*, 5765-5768; b) P. P. Neelakandan, M. Hariharan, D. Ramaiah, *J. Am. Chem. Soc.* **2006**, *128*, 11334-11335.

[57] a) S. L. Wiskur, H. Ait-Haddou, J. J. Lavigne, E. V. Anslyn, *Acc. Chem. Res.* **2001**, *34*, 963-972; b) G. Ghale, W. M. Nau, *Acc. Chem. Res.* **2014**, *47*, 2150-2159.

[58] L. Cheng, H. Zhang, Y. Dong, Y. Zhao, Y. Yu, L. Cao, *Chem. Commun.* **2019**, *55*, 2372-2375.

[59] B. Sookcharoenpinyo, E. Klein, C. Ke, A. P. Davis, *Supramol. Chem.* **2013**, *25*, 650-655.

[60] a) E. Klein, M. P. Crump, A. P. Davis, *Angew. Chem. Int. Ed.* **2005**, *44*, 298-302; b) B. Sookcharoenpinyo, E. Klein, Y. Ferrand, D. B. Walker, P. R. Brotherhood, C. Ke, M. P. Crump, A. P. Davis, *Angew. Chem. Int. Ed.* **2012**, *51*, 4586-4590.

[61] M.-H. Li, F. Kwok, W.-R. Chang, C.-K. Lau, J.-P. Zhang, S. C. L. Lo, T. Jiang, D.-C. Liang, *J. Biol. Chem.* **2002**, *29*, 46385-46390.

[62] P. A. Gale, J. W. Steed, *Supramolecular Chemistry: From Molecules to Nanomaterials. Vol. 3: Molecular Recognition*, John Wiley & Sons, Chichester, **2012**.

[63] a) N. Marcotte, A. Taglietti, *Supramol. Chem.* **2003**, *15*, 617-625; b) M. Zhang, W.-J. Ma, C.-T. He, L. Jiang, T.-B. Lu, *Inorg. Chem.* **2013**, *52*, 4873-4879; c) P. Hu, S. Yang, G. Feng, *Org. Biomol. Chem.* **2014**, *12*, 3701-3706.

[64] C. Y. Huang, *Methods Enzymol.* **1982**, *87*, 509-525.

[65] L. K. S. von Krbek, C. A. Schalley, P. Thordarson, *Chem. Soc. Rev.* **2017**, *46*, 2622-2637.

[66] a) D. Monchaud, A. Granzhan, N. Saettel, A. Guédin, J.-L. Mergny, M.-P. Teulade-Fichou, *J. Nucleic Acids* **2010**, 1-19; b) A. Granzhan, D. Monchaud, N. Saettel, A. Guédin, J.-L. Mergny, M.-P. Teulade-Fichou, *J. Nucleic Acids* **2010**, 1-11.

[67] a) C. Jasper, T. Schrader, J. Panitzky, F.-G. Klärner, *Angew. Chem. Int. Ed.* **2002**, *41*, 1355-1358; b) P. Talbiersky, F. Bastkowski, F.-G. Klärner, T. Schrader, *J. Am. Chem. Soc.* **2008**, *130*, 9824-9828.

[68] L. Chen, H.-Y. Zhang, Y. Liu, *J. Org. Chem.* **2012**, *77*, 9766-9773.

[69] a) N. Sewald, H.-D. Jakubke, *Peptides: Chemistry and Biology*, Wiley VCH, Weinheim, **2002**; b) S. Doonan, *Peptides and Proteins*, The Royal Society of Chemistry, Cambridge, **2002**.

[70] J. Lagona, B. D. Wagner, L. Isaacs, *J. Org. Chem.* **2006**, *71*, 1181-1190.

[71] K. I. Assaf, W. M. Nau, *Chem. Soc. Rev.* **2015**, *44*, 394-418.

[72] S. M. Ngola, P. C. Kearney, S. Mecozzi, K. Russell, D. A. Dougherty, *J. Am. Chem. Soc.* **1999**, *121*, 1192-1201.

[73] P. C. Kearney, L. S. Mizoue, R. A. Kumpf, J. E. Forman, A. McCurdy, D. A. Dougherty, *J. Am. Chem. Soc.* **1993**, *115*, 9907-9919.

[74] a) L. A. Ingerman, M. E. Cuellar, M. L. Waters, *Chem. Commun.* **2010**, *46*, 1839-1841; b) N. K. Pinkin, M. L. Waters, *Org. Biomol. Chem.* **2014**, *12*, 7059-7067; c) J. E. Beaver, B. C. Peacor, J. V. Bain, L. I. James, M. L. Waters, *Org. Biomol. Chem.* **2015**, *13*, 3220-3226; d) I. N. Gober, M. L. Waters, *Org. Biomol. Chem.* **2017**, *15*, 7789-7795.

[75] a) L. I. James, J. E. Beaver, N. W. Rice, M. L. Waters, *J. Am. Chem. Soc.* **2013**, *135*, 6450-6455; b) A. G. Mullins, N. K. Pinkin, J. A. Hardin, M. L. Waters, *Angew. Chem. Int. Ed.* **2019**, *58*, 5282-5285.

[76] M. Matache, E. Bogdan, N. D. Hădade, *Chem. Eur. J.* **2014**, *20*, 2106-2131.

[77] T. Gruber, *ChemBioChem* **2018**, *19*, 2324-2340.

[78] C. Li, J. Ma, L. Zhao, Y. Zhang, Y. Yu, X. Shu, J. Li, X. Jia, *Chem. Commun.* **2013**, *49*, 1924-1926.

[79] Q. Duan, W. Zhao, K. Lu, *Tetrahedron Lett.* **2017**, *58*, 4403-4406.

[80] J. K. W. Chui, T. M. Fyles, *Supramol. Chem.* **2008**, *20*, 397-405.

[81] a) M. Herm, T. Schrader, *Chem. Eur. J.* **2000**, *6*, 47-53; b) M. Herm, O. Molt, T. Schrader, *Angew. Chem. Int. Ed.* **2001**, *40*, 3148-3151; c) M. Herm, O. Molt, T. Schrader, *Chem. Eur. J.* **2002**, *8*, 1485-1499; d) O. Molt, D. Rübeling, G. Schäfer, T. Schrader, *Chem. Eur. J.* **2004**, *10*, 4225-4232.

[82] D. A. Dougherty, D. A. Stauffer, *Science* **1990**, *250*, 1558-1560.

[83] D.-S. Guo, V. D. Uzunova, X. Su, Y. Liu, W. M. Nau, *Chem. Sci.* **2011**, *2*, 1722-1734.

[84] A. Paudics, M. Kubinyi, I. Bitter, M. Bojtár, *RSC Adv.* **2019**, *9*, 16856-16862.

[85] a) A. P. Davis, *Org. Biomol. Chem.* **2009**, *7*, 3629-3638; b) C. E. Miron, A. Petitjean, *ChemBioChem* **2015**, *16*, 365-379.

[86] a) E. J. Toone, *Curr. Opin. Struct. Biol.* **1994**, *4*, 719-728; b) M. Ambrosi, N. R. Cameron, B. G. Davis, *Org. Biomol. Chem.* **2005**, *3*, 1593-1608.

[87] J. A. Peters, *Coord. Chem. Rev.* **2014**, *268*, 1-22.

[88] P. Rios, T. S. Carter, T. J. Mooibroek, M. P. Crump, M. Lisbjerg, M. Pittelkow, N. T. Supekar, G.-J. Boons, A. P. Davis, *Angew. Chem. Int. Ed.* **2016**, *55*, 3387-3392.

[89] Y. Ferrand, E. Klein, N. P. Barwell, M. P. Crump, J. Jiménez-Barbero, C. Vicent, G.-J. Boons, S. Ingale, A. P. Davis, *Angew. Chem. Int. Ed.* **2009**, *48*, 1775-1779.

[90] R. A. Tromans, T. S. Carter, L. Chabanne, M. P. Crump, H. Li, J. V. Matlock, M. G. Orchard, A. P. Davis, *Nat. Chem.* **2019**, *11*, 52-56.

[91] a) N. P. Barwell, M. P. Crump, A. P. Davis, *Angew. Chem. Int. Ed.* **2009**, *48*, 7673-7676; b) G. Joshi, A. P. Davis, *Org. Biomol. Chem.* **2012**, *10*, 5760-5763.

[92] P. K. Mandal, B. Kauffmann, H. Destecroix, Y. Ferrand, A. P. Davis, I. Huc, *Chem. Commun.* **2016**, *52*, 9355-9358.

[93] a) H. Destecroix, C. M. Renney, T. J. Mooibroek, T. S. Carter, P. F. N. Stewart, M. P. Crump, A. P. Davis, *Angew. Chem. Int. Ed.* **2015**, *54*, 2057-2061; b) P. Stewart, C. M. Renney, T. J. Mooibroek, S. Ferheen, A. P. Davis, *Chem. Commun.* **2018**, *54*, 8649-8652.

[94] P. Rios, T. J. Mooibroek, T. S. Carter, C. Williams, M. R. Wilson, M. P. Crump, A. P. Davis, *Chem. Sci.* **2017**, *8*, 4056-4061.

[95] T. J. Mooibroek, J. M. Casas-Solvas, R. L. Harniman, C. M. Renney, T. S. Carter, M. P. Crump, A. P. Davis, *Nat. Chem.* **2015**, *8*, 69.

[96] V. Král, O. Rusin, F. P. Schmidtchen, *Org. Lett.* **2001**, *3*, 873-876.

[97] O. Francesconi, M. Martinucci, L. Badii, C. Nativi, S. Roelens, *Chem. Eur. J.* **2018**, *24*, 6828-6836.

[98] A. Vacca, C. Nativi, M. Cacciarini, R. Pergoli, S. Roelens, *J. Am. Chem. Soc.* **2004**, *126*, 16456-16465.

[99] a) H. Kim, S. O. Sablin, R. R. Ramsay, *Arch. Biochem. Biophys.* **1997**, *337*, 137-142; b) Y. Yamazaki, Y. Kawano, *Chem. Pharm. Bull.* **2011**, *59*, 388-391; c) C. Li, Y. Wang, C.-Y. Wang, X. Yi, M. Li, X. He, *Phytomedicine* **2017**, *28*, 10-18.

[100] A. K. Yatsimirsky, *Nat. Prod. Commun.* **2012**, *7*, 369-380.

[101] S. Hamieh, R. F. Ludlow, O. Perraud, K. R. West, E. Mattia, S. Otto, *Org. Lett.* **2012**, *14*, 5404-5407.

[102] P. T. Corbett, J. K. M. Sanders, S. Otto, *Chem. Eur. J.* **2008**, *14*, 2153-2166.

[103] Z. Qi, K. Achazi, R. Haag, S. Dong, C. A. Schalley, *Chem. Commun.* **2015**, *51*, 10326-10329.

[104] a) Z. Miskolczy, L. Biczók, *J. Phys. Chem. B* **2014**, *118*, 2499-2505; b) Z. Miskolczy, L. Biczók, *Phys. Chem. Chem. Phys.* **2014**, *16*, 20147-20156; c) S. Hazra, M. Hossain, G. S. Kumar, *J. Incl. Phen. Macrocycl. Chem.* **2014**, *78*, 311-323; d) S. A. Ahmed, D. Seth, *Chem. Phys. Lett.* **2018**, *692*, 340-344.

[105] R. A. Bradshaw, E. A. Dennis, *Handbook of Cell Signaling*, Elsevier/Academic Press, Cambridge, **2010**.

[106] a) R. K. Montange, R. T. Batey, *Annu. Rev. Biophys.* **2008**, *37*, 117-133; b) P. H. v. Hippel, *Annu. Rev. Biophys. Biomol. Struct.* **2007**, *36*, 79-105.

[107] E. Fischer, *Ber. Dtsch. Chem. Ges.* **1894**, *27*, 2985-2993.

[108] a) I. Wong, S. S. Patel, K. A. Johnson, *Biochemistry* **1991**, *30*, 526-537; b) D. C. Swinney, *Nat. Rev. Drug Discov.* **2004**, *3*, 801-808; c) J.-P. Changeux, *Annu. Rev. Biophys.* **2012**, *41*, 103-133.

[109] a) N. Pozzi, A. D. Vogt, D. W. Gohara, E. Di Cera, *Curr. Opin. Struct. Biol.* **2012**, *22*, 421-431; b) K. S. Chakrabarti, R. V. Agafonov, F. Pontiggia, R. Otten, M. K. Higgins, G. F. X. Schertler, D. D. Oprian, D. Kern, *Cell Rep.* **2016**, *14*, 32-42.

[110] C. A. Fierke, G. G. Hammes, *Methods Enzymol.* **1995**, *249*, 3-37.

[111] a) P. J. Tummino, R. A. Copeland, *Biochemistry* **2008**, *47*, 5481-5492; b) S. Gianni, J. Dogan, P. Jemth, *Biophys. Chem.* **2014**, *189*, 33-39.

[112] A. D. Vogt, E. Di Cera, *Biochemistry* **2012**, *51*, 5894-5902.

[113] a) F.-J. Meyer-Almes, *Eur. Biophys. J.* **2016**, *45*, 245-257; b) F. Paul, T. R. Weikl, *PLOS Comput. Biol.* **2016**, *12*, e1005067.

[114] a) P. Csermely, R. Palotai, R. Nussinov, *Trends Biochem. Sci.* **2010**, *35*, 539-546; b) D.-A. Silva, G. R. Bowman, A. Sosa-Peinado, X. Huang, *PLOS Comput. Biol.* **2011**, *7*, e1002054; c) A. D. Vogt, E. Di Cera, *Biochemistry* **2013**, *52*, 5723-5729.

[115] a) G. G. Hammes, Y.-C. Chang, T. G. Oas, *Proc. Natl. Acad. Sci. U.S.A.* **2009**, *106*, 13737-13741; b) K. G. Daniels, N. K. Tonthat, D. R. McClure, Y.-C. Chang, X. Liu, M. A. Schumacher, C. A. Fierke, S. C. Schmidler, T. G. Oas, *J. Am. Chem. Soc.* **2014**, *136*, 822-825; c) D. Michel, *Biochimie* **2016**, *128-129*, 48-54.

[116] a) T. Haino, D. M. Rudkevich, A. Shivanyuk, K. Rissanen, J. Rebek Jr., *Chem. Eur. J.* **2000**, *6*, 3797-3805; b) R. D. Rasberry, K. D. Shimizu, *Org. Biomol. Chem.* **2009**, *7*, 3899-3905; c) Q.-Q. Wang, D.-X. Wang, H.-B. Yang, Z.-T. Huang, M.-X. Wang, *Chem. Eur. J.* **2010**, *16*, 7265-7275; d) M. Albrecht, E. Isaak, M. Baumert, V. Gossen, G. Raabe, R. Fröhlich, *Angew. Chem. Int. Ed.* **2011**, *50*, 2850-2853; e) T. Sawada, H.

Hisada, M. Fujita, *J. Am. Chem. Soc.* **2014**, *136*, 4449-4451; f) C. M. Hong, D. M. Kaphan, R. G. Bergman, K. N. Raymond, F. D. Toste, *J. Am. Chem. Soc.* **2017**, *139*, 8013-8021; g) F. J. Rizzuto, J. R. Nitschke, *Nat. Chem.* **2017**, *9*, 903; h) Y.-Y. Zhan, T. Kojima, T. Nakamura, T. Takahashi, S. Takahashi, Y. Haketa, Y. Shoji, H. Maeda, T. Fukushima, S. Hiraoka, *Nat. Commun.* **2018**, *9*, 4530; i) A. S. Oshchepkov, T. A. Shumilova, M. Zerson, R. Magerle, V. N. Khrustalev, E. A. Kataev, *J. Org. Chem.* **2019**, *84*, 9034-9043.

[117] Y. Sakata, M. Tamiya, M. Okada, S. Akine, *J. Am. Chem. Soc.* **2019**, *141*, 15597-15604.

[118] F. Würthner, A. Sautter, J. Schilling, *J. Org. Chem.* **2002**, *67*, 3037-3044.

[119] F. Wang, J. Tang, J. Liu, Y. Wang, R. Wang, L. Niu, L. Huang, Z. Huang, *J. Phys. Org. Chem.* **2011**, *24*, 1101-1109.

[120] R. Chinchilla, C. Nájera, *Chem. Soc. Rev.* **2011**, *40*, 5084-5121.

[121] E. Haldon, M. C. Nicasio, P. J. Perez, *Org. Biomol. Chem.* **2015**, *13*, 9528-9550.

[122] a) Q. Wang, T. R. Chan, R. Hilgraf, V. V. Fokin, K. B. Sharpless, M. G. Finn, *J. Am. Chem. Soc.* **2003**, *125*, 3192-3193; b) P. S. Donnelly, S. D. Zanatta, S. C. Zammit, J. M. White, S. J. Williams, *Chem. Commun.* **2008**, 2459-2461.

[123] E.-H. Ryu, Y. Zhao, *Org. Lett.* **2005**, *7*, 1035-1037.

[124] a) K. Kratzat, H. Finkelmann, *Liq. Cryst.* **1993**, *13*, 691-699; b) I.-B. Kim, R. Phillips, U. H. F. Bunz, *Macromolecules* **2007**, *40*, 5290-5293.

[125] a) S. M. Biros, J. Rebek Jr., *Chem. Soc. Rev.* **2007**, *36*, 93-104; b) G. V. Oshovsky, D. N. Reinhoudt, W. Verboom, *Angew. Chem. Int. Ed.* **2007**, *46*, 2366-2393; c) N. Sakai, J. Mareda, S. Matile, *Acc. Chem. Res.* **2008**, *41*, 1354-1365; d) S. Kubik, *Chem. Soc. Rev.* **2010**, *39*, 3648-3663; e) E. A. Kataev, C. Müller, *Tetrahedron* **2014**, *70*, 137-167.

[126] a) E. V. Anslyn, *J. Org. Chem.* **2007**, *72*, 687-699; b) A. E. Hargrove, S. Nieto, T. Zhang, J. L. Sessler, E. V. Anslyn, *Chem. Rev.* **2011**, *111*, 6603-6782; c) O. H. Rubio, R. Taouil, F. M. Muñiz, L. M. Monleón, L. Simón, F. Sanz, J. R. Morán, *Org. Biomol. Chem.* **2017**, *15*, 477-485; d) L. K. S. von Krbek, A. J. Achazi, S. Schoder, M. Gaedke, T. Biberger, B. Paulus, C. A. Schalley, *Chem. Eur. J.* **2017**, *23*, 2877-2883.

[127] a) C. Schmuck, M. Heil, *Chem. Eur. J.* **2006**, *12*, 1339-1348; b) R. N. Dsouza, A. Hennig, W. M. Nau, *Chem. Eur. J.* **2012**, *18*, 3444-3459; c) J. Shao, H. Sun, H. Guo, S. Ji, J. Zhao, W. Wu, X. Yuan, C. Zhang, T. D. James, *Chem. Sci.* **2012**, *3*, 1049-1061; d) D. Maity, M. Li, M. Ehlers, A. Gigante, C. Schmuck, *Chem. Commun.* **2017**, *53*, 208-211.

[128] P. Rios, T. S. Carter, T. J. Mooibroek, M. P. Crump, M. Lisbjerg, M. Pittelkow, N. T. Supekar, G.-J. Boons, A. P. Davies, *Angew. Chem. Int. Ed.* **2016**, *55*, 3387-3392.

[129] a) H. L. Anderson, J. K. M. Sanders, *Angew. Chem. Int. Ed. Engl.* **1990**, *29*, 1400-1403; b) E. M. Seward, R. B. Hopkins, W. Sauerer, S. W. Tam, F. Diederich, *J. Am. Chem. Soc.* **1990**, *112*, 1783-1790; c) D. B. Smithrud, F. Diederich, *J. Am. Chem. Soc.* **1990**, *112*, 339-343.

[130] B. Odell, M. V. Reddington, A. M. Z. Slawin, N. Spencer, J. F. Stoddart, D. J. Williams, *Angew.Chem. Int. Ed. Engl.* **1988**, *27*, 1547-1550.

[131] K. C. Nicolaou, S. A. Snyder, *Classics in total synthesis II*, Wiley VCH, Weinheim, **2003**.

[132] K. E. Brown, W. A. Salamant, L. E. Shoer, R. M. Young, M. R. Wasielewski, *J. Phys. Chem. Lett.* **2014**, *5*, 2588-2593.

[133] a) B. Fimmel, M. Son, Y. M. Sung, M. Grüne, B. Engels, D. Kim, F. Würthner, *Chem. Eur. J.* **2015**, *21*, 615-630; b) J. M. Giaimo, J. V. Lockard, L. E. Sinks, A. M. Scott, T. M. Wilson, M. R. Wasielewski, *J. Phys. Chem. A* **2008**, *112*, 2322-2330.

[134] H. A. Benesi, J. H. Hildebrand, *J. Am. Chem. Soc.* **1949**, *71*, 2703-2707.

[135] P. Thordarson, *Chem. Soc. Rev.* **2011**, *40*, 1305-1323.

[136] K. Stolle, D. Gröger, *Arch. Pharm. Pharm. Med. Chem.* **1968**, *301*, 561-571.

[137] J. N. Israelachvili, D. J. Mitchell, B. W. Ninham, *Biochim. Biophys. Acta Biomembr.* **1977**, *470*, 185-201.

[138] a) C. Mattos, A. C. Clark, *Arch. Biochem. Biophys.* **2008**, *469*, 118-131; b) M.-C. Bellissent-Funel, A. Hassanali, M. Havenith, R. Henchman, P. Pohl, F. Sterpone, D. van der Spoel, Y. Xu, A. E. Garcia, *Chem. Rev.* **2016**, *116*, 7673-7697.

[139] a) J. M. Fox, M. Zhao, M. J. Fink, K. Kang, G. M. Whitesides, *Annu. Rev. Biophys.* **2018**, *47*, 223-250; b) S. Geschwindner, J. Ulander, P. Johansson, *J. Med. Chem.* **2015**, *58*, 6321-6335.

[140] a) E. Krieg, M. M. C. Bastings, P. Besenius, B. Rybtchinski, *Chem. Rev.* **2016**, *116*, 2414-2477; b) Z. Laughrey, B. C. Gibb, *Chem. Soc. Rev.* **2011**, *40*, 363-386.

[141] a) D. Görl, B. Soberats, S. Herbst, V. Stepanenko, F. Würthner, *Chem. Sci.* **2016**, *7*, 6786-6790; b) E. Krieg, A. Niazov-Elkan, E. Cohen, Y. Tsarfati, B. Rybtchinski, *Accounts of Chemical Research* **2019**, *52*, 2634-2646.

[142] a) F. Biedermann, W. M. Nau, H. J. Schneider, *Angew. Chem. Int. Ed.* **2014**, *53*, 11158-11171; b) D.-S. Guo, V. D. Uzunova, K. I. Assaf, A. I. Lazar, Y. Liu, W. M. Nau, *Supramol. Chem.* **2016**, *28*, 384-395.

[143] D. Görl, F. Würthner, *Angew. Chem. Int. Ed.* **2016**, *55*, 12094-12098.

[144] a) P. Friedhoff, A. Schneider, E.-M. Mandelkow, E. Mandelkow, *Biochemistry* **1998**, *37*, 10223-10230; b) K. E. Kadler, Y. Hojima, D. J. Prockop, *J. Biol. Chem.* **1988**, *263*, 10517-10523.

[145] a) H. Fenniri, B.-L. Deng, A. E. Ribbe, K. Hallenga, J. Jacob, P. Thiyagarajan, *Proc. Natl. Acad. Sci. U.S.A.* **2002**, *99*, 6487-6492; b) N. Saito, H. Kobayashi, M. Yamaguchi, *Chem. Sci.* **2016**, *7*, 3574-3580; c) P. Dey, P. Rajdev, P. Pramanik, S. Ghosh, *Macromolecules* **2018**, *51*, 5182-5190.

[146] T. F. A. de Greef, E. W. Meijer, *Nature* **2008**, *453*, 171-173.

[147] P. P. N. Syamala, B. Soberats, D. Görl, S. Gekle, F. Würthner, *Chem. Sci.* **2019**, 9358-9366.

[148] E. Fron, G. Schweitzer, P. Osswald, F. Würthner, P. Marsal, D. Beljonne, K. Müllen, F. C. De Schryver, M. Van der Auweraer, *Photochem. & Photobiol. Sci.* **2008**, *7*, 1509-1521.

[149] K. A. Kistler, C. M. Pochas, H. Yamagata, S. Matsika, F. C. Spano, *J. Phys. Chem. B* **2012**, *116*, 77-86.

[150] M. Sapotta, A. Hofmann, D. Bialas, F. Würthner, *Angew. Chem. Int. Ed.* **2019**, *58*, 3516-3520.

[151] a) M. Kasha, H. R. Rawls, M. A. El-Bayoumi, *Pure Appl. Chem.* **1965**, *11*, 371-392; b) N. J. Hestand, F. C. Spano, *Acc. Chem. Res.* **2017**, *50*, 341-350.

[152] a) E. E. Jelley, *Nature* **1936**, *138*, 1009-1010; b) G. Scheibe, *Angew. Chem.* **1936**, *49*, 563; c) F. Würthner, T. E. Kaiser, C. R. Saha-Möller, *Angew. Chem. Int. Ed.* **2011**, *50*, 3376-3410; d) S. Choi, J. Bouffard, Y. Kim, *Chem. Sci.* **2014**, *5*, 751-755.

[153] a) Z. Chen, A. Lohr, C. R. Saha-Möller, F. Würthner, *Chem. Soc. Rev.* **2009**, *38*, 564-584; b) F. Fennel, S. Wolter, Z. Xie, P.-A. Plötz, O. Kühn, F. Würthner, S. Lochbrunner, *J. Am. Chem. Soc.* **2013**, *135*, 18722-18725.

[154] Z. Chen, B. Fimmel, F. Wurthner, *Org. Biomol. Chem.* **2012**, *10*, 5845-5855.

[155] F. Schlosser, V. Stepanenko, F. Würthner, *Chem. Commun.* **2010**, *46*, 8350-8352.

[156] Z. Chen, U. Baumeister, C. Tschierske, F. Würthner, *Chem. Eur. J.* **2007**, *13*, 450-465.

[157] J. Gershberg, F. Fennel, T. H. Rehm, S. Lochbrunner, F. Würthner, *Chem. Sci.* **2016**, *7*, 1729-1737.

[158] P. P. N. Syamala, F. Würthner, Unpublished Results.

[159] M. Sapotta, P. Spenst, C. R. Saha-Möller, F. Würthner, *Org. Chem. Front.* **2019**, *6*, 892-899.

[160] M. M. Safont-Sempere, P. Osswald, M. Stolte, M. Grüne, M. Renz, M. Kaupp, K. Radacki, H. Braunschweig, F. Würthner, *J. Am. Chem. Soc.* **2011**, *133*, 9580-9591.

[161] a) F.-G. Klärner, B. Kahlert, A. Nellesen, J. Zienau, C. Ochsenfeld, T. Schrader, *J. Am. Chem. Soc.* **2006**, *128*, 4831-4841; b) B. Branchi, P. Ceroni, V. Balzani, M. Casas Cartagena, F.-G. Klärner, T. Schrader, F. Vögtle, *New. J. Chem.* **2009**, *33*, 397-407; c) M. A. Beatty, J. A. Busmann, N. G. Fagen, G. A. E. Garnett, F. Hof, *Supramol. Chem.* **2019**, *31*, 101-107.

[162] E. V. Anslyn, D. A. Dougherty, *Modern Physical Organic Chemistry*, University Science Books, Sausalito, **2006**.

[163] J. P. Behr, *The Lock-and-Key Principle: The State of the Art - 100 Years On*, John Wiley & Sons, Chichester, **2005**.

[164] H.-J. Schneider, A. K. Yatsimirsky, *Chem. Soc. Rev.* **2008**, *37*, 263-277.

[165] H. Wu, Y. Chen, L. Zhang, O. Anamimoghadam, D. Shen, Z. Liu, K. Cai, C. Pezzato, C. L. Stern, Y. Liu, J. F. Stoddart, *J. Am. Chem. Soc.* **2019**, *141*, 1280-1289.

[166] M. Juríček, N. L. Strutt, J. C. Barnes, A. M. Butterfield, E. J. Dale, K. K. Baldridge, J. F. Stoddart, J. S. Siegel, *Nat. Chem.* **2014**, *6*, 222.

[167] G. H. Wagnière, *On Chirality and the Universal Asymmetry: Reflections on Image and Mirror Image*, Wiley-VCH, Weinheim, **2007**.

[168] a) K. Maeda, E. Yashima, *Top. Curr. Chem.* **2006**, *265*, 47-88; b) T. Tazawa, S. Yagai, Y. Kikkawa, T. Karatsu, A. Kitamura, A. Ajayaghosh, *Chem. Commun.* **2010**, *46*, 1076-1078; c) F. García, L. Sánchez, *J. Am. Chem. Soc.* **2012**, *134*, 734-742; d) S. J. George, R. de Bruijn, Ž. Tomović, B. Van Averbeke, D. Beljonne, R. Lazzaroni, A. P. H. J. Schenning, E. W. Meijer, *J. Am. Chem. Soc.* **2012**, *134*, 17789-17796; e) R. J. Hafner, L. Tian, J. C. Brauer, T. Schmaltz, A. Sienkiewicz, S. Balog, V. Flauraud, J. Brugger, H. Frauenrath, *ACS Nano* **2018**, *12*, 9116-9125.

[169] a) S. Allenmark, *Chirality* **2003**, *15*, 409-422; b) N. Berova, G. Pescitelli, A. G. Petrovic, G. Proni, *Chem. Commun.* **2009**, 5958-5980; c) L. Martínez-Rodríguez, N. A. G. Bandeira, C. Bo, A. W. Kleij, *Chem. Eur. J.* **2015**, *21*, 7144-7150; d) J. Labuta, J. P.

Hill, S. Ishihara, L. Hanyková, K. Ariga, *Acc. Chem. Res.* **2015**, *48*, 521-529; e) R. Li, J. J. Holstein, W. Hiller, J. Andréasson, G. H. Clever, *J. Am. Chem. Soc.* **2019**.

[170] a) P. Osswald, F. Würthner, *Chem. Eur. J.* **2007**, *13*, 7395-7409; b) A. Nowak-Król, M. I. S. Röhr, D. Schmidt, F. Würthner, *Angew. Chem. Int. Ed.* **2017**, *56*, 11774-11778.

[171] a) F. Würthner, Z. Chen, F. J. M. Hoeben, P. Osswald, C.-C. You, P. Jonkheijm, J. van Herrikhuyzen, A. P. H. J. Schenning, P. P. A. M. van der Schoot, E. W. Meijer, E. H. A. Beckers, S. C. J. Meskers, R. A. J. Janssen, *J. Am. Chem. Soc.* **2004**, *126*, 10611-10618; b) Z. Xie, V. Stepanenko, K. Radacki, F. Würthner, *Chem. Eur. J.* **2012**, *18*, 7060-7070.

[172] a) Y.-J. Wu, H. He, L.-Q. Sun, A. L'Heureux, J. Chen, P. Dextraze, J. E. Starrett, C. G. Boissard, V. K. Gribkoff, J. Natale, S. I. Dworetzky, *J. Med. Chem.* **2004**, *47*, 2887-2896; b) D. Marcoux, A. B. Charette, *Adv. Synth. Catal.* **2008**, *350*, 2967-2974.

[173] S. Brenet, F. Berthiol, J. Einhorn, *Eur. J. Org. Chem.* **2013**, *2013*, 8094-8096.

[174] W. Wang, A. D. Shaller, A. D. Q. Li, *J. Am. Chem. Soc.* **2008**, *130*, 8271-8279.

[175] M. Hesse, H. Meier, B. Zeeh, *Spectroscopic Methods in Organic Chemistry*, Thieme, Stuttgart, **1997**.

[176] Z. Xie, F. Würthner, *Org. Lett.* **2010**, *12*, 3204-3207.

[177] P. Osswald, M. Reichert, G. Bringmann, F. Würthner, *J. Org. Chem.* **2007**, *72*, 3403-3411.

[178] N. J. Schuster, D. W. Paley, S. Jockusch, F. Ng, M. L. Steigerwald, C. Nuckolls, *Angew. Chem. Int. Ed.* **2016**, *55*, 13519-13523.

[179] N. Berova, K. Nakanashi, R. W. Woody, R. Woody, *Circular Dichroism: Principles and Applications*, John Wiley & Sons, New York, **2000**.

[180] M. M. Safont-Sempere, P. Osswald, K. Radacki, F. Würthner, *Chem. Eur. J.* **2010**, *16*, 7380-7384.

[181] D. E. Koshland Jr., *J. Cell. Comp. Physiol.* **1959**, *54*, 245-258.

[182] A. D. Vogt, N. Pozzi, Z. Chen, E. Di Cera, *Biophys. Chem.* **2014**, *186*, 13-21.

[183] G. Seybold, G. Wagenblast, *Dyes Pigm.* **1989**, *11*, 303-317.

[184] H. Ceyman, *Synthesis and Optical Spectroscopic Properties of Squaraine Superchromophores*, Julius-Maximilians-Universität Würzburg, **2016**.

[185] P. K. Arora, N. J. Riachi, G. C. Fiedler, M. P. Singh, F. Abdallah, S. I. Harik, L. M. Sayre, *Life Sci.* **1990**, *46*, 379-390.

[186] H. Schieferstein, M. Piel, F. Beyerlein, H. Lüddens, N. Bausbacher, H.-G. Buchholz, T. L. Ross, F. Rösch, *Bioorg. Med. Chem.* **2015**, *23*, 612-623.

[187] J. J. P. Stewart, *J. Mol. Model.* **2013**, *19*, 1-32.

[188] a) J. D. C. Maia, G. A. U. Carvalho, C. P. Mangueira, S. R. Santana, L. A. F. Cabral, G. B. Rocha, *J. Chem. Theory and Comput.* **2012**, *8*, 3072-3081; b) J. J. P. Stewart, MOPAC2012, version 14.045, http://OpenMOPAC.net, Stewart Computational Chemistry.

[189] J. J. P. Stewart, *J. Mol. Model.* **2007**, *13*, 1173-1213.

[190] J. Řezáč, P. Hobza, *J. Chem. Theory Comput.* **2012**, *8*, 141-151.

[191] J. J. P. Stewart, MOPAC2016, version 18.346L, http://OpenMOPAC.net, Stewart Computational Chemistry.

[192] A. Klamt, G. Schüürmann, *J. Chem. Soc., Perkin Trans. 2* **1993**, 799-805.

Danksagung

Mein besonderer Dank gilt Prof. Dr. Frank Würthner für die interessante Themenvergabe, für seine stete Unterstützung und zahlreichen Ratschläge sowie für seine wissenschaftliche Betreuung und die gleichzeitig gewährten Freiheiten während der Promotionszeit. Darüber hinaus danke ich für die Bereitstellung der hervorragenden Arbeitsbedingungen im Arbeitskreis.

Weiterhin möchte ich auch Herrn Dr. Chantu R. Saha-Möller für die wissenschaftliche Betreuung sowie zahlreiche fachliche Diskussion und die Unterstützung beim Schreiben der Manuskripte danken. Auch bei Dr. David Bialas und Dr. Matthias Stolte bedanke ich mich für die Hilfe bei fachlichen Fragestellungen.

Für das Korrekturlesen dieser Arbeit danke ich herzlich Magnus Mahl, Carina Mützel, Rodger Rausch, Jessica Rühe, Alexander Schulz und Chia-An Shen.

Ganz besonders bedanke ich mich bei Anja Rausch und meiner Auszubildenden Denise Hohner für die Hilfe bei der synthetischen Arbeit. Außerdem danke ich meinen Praktikanten Ilona Paulus, Tobias Tröster, Christian Luz und Eduard Glok.

Für die Durchführung theoretischer Rechnungen möchte ich mich herzlich bei Dr. David Bialas und Dr. Joachim Lindner bedanken. Dr. Vladimir Stepanenko bin ich für die AFM-Aufnahmen zu Dank verpflichtet. Bei Dr. Matthias Grüne, Patrizia Altenberger und Marvin Grüne bedanke ich mich für die Aufnahme diverser NMR-Spektren am 600 MHz-NMR-Gerät sowie für die Unterstützung bei fachlichen Fragen. Für die Aufnahme der Massenspektren danke ich Dr. Michael Büchner, Antje Hautzinger und ganz besonders Juliane Adelmann.

Weiterhin gilt mein Dank Petra Seufert-Baumbach, Joachim Bialas und Anja Rausch für die Bestellung von Chemikalien und die Organisation eines reibungslosen Laboralltags. Bei Eleonore Klaus und Christiana Toussaint bedanke ich mich für die Hilfsbereitschaft bei Formalitäten.

Bei allen aktuellen und ehemaligen Arbeitskreismitgliedern danke ich für das wundervolle Arbeitsklima, für ihre Hilfsbereitschaft und für die schöne gemeinsame Zeit während den letzten Jahren.

Nicht zuletzt möchte ich mich auch bei meiner Familie und meinen Freunden bedanken, die mich während meines Studiums stets unterstützt haben und mir immer bedingungslos zur Seite standen.